

TECHNISCHE  
UNIVERSITÄT  
DRESDEN

---

# Chaotic transport and trapping close to regular structures in 4D symplectic maps

Dissertation  
zur Erlangung des wissenschaftlichen Grades  
Doctor rerum naturalium

vorgelegt von

Steffen Lange  
geboren am 06.02.1988 in Dresden

Institut für Theoretische Physik  
Fachrichtung Physik  
Fakultät für Mathematik und Naturwissenschaften  
Technische Universität Dresden  
2016

Eingereicht am 26. Mai 2016

1. Gutachter: Prof. Dr. Roland Ketzmerick
2. Gutachter: Prof. Dr. James Meiss

---

## Abstract

Higher-dimensional Hamiltonian systems usually exhibit a mixed phase space in which regular and chaotic motion coexist. While regular trajectories are confined to regular tori, chaotic trajectories can be transported through a web of so called resonance channels which disrupt the regular structures. The focus of this thesis are time-discrete 4D symplectic maps which represent the lowest dimensional system for which the chaotic transport can circumvent regular tori. While the dynamics of 2D maps are well established, many fundamental questions are open for maps of dimension four and higher due to this property. In particular, the mechanism of the power-law trapping is unknown for these maps. In this thesis, the organization and hierarchy of the regular structures of 4D maps is uncovered and the slow chaotic transport close to these structures is examined. Specifically, this transport is shown to be organized by a set of overlapping resonance channels. The transport across these channels is found to be governed by partial transport barriers. For the transport along a channel a stochastic process including a drift is conjectured. Based on each of these two types of chaotic transport a possible mechanism for the power-law trapping in higher-dimensional systems is proposed.

## Zusammenfassung

Der Phasenraum höherdimensionaler Hamilton'scher Systeme weist üblicherweise sowohl Bereiche regulärer als auch chaotischer Dynamik auf. Reguläre Trajektorien sind eingeschränkt auf reguläre Tori. Im Gegensatz dazu können chaotische Trajektorien durch ein Netz von sogenannten Resonanzkanälen, welche den regulären Bereich durchziehen, transportiert werden. Der Schwerpunkt dieser Doktorarbeit sind zeitdiskrete, vierdimensionale, symplektische Abbildungen, da diese das niedrigstdimensionale System darstellen für welches der chaotische Transport die regulären Tori umgehen kann. Aufgrund dieser Eigenschaft ist der chaotische Transport in vier- oder höherdimensionalen Abbildungen kaum verstanden, während die Dynamik von zweidimensionalen Abbildungen allgemein bekannt ist. Insbesondere ist die Ursache für den algebraischen Zerfall der Poincaré-Rückkehrzeiten unklar für höherdimensionale Abbildungen. In dieser Arbeit wird die Organisation und Hierarchie der regulären Tori erklärt. Es stellt sich heraus, dass der chaotische Transport in der Nähe der regulären Bereiche durch überlappende Resonanzkanäle organisiert wird. Es wird gezeigt, dass der Transport transversal zu diesen Kanälen Signaturen von partiellen Barrieren aufweist. Als Modell für den Transport entlang eines Kanals wird ein stochastischer Prozess mit einem physikalisch motivierten Drift vorgeschlagen. Ausgehend von jeder dieser beiden Transportrichtungen wird eine mögliche Ursache für den algebraischen Zerfall der Poincaré-Rückkehrzeiten hergeleitet.



# Contents

<b>1</b>	<b>Introduction</b>	<b>1</b>
<b>2</b>	<b>Regular and chaotic dynamics</b>	<b>5</b>
2.1	Dynamics of Hamiltonian mixed systems . . . . .	5
2.2	Chaotic transport and power-law trapping . . . . .	9
2.3	Example system - coupled standard map . . . . .	12
2.4	Dynamics in 2D maps . . . . .	14
2.5	Dynamics in 4D maps . . . . .	17
2.5.1	Transport and phase-space structures . . . . .	18
2.5.2	Trapping and stickiness . . . . .	19
2.6	Preliminary studies . . . . .	20
2.6.1	3D phase-space slices . . . . .	21
2.6.2	Frequency space in relation to phase space . . . . .	23
2.6.3	Power-law trapping . . . . .	24
<b>3</b>	<b>Organization of regular tori in 4D maps</b>	<b>29</b>
3.1	Skeleton of elliptic 1D tori . . . . .	30
3.2	Origins of 1D tori . . . . .	33
3.2.1	Lyapunov families . . . . .	34
3.2.2	Break-up of resonant tori . . . . .	35
3.2.3	Families due to resonant tori . . . . .	39
3.3	Hierarchy of families of elliptic 1D tori . . . . .	41
3.3.1	Self-similar hierarchy . . . . .	42
3.3.2	Frequency analysis along hierarchy . . . . .	45
3.3.3	Hierarchy of regular tori . . . . .	48
3.4	Bifurcations of families of elliptic 1D tori . . . . .	49
3.5	Coupled twist maps . . . . .	50
3.5.1	Sticky regions . . . . .	53

---

<b>4</b>	<b>Transport and trapping in 4D maps</b>	<b>59</b>
4.1	Sticky region and resonance channels . . . . .	60
4.2	Four transport processes in resonance channels (I–IV) . . . . .	69
4.3	I) Transport across a resonance channel . . . . .	81
4.4	II) Trapping in deeper class of hierarchy . . . . .	86
4.5	III) Trapping at a resonance junction . . . . .	91
4.6	IV) Transport along a resonance channel . . . . .	95
4.6.1	Stochastic processes and power-law escape . . . . .	96
4.6.2	Origin of drift along resonances . . . . .	102
4.6.3	Numerical results . . . . .	106
<b>5</b>	<b>Summary and outlook</b>	<b>113</b>
<b>A</b>	<b>Appendix</b>	<b>115</b>
A.1	Measuring transport along resonance channels . . . . .	115
A.2	Model for channel transport . . . . .	127
A.3	Resonances . . . . .	133
A.4	Resonance module and junctions . . . . .	143
A.5	Action space . . . . .	151
A.6	Action from fixed points in higher dimensions . . . . .	156
A.7	Sticky regions of 4D map $F_{\text{SC}}$ . . . . .	158
	<b>List of Figures</b>	<b>161</b>
	<b>Bibliography</b>	<b>163</b>

# 1 Introduction

Hamiltonian systems occur in many areas of physics, chemistry, and mathematics. In principle, the time evolution of a trajectory or orbit within a Hamiltonian system is uniquely determined by its initial condition in phase space, i.e. the initial coordinates of position and momentum. However, a reliable long-term prediction of this time evolution is often impossible as the dynamics typically exhibits an exponential sensitivity to the initial conditions. This phenomenon is referred to as deterministic chaos [1]. An example is the solar system which is chaotic [2] such that no reliable predictions are possible beyond sixty million years [3] and even collisions between earth and other planets may occur. The transport of orbits due to chaotic motion is denoted as chaotic transport. Understanding chaotic transport is key to, e.g., predict the stability of celestial motion [4–11], control the beams of particle accelerators [12–16], and to describe reactions of atoms and molecules [17–21].

The counterpart of chaos is regular motion which takes place on invariant regular tori. Typical Hamiltonian systems have a mixed phase space in which regions of chaotic and regular dynamics coexist. The interface between the two types of motion fundamentally affects the chaotic transport as chaotic orbits tend to stick to the vicinity of the regular phase-space structures for long times. More precisely, the probability  $P(T)$  that a chaotic orbit spends the time  $T$  in the neighborhood of these structures decays as a power law  $P(T) \sim T^{-\gamma}$ , i.e. much slower than for a fully chaotic phase space for which  $P(T)$  decays exponentially. This so-called power-law trapping entails dramatic consequences for the transport properties in many systems, e.g., comet orbits in the solar system [22], many-body systems in disordered environments [23], DNA [24], molecular diffusion [25], microwave ionization of Rydberg atoms [26, 27], and even affects quantum dynamics [28, 29]. The trapping causes anomalous diffusion, intermittent non-ergodicity, and slow decay of time correlations [30–33].

Chaotic transport in the vicinity of regular structures is well understood for Hamiltonian systems with two degrees of freedom [34]: The invariant regular tori are barriers in phase space such that chaotic orbits cannot cross them. In their vicinity so called partial transport barriers of same dimension exist which allow for a limited flux of chaotic phase-space volume across them. A hierarchy of these partial barriers governs the dynamics

and causes the power-law trapping. However, most of the relevant systems have three or more degrees of freedom and much less is known about their dynamics: A distinctive feature of these higher-dimensional systems is that the invariant regular tori have an insufficient dimension to be barriers in phase space. An intuitive way to picture this is a closed ring in a 3D space. This ring does not constitute a barrier as any two points in this space can be connected with a line which does not cross the ring. The absence of barriers has two major consequences: Firstly, chaotic orbits can get arbitrarily close to any point in phase space. Secondly, the mechanism of the power-law trapping of two degrees of freedom cannot be generalized to higher dimensions. Thus, even though the power-law trapping occurs also in higher-dimensional systems [32,35–37] its mechanism is unknown.

Understanding the regular structures and chaotic transport of higher-dimensional Hamiltonian systems is challenging as the phase space cannot directly be visualized: Time-continuous systems can be reduced to time-discrete maps, i.e. an autonomous Hamiltonian system with  $f$  degrees of freedom corresponds to a  $(2f - 2)$ -dimensional symplectic map [1]. In this sense, 4D maps are of particular interest as they represent systems with three degrees of freedom, which are the lowest dimensional systems for which chaotic transport can circumvent regular tori. Furthermore, higher-dimensional systems are usually studied in action space [38–40] or in frequency space [20,41–46], which require only half of the dimensions of the corresponding phase space. In frequency space each regular 2D torus of a 4D map is represented by a point corresponding to its two frequencies  $\boldsymbol{\nu} = (\nu_1, \nu_2) \in [0, 1]^2$ . These frequencies define the dynamics on the torus which can be locally described by action–angle variables  $\mathbf{I} \in \mathbb{R}^2$ ,  $\boldsymbol{\Theta} \in [0, 2\pi)^2$ , i.e. the  $t$ -th iteration of an orbit on the torus reads  $\mathbf{I}(t) = \text{const.}$  and  $\boldsymbol{\Theta}(t) = \boldsymbol{\Theta}_0 + 2\pi\boldsymbol{\nu}(\mathbf{I})t$ . If a system is integrable, that is all orbits lie on regular tori, a part of the frequency space is densely filled with points. If a non-integrable perturbation is added, e.g., electromagnetic fields to a hydrogen atom [18,44,47], regular tori whose frequencies are close to a resonance condition,  $\mathbf{m}\boldsymbol{\nu} = n$  for some  $\mathbf{m} \in \mathbb{Z}^2 \setminus \{\mathbf{0}\}$ ,  $n \in \mathbb{Z}$ , break up. This break-up leaves band-like gaps in frequency space, so called resonance channels, which can be accessed by chaotic orbits.

The chaotic transport in higher-dimensional maps is governed by the web of intersecting resonance channels: Chaotic orbits diffuse along the channels by various mechanisms [1,48–55] including Arnold diffusion [1,7,48,49,56]. They also can switch between overlapping channels [49,57–59] or exhibit even more complex dynamics at the junction of channels [30,31,39,41,60,61]. While the diffusion along a channel is sometimes found [43,62,63] and often assumed [39,40,64] to be normal, its generic nature remains unknown [56,65]. Some features of the chaotic transport in higher-dimensional systems



can be explained by lower-dimensional subsystems perturbing each other [32, 62, 66]. However, many generic aspects of the chaotic transport, including power-law trapping, have not been understood and are assumed to be truly higher-dimensional effects without an analog in systems with two degrees of freedom [32, 66]. While generalizations of the partial transport barriers governing the trapping in 2D maps exist [41, 67–70], these objects seem to lack a sufficient hierarchy and their influence on the higher-dimensional dynamics is hardly known. Additionally, many studies in the literature are performed on near-integrable or weakly coupled systems in which the actions and angles of the unperturbed or uncoupled system are still a good approximation to measure the chaotic transport. However, many practical applications are concerned with generic, strongly-coupled, non-perturbative systems [18, 20, 71]. These systems exhibit prominent features such as a large chaotic region surrounding regular structures and resonance channels which are reaching far into the chaotic region.

In this thesis the slow chaotic transport close to regular structures is examined for the prototypical 4D map of two coupled standard maps. Firstly, using a combination of 3D phase-space slices and frequency analysis the organization and hierarchy of the regular structures is uncovered. Secondly, the chaotic transport is shown to be organized by a set of overlapping resonance channels. While the transport across these channels is found to be governed by partial transport barriers, a stochastic process including a drift is conjectured for the transport along a channel. It is demonstrated how each of these two types of transport may constitute a mechanism for the power-law trapping.

This thesis is organized as following: Chapter 2 contains an introduction and overview of the state of the art on chaotic transport in higher-dimensional systems including a review of preliminary results of the author. In Chapter 3 it is explained how the regular 2D tori of 4D maps are arranged around a skeleton of families of elliptic 1D tori. The origins of these families are uncovered and a hierarchy of the families similar to the one present in 2D maps is constructed. Based on these insights about the organization of phase space a new designed map, the coupled twist maps, is proposed which facilitates the quantification of the generic chaotic transport. In Chapter 4 the chaotic transport and power-law trapping is discussed. Trapped orbits are found to stick to the surface of the regular structures, where their transport is organized by a set of overlapping resonance channels. This transport is decomposed into four basic phenomena which are examined separately, namely I) transport across resonance channels, II) trapping deeper into the hierarchy, III) trapping at resonance junctions, and IV) transport along resonance channels. The first three phenomena I), II), and III) are shown to be governed by higher-dimensional partial barriers. While the hierarchy and junctions appear to be less relevant for the chaotic transport, the transport between resonance channels is

shown to provide a mechanism for power-law trapping in higher-dimensional systems. However, numerical results suggest that generically IV) the transport along resonance channels is responsible for the power-law trapping. A one-dimensional stochastic model for this transport including a physically motivated drift along the channel is proposed. The challenges of a numerical verification of this model are discussed.

In conclusion, while no definite answer to the question about the mechanism of the power-law trapping is given, the results significantly advance the comprehension of transport in 4D maps. In particular, an intuitive picture of the chaotic transport near regular structures is presented, similar to the excellent understanding available for generic 2D maps. It should be possible to generalize the results from 4D maps to even higher-dimensional systems as all these systems share the crucial property that regular tori are no dynamical barriers in phase space.

## 2 Regular and chaotic dynamics

Typical Hamiltonian systems are neither integrable nor fully chaotic but have a mixed phase space in which regular and chaotic dynamics coexist. While the interface between the two types of motion has a huge impact on the chaotic transport, it is not well understood for the phase space of higher-dimensional systems. Fundamental insights about Hamiltonian systems can be obtained from the study of symplectic maps. While the mechanisms within 2D maps are well known, these results can not simply be generalized to higher-dimensional maps as their regular tori have an insufficient dimension to be barriers in phase space. The lowest-dimensional maps with this property are four-dimensional. This chapter outlines some aspects of chaotic transport with a focus on 2D and 4D maps, including the phenomenon of power-law trapping.

In Sec. 2.1 fundamental concepts of mixed Hamiltonian systems are introduced, including symplectic maps as a representation of time-continuous systems. In Sec. 2.2 the crucial role of higher-dimensional chaotic transport, in particular trapping of chaotic orbits, is reviewed. In Sec. 2.3 the coupled standard maps are introduced, which serve as a prototypical 4D map in this thesis. In Sec. 2.4 chaotic transport and phase-space structures in 2D maps are outlined. In Sec. 2.5 previous results about regular and chaotic dynamics of 4D maps are discussed. In Sec. 2.6 preliminary studies of the author are presented which demonstrate that the mechanism of the power-law trapping in 4D maps differs considerably from the one in 2D maps [72].

### 2.1 Dynamics of Hamiltonian mixed systems

Some fundamental concepts of mixed Hamiltonian systems are introduced in the following. First, basic properties of regular and chaotic dynamics are outlined, including the Kolmogorov-Arnold-Moser (KAM) theorem, which describes the coexistence of these dynamics due to resonances. Second, the transition from time-continuous Hamiltonian systems to symplectic maps is sketched. Finally, after a discussion of the stability in 2D and 4D symplectic maps the fundamental difference between 2D and all higher-dimensional maps is pointed out. A nice overview of the basic principles of Hamiltonian

systems, mixed phase space, and transport for kicked systems with one degree of freedom can be found in Michler [73, sections 2 and 3].

Consider a time-continuous Hamiltonian system  $H(\mathbf{p}, \mathbf{q}, t)$  with  $N$  degrees of freedom. This dynamical system is described in the phase space  $(\mathbf{p}, \mathbf{q}) \in U \subseteq \mathbb{R}^N \times \mathbb{R}^N$ , where  $\mathbf{p}$  and  $\mathbf{q}$  denote the momentum and the position vectors, and the time  $t \in \mathbb{R}$  [1, 74]. The canonical equations of motion are

$$\dot{\mathbf{p}} = -\frac{\partial H(\mathbf{p}, \mathbf{q}, t)}{\partial \mathbf{q}} \quad \dot{\mathbf{q}} = \frac{\partial H(\mathbf{p}, \mathbf{q}, t)}{\partial \mathbf{p}} . \quad (2.1)$$

Based on these equations an initial condition  $\mathbf{x}_0$  can be integrated to an orbit  $\mathbf{x}(t)$  with  $\mathbf{x}(0) = \mathbf{x}_0$ . For an integrable system, i.e. a system with  $N$  integrals of motion, local canonical transformation exists that converts its phase-space coordinates  $(\mathbf{p}, \mathbf{q})$  to action–angle coordinates  $(\mathbf{I}, \Theta) \in \mathbb{R}^N \times \mathbb{T}^N$  for which the equations of motions Eq. (2.1) change to

$$\dot{\mathbf{I}} = -\frac{\partial H(\mathbf{I})}{\partial \Theta} = 0 \quad \dot{\Theta} = \frac{\partial H(\mathbf{I})}{\partial \mathbf{I}} =: 2\pi\boldsymbol{\nu}(\mathbf{I}) , \quad (2.2)$$

with the  $N$ -dimensional vector of the fundamental frequencies  $\boldsymbol{\nu} \in [0, 1)^N$  and the periodic domain  $\mathbb{T} = [0, 2\pi)$  of each angle  $\Theta_i$ . The frequencies define the dynamics on a  $N$ -dimensional torus, i.e. an initial point  $\mathbf{x}_0 = (\mathbf{p}(\mathbf{I}_0, \Theta_0), \mathbf{q}(\mathbf{I}_0, \Theta_0))$  leads to a so called regular orbit

$$\mathbf{x}(t) = (\mathbf{p}(\mathbf{I}(t), \Theta(t)), \mathbf{q}(\mathbf{I}(t), \Theta(t)))$$

with

$$\mathbf{I}(t) = \mathbf{I}_0 \quad \Theta(t) = (\Theta_0 + 2\pi\boldsymbol{\nu}(\mathbf{I}_0)t) \pmod{2\pi} \quad (2.3)$$

Hence, such a regular torus is characterized by its actions  $\mathbf{I}$  which can be computed by

$$I_i = \frac{1}{2\pi} \oint_{\gamma_i} \sum_{j=1}^N p_j dq_j \quad (2.4)$$

where the closed path  $\gamma_i$  is a fundamental path on the torus parametrized by the corresponding angle  $\Theta_i \in \mathbb{T}$  and all other angles being constant. Note that the action–angle coordinates and thus also the frequencies  $\boldsymbol{\nu}$  of any torus are only defined up to unimodular transformations  $\mathcal{U} = (u_{ij})$  with  $i, j \in \{1, \dots, N\}$ ,  $u_{ij} \in \mathbb{Z}$ , and  $\det \mathcal{U} = \mathbb{I}$ ,  $\mathbb{I} \in \{-1, 1\}$ , see Ref. [75, Sec. 15] and Refs. [47, 76]. More precisely, if  $(\mathbf{I}, \Theta)$  are

action–angle variables, then  $(\tilde{\mathbf{I}}, \tilde{\Theta})$  are also action–angle variables with

$$\tilde{\mathbf{I}} = (\mathcal{U}^T)^{-1} \mathbf{I} \qquad \tilde{\Theta} = \mathcal{U} \Theta \qquad \rightarrow \qquad \tilde{\nu} = \mathcal{U} \nu . \qquad (2.5)$$

However, there is a preferred choice given by Eq. (2.4) with the minimal, fundamental paths on the torus. This action is consistent with the linearization around stable fixed points and is relevant for the quantized version of the dynamics [47]. Also note that the action along any closed path on the torus is a superposition of the fundamental actions, i.e. the action  $\tilde{I}$  along a path  $\tilde{\gamma}$  with  $m_1$  and  $m_2$  full rotations around  $\Theta_1$  and  $\Theta_2$ , respectively, is  $\tilde{I} = m_1 I_1 + m_2 I_2$ .

Generic Hamiltonian systems exhibit chaotic dynamics [74, section 1]. Chaos means that orbits  $\mathbf{x}(t)$  of the system are exponentially sensitive with respect to their initial condition  $\mathbf{x}(0)$ : a small deviation of the initial condition,  $\Delta \mathbf{x}_0 = \mathbf{x}'(0) - \mathbf{x}(0)$  with  $\|\Delta \mathbf{x}_0\| \ll 1$ , leads to an orbit  $\mathbf{x}'(t)$  exponentially diverging from the original one,  $\|\mathbf{x}(t) - \mathbf{x}'(t)\| \sim e^{\lambda t}$  with a Lyapunov exponent  $\lambda$ . Such an orbit  $\mathbf{x}(t)$  is called chaotic and regions containing just chaotic orbits are denoted chaotic as well. While a regular orbit is confined to a torus, a chaotic orbit can propagate through connected chaotic regions leading to chaotic transport in phase space.

Generic Hamiltonian systems  $H$  are neither integrable nor fully chaotic, but rather mixed [77]. An important insight about the transition from integrable to chaotic dynamics is given by the KAM theorem [1, 74]. Consider a system given in form of a sum  $H = H_0 + K \cdot H_1$  of an integrable Hamiltonian  $H_0$  and a perturbation in form of a non-integrable Hamiltonian  $K \cdot H_1$ . The parameter  $K > 0$  determines the strength of the perturbation. The KAM theorem makes statements about the tori of the phase space of  $H$ , depending on their fundamental frequencies  $\nu$ . That is, frequencies  $\nu$  fulfilling a resonance condition

$$\mathbf{m} \cdot \nu = 0 \qquad (2.6)$$

for any  $\mathbf{m} \in \mathbb{Z}^N \setminus \{\mathbf{0}\}$  are called commensurable and the corresponding torus is called resonant torus. The set of resonant tori is dense in phase space of  $H_0$  but of measure zero. The non-resonant tori with frequencies  $\nu$  in the vicinity of a resonance, i.e. for which

$$|\mathbf{m} \cdot \nu| \leq \gamma(\nu) m^{-(N+1)} \qquad m = \sum_{i=1}^N |m_i| \qquad \forall \mathbf{m} \in \mathbb{Z}^N \setminus \{\mathbf{0}\} \qquad (2.7)$$

with some factor  $\gamma(\boldsymbol{\nu})$  independent of  $K$  and the order  $m$  of the resonance  $\mathbf{m}$ , are considered to be close to resonant tori [74, section 7.3]. The remaining set of non-resonant tori, which are not close to resonant tori are of finite measure in the phase space. From Eqs. (2.3) and (2.6) follows that orbits on non-resonant tori are dense on these tori for  $t \rightarrow \infty$ .

For  $K = 0$  the phase space of  $H$  is identical to the regular phase space of the integrable Hamiltonian  $H_0$ . For a small perturbation  $K \ll 1$  all resonant and close to resonant tori cease to exist. These regular tori are replaced by chaotic regions and new regular tori of a different topology. The details of this break-up process of resonant tori are presented in Sec. 2.4 for lower-dimensional and in Sec. 3.2.2 for higher-dimensional systems. The remaining non-resonant tori are deformed but still present for a small perturbation. They are referred to as KAM tori. Hence, the former regular phase space contains now both regular regions with KAM tori and chaotic regions. Such a phase space is called near-integrable. When the perturbation is increased further, more and more KAM tori break, starting with the tori which are closest to resonances in the sense of Eq. (2.7). A broken KAM torus is called cantorus as its remnants are given by Cantor sets in phase space [78]. For a system with an external driving the resonance condition Eq. (2.6) is generalized to

$$\mathbf{m} \cdot \boldsymbol{\nu} = n \quad (2.8)$$

with  $\mathbf{m} \in \mathbb{Z}^N \setminus \{\mathbf{0}\}$  and  $n \in \mathbb{Z}$ . The resonance condition Eq. (2.8) is abbreviated as

$$\underbrace{m_1 : \dots : m_N}_N : n \quad (2.9)$$

still with order  $m$  according to Eq. (2.7) and said to be a coupling resonance if  $n = 0$  [49].

Due to energy conservation and using a stroboscopic Poincaré section the dynamics of the autonomous Hamiltonian system  $H(\mathbf{p}, \mathbf{q})$  can be reduced to a  $2N - 2$ -dimensional symplectic map  $F$  [74, section 1.3]. For instance, a 4D symplectic map corresponds either to an autonomous system with three degrees of freedom or to a system with two degrees of freedom under time-periodic driving. Symplectic means that the map  $F$  is an orientation and volume preserving diffeomorphism on the phase space

$$\begin{aligned} F: U &\rightarrow U & (\mathbf{p}', \mathbf{q}') &= F(\mathbf{p}, \mathbf{q}) \\ (DF)^T J (DF) &= J & J &= \begin{pmatrix} \mathbf{0} & -\mathbf{1} \\ \mathbf{1} & \mathbf{0} \end{pmatrix} \end{aligned} \quad (2.10)$$

with the Jacobian  $DF$  and the identity matrix  $\mathbf{1}$ . The iterations of the map  $F$  are

$$\mathbf{x}(t) = F^t(\mathbf{x}(0)) = \underbrace{F \otimes \dots \otimes F}_t(\mathbf{x}_0)$$

where the sequence  $\mathbf{x}(t)$  with  $t \in \mathbb{N}$  is called orbit with the initial condition  $\mathbf{x}(0) = \mathbf{x}_0$ . The integer iterations  $t$  represent the time and also backward iterations are possible using the inverse map  $F^{-1}$ , i.e.  $t \in \mathbb{Z}$ .

For any symplectic map  $F$  with a fixed point  $F(\vec{u}_{\text{fp}}) = \vec{u}_{\text{fp}}$  or a period- $p$  orbit  $F^p(\vec{u}_{\text{p}}) = \vec{u}_{\text{p}}$  the eigenvalues of the Jacobian matrix  $DF(\vec{u}_{\text{fp}})$  or  $DF^p(\vec{u}_{\text{p}})$  occur in form of four-tuples  $(\lambda, \bar{\lambda}, 1/\lambda, 1/\bar{\lambda})$  [1, section 3.3]. For 2D maps there are two types of fixed points. Firstly, if both eigenvalues of  $DF(\vec{u}_{\text{fp}})$  have a zero imaginary part and are not on the unit circle, then the linearized dynamics around the point  $\vec{u}_{\text{fp}}$  or  $\vec{u}_{\text{p}}$  has a stable and unstable direction and the point is called hyperbolic periodic point. Secondly, if both eigenvalues are on the unit circle, then the linearized dynamics around the point is stable and given by tori centered around the point, which is then called elliptic periodic point. In a 4D map there are four possibilities, i.e. elliptic-elliptic, elliptic-hyperbolic, hyperbolic-hyperbolic and complex unstable [79]. While the first three cases are just a combination of the 2D cases, abbreviated in the following with EE, EH, and HH, respectively, the complex unstable case means that all four eigenvalues are not on the unit circle and have a non-zero imaginary part.

According to Eq. (2.3), regular tori have codimension  $N$  in the phase space of the  $2N$ -dimensional symplectic map. For 2D maps their codimension is one, meaning that they are barriers in phase space. For all maps of dimension four and higher the regular tori have an insufficient dimension to be barriers, which makes these higher-dimensional systems fundamentally different.

## 2.2 Chaotic transport and power-law trapping

Chaotic transport in Hamiltonian systems is important in many areas of physics and chemistry. The regular phase-space structures strongly affect the chaotic dynamics in their vicinity, i.e. the chaotic transport in phase space can be slowed down considerably. For Hamiltonian systems with two degrees of freedom this is well understood [70, 80], while for higher-dimensional systems many fundamental questions remain open. In this section, the crucial role of chaotic transport in higher-dimensional systems is reviewed. The phenomenon of stickiness, especially power-law trapping, is introduced in

this section and its impact on chaotic transport is outlined. The mechanism causing the power-law trapping is a long standing open question.

As mentioned in the introduction, understanding chaotic transport is crucial to predict the stability of celestial motion [4–11], control the beams of particle accelerators [12–16], and to describe atoms and molecules [17–21]. For instance it is known that the solar system is chaotic [2] and that no reliable predictions are possible beyond sixty million years [3]. Insights about the structure of higher-dimensional phase spaces could support space missions [81]. Chaotic transport is considered in scattering processes, which are a fundamental tool to reveal characteristics of natural processes [82, 83]. Many real life systems are modeled by the coupling of two degree of freedom systems [84–86] including issues of synchronization [87–89] and thermal conductivity [90]. In chemistry chaotic transport appears for instance in connection with weak van der Waals bonds [91, 92], isomerization [30, 31], and intramolecular energy redistribution [41, 46, 60, 93]. It is interesting to note, that while molecular dynamics are of quantum nature, many insights are obtained from classical counterparts, e.g., the famous transition state theory is a purely classical theory [46, 91]. Nevertheless, many questions about the dynamics of higher-dimensional systems remain [94–96].

A particular open question concerns the power-law trapping. The Poincaré recurrence theorem states that for a symplectic map  $F$  with a confined phase space  $U$  every region  $\Gamma \subseteq U$  is mapped almost completely onto itself in the limits of large times [74, 97, section 7.1.3]. More precisely,  $\forall \mathbf{x}(0) \in \Gamma \setminus \Gamma_0: \exists t > 0: \mathbf{x}(t) \in \Gamma$ , where the excluded subset  $\Gamma_0 \subseteq \Gamma$  is of measure zero. The first time  $T$  an orbit returns to its initial region  $\Gamma$  is called Poincaré recurrence. The statistics of Poincaré recurrences  $P(T)$  gives the probability that an orbit  $\mathbf{x}(t)$ , with  $\mathbf{x}(0) \in \Gamma$ , has not returned to  $\Gamma$  until time  $T$ . As only the first recurrence is of interest here, the following sections assume that for any orbit  $\mathbf{x}(t)$  the time is bounded  $t \in [0, T]$  with the recurrence time  $T$  of the orbit.

For a fully chaotic map  $F_{\text{chaotic}}$  the statistics  $P(T)$  is analogous to the probability of a coin toss  $P_{\text{chaotic}}(T) \sim 1/2^T$ , i.e. decays exponentially  $P_{\text{chaotic}}(T) \sim e^{-\beta T}$  [98, 99]. However, in generic mixed systems chaotic orbits are observed to stick to the vicinity of the regular structures for long times. Thus, this vicinity is also called sticky region. This stickiness crucially affects the chaotic transport. Most importantly, the statistics of Poincaré recurrences exhibits a power-law decay  $P(T) \sim T^{-\gamma}$  [35]. This so called power-law trapping is well understood for 2D maps [34]. For the much less investigated higher-dimensional maps, the power-law decay of  $P(T)$  is also observed, despite the fact that these maps are fundamentally different. An explanation for the power-law trapping in higher-dimensional systems is missing so far.



As mentioned in the introduction, the power-law trapping entails dramatic consequences for classical transport, such as anomalous diffusion, and for quantum mechanical properties, such as conductance fluctuations and long-range interaction, see Refs. [20, 45, 100] and references therein. More precisely, power-law trapping causes intermittent non-ergodicity and slow decay of time correlations [101, 102] with  $1/f$  spectra [30, 31, 103, 104]. It is an origin of anomalous diffusion as the slow trapped orbits may cause subdiffusion or sticking to so called accelerator modes may enhance transport causing superdiffusion [32, 33, 105, 106]. Thus, power-law trapping is an important aspect for many systems, e.g., comet orbits in the solar system [22], many body systems in disordered environments [23], molecular diffusion [25], microwave ionization of Rydberg atoms [26, 27], and even for DNA [24]. The recurrence statistics have also been used as indicator of chaos and synchronization [107]. In chemical reactions the recurrence time is related to the reactant lifetime [91, 92, 108]. The trapping even affects quantum dynamics [28, 29], although in real systems the long time dynamics is probably governed mostly by quantum mechanical effects [91]. In 2D maps the understanding of the power-law trapping enables efficient control of this phenomenon [109].

For the well studied case of 2D symplectic generic maps the exponent  $\gamma$  of the power-law decay is found to be on average  $\gamma \approx 1.5$  [22, 34, 35, 110–113] and is believed to be universal [114–116]. Based on the trapping at marginally unstable periodic orbits an upper bound for the power-law exponent  $\gamma \leq 2$  in 2D maps is given [117]. The exponent is observed in the range  $1.1 < \gamma < 1.5$  for 4D,  $1.7 < \gamma < 2$  for 6D and  $1.3 < \gamma < 5.5$  for maps with  $N = 25$  degrees of freedom [32, 35–37] and it has been conjectured that independently of the degrees of freedom the exponent is universal  $\gamma \approx 1.3 \dots 1.4$  [37]. Note that there is a difference for the value of  $\gamma$  between maps and time-continuous systems and sometimes the power-law is more straight in the time-continuous case [22].

There are some other commonly used statistics which are related to  $P(T)$ . One is the survival time  $S(T)$ , which denotes the probability that an orbit is still in the initial region  $\Gamma$  at time  $T$ . If the initial region for the survival times  $S(T)$  is chosen to be the complement of the initial region for the Poincaré recurrences  $P(T)$  with a power-law  $P(T) \sim T^{-\gamma}$ ,  $S(T)$  exhibits a power-law  $S(T) \sim rT^{-(\gamma-1)}$  [101, 117, 118]. A third option is to measure the time orbits require to escape from a small part of the sticky region to the chaotic sea. This escape or survival time should exhibit the same long-time decay as the statistics of Poincaré recurrences.

## 2.3 Example system - coupled standard map

Higher-dimensional systems are often studied through using symplectic maps of dimension four and higher. Such maps have a lower dimension than the corresponding time-continuous systems and are numerically more convenient. A typical model system is the coupled standard map, which is mainly used in this thesis. Thus, the following sections use without loss of generality such time-discrete maps. After a short review of applications of symplectic maps, the standard map and the coupled standard map are introduced and the choice of the parameters is discussed. While in the literature 4D maps are mainly studied for weak coupling or in the near-integrable regime, the focus in this thesis is on generic, fully coupled systems. The standard map serves as reference for a generic 2D symplectic map with which the results for the higher-dimensional systems can be compared.

Symplectic maps are often used to investigate fundamental aspects of chaotic transport and instability [70]. Maps of dimension two allow to investigate chaotic transport in plasmas and fluids [119], maps of dimension two and four are used to study dynamics of particle accelerators [12, 13, 16, 38, 120], molecular fragmentation [91, 92], and galactic dynamics [4, 9, 11, 22] and are also relevant in crystal physics [121]. Coupled symplectic maps are used to understand synchronization [87, 88] and thermal conductivities [90], and can exhibit physical properties similar to those of disordered Hamiltonian systems [86].

The well studied 2D standard map corresponds to the Hamiltonian  $H_{2\text{d}}(p, q, t)$  of the kicked rotor

$$\begin{aligned}
 H_{2\text{d}}(p, q, t) &= T_{2\text{d}}(p) + \sum_{n \in \mathbb{Z}} \delta(t - n) V_{2\text{d}}(q) & T_{2\text{d}}(p) &= \frac{p^2}{2} \\
 V_{2\text{d}}(q) &= \frac{K}{4\pi^2} \cos(2\pi q)
 \end{aligned}
 \tag{2.11}$$

with the kinetic energy  $T_{2\text{d}}$ , the potential  $V_{2\text{d}}$ , and the kicking strength  $K$ . The domains are  $p \in [-0.5, 0.5)$  and  $q \in [0, 1)$  with periodic boundaries. From the Hamiltonian  $H_{2\text{d}}(p, q, t)$  follows for times  $t = n + \epsilon > n$ , right after the kick, the symplectic map  $F_{2\text{d}}$

$$\begin{aligned}
 (p', q') &= F_{2\text{d}}(p, q) \\
 p' &= p + \frac{K}{2\pi} \sin(2\pi q') \\
 q' &= q + p
 \end{aligned}
 \tag{2.12}$$

solving the equation of motion emerging from Eq. (2.11) over one period of the driving. While the system is integrable for  $K = 0$ , here usually  $K = 2.25$  or  $K = 2.5$  is chosen. For these parameters the phase space of  $F_{2D}$  has an elliptic fixed point in the center at  $(p, q) = (0, 0.5)$  surrounded by a regular island, which is embedded in a chaotic sea.

The coupled standard map, suggested by Arnold and devised by Froeschlé [122] corresponds to the Hamiltonian  $H_N(\mathbf{p}, \mathbf{q}, t)$  of  $N$  coupled, kicked rotors is

$$\begin{aligned}
 H_N(\mathbf{p}, \mathbf{q}, t) &= T_N(\mathbf{p}) + \sum_{n \in \mathbb{Z}} \delta(t - n) V_N(\mathbf{q}) & T_N(\mathbf{p}) &= \sum_{i=1}^N \frac{p_i^2}{2} \\
 V_N(\mathbf{q}) &= \sum_{i=1}^N \frac{K_i}{4\pi^2} \cos(2\pi q_i) + \frac{\xi}{4\pi^2} \cos\left(2\pi \left(\sum_{i=1}^N q_i\right)\right)
 \end{aligned} \tag{2.13}$$

with the kinetic energy  $T_N$ , the potential  $V_N$ , the kicking strengths  $K_i$  and the coupling parameter  $\xi$ . The domains of the momentum  $\mathbf{p}$  and position  $\mathbf{q}$  are  $\mathbf{p} \in [-0.5, 0.5]^N$  and  $\mathbf{q} \in [0, 1]^N$  with periodic boundaries. From the Hamiltonian  $H_N(\mathbf{p}, \mathbf{q}, t)$  follows for  $N = 2$  the two coupled standard maps  $F_{SC}$

$$\begin{aligned}
 (\mathbf{p}', \mathbf{q}') &= F_{SC}(\mathbf{p}, \mathbf{q}) \\
 p'_1 &= p_1 + \frac{K_1}{2\pi} \sin(2\pi q'_1) + \frac{\xi}{2\pi} \sin(2\pi(q'_1 + q'_2)) \\
 p'_2 &= p_2 + \frac{K_2}{2\pi} \sin(2\pi q'_2) + \frac{\xi}{2\pi} \sin(2\pi(q'_1 + q'_2)) \\
 q'_1 &= q_1 + p_1 \\
 q'_2 &= q_2 + p_2
 \end{aligned} \tag{2.14}$$

where the kicking strengths are set to  $K_1 = 2.25$  and  $K_2 = 3.0$ . A strong coupling  $\xi = 1.0$  is chosen.

The perturbation and coupling parameters  $K_i$ ,  $\xi$  are chosen large to ensure that  $F_{SC}$  is a generic 4D map. This choice is motivated by the following: In the literature usually weakly coupled systems [4, 32, 60, 62, 66, 123–126], e.g.,  $\xi < 10^{-2}$ , or near-integrable systems [39, 40, 127] are considered such that the actions of the uncoupled or unperturbed system are still a good approximation to measure chaotic transport. This also allows to obtain results by normal-form tools [39, 128–134] or other perturbative schemes [135–137]. However, many practical applications are concerned with generic, strongly coupled, non-perturbative systems [71] such as the hydrogen atom in crossed fields [18, 44, 47] or energy flow in planar OCS molecules [20, 45]. In principle, also issues of ionization, attosecond fields, and plasma oscillations should belong to this kind of systems. Thus, it is particularly relevant to investigate the dynamics in systems far

from integrability and far from fixed points. Such dynamics are studied with the chosen map  $F_{\text{SC}}$ .

The linearization of the map  $F_{\text{SC}}$  at a point  $(p_1, p_2, q_1, q_2)$  is given by the Jacobian  $DF_{\text{SC}}(\vec{u}_{\text{fp}})$

$$DF_{\text{SC}}(\mathbf{x}_f) = \left( \frac{\partial(F_{\text{SC}}(\mathbf{x}_f) \cdot \mathbf{e}_j)}{\partial x_i} \right)_{ij} = \begin{pmatrix} 1 + B_1 + C & C & B_1 + C & C \\ C & 1 + B_2 + C & C & B_2 + C \\ 1 & 0 & 1 & 0 \\ 0 & 1 & 0 & 1 \end{pmatrix}$$

with  $B_i = K_i \cos(2\pi(p_i + q_i))$  and  $C = \xi \cos(2\pi(p_1 + p_2 + q_1 + q_2))$ . Hence, the phase space of  $F_{\text{SC}}$  has an EE fixed point at the center  $\vec{u}_{\text{fp}} = (0, 0, 0.5, 0.5)$ . The eigenvalues  $(\lambda_1^{\text{fp}}, \bar{\lambda}_1^{\text{fp}}, \lambda_2^{\text{fp}}, \bar{\lambda}_2^{\text{fp}})$  of the linearized dynamics around  $\vec{u}_{\text{fp}}$  are  $(\exp(\pm i 2\pi\nu_1^{\text{fp}}), \exp(\pm i 2\pi\nu_2^{\text{fp}}))$  with  $(\nu_1^{\text{fp}}, \nu_2^{\text{fp}}) = (0.30632, 0.12173)$  and corresponding eigenvectors

$$\begin{aligned} \mathbf{v}_{1a}^{\text{fp}} &= \bar{\mathbf{v}}_{1b}^{\text{fp}} = (-0.4864, 0.7019, 0.2432 + 0.1694i, -0.3509 - 0.2445i) \\ \mathbf{v}_{2a}^{\text{fp}} &= \bar{\mathbf{v}}_{2b}^{\text{fp}} = (0.1834 - 0.4561i, 0.1271 - 0.3160i, -0.6587, -0.4565). \end{aligned} \quad (2.15)$$

The center  $\vec{u}_{\text{fp}}$  is also used as point of origin. Also the period-7 EE orbit with one point  $\vec{u}_{\text{p}} = (0.0, 0.0, 0.583438087, 0.618666288)$  is frequently used. Its eigenvalues with respect to the 7-th iteration are  $(\exp(\pm i 2\pi\nu'_1), \exp(\pm i 2\pi\nu'_2))$  with  $(\nu'_1, \nu'_2) = (0.1515, 0.0838)$ . Note that there is another period-7 orbit analogous to  $\vec{u}_{\text{p}}$  [138].

## 2.4 Dynamics in 2D maps

The dynamics of 2D maps have been extensively studied. In particular, the organization of phase space in terms of class and level hierarchies and the chaotic transport in terms of partial barriers is well known [70, 139]. Furthermore, the mechanism of the power-law decay of the statistics of Poincaré recurrences for generic 2D maps in terms of a hierarchy of partial barriers is well understood. In this section, the break-up process of resonant tori is reviewed along with the consequences for the hierarchy of the phase space and chaotic transport. In particular, some of the structures resulting from the break-up cause the trapping close to KAM tori.

According to the KAM theorem, discussed in Sec. 2.1, tori close to a resonance break up in case of a small perturbation of the integrable Hamiltonian. In the 2D phase space the tori are 1D invariant, closed lines with one fundamental frequency  $\nu$ , see Eq. (2.3). Thus, a torus is resonant if this frequency is a rational number  $\nu = n/m$ , see Eq. (2.8). Every orbit on this resonant torus is a periodic orbit with period  $m$ . The Poincaré-

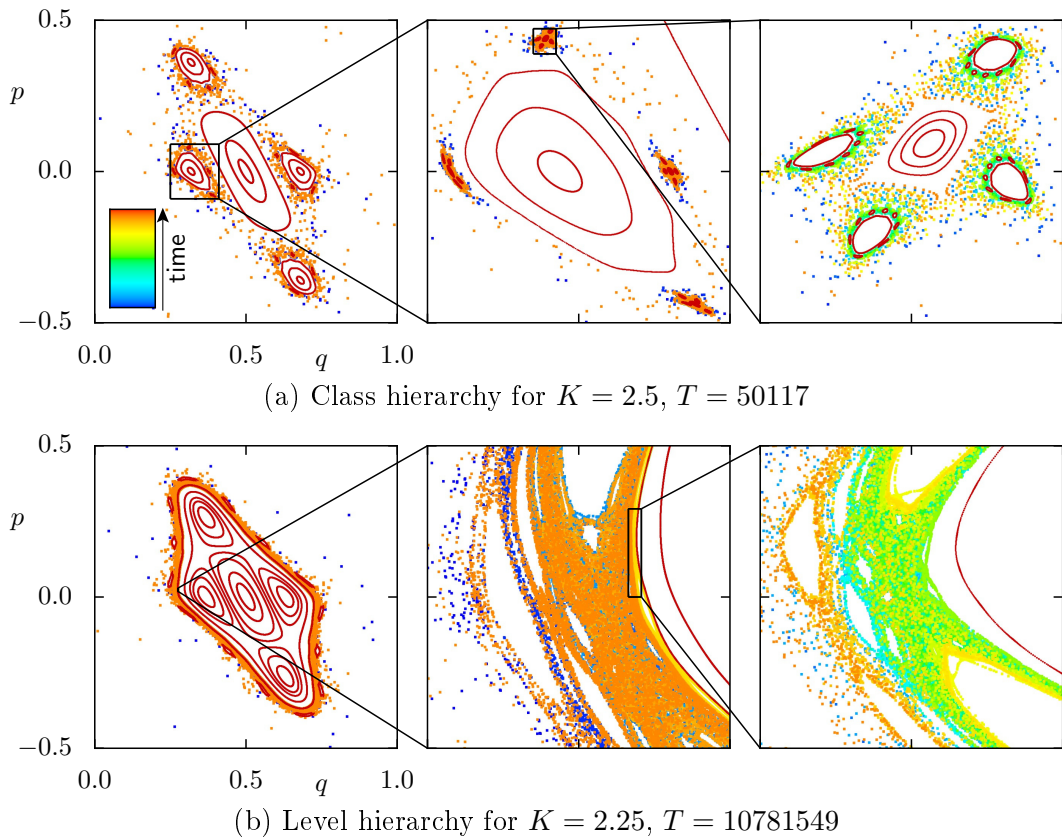


**Figure 2.1:** Chaotic orbits trapped in the hierarchical phase space of the 2D map  $F_{2D}$ , i.e. mainly trapped along (a) the class hierarchy for  $K = 2.5$  and (b) the level hierarchy for  $K = 2.25$ . The points of the chaotic orbits are colored according to their iteration time  $t \in [0, T]$  and some regular orbits are shown in red. The initial region is  $\Gamma = \{(p, q) \in U : q < 0.1\}$

Birkhoff theorem states that  $2k$  of these period- $m$  orbits with  $k \in \mathbb{N}$ ,  $k \geq 1$  remain when the resonant torus breaks up due to a perturbation. These periodic orbits form a chain of alternating hyperbolic and elliptic periodic orbits.

The dynamics in the vicinity of an elliptic point can be approximated by a Hamiltonian similar to the one presented in Sec. 2.1 given by an integrable part with a small perturbation. Hence, this subsystem denoted as regular island is again subject to both the KAM and Poincaré-Birkhoff theorem. This leads to two self-similar hierarchies of island chains in the phase space, the class hierarchy and the level hierarchy [1, 139]. It should be pointed out that recent investigations showed that while each of the hierarchies exhibits universal properties, these properties differ between the two types [140].

The class hierarchy denotes the hierarchy due to the organization of islands around islands. In Fig. 2.1(a) the phase space of the map  $F_{2D}$  for  $K = 2.5$  with some regular tori in red and one chaotic orbit colored according to its iteration time is shown on different scales in order to demonstrate the class hierarchy. In the left plot the regular

tori surrounding the elliptic fixed point in the center at  $(p, q) = (0, 0.5)$  are visible. This central island is surrounded by a period-4 island chain whose elliptic periodic orbit is part of the remains of a broken resonant torus. In the magnification of one of the subislands again four smaller subislands appear, and this hierarchy is continued for another scale. The phase space structures can be labeled according to their position in this hierarchy. For instance an elliptic fixed point of class  $c$  is surrounded by regular tori of class  $c + 1$ . A periodic orbit from a broken resonant torus of class  $c + 1$  is also  $c + 1$  and its surrounding regular tori are of class  $c + 2$ .

The level hierarchy describes the hierarchy of island chains within one class approaching the outermost KAM torus. As generally the frequencies of the regular tori around an elliptic fixed point change monotonically, there exists a series of island chains whose rational frequencies  $\nu = n/m$  approach the frequency of the outermost KAM torus. Their sequence in phase space is governed by the sequence of their frequencies. In Fig. 2.1(b) the phase space of the map  $F_{2D}$  with  $K = 2.25$  is shown analogous to Fig. 2.1(a) in order to demonstrate the class hierarchy. At this parameter the period-4 island chain is surrounded by KAM tori, which denies orbits from the chaotic sea to access the vicinity of this chain. Instead, the area filled by the chaotic orbit in the magnifications reveals several white holes corresponding to other island chains whose sequence converges to the outermost KAM torus. Note that around each of these island chains deeper classes can be found.

The hyperbolic points which are in between the elliptic points of an island chain are not shown in Fig. 2.1. The stable direction of a hyperbolic point  $\mathbf{x}_h$  gives rise to a smooth stable invariant manifold  $W^s(\mathbf{x}_h) = \{\mathbf{x} \in U : \lim_{t \rightarrow \infty} F^t \mathbf{x} = \mathbf{x}_h\}$  and the unstable direction to a smooth unstable invariant manifold  $W^u(\mathbf{x}_h) = \{\mathbf{x} \in U : \lim_{t \rightarrow \infty} F^{-t} \mathbf{x} = \mathbf{x}_h\}$ . The point intersections of two manifolds  $W^s(\mathbf{x}_h)$  and  $W^u(\tilde{\mathbf{x}}_h)$  are called homoclinic points if  $\mathbf{x}_h = \tilde{\mathbf{x}}_h$  and heteroclinic points if  $\mathbf{x}_h \neq \tilde{\mathbf{x}}_h$ . Besides being an origin of chaotic dynamics [141], these intersections give rise to partial transport barriers with a very limited chaotic flux across them. Cantori are another type of partial barrier.

In an island chain the chaotic area embedded in between the regular islands of the elliptic periodic orbits and the manifolds of the hyperbolic periodic orbits is called stochastic layer. Thus, there is chaotic dynamics in the stochastic layers while transport in between the layers of an island chain and its adjacent island chains only happens once in a while. In principle, each stochastic layer has three adjacent layers, one level towards and one level away from the outermost KAM torus of the current class  $c$ , and one class  $c + 1$  deeper into the hierarchy. Of course for some layers one level away from the outermost torus corresponds to going into a higher class  $c - 1$ . This dynamics is visible for the trapped orbits colored according to their iteration time in Fig. 2.1. In

Fig. 2.1(a) the colors of the trapped orbit illustrate how it is swiftly transported from the chaotic sea three classes deep into the hierarchy and back into the chaotic sea. Due to the decreasing flux deeper into the hierarchy, the orbit spends most of the time in the deepest class it reaches. In Fig. 2.1(b) the orbit is mostly transported from the chaotic sea along the levels towards the outermost KAM torus. The differently colored bands with sharp transitions between them demonstrate the stochastic layers with small flux in between them. Again the orbit spends most of its time within the deepest levels it reaches. In Sec. 4.2 it is demonstrated that partial barriers and the hierarchies of 2D maps are also well detectable in frequency space.

Based on the transport within the class and level hierarchy, a Markov tree can be constructed explaining the power-law decay of the statistics of Poincaré recurrences as a superposition of exponential decays from the individual layers [34]. Thus, there are log-periodic oscillations on the power-law decay observed in 2D maps. While a Markov chain can be constructed for class [105] and level [102] hierarchy individually, both hierarchies are needed to simulate the transport correctly [100]. Also note that cantori are the partial barriers which dominantly inhibit the chaotic transport [34]. Models to quantify the flux through them are based on the sequence of island chains whose rational frequencies converge towards the irrational frequency of the cantorus in terms of a continued fraction expansion.

## 2.5 Dynamics in 4D maps

The chaotic transport in terms of partial barriers as sketched in Sec. 2.4 for 2D maps can not simply be generalized to higher dimensions as the regular tori have an insufficient dimension to be barriers in phase space. This allows chaotic orbits to get transported arbitrarily close to any point in phase space by the so called Arnold diffusion. The lowest-dimensional maps with this fundamental property are 4D maps which are the focus of this thesis. In this section, previous results for phase-space structures, chaotic transport, and trapping in higher-dimensional systems are outlined. While the chaotic transport is known to be majorly organized by resonance channels, next to nothing is understood about the mechanism of the power-law trapping.

In Sec. 2.5.1 chaotic transport, relevant phase-space structures and established methods for examining higher-dimensional systems are discussed, mostly in frequency space. In Sec. 2.5.2 results on power-law trapping and stickiness are reviewed.

### 2.5.1 Transport and phase-space structures

Higher-dimensional systems are usually studied in the frequency space [20, 41–46] or the action space [38–40]. For instance, each regular 2D torus of a 4D map is represented by a point marking its two frequencies  $\boldsymbol{\nu} = (\nu_1, \nu_2) \in [0, 1]^2$  or the corresponding two actions  $\mathbf{I}$ , see Eq. (2.3). As this thesis presents results mainly in the frequency space, the action space is not discussed in the following. In an integrable system the phase space is foliated by regular tori and the frequency space is densely covered with points. But if a non-integrable perturbation is added, e.g., electromagnetic fields to a hydrogen atom [18, 44, 47], according to the KAM theorem only diophantine regular tori survive, i.e. not fulfilling Eq. (2.7). Consequently, the densely covered areas are disrupted by straight channels. While infinitely many of these so called resonance channels exist, both their width in frequency space and their phase-space volume decreases exponentially with increasing order of the resonance [39, 40, 49, 62].

The resonance channels can be accessed by chaotic orbits. One kind of chaotic transport along a channel is Arnold diffusion [1, 7, 48, 49, 56] and thus the network of intersecting channels is called Arnold web [48, 49]. Several mechanisms have been proposed in the mathematical literature in order to describe and quantify the details of Arnold diffusion [48, 49, 53–55]. For instance the heteroclinic intersections of the invariant manifolds along families of hyperbolic 1D tori are believed to mediate a transport. Five regimes of transport are usually distinguished in the Arnold web: Arnold diffusion along a single channel, modulational diffusion along partially overlapping channels [1, 52], resonance streaming along a single channel [1, 50, 51], the transport at overlapping channels, the so called Chirikov overlap [49, 57–59], and the dynamics at an intersection of two channels, so called resonance junctions [30, 31, 39, 41, 60, 61]. A junction of resonances has an intricate phase-space structure consisting of periodic orbits of different types of stability, families of elliptic and hyperbolic lower-dimensional tori, surrounding higher-dimensional tori, and corresponding invariant manifolds. Note that at resonance junctions the chaotic transport is inhibited along the resonances due to trapping [41, 60] as well as facilitated across the resonances due to resonance overlap [39, 60, 142]. The Nekhoroshev estimate gives an upper bound for the long-time stability depending on the strength of the perturbation [1, 59]. In some situations the local diffusion coefficients  $\mathbf{D}(\mathbf{I}) \in \mathbb{R}^2$  of these processes can be obtained by normal form analysis [39] or semi-analytical methods [66]. However, while the diffusion along a channel is sometimes found [43, 62, 63] and often assumed [39, 40, 64] to be normal, its generic nature is unknown [56, 65]. For instance, in some cases a subdiffusive transport is observed, which is not yet understood [66]. Furthermore, a drift along resonance chan-



nels due to the curvature of the tori is expected [143, 144]. Also for near-integrable systems [39, 40, 145] or systems consisting of two low dimensional systems which are weakly coupled [32, 62, 64, 66] the dependence of the diffusion coefficients on the strength of the perturbation [39, 40, 64, 66, 125] or the coupling parameter has been studied [4, 62, 64, 125]. The studies in weakly coupled systems traced back some features of the transport in higher-dimensional systems to effects caused by one lower-dimensional system perturbing the other [32, 62, 66]. However, many generic aspects of the chaotic transport have not been explained and are assumed to be truly higher-dimensional effects. Sometimes, chaotic transport is measured in the frequency space. For this, frequency or wavelet analysis is used to numerically assign frequencies to segments of a chaotic orbit [41, 43, 146]. Also there exist a number of chaos indicators to distinguish regular and chaotic dynamics like finite-time Lyapunov exponents [33, 147, 148], Fast Lyapunov Indicator [149–151], and many more, see e.g. [152–154] and references therein.

While the representation of regular tori in the frequency space is convenient, their organization in phase space is more complicated: For a  $2N$ -dimensional symplectic map the corresponding phase space in general contains regular tori of dimensions  $d = 0, \dots, N$  [128–131], in the following denoted as  $d$ -tori. The behavior normal to lower-dimensional tori ( $0 < d < N$ ) and fixed points ( $d = 0$ ) can be an arbitrary combination of hyperbolic and elliptic components [134, 155, 156]. A  $d$ -torus is called elliptic or hyperbolic if all its normal components are elliptic or hyperbolic [155]. Hyperbolic tori, also called whiskered tori, are important for many dynamical properties of a system including Arnold diffusion [21, 48, 95, 128, 129]. The regular tori have a hierarchical ordering in the sense that Cantor families of elliptic  $d$ -tori are arranged around elliptic  $(d-1)$ -tori for  $0 < d \leq N$  in an intricate way [134, 155, 157]. It is known that 2D tori can break up into elliptic and hyperbolic 1D tori [132] or EE, EH and HH periodic orbits [79]. There exist also some results on the bifurcation of 1D tori [158–161]. However, there is no comparable theory to Greene’s criterion in higher dimensions, which describes the robustness and destruction of multi-dimensional tori [14, 160, 162].

## 2.5.2 Trapping and stickiness

Power-law trapping is only well understood in 2D maps, where the chaotic orbits stick to the vicinity of the regular tori due to a hierarchy of partial barriers, see Sec. 2.4. These partial barriers result from stable and unstable manifolds of hyperbolic periodic orbits or cantori. While there are generalizations of these barriers to higher dimensions via normally hyperbolic invariant manifolds [68, 163–165], analogues of broken separatrices [92, 166, 167] and higher-dimensional concepts of cantori [41, 60, 67, 69], they

seem to lack a sufficient hierarchy. A nice detection of normally hyperbolic invariant manifolds in relation with the Arnold web can be found in Ref. [168]. While the existence of cantori is proven in higher-dimensional systems [69], only a few indications of their nature and manifestation have been reported [41, 46, 60]. In higher-dimensional systems such partial barriers also have holes due to intersecting resonances [41], see also the introduction of Ref. [72]. The short time behavior of the statistics of Poincaré recurrence times of 4D maps can be modeled by white noise perturbing a generic 2D map [32, 82, 108, 118, 169]. More precisely, for short times after an exponential decay due to the chaotic sea the power-law decay of an uncoupled 2D map is observed. After that, enhanced trapping  $P(T) \sim T^{-1/2}$  occurs due to a random walk within the regular island of the 2D map which is followed by an exponential cut-off due to the finite size of the island. However, for even longer times, stronger perturbation, or coupling a power-law decay is observed which can not be explained by noise on a 2D map and is suspected to be a genuinely higher-dimensional effect. Features of this higher-dimensional trapping are a very straight power-law decay without the oscillations typical for 2D systems [37] and in 4D maps both Lyapunov exponents of trapped orbits suddenly becoming close to zero [170]. It was conjectured that for higher-dimensional systems the stickiness resembles the trapping at marginally unstable periodic orbits  $P(T) \sim T^{-2}$  [117], but the relevance of such periodic orbits is questionable [169, 171]. For very large times the superexponential stickiness of Lagrangian tori may play a role [155, 172]. Also the transport in the Arnold web may cause a power-law decay due to a one-dimensional  $P(T) \sim T^{-1/2}$  or two-dimensional  $P(T) \sim T^{-1}$  random walk through the web [64, 125]. However, none of these results explain the observed power-laws. In Refs. [30, 31] orbits starting from a chaotic saddle and getting trapped in the Arnold web pass a region far away from major junctions on their way in and out of the Arnold web. This region causes a power-law decay and subdiffusion, while the junctions of the Arnold web rather cause an exponential decay and normal diffusion. This regime could be related to the trapping observed in Ref. [72], see Sec. 2.6.3.

## 2.6 Preliminary studies

In this section, studies performed by the author during his diploma thesis are reviewed [72]. The combination of a new visualization method and frequency analysis enables unprecedented insights into the higher-dimensional phase space of 4D maps. In particular, chaotic orbits are found to be trapped at the surface of regular structures outside of the usual Arnold web. In contrast to the power-law trapping in 2D maps, the trapped orbits exhibit no signs of a hierarchy. Instead, their transport seems to be

governed by a set of open resonance channels. As the presented methods are also employed in this thesis, this section also contains basic parameter choices and algorithms used in the following chapters.

In Sec. 2.6.1 the 3D phase-space slices are introduced in order to display the 4D phase space in a comprehensible way. In Sec. 2.6.2 this representation of the phase space is complemented by frequency analysis, which is also performed on trapped orbits. In Sec. 2.6.3 the preliminary results regarding trapping obtained by these methods are reviewed and illustrated, introducing the new notions of open and closed resonance channels.

### 2.6.1 3D phase-space slices

Many insights about the classical and quantum dynamics of 2D maps have been obtained from phase-space pictures, such as Fig. 2.1. Such a direct visualization of phase space is not possible for higher-dimensional systems. Starting with the pioneering work of Froeschlé [173, 174], several methods have been introduced to display the dynamics in a lower-dimensional space. Examples are two-dimensional plots of multi-sections [151, 174] or projections to two [5, 173, 175, 176] or three [177–179] dimensions, also including color to indicate the projected coordinate [180, 181], frequency analysis [41, 43, 44, 46], and action-space plots [38].

In Ref. [72] and this thesis the 4D phase space is visualized using 3D phase-space slices [182, 183]. In Fig. 2.2(a) an example for the two coupled standard maps  $F_{\text{SC}}$  is shown, where the slice condition for one coordinate is  $|p_2 - p_2^*| \leq \varepsilon$  with  $p_2^* = 0$  and  $\varepsilon = 10^{-4}$ . Whenever a point of an orbit lies within this slice, the remaining coordinates  $(p_1, q_1, q_2)$  are displayed in a 3D plot. The 3D impression is considerably enhanced when the figure is rotated. Note that more generally one can define a rotated 3D phase-space slice by the slice condition

$$|\vec{u} \cdot \vec{n} - D| \leq \varepsilon, \quad (2.16)$$

for points  $\vec{u}$  in phase space, where  $\vec{n}$  is the normal vector of the chosen slice and  $D$  is the distance of the slice to the origin.

Objects of the 4D phase space appear reduced by one dimension in the 3D phase-space slice, e.g., each 2D regular torus typically leads to a pair of 1D rings. However, also none, i.e. the slice does not intersect the torus, or more rings are possible. Periodic orbits will usually not be visible in the 3D phase-space slice. A typical chaotic trajectory fills a 4D volume in the 4D phase space. In the 3D phase-space slice this leads to a sequence of points filling a 3D volume. In Fig. 2.2(a) several groups of regular tori are displayed

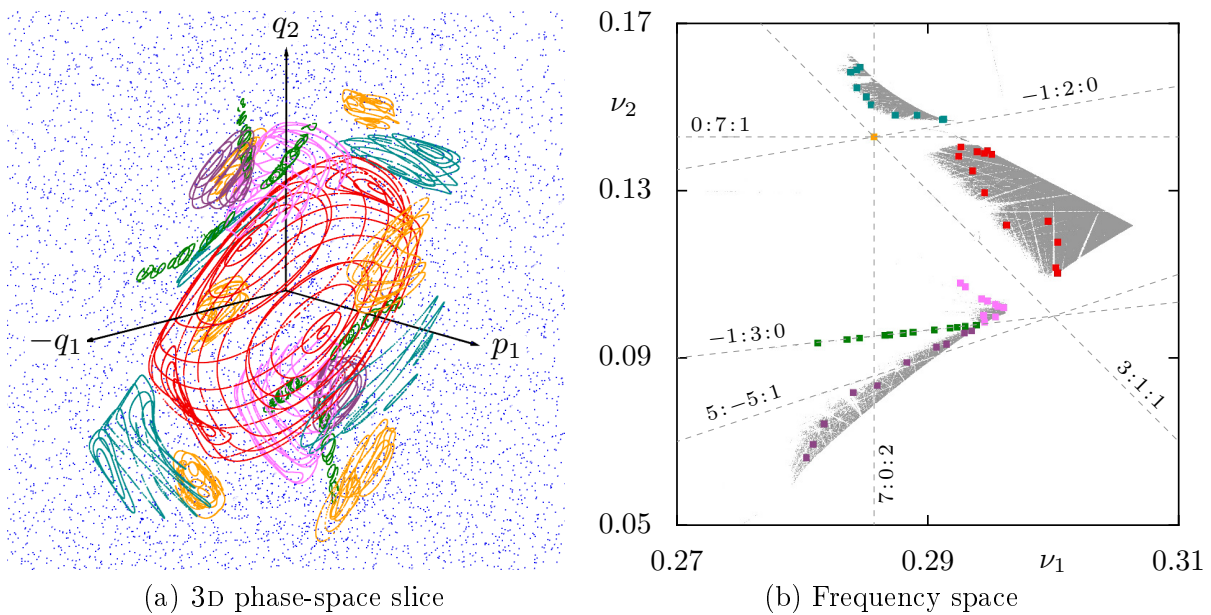


**Figure 2.2:** (a) Visualization of the phase space of the two coupled standard maps  $F_{\text{SC}}$  using a 3D phase-space slice with  $|p_2| \leq 10^{-4}$  with some regular 2D tori appearing as colored 1D lines and a chaotic orbit in blue. Each regular torus is iterated such that 4000 points are in the slice. The differently colored regions of regular tori are denoted in the text. (b) Corresponding frequency space of  $F_{\text{SC}}$  with regular tori shown as gray points. The regular tori from (a) are highlighted in corresponding colors. Some resonances are indicated as dashed lines and labeled by their coefficients  $m_1 : m_2 : n$ , see Eq. (2.8). The EE fixed point  $\vec{u}_{\text{fp}}$  corresponds to the center in (a) and to the rightmost tip in (b) with frequencies  $(\nu_1^{\text{fp}}, \nu_2^{\text{fp}}) = (0.30632, 0.12173)$ , see Sec. 2.3. [Modified from Ref. [182]]

in different colors along with a chaotic orbit in blue, which indicates the surrounding chaotic sea. This nicely demonstrates how a 3D phase-space slice allows for displaying several different orbits at the same time and provides a global visualization of their arrangement in phase space.

The different regions of regular tori colored differently in Fig. 2.2(a) are denoted as following: central island (red), horseshoe and inner end of the horseshoe (pink), outer ring (cyan), top tower (purple), region around the resonance  $-1 : 3 : 0$  (green), and period 7 islands (orange). The horseshoe, named according to the appearance of its regular tori in the 3D phase-space slice in Fig. 2.2(a), will turn out to be the most relevant region for this thesis. Also note that some of the 3D phase-space slices presented in this thesis are modified versions of slices from papers of the author. For these slices videos with a rotating view are available as supplemental material on the journals website or <http://www.comp-phys.tu-dresden.de/supp/>.

## 2.6.2 Frequency space in relation to phase space

The combination of 3D phase-space slices and the established frequency space has proven very fruitful [182]. On the one hand, the frequency space allows to explain gaps and characteristics in the phase space by resonances and to separate distinct regions. On the other hand, the 3D phase-space slices enable to interpret ambiguous frequencies, e.g., at resonances, and to consistently assign frequencies. In this section, this mutual complementation of the phase and frequency space is demonstrated for regular tori of the map  $F_{\text{SC}}$ . At the end of this section, some technical details of the frequency analysis are outlined including the parameters used throughout this thesis. Also the frequency analysis for chaotic orbits is discussed.

Each frequency pair  $(\nu_1, \nu_2)$  of a regular torus is calculated from  $\Delta t = 4096$  iterations using a fast, analytical interpolation method [146, Sec. 4.2.4]. The error of this method scales with  $\Delta t^{-4}$  like the original method of Laskar [42, 43]. The regular tori of Fig. 2.2(a) are shown in the frequency space in Fig. 2.2(b) by correspondingly colored points. The gray points represent regular tori obtained by starting  $10^8$  initial conditions with uniformly, random chosen  $p_1, p_2 \in [-0.2, 0.2]$  and  $q_1, q_2 \in [0.3, 0.7]$  in the 4D phase space of  $F_{\text{SC}}$ . Note that for strongly coupled maps far from integrability a sampling on 2D planes is not sufficient as this will typically miss some regions with regular motion. To decide whether an orbit is regular the frequency criterion

$$\max(|\nu_1 - \tilde{\nu}_1|, |\nu_2 - \tilde{\nu}_2|) < 10^{-7}, \quad (2.17)$$

is used where the frequency pair  $(\tilde{\nu}_1, \tilde{\nu}_2)$  is calculated from  $\Delta t$  further iterations. As expected, areas of gray points are disrupted by resonance channels in Fig. 2.2(b). Some important resonances are labeled and indicated by dashed lines.

A comparison as in Fig. 2.2 allows to explain features in phase space by resonances in frequency space. For instance, the orange island chain in the phase space in Fig. 2.2(a) represents a part of the junction of the resonances  $7 : 0 : 2$  and  $0 : 7 : 1$  in Fig. 2.2(a) and the green tower-like structure is caused by the resonance channel of the resonance  $-1 : 3 : 0$ . Also the gap between the cyan structure and the red one in Fig. 2.2(a) is caused by the resonance  $-1 : 2 : 0$  in Fig. 2.2(b).

Note that the frequencies  $(\nu_1, \nu_2)$  are only defined up to a unimodular transformation, see Sec. 2.1. Using the 3D phase-space slices we can choose the frequencies consistently such that regular tori which are close in phase space are also close in the frequency space. Explicitly, we make the following transformations: i) if  $\nu_i > 0.5$  then  $\nu_i \mapsto 1 - \nu_i$ , ii) if  $\nu_2 > \nu_1$  then  $(\nu_1, \nu_2) \mapsto (\nu_2, \nu_1)$ , iii) for tori of the type shown in pink in Fig. 2.2(a) with  $\nu_2 > 0.25$  we use  $(\nu_1, \nu_2) \mapsto (\nu_1, -4\nu_1 + \nu_2)$ . The resulting frequency pairs reside in

the small region of the frequency space. Determining the correct transformation is also accomplished with the help of 3D projections [182] as the remnants of broken resonant tori display a geometry from which the original resonance can be read off [132, 159], see also Sec. 3.2.2. For thin or distorted tori the computation of the correct frequency pair is challenging [72, 184, 185], as is the interpretation of frequencies with respect to different fixed structures, see Sec. 3.3.2. Note that there are a few concepts for straightening out tori analytically [71].

As mentioned in Sec. 2.5.1, frequency analysis is also applied to chaotic orbits by assigning numerical frequencies to segments of length  $\Delta t$ . More precisely, a chaotic orbit  $\mathbf{x}(t)$  with recurrence time  $T$  is mapped to a sequence of frequencies  $\boldsymbol{\nu}(t)$  by

$$\begin{aligned} \{\mathbf{x}(0), \dots, \mathbf{x}(\Delta t - 1)\} &\mapsto \boldsymbol{\nu}(0) \\ \{\mathbf{x}(\Delta t), \dots, \mathbf{x}(2\Delta t - 1)\} &\mapsto \boldsymbol{\nu}(\Delta t) \\ &\vdots \\ \{\mathbf{x}(n\Delta t), \dots, \mathbf{x}(T)\} &\mapsto \boldsymbol{\nu}(n\Delta t) \end{aligned} \tag{2.18}$$

with  $n = (\hat{T} - (\hat{T} \bmod \Delta t)) / \Delta t - 1$  and  $\hat{T} = T + 1$ . Apart from displaying  $\boldsymbol{\nu}(t)$  in the frequency space, the components can also be presented in time–frequency plots [41, 43, 60]. The frequencies are computed from the complex signal  $z_i(t) = q_i(t) - ip_i(t)$ . For the two coupled standard maps the frequencies are obtained from the first degree of freedom  $z_1(t)$  by determining the dominant frequency first, subtracting all harmonics up to order three from the Fourier spectrum and then determining the next most important frequency. For details on this procedure including pitfalls see Ref. [72]. For the coupled twist maps introduced in Sec. 3.5 each frequency  $\nu_i(t)$  is obtained as dominant frequency from the corresponding degree of freedom  $z_i(t)$ . Note that for noisy signals, like trapped orbits, one expects from considerations and numerical simulations that the interpolation method is less accurate than the original method of Laskar, in particular, frequencies tend to be shifted away from values  $\nu = j/\Delta t$ ,  $j \in N$ . This artifact depends on the strength of the noise and is not a priori problematic as for noisy signals or signals with varying frequency the mapping to a single frequency is ambiguous anyway. Nevertheless, all results are checked for consistency using both methods and for all density-like plots in chapter Sec. 4 the original method is used to avoid confusion.

### 2.6.3 Power-law trapping

In this section, preliminary results [72] regarding the power-law trapping are reviewed and illustrated. In Ref. [72] the 4D symplectic map  $F_{\text{SC}}$  is studied, which has a regular

region embedded in a large chaotic sea, i.e. it is far away from the near-integrable regime. Using a combination of 3D phase-space slices and frequency space, it could be determined that the trapped chaotic orbits, which cause the slow power-law decay of escape times, stick to the surface of the regular structures. The following statements about the power-law trapping could be made: It is clearly different from trapping in 2D maps, as the trapped orbits do not explore the hierarchy of the 4D phase space. Moreover, it is not related to the typical Arnold web. Instead, the trapped orbits seem to be governed by a heterogeneous, anisotropic, anomalous 2D stochastic process through the sticky region, which consists of a large set of overlapping resonance channels. In this context the notion of an open resonance channel is introduced. A special representation for the frequencies of the horseshoe is chosen for the following chapters.

In order to obtain the statistics of the Poincaré recurrences  $P(T)$ , see Sec. 2.2, the initial region  $\Gamma$  is chosen for the map  $F_{\text{SC}}$  with the phase space  $U$  as

$$\Gamma = \{(p_1, p_2, q_1, q_2) \in U : q_1 < 0.1\} . \quad (2.19)$$

By visualization of the phase space it is confirmed that  $\Gamma$  lies completely in the chaotic sea. The region  $\Gamma$  is indicated in Fig. 2.3 by the blue box to the left of the 3D phase-space slice shown as inset. Since  $\Gamma$  covers 10% of the phase space and the chaotic region is quite big, it is assumed that once a trapped orbit returns to the chaotic sea, it recurs. This means that for all orbits the observed effects result from the properties of a single sticky region and not from repeated trapping at different regions. In Fig. 2.3 the statistics  $P(T)$  are determined for  $F_{\text{SC}}$  using  $\approx 10^{13}$  initial conditions uniformly distributed within  $\Gamma$ . The distribution shows a very straight power-law decay  $P(T) \sim T^{-\gamma}$  with an exponent  $\gamma \approx 1.6$  over more than 5 orders of magnitude. The typical exponential decay for small times is due to the chaotic sea. The inset shows the 3D phase-space slice with the regular tori from Fig. 2.2(a) in red and a trapped orbit in blue. The trapped orbit is iterated beyond its recurrence to  $\Gamma$  in order to indicate the chaotic sea.

In order to understand the trapping mechanism frequency analysis is performed on all trapped orbits with recurrence times  $T > 10^4$ . An example is shown in Fig. 2.4 both in a conveniently chosen 3D phase-space slice and frequency space. In Fig. 2.4(a) the trapped orbit, shown as points colored by iteration time, is distributed over the surface of the regular structure, represented by regular 2D tori appearing as gray rings. In the center of the tower formed by the regular tori, a family of elliptic 1D tori is shown as orange points grouped to a line. The sticky region is even better visible in the frequency space in Fig. 2.4(b), where in addition to the frequencies of the trapped orbit and the elliptic family shown in Fig. 2.4(a) many more 2D tori in gray are included.

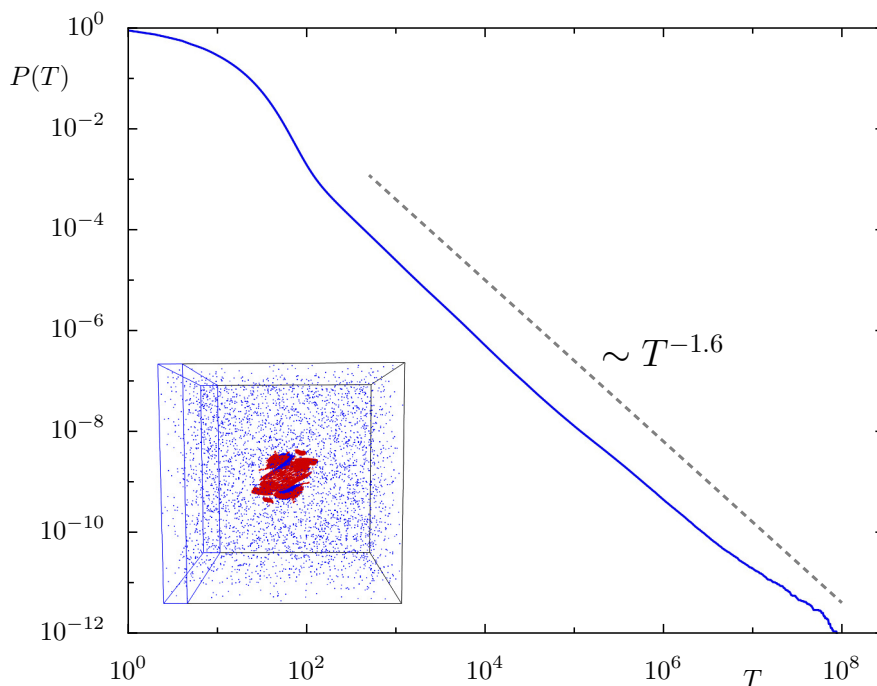


**Figure 2.3:** Statistics of Poincaré recurrences  $P(T)$  for the map  $F_{\text{SC}}$ . For comparison the gray, dashed line represents a power-law  $P(T) \sim T^{-\gamma}$ , with  $\gamma = 1.6$ . The inset sketches the position of the initial region  $\Gamma$  (blue box) in the 3D phase-space slice  $|p_2| < 10^{-5}$  with regular tori (red) and a trapped orbit (blue, iterated beyond its recurrence to indicate the chaotic sea). For the statistics about  $10^{13}$  chaotic orbits are started uniformly in  $\Gamma$  from which 8608055 have  $T > 300$  and 3354864 have  $T > 10^4$ .

More precisely, the frequency space shows that the chaotic orbit propagates through a network of overlapping resonance channels which is located at the surface of the regular region. Closer to the elliptic family in orange the resonance channels are confined by dense areas of regular tori, which makes the width of each channel visible. These confined parts of the channels are usually considered as the Arnold web. The trapped orbit does not penetrate into these parts during the considered time scales, implying that they are not necessary for the power-law trapping. Instead, in Ref. [72] the chaotic transport in the sticky region in frequency space is examined in terms of a 2D stochastic process. It turns out that the transport along the surface of the regular structure is an order of magnitude faster than the transport away from the regular structure. More precisely, the transport along the surface seems to follow a random walk, while the transport away from the region is subdiffusive. The transport in both directions gets more rapid with increasing distance to the regular structure.

As mentioned before, almost every resonance channel has two parts, an inner part being confined by regular tori and an outer part overlapping with other channels. Instructive illustrations of these two different regimes can be found in Ref. [186] and [39, Figs. 1 and 7c]. In the following, the outer part is referred to as open resonance channel and



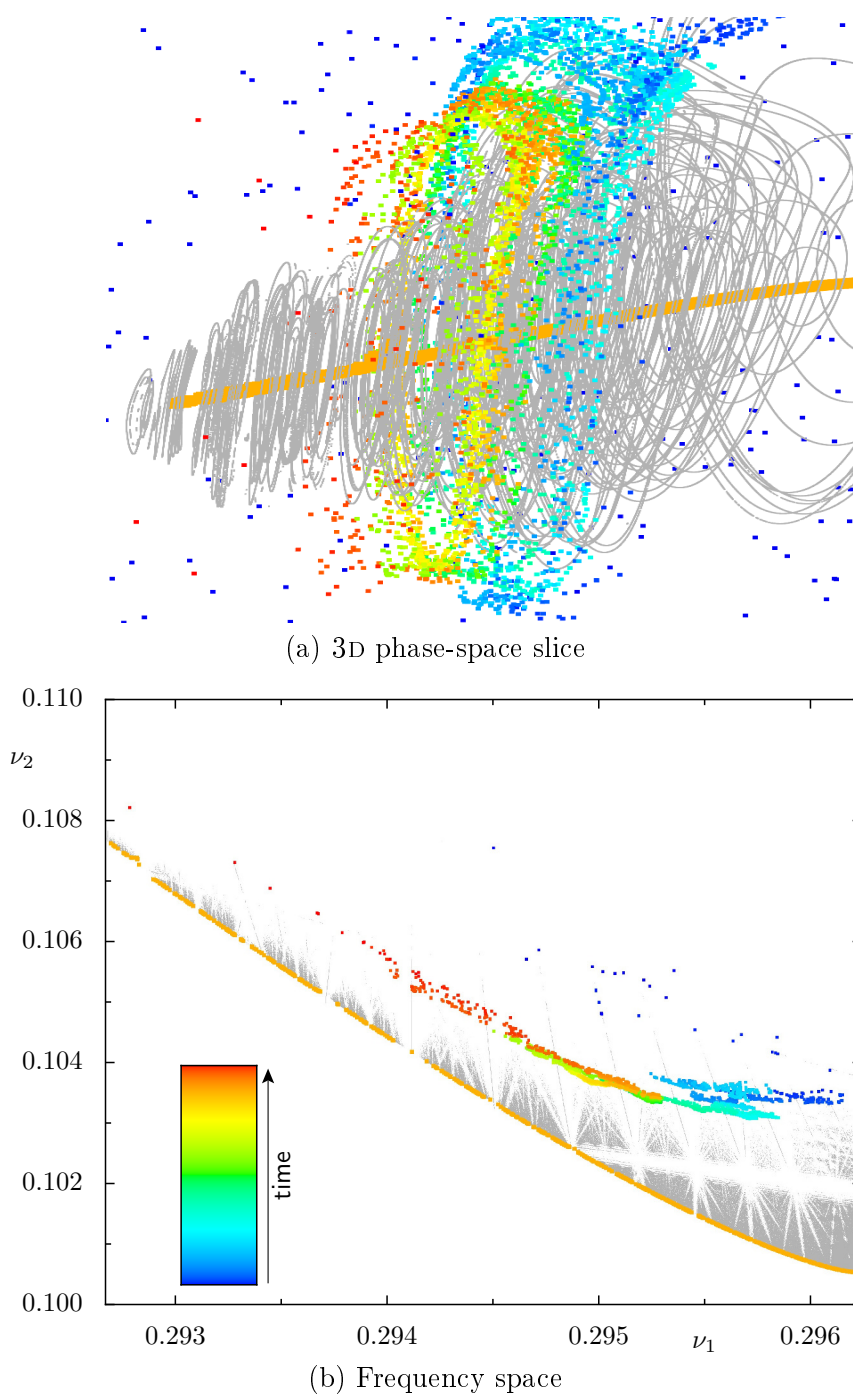


**Figure 2.4:** Chaotic orbit trapped in the neighborhood of a regular region of  $F_{SC}$  (a) in a 3D phase-space slice and (b) in frequency space with the iteration time  $t \in [0, T \approx 1.7 \cdot 10^7]$  encoded in color (see color bar), regular tori in gray, and the central family of elliptic 1D tori in orange. The parameters of the 3D phase-space slice are  $\vec{n} = (0.63234022, 0.61078167, 0.31384557, 0.35859804)$  and  $D = 0.321827835126$ , see Eq. (2.16). The regular region is the horseshoe shown in pink in Fig. 2.2. In (b) some resonance channels are visible as band shaped gaps in the gray areas and as lines populated by the gray points of the regular tori.

the inner part as closed resonance channel. As pointed out, only the open resonance channels are visited by trapped orbits for the considered time scales.

The regular region shown in Fig. 2.4 is the horseshoe shown in pink in Fig. 2.2. This region is important as most of the trapped orbits stick to this structure, i.e. 938384 of the 3354864 trapped orbits with  $T > 10^4$  stick to the horseshoe and 61600 of them even for  $T > 10^5$ , see also Sec. 4.1. However, this regular region is a result of the resonance  $3 : 1 : 1$  and thus has a fold in frequency space close-by, i.e. the torsion  $d\nu/dI$  changes sign [15, 76, 187], see Sec. 3.4 and Figs. 3.2 and A.10(b). However, due to the peculiar geometry of the regular 2D tori of the horseshoe an overtone of  $\nu_2$  is obtained from frequency analysis, allowing to distinguish the horseshoe and its surrounding from close-by regular regions, see transformation iii) in Sec. 2.6.2. In order to avoid confusion of the frequencies of the horseshoe and close-by regular regions, the transformation iii) is not performed. This means in the following the horseshoe is not shown as in Fig. 2.4(b) but rather in the untransformed frequencies also used in Ref. [72]. This representation is also beneficial as the interesting area is extended more in  $\nu_2$ -direction which resolves the details better. However, this means that in the following chapters a resonances  $k_1 : k_2 : k_3$  corresponds to resonance  $(k_1 + 4k_2) : k_2 : (k_3 + k_2)$  in the frequencies of Figs. 2.2(b) and 2.4(b). In practice, the resonances which are directed more along the surface of the horseshoe tend to have smaller order in the latter form, while the opposite is true for resonances perpendicular to the surface.

# 3 Organization of regular tori in 4D maps

In generic systems with a mixed phase space the chaotic transport is slowed down considerably in the vicinity of regular structures, which leads for instance to the power-law trapping discussed in Chapter 2. In order to study such slow chaotic transport it is important to understand the organization of the regular structures. In 2D maps regular tori are organized around elliptic periodic orbits forming a self-similar level and class hierarchy. These hierarchies are key to the power-law trapping in 2D maps. In this chapter it is revealed that the regular 2D tori in 4D maps are organized around one-parameter Cantor families of elliptic 1D tori, which exhibit a class hierarchy. This hierarchy has implications for the inner structure of resonance channels. The insight into the organization of the regular structures is exploited by designing a map which facilitates the quantification of chaotic transport notably. This map is essential for the investigation of the trapping mechanism in Chapter 4.

In Sec. 3.1 it is demonstrated how 2D tori are organized around families of elliptic 1D tori. By comparison of this organization in phase and frequency space, gaps within the regular structures are shown to be caused by resonance channels. In Sec. 3.2 features of the families of elliptic 1D tori, like origin, actions, and frequencies, are examined. In Sec. 3.3 the class hierarchy of these families analogous to 2D maps is explained. In particular, the regular structures present within any resonance channel or any resonance junction represent a deeper class. Due to the self-similarity, the trapping at these structures should be analogous to the trapping at a generic regular structure embedded in a chaotic sea. Consequently, the generic power-law trapping is relevant for the chaotic transport within any Arnold web, even for maps in the near-integrable regime. In Sec. 3.4 bifurcations along the families of elliptic 1D tori are briefly discussed. The horseshoe which is relevant for the power-law trapping in the 4D map  $F_{SC}$  is revealed to be a deeper class due to a resonance. The insights about the organization of the regular tori are exploited in Sec. 3.5 by designing a convenient map which allows for a more accurate measurement of the chaotic transport. While the map exhibits all relevant characteristics of a generic system, it also contains a region with a special

trapping mechanism, which is related to trapping along the level hierarchy in 2D maps. In addition, the hyperbolic structures which are also present are briefly discussed. Note that the results of the following sections are in part a review of papers the author co-produced [138,186] and some text passages closely follow these publications.

### 3.1 Skeleton of elliptic 1D tori

According to the literature, reviewed in Sec. 2.5.1, each regular elliptic torus of dimension  $d > 0$  is arranged around a regular elliptic torus of dimension  $d - 1$ . In this section, it is shown how in 4D maps regular 2D tori are organized around families of elliptic 1D tori. To this end, elliptic 1D tori of the two coupled standard maps  $F_{\text{SC}}$  are computed, using a refined version of an algorithm conceived in an earlier work [72], and displayed in 3D phase-space slices along with 2D tori. The algorithm is discussed in Sec. 3.3.2. A comparison with the frequency space substantiates the organization and reveals how gaps in the skeleton are due to resonances.

In order to understand the relation of 2D tori and elliptic 1D tori, consider a 2D torus which has a minor and a major radius. Contracting the minor radius, while leaving the major radius constant, results in a 1D torus or ring in the center of the original 2D torus. In case of a 4D map the tori are embedded in a 4D phase space. In a typical 3D phase-space slice the 2D torus appears as two rings and the 1D torus as two points, each in the center of one of the two rings. In this geometric sense the 2D torus is organized around the 1D torus. Since a 2D torus has codimension two in a 4D phase space this relation is not unique, i.e. several elliptic 1D tori qualify as center of a 2D torus. Performing the described contraction for many 2D tori of the two coupled standard maps  $F_{\text{SC}}$  results in colored lines in the 3D phase-space slice shown in Fig. 3.1(a). More precisely, in Fig. 3.1(a) the differently colored points of the elliptic 1D tori approximately compose 1D lines. Each gray ring, representing a 2D torus in the slice, is centered around one of these lines. This is also visible, e.g., for the 2D tori around orange and purple lines. Thus, these lines are denoted as central lines  $\mathcal{C}$ . The fact that the elliptic 1D tori compose such lines in a 3D phase-space slice implies that these tori occur as one-parameter families  $\mathcal{M}$  in the 4D phase space. Corresponding central lines  $\mathcal{C}$  and families  $\mathcal{M}$  are denoted with matching indices. Figures 3.1(c) and 3.1(d) show 3D color projections for the orange and red families  $\mathcal{M}_1^{\text{fp}}$  and  $\mathcal{M}_2^{\text{fp}}$  as well as for the purple family  $\mathcal{M}^{\text{res}}$ , respectively. In these projections the individual 1D tori are visible and they populate seemingly smooth 2D manifolds  $\mathcal{M}$ . The intersections  $\mathcal{C}$  with the 3D phase-space slice are included in the projections in the same colors as in Fig. 3.1(a). They illustrate the fact that each 1D torus intersects several times with

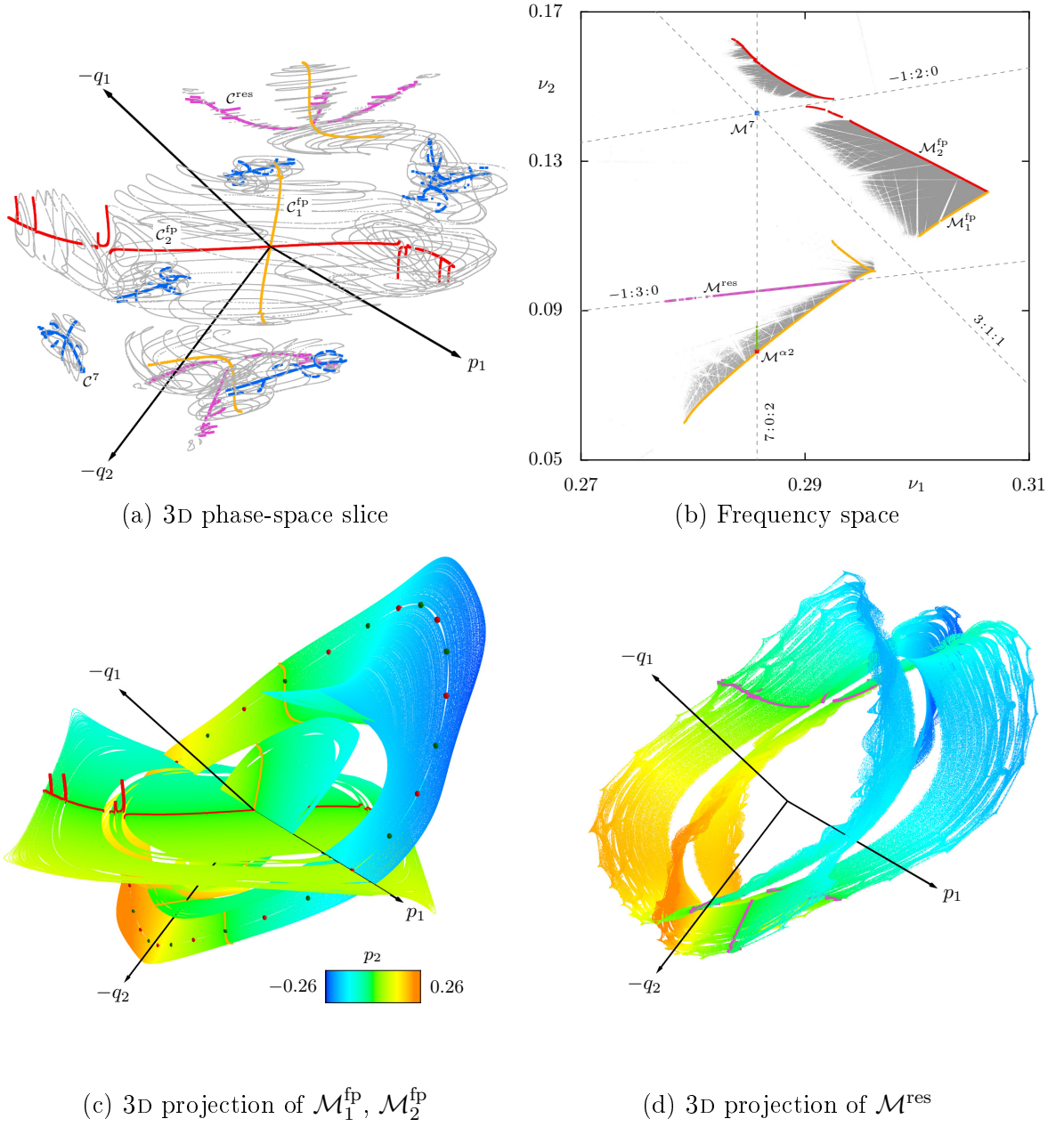


**Figure 3.1:** Visualization of the families  $\mathcal{M}_1^{\text{fp}}, \mathcal{M}_2^{\text{fp}}, \mathcal{M}^{\text{res}}$ , and  $\mathcal{M}^7$  (orange, red, blue, and purple) of elliptic 1D tori of the map  $F_{\text{SC}}$  in (a) the 3D phase-space slice  $|p_2| < 10^{-4}$ , (b) frequency space, and (c), (d) 3D projections. (a) and (b) correspond to Fig. 2.2 with regular 2D tori in gray which are organized around the families. In (c), (d) for a selection of 1000 1D tori (excluding the strong bends of  $\mathcal{M}_2^{\text{fp}}$ ) 2000 iterates under the map  $F_{\text{SC}}$  are computed and projected on  $(p_1, q_1, q_2)$  with  $p_2$  encoded in color. The intersections of the 1D tori with  $p_2 = 0$  composing the central lines  $C_1^{\text{fp}}, C_2^{\text{fp}}$ , and  $C^{\text{res}}$  are colored as in (a), (b). While the families  $\mathcal{M}_1^{\text{fp}}, \mathcal{M}_2^{\text{fp}}$  emanate from the EE fixed point  $\vec{u}_{\text{fp}}$  and continue beyond large gaps in (a) and (b),  $\mathcal{M}^{\text{res}}$  corresponds to the resonance  $-1:3:0$  and  $\mathcal{M}^7$  to the resonance junction  $(2/7, 1/7)$  as seen in (b). In (c) the spheres in a gap of  $\mathcal{M}_1^{\text{fp}}$  correspond to two EE (red) and two EH (green) period-7 orbits which are related to the family  $\mathcal{M}^{\alpha 2}$  indicated in green in (b) which is discussed in Sec. 3.3.1. [Modified from Ref. [138]]

the slice, e.g., twice in case of  $\mathcal{M}_1^{\text{fp}}$  and  $\mathcal{M}_2^{\text{fp}}$  in Fig. 3.1(c) and six times in the case of  $\mathcal{M}^{\text{res}}$  in Fig. 3.1(d). Thus, the several branches appearing for each of these examples in Fig. 3.1(a) are dynamically connected and belong to a single family of 1D tori.

In both the 3D phase-space slice and the 3D projections gaps and bends are visible along the families  $\mathcal{M}$ . These features are due to crossing resonances, which is demonstrated in the frequency space in Fig. 3.1(b). In addition to the regular 2D tori in gray the frequencies of the elliptic 1D tori of Fig. 3.1(a) are shown in corresponding colors. In contrast to a 2D torus, the dynamics on a 1D torus is only described by one longitudinal frequency  $\nu_L$ , also called intrinsic frequency. For example, in Fig. 3.1(b) this frequency  $\nu_L$  corresponds to  $\nu_1$  in case of the family  $\mathcal{M}_1^{\text{fp}}$  and to  $\nu_2$  for  $\mathcal{M}_2^{\text{fp}}$ . The remaining frequency  $\nu_N$ , called normal or librating frequency, is defined by the dynamical behavior normal to a elliptic 1D torus and can be calculated from the linearized dynamics [156, 188, 189]. Another way to interpret the normal frequency is in terms of the above described contraction, see also Sec. 3.3.2. Consider a series of 2D tori  $T_i$ ,  $i \in \mathbb{N}$  whose dynamics around the minor radius is described by a normal frequency  $\nu_{i,N}$  and around the major radius by a longitudinal frequency  $\nu_{i,L}$ . If this series contracts towards a particular 1D torus  $T_{1\text{D}}$  with frequencies  $(\nu_L, \nu_N)$ , e.g., the major radius  $r_{i,L}$  stays constant and the minor radius contracts  $r_{i,N} < r_{j,N}$  for  $i > j$ , then the 2D tori converge  $T_i \rightarrow T_{1\text{D}}$  and hence also their frequencies  $(\nu_{i,L}, \nu_{i,N}) \rightarrow (\nu_L, \nu_N)$  for  $i \rightarrow \infty$ .

In frequency space in Fig. 3.1(b), the sharp edges emanating from the EE fixed point  $(\nu_1^{\text{fp}}, \nu_2^{\text{fp}})$  correspond to the orange and red families  $\mathcal{M}_1^{\text{fp}}$  and  $\mathcal{M}_2^{\text{fp}}$ , respectively. The regular 2D tori in gray are attached to these edges, which demonstrates how the families of elliptic 1D tori also organize the 2D tori in frequency space. Since the frequencies are functionals of the actions, see Eq. (2.3), the 1D tori organize the actions of the 2D tori similarly. More precisely, in action space the families  $\mathcal{M}_1^{\text{fp}}$  and  $\mathcal{M}_2^{\text{fp}}$  lie on the  $I_2 = 0$  and  $I_1 = 0$  axis, respectively, with the actions of the 2D tori attached to them. This can be illustrated again by the series of 2D tori  $T_i$  as described above. Note that the longitudinal and normal frequencies  $(\nu_{i,L}, \nu_{i,N})$  on 2D tori  $T_i$  define the dynamics of the angle coordinates  $(\Theta_{i,L}, \Theta_{i,N})$ . The corresponding actions  $(I_{i,L}, I_{i,N})$  are defined by the pathintegrals  $I_{i,k} = 1/(2\pi) \oint_{\gamma_{i,k}} \sum_{j=1}^2 p_j dq_j$  with  $k \in \{L, N\}$  and the paths  $\gamma_{i,k}$  on a torus  $T_i$  along one angle, e.g.,  $\gamma_{i,L}$  defines the closed path with  $\Theta_{i,L} \in [0, 2\pi]$  and  $\Theta_{i,N}$  being constant, see Sec. 2.1. Obviously, the normal action  $I_N$  of a 1D torus is zero. Thus, for a contraction  $i \rightarrow \infty$  the actions of the 2D tori converge  $(I_{i,L}, I_{i,N}) \rightarrow (I_L, 0)$ . Taking into account that for the family  $\mathcal{M}_1^{\text{fp}}$  it is  $I_N = I_2$  whereas for  $\mathcal{M}_2^{\text{fp}}$  it is  $I_N = I_1$  and the fact that the actions of a fixed point are both zero, it is clear that the families reside on the corresponding axes in action space and emanate from the origin, which

represents the EE fixed point  $\vec{u}_{\text{fp}}$ . The actions of regular tori in 4D maps are discussed in more detail in Appendix A.5 including numerical results.

In the frequency space in Fig. 3.1(b) the families  $\mathcal{M}_1^{\text{fp}}$  and  $\mathcal{M}_2^{\text{fp}}$  are interrupted by resonances on arbitrary fine scale. Thus, the families of 1D tori are rather Cantor families. By comparing Figs. 3.1(a) and 3.1(b) the gaps and bends along the families in phase space can be associated to the responsible resonances. The most prominent example is the large gap in the orange family  $\mathcal{M}_1^{\text{fp}}$  with a large bend of the family on one side, which is caused by the resonance  $3 : 1 : 1$ . The different types of gaps can be explained by different types of bifurcations, see Sec. 3.4. In the frequency space also a crucial difference between the families  $\mathcal{M}_1^{\text{fp}}$  and  $\mathcal{M}_2^{\text{fp}}$  and the other families,  $\mathcal{M}^{\text{res}}$  and  $\mathcal{M}^7$ , is apparent. While the families  $\mathcal{M}_1^{\text{fp}}$  and  $\mathcal{M}_2^{\text{fp}}$  emanate from one point, that is the central EE fixed point  $\vec{u}_{\text{fp}}$ , the purple family  $\mathcal{M}^{\text{res}}$  resides on the resonance  $-1 : 3 : 0$  and the two blue families  $\mathcal{M}^7$  are confined to a junction of resonances in Fig. 3.1(b). The two families  $\mathcal{M}^7$  emanate from an EE period-7 periodic orbit  $\vec{u}_{\text{p}}$  in phase space. In the following sections, it is explained how these families and periodic orbits originate from the break-up of resonant 2D tori and how their frequencies have to be analyzed.

## 3.2 Origins of 1D tori

The regular 2D tori are organized around a skeleton of families of elliptic 1D tori. Thus, in order to understand the regular structures it is important to focus on the properties of these families. In this section, the origins of these families are explained and their actions and frequencies are discussed. The families originate either from EE periodic orbits or are due to resonances. In the latter case there exist families of hyperbolic 1D tori which are like counterparts to the elliptic families with related actions and frequencies. Each pair of an elliptic and a hyperbolic family may be considered as the skeleton of the corresponding resonance channel.

In Sec. 3.2.1 Lyapunov families from EE periodic orbits are reviewed and a nice match of their actions with predictions from the linearized dynamics is found. In Sec. 3.2.2 the break-up of resonant 2D tori is revised, including a novel type of break-up, and the geometry of remaining elliptic and hyperbolic 1D tori is discussed. Considering not a single resonant 2D torus but a whole one-parameter family of 2D tori sharing the same resonance condition gives an origin of pairs of families of elliptic and hyperbolic 1D tori. This is explained in Sec. 3.2.3 along with relations between the actions and frequencies of the two families. Also a hybrid case to which both origins apply is discussed.

### 3.2.1 Lyapunov families

At each EE periodic orbit or fixed point two families of elliptic 1D tori are attached. They are predicted by the Lyapunov center theorem [190], called Lyapunov families of invariant curves [133,156] or cantorian central submanifolds [134], and have been studied in the near-integrable regime [134, 135, 191, 192]. The frequencies  $(\nu_L, \nu_N)$  and action  $I_L$  of the elliptic 1D tori of a Lyapunov family can be approximated by the linearized dynamics at the corresponding EE point. In this section, results are presented for the example of the Lyapunov families  $\mathcal{M}_1^{\text{fp}}$  and  $\mathcal{M}_2^{\text{fp}}$  which originate from the EE fixed point  $\vec{u}_{\text{fp}}$ . Another example are the families  $\mathcal{M}^7$  originating from the period-7 EE periodic orbit  $\vec{u}_p$ . Note that certain Lyapunov families are embedded in bigger families of 1D tori, see Appendix A.4.

The normal and longitudinal frequencies  $(\nu_L, \nu_N)$  of the 1D tori of each family converge to the frequencies obtained from the linearization at the corresponding EE point. For instance, the families  $\mathcal{M}_1^{\text{fp}}$  and  $\mathcal{M}_2^{\text{fp}}$  meet in the frequency space in Fig. 3.1(b) at the frequencies  $(\nu_1^{\text{fp}}, \nu_2^{\text{fp}})$  of the EE fixed point  $\vec{u}_{\text{fp}}$ .

In the vicinity of the EE point, the actions  $I_L$  of the elliptic 1D tori can be approximated by the actions of the harmonic oscillator which is defined by the linearized dynamics in each degree of freedom at the EE point. In Appendix A.6 the linear approximation for the actions  $I_L$  in an elliptic degree of freedom of a fixed point is derived. The action  $I_L$  is expressed both with respect to the mean squared radius  $\mathbb{E}[r^2]$  and the circumference  $s$  of the 1D tori. The action  $I_L$  of a 1D torus can easily be computed by using an orbit  $\mathbf{x}(t)$  on it and its longitudinal frequency  $\nu_L$  obtained from frequency analysis. The points  $\mathbf{x}(t)$  of the orbit can be associated to angles  $\Theta(t) = 2\pi\nu_L t \pmod{2\pi}$  and ordered with ascending angle. These ordered points approximate the path along the 1D torus and thus the action  $I_L = 1/(2\pi) \oint_{\gamma_L} \sum_{j=1}^2 p_j dq_j$  can be computed numerically. Likewise, the ordered points can also be used to numerically compute the circumference  $s$  of the 1D torus. The radius  $r$  is the distance to the corresponding fixed point and the average is done for all points of the orbit. Note that using the circumference  $s$  seems more plausible, as this entity is also meaningful in the 4D space, while the radius  $r$  of a 1D closed line on a curved 2D manifold in 4D seems not well defined.

In Fig. 3.2 the linear approximations and numerical results for  $I_L$  of elliptic 1D tori of  $\mathcal{M}_1^{\text{fp}}$  and  $\mathcal{M}_2^{\text{fp}}$  are shown. The 1D tori correspond to the ones presented in Ref. [72]. For each 1D torus an orbit  $\mathbf{x}(t)$  of 2000 iterations is considered. For both dependencies  $I_L(\mathbb{E}[r^2])$  and  $I(s^2)$  the analytic approximations and the numerical results virtually coincide even far away from the fixed point. More precisely, larger deviations become visible after the crossing of the resonance  $-1 : 2 : 0$  and  $\mathcal{M}_2^{\text{fp}}$  at  $\mathbb{E}[r^2] \approx 0.02$  and



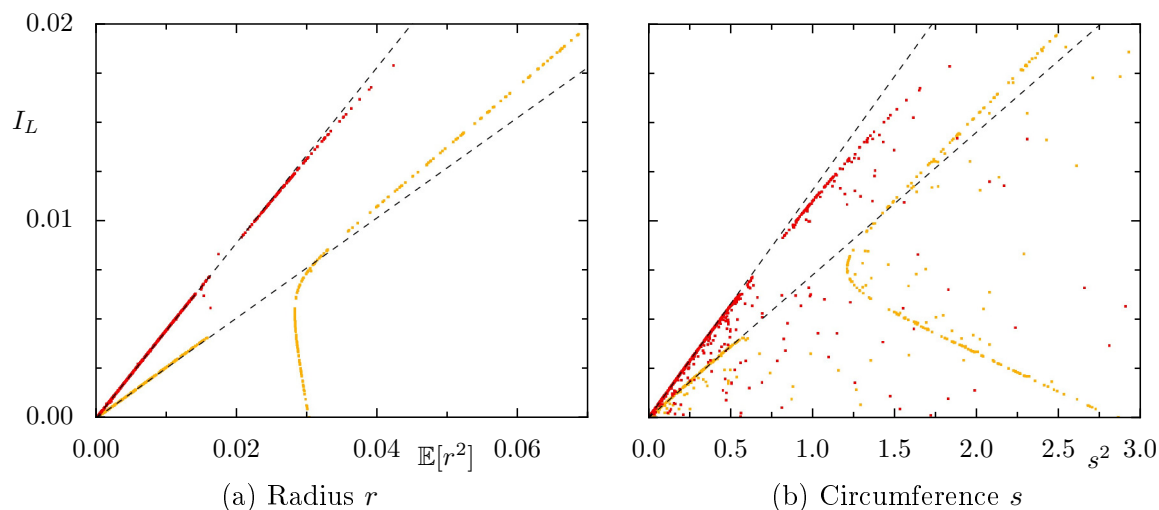


**Figure 3.2:** Actions  $I_L$  of elliptic 1D tori of the families  $\mathcal{M}_1^{\text{fp}}$ ,  $\mathcal{M}_2^{\text{fp}}$  (orange, red) with respect to their (a) mean square radius  $\mathbb{E}[r^2]$  and (b) square circumference  $s^2$ . The linear approximations obtained from the EE fixed point  $\vec{u}_{\text{fp}}$  according to Appendix A.6 are indicated as dashed lines. The parameters  $R$  and  $s_0(R)$  follow from the eigenvectors, see Eq. (2.15), i.e. for  $\mathcal{M}_1^{\text{fp}}$  and  $\mathcal{M}_2^{\text{fp}}$  one has  $R = 0.27293$ ,  $s_0(R) = 2.07325$  and  $R = 0.61041$ ,  $s_0(R) = 1.64266$ , respectively.

$s^2 \approx 0.75$  and the crossing of the resonance  $3 : 1 : 1$  and  $\mathcal{M}_1^{\text{fp}}$  at  $\mathbb{E}[r^2] \approx 0.025$  and  $s^2 \approx 1.0$ . In particular, the horseshoe corresponding to the strong bend on  $\mathcal{M}_1^{\text{fp}}$  in frequency and phase space in Fig. 3.1 due to the resonance  $3 : 1 : 1$  is visible. In Fig. 3.2(b) the numerical results are far more scattered, which illustrates that some of the used orbits actually lie on thin 2D tori instead of 1D tori. For these orbits the numerical computation of the circumference  $s$  produces always bigger values than expected from a close-by 1D torus. The mean squared radius  $\mathbb{E}[r^2]$  is more robust against such bad approximations of 1D tori.

### 3.2.2 Break-up of resonant tori

In order to understand the origin of families of elliptic 1D tori, which are not Lyapunov families due to EE fixed points, the break-up of resonant tori has to be taken into account. For this, the results of Todesco are reviewed and illustrated [132]. While these results are derived for the vicinity of an EE fixed point, the described behavior is confirmed for resonant tori far away from a fixed point and even in absence of any fixed point. In this section, it is additionally demonstrated how the geometry of the original resonant 2D torus and its resonance determine the geometry of the phase-space structures, which remain after the break-up. This includes a geometric relation between periodic orbits and 1D tori close to them. Finally, a new case, the break-up of a 1D torus

with rational longitudinal frequency is discussed along with the hierarchy of hyperbolic 1D tori <sup>1</sup>.

Without loss of generality, the following cases always consider the scenario of an original 2D torus of an integrable 4D symplectic map, which broke up according to the KAM theorem when a non-integrable perturbation was added. This break-up depends on the number  $k$  of fulfilled, linearly independent resonance conditions  $m_1\nu_1 + m_2\nu_2 = n$ ,  $m_1, m_2, n \in \mathbb{Z}$ , denoted as *rank*  $k$ , and whether the resonance is *coupled* or *uncoupled*. The four possible cases are illustrated by examples from the two coupled standard maps  $F_{\text{SC}}$  in phase space and the frequency plane, see Fig. 3.3. Note that Fig. 3.3(a) is a detail of the frequency space in Fig. 3.1(b). The example tori are chosen as close as possible to each other such that the geometry of their original 2D tori resemble each other. Thus, the examples look like different cases of resonances for geometrically the same torus. The involved hyperbolic 1D tori are not shown but are added in Ref. [189].

*Rank-0*: On a non-resonant 2D torus of the integrable system each orbit is dense. Such a 2D torus will in general survive a perturbation and just be deformed. An example is shown in Fig. 3.3(b) and marked as point  $\textcircled{b}$  in Fig. 3.3(a). Such 2D tori have been called *rotational* [179, 181] but are actually *librational* as they are contractable [1].

*Rank-1, uncoupled*: If one uncoupled resonance condition  $m_1\nu_1 = n$  with  $m_1 \neq 0$  is fulfilled on a 2D torus of the integrable system, each orbit on it densely fills  $m_1$  disjoint lines. At least  $2m_1$  of these infinite number of lines survive a perturbation, alternating between normally elliptic and normally hyperbolic [193]. An example is shown in Fig. 3.3(c) and marked as point  $\textcircled{c}$  in Fig. 3.3(a). The original 2D torus broke since it was on the resonance  $7 : 0 : 2$  leaving a 1D torus consisting of seven elliptic lines (hyperbolic lines not shown). This 1D torus is displayed in Fig. 3.3(c) along with a 2D torus from its elliptic surrounding. In this example there are another seven elliptic lines, which are not shown.

*Rank-1, coupled*: If one coupled resonance condition with both  $m_1$  and  $m_2$  non-zero is fulfilled on a 2D torus of the integrable system, each orbit on it densely fills  $\text{gcd}(m_1, m_2)$  disjoint lines [159]. At least one elliptic and one hyperbolic line survive a perturbation. An example is shown in Fig. 3.3(d) and marked as point  $\textcircled{d}$  in Fig. 3.3(a). The original 2D torus broke since it was on the resonance  $-1 : 3 : 0$  leaving one elliptic line (hyperbolic line not shown). This 1D torus and a thin 2D torus from its elliptic surrounding are displayed in Fig. 3.3(d). Such 2D tori of rank-1 resonances have been called *tube tori* [179, 181].

---

<sup>1</sup>The discussion quotes several passages of a section of Ref. [138]. For brevity, these passages are not individually indicated.

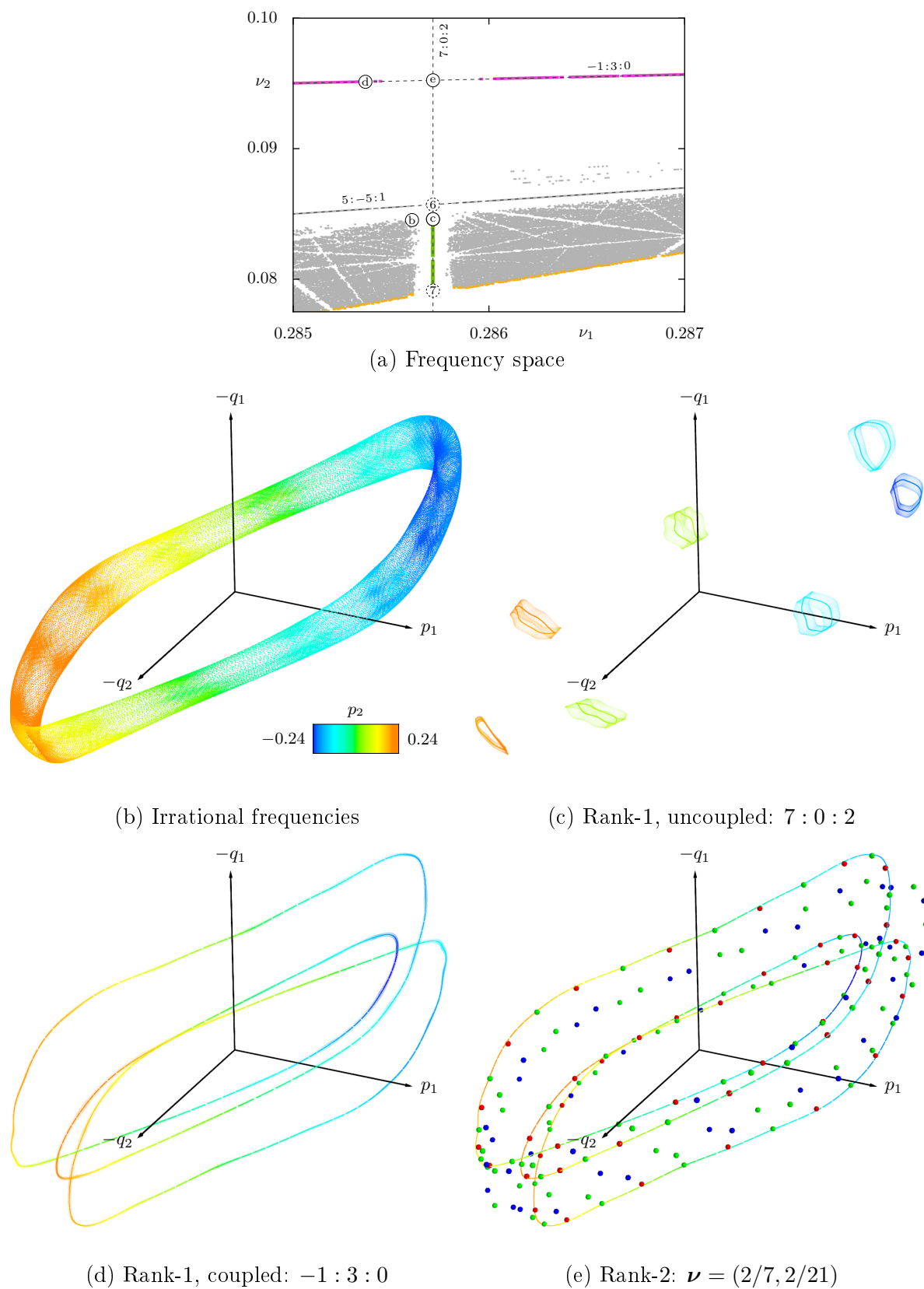


**Figure 3.3:** Illustration of the break-up of resonant 2D tori in (a) frequency space and (b)–(d) 3D projections as in Fig. 3.1. (a) Detail of Fig. 3.1(b) with circled letters marking the frequencies of the example tori (b)–(e) and Fig. 3.4. In (c), (d) an elliptic 1D torus and a surrounding 2D torus are shown and in (e) the 1D torus of (d) is added for comparison with the EE (red), EH (green), and HH (blue) period-21 orbits. [Modified from Ref. [138]]

*Rank-2 (resonance junction):* If two independent resonance conditions are fulfilled on a 2D torus of the integrable system, each orbit on it is periodic. If such a resonance junction is at  $(\nu_1 = n_1/m_1, \nu_2 = n_2/m_2)$  then the period is given by  $lcm(m_1, m_2)$ . At least four periodic orbits survive a perturbation: either one EE, one HH, and two EH periodic orbits or two complex unstable and two EH periodic orbits. Such a break-up has also been derived from symmetry considerations [79] and has been analyzed also for the case of strong resonances [61]. An example for a rank-2 resonance is shown in Fig. 3.3(e) and marked as point ⑤ in Fig. 3.3(a). The original 2D torus broke since it was at the intersection of the resonances  $7 : 0 : 2$  and  $-1 : 3 : 0$  leaving two EE, two HH, and four EH periodic orbits of period 21. The twofold number of periodic orbits is analogous to the twofold number of surviving 1D tori for the resonance  $7 : 0 : 2$ . Another example for a rank-2 resonance are the period-7 orbits  $\vec{u}_p$  from which the blue family  $\mathcal{M}^7$  in Fig. 3.1(a) emanates. These periodic orbits result from the rank-2 resonance at the intersection of the resonances  $7 : 0 : 2$  and  $3 : 1 : 1$ , see Fig. 3.1(b). Note that a resonance junction is an intricate region in phase space, considering the phase space structures associated with the periodic orbits, like stable and unstable 2D manifolds. Note that at any resonance junction infinitely many resonance conditions are fulfilled. In Appendix A.4 a semi-analytical procedure is derived to determine the lowest order resonance of a junction.

For reasons of continuity the periodic orbits due to a rank-2 resonance are expected to be located where the surviving lines of the two crossing rank-1 resonances get close to each other in phase space. For example, an EE periodic orbit is expected, where an elliptic line of the first rank-1 resonance and an elliptic line of the second one get close to each other. This is illustrated by the rank-2 resonance in Fig. 3.4(a) which is marked as point ⑥ in Fig. 3.3(a). There each of the elliptic 1D tori of the resonances  $5 : -5 : 1$  and  $7 : 0 : 2$  almost coincides with a chain of alternating EE and EH periodic orbits. EE points occur where these elliptic 1D tori almost intersect. Note again that there exists another elliptic 1D torus from the resonance  $7 : 0 : 2$  in between the shown ones.

From this argument also the number and stability of periodic orbits resulting from a rank-2 resonance becomes plausible: The elliptic ( $E_1$ ) and the hyperbolic ( $H_1$ ) line of the first rank-1 resonance intersect in four kind of points with the elliptic ( $E_2$ ) and hyperbolic ( $H_2$ ) line of a second rank-1 resonance, giving periodic orbits with stability  $E_1E_2$ ,  $E_1H_2$ ,  $E_2H_1$ , and  $H_1H_2$ .

An origin for periodic orbits not discussed in the literature is the break-up of an elliptic 1D torus with rational longitudinal frequency. It is observed that from this break-up a one-dimensional chain of EE and EH periodic orbits arises. This case is illustrated in Fig. 3.4(b) for the intersection of the  $7 : 0 : 2$  resonance and  $\mathcal{M}_1^{\text{fp}}$ , which

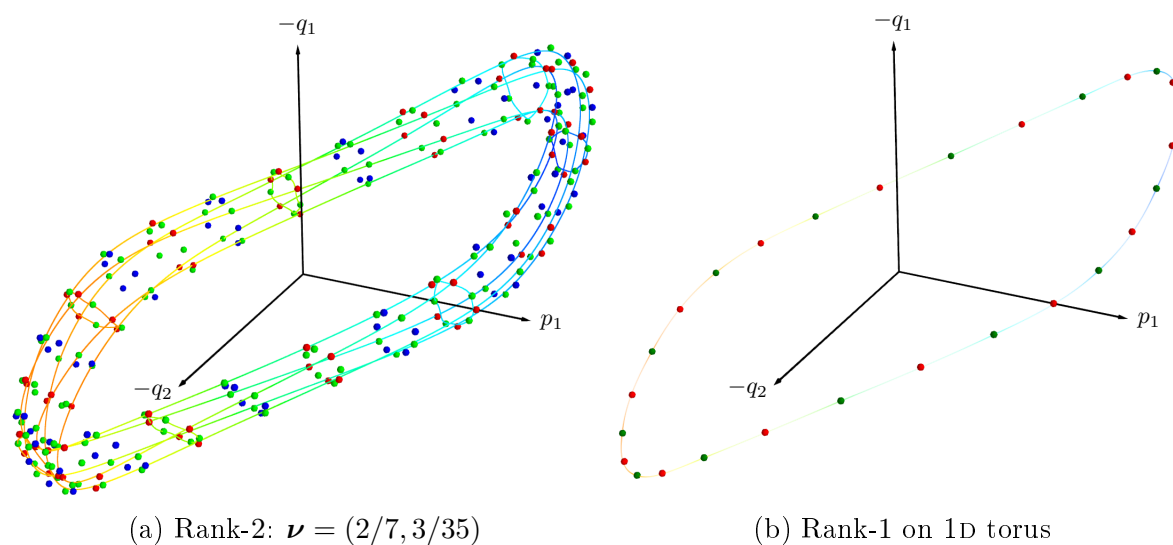


**Figure 3.4:** Arrangement of EE (red), EH (green), and HH (blue) periodic orbits. (a) Rank-2 resonance at the junction of the resonances  $5 : -5 : 1$  and  $7 : 0 : 2$  (marked by ⑥ in Fig. 3.3(a)). Two EE, four EH, and two HH period-35 orbits and two elliptic 1D tori, one from the resonance  $5 : -5 : 1$  and one from Fig. 3.3(c), are shown. (b) Alternating 1D chain of EE, EH period-7 orbits (also shown in Fig. 3.1(c)) at the intersection of the resonance  $7 : 0 : 2$  and the family  $\mathcal{M}_1^{\text{fp}}$  (marked by ⑦ in Fig. 3.3(a)) with a close-by elliptic 1D torus of  $\mathcal{M}_1^{\text{fp}}$  for comparison. [Modified from Ref. [138]]

is marked as point ⑦ in Fig. 3.3(a). This example is also included in Fig. 3.1(b) where the two EE and two EH period-7 periodic orbit appear as an alternating chain in a small gap of  $\mathcal{M}_1^{\text{fp}}$ . As demonstrated by the example, the break-up of a 1D torus with rational frequency looks like an application of the Poincaré-Birkhoff theorem of 2D maps to the 2D manifold of the family  $\mathcal{M}_1^{\text{fp}}$ . In particular, the hyperbolic degree of freedom of the EH orbit and one elliptic degree of freedom of the EE orbit are embedded within this manifold, see Sec. 3.3.1. This break-up scenario also applies to hyperbolic 1D tori with rational frequency, which break up into a chain of EH and HH periodic orbits. However, the family of hyperbolic 1D tori originating from such a EH periodic orbit is embedded within the bigger family of hyperbolic 1D tori. Thus, families of hyperbolic 1D tori do not cause further large families outside of themselves and the hierarchy within them is neglected in the following sections.

### 3.2.3 Families due to resonant tori

In this section, the results of the previous section are used to explain the origin of families of elliptic 1D tori like  $\mathcal{M}^{\text{res}}$ , which are not Lyapunov families of EE fixed points or periodic orbits: Such a family arises from the break-up of a one-parameter family of 2D tori which share the same resonance condition. In particular, no fixed point or

periodic orbit is required. Some properties of these families resulting from resonances are discussed as well as their relevance for resonance channels. Also a hybrid case is mentioned.

According to the previous section, a 2D torus whose frequencies  $(\nu_1, \nu_2)$  fulfill a single resonance condition  $m_1\nu_1 + m_2\nu_2 = n$  with  $m_1, m_2, n \in \mathbb{Z}$  breaks up into an equal number of elliptic and hyperbolic 1D tori. As a resonance condition defines a line in frequency space, in an integrable 4D map generically a one-parameter family of 2D tori exists fulfilling this condition. Consequently, for each family at least two one-parameter Cantor families of 1D tori, one hyperbolic and one elliptic, should remain when a perturbation is added. The position of these 1D tori is such that they form the manifolds described in Sec. 3.1. An example is the family  $\mathcal{M}^{\text{res}}$  shown in purple in Fig. 3.1 which originates in this sense from the resonance  $-1 : 3 : 0$ . In the frequency space in Fig. 3.1(b) the results of the frequency analysis for these 1D tori all fall on this resonance line. This is caused by the geometry of these 1D tori, which resembles orbits on the original resonant 2D tori, as seen in Fig. 3.3(d). Due to that the resonant frequencies of the broken 2D tori are dominant in the Fourier spectrum of these 1D tori and their surrounding structures. The longitudinal and normal frequencies of these 1D tori are discussed in Secs. 3.3.1 and 3.3.2. In Ref. [189] several other examples of families of 1D tori resulting from single resonances are presented, including the hyperbolic 1D tori.

The families of hyperbolic and elliptic 1D tori arising from resonances have several related properties. Each of these elliptic 1D tori has a hyperbolic counterpart which originates from the same resonant 2D torus. Thus, the hyperbolic and elliptic 1D torus have the same longitudinal frequency  $\nu_L$ . They also have a similar longitudinal action  $I_L$ . More precisely, as the 1D tori described equivalent paths on the resonant 2D torus, their action  $I_L$  is approximately the action  $\tilde{I}_L$  along this path on the 2D torus. Note that this action  $\tilde{I}_L$  is a superposition of the fundamental actions  $(I_1, I_2)$  of the 2D torus see Sec. 2.1, i.e. in case of a resonance  $m_1\nu_1 + m_2\nu_2 = n$  the action is  $I_L \approx \tilde{I}_L = m_2I_1 + m_1I_2$ . In Appendix A.5 an application of this fact is discussed. The deviation of  $I_L$  from  $\tilde{I}_L$  is expected to increase with the strength of the perturbation. This is also expected for the difference between  $I_L$  for the elliptic and the hyperbolic 1D torus, which should be analogous to the action difference of minimax and minimizing orbits in 2D maps [80]. In Ref. [189] these relations of the actions are mostly confirmed. There also is a proximity between the normal frequency  $\nu_N$  of the elliptic and the Lyapunov exponent  $\lambda_N$  of the hyperbolic 1D torus originating from the same resonant 2D torus is found  $2\pi\nu_N \approx \lambda$ , which can be explained by the linearized dynamics.

It should be pointed out that the families of hyperbolic and elliptic 1D tori arising from resonances form essentially the skeleton of the corresponding resonance channel. In particular, the transport along and the escape from a channel are expected to be largely governed by the stable and unstable manifolds of the hyperbolic 1D tori. Thus, it is important to study these families.

Finally, note that the case of an elliptic 1D torus with rational longitudinal frequency  $\nu_L = n/m$  mentioned in Sec. 3.2.2 causes hybrid families of elliptic and hyperbolic 1D tori. The EE and EH periodic orbits remaining after the break-up of such a rational 1D torus are the origin of two special families. That is, one family of elliptic and one family of hyperbolic 1D tori, respectively, which are not embedded in the family of elliptic 1D tori to which the rational 1D torus belongs. Since these families emanate from periodic orbits, they are Lyapunov families, see Sec. 3.2.1. However, they also coincide with the families caused by the uncoupled resonance condition  $m\nu_L + 0 \cdot \nu_N = n$ . An example for this hybrid case is the family  $\mathcal{M}^{\alpha 2}$  from the intersection of the resonance  $7 : 0 : 2$  with the family  $\mathcal{M}_1^{\text{fp}}$  highlighted in green in Figs. 3.1(b) and 3.3(a).

### 3.3 Hierarchy of families of elliptic 1D tori

In symplectic 2D maps the regular 1D tori are not only organized around elliptic periodic orbits, but there are two hierarchies of these orbits, namely classes and levels, as outlined in Sec. 2.4. As explained in the previous sections, in symplectic 4D maps the regular 2D tori are organized around families of elliptic 1D tori. In this section, a hierarchy of these families analogous to the hierarchy of classes, also called islands-around-islands, in 2D maps is established. In particular, there are three principal ways to continue the hierarchy into a deeper class that is by  $(\alpha_1)$  two resonance conditions on a 2D torus,  $(\beta)$  one resonance condition on a one-parameter family of 2D tori, or  $(\alpha_2)$  one uncoupled resonance condition on a 1D torus. As mentioned in the previous sections, the case  $(\alpha_1)$  is present at every resonance junction and the case  $(\beta)$  in every resonance channel. Hence, trapping at the regular structures within the Arnold web means trapping in a deeper class. Due to the self-similarity along the hierarchy, understanding the mechanism of power-law trapping implies understanding the influence of the regular structures within the Arnold web.

In Sec. 3.3.1 the three possible cases for one step deeper into the class hierarchy is explained in phase and frequency space and the self-similarity is pointed out. Due to this similarity the hierarchy can be continued along any resonance or resonance junction into deeper classes. In Sec. 3.3.2 a general way to perform the frequency analysis for a deeper class is described. This is crucial for examining trapping in a deeper class

and supports future studies of scaling and universality along the hierarchy. Also the longitudinal frequencies of the deeper class are essential for many algorithms which compute invariant structures. In Sec. 3.3.3 the order and labeling of the classes along the hierarchy analogous to 2D maps is introduced. Note that the hierarchy of the hyperbolic structures is briefly discussed in Secs. 3.2.2 and 3.3.3.

### 3.3.1 Self-similar hierarchy

The didactic scenario of Secs. 3.2.2 and 3.2.3 is an integrable system to which a non-integrable perturbation is added: Families of elliptic 1D tori in the perturbed system in principle originate from the break-up of resonant 2D or 1D tori of the integrable system. This implies that the 2D tori which are organized around such families in the perturbed system do not exist in the integrable system. In this sense, these 2D tori are in a deeper class than the 2D tori which exist in both systems, i.e. which survive the perturbation. In this section, the similarity between two consecutive classes is illustrated for the three possible origins  $(\alpha_1)$ ,  $(\beta)$ ,  $(\alpha_2)$  of families of elliptic 1D tori. A family of elliptic 1D tori is either  $(\alpha_1, \alpha_2)$  attached to EE periodic orbits or  $(\beta)$  the remains of broken 2D tori sharing a single resonance condition. The EE periodic orbits can arise from  $(\alpha_1)$  resonance junctions, i.e. broken 2D tori fulfilling more than one resonance condition, or  $(\alpha_2)$  broken elliptic 1D tori with rational longitudinal frequency.

Consider the EE fixed point  $\vec{u}_{\text{fp}}$  and the attached families  $\mathcal{M}_1^{\text{fp}}$  and  $\mathcal{M}_2^{\text{fp}}$  as the top class of the 4D map  $F_{\text{SC}}$ , see Fig. 3.1. Then, according to Secs. 3.1 and 3.2 the families  $\mathcal{M}^7$ ,  $\mathcal{M}^{\text{res}}$ , and  $\mathcal{M}^{\alpha_2}$  are examples for the cases  $(\alpha_1)$ ,  $(\beta)$ , and  $(\alpha_2)$ , respectively. In Fig. 3.5 each of these families and their surrounding 2D tori are presented in detail in a 3D phase-space slice and frequency space. As mentioned in Sec. 3.2.3, a straightforward frequency analysis for these structures produces the resonant frequencies of the broken 2D tori, from which the structures originate. In contrast, here the frequency analysis is performed with respect to the organizing center of each case, as explained in detail in the following and in Sec. 3.3.2.

$(\alpha_1)$  In Fig. 3.5(a) a detail around one of the EE periodic points  $\vec{u}_{\text{p}}$  from which the families  $\mathcal{M}^7$  emanate, more precisely now  $\mathcal{M}^7_1$  and  $\mathcal{M}^7_2$ , is magnified. The periodic point  $\vec{u}_{\text{p}}$  is shown in purple and the central lines  $\mathcal{C}^7_1$  and  $\mathcal{C}^7_2$  of the families are shown in blue and labeled accordingly. Along with the surrounding 2D tori in gray the regular structure in Fig. 3.5(a) is equivalently organized as the regular structure on the top class with  $\mathcal{M}_1^{\text{fp}}$ ,  $\mathcal{M}_2^{\text{fp}}$ ,  $\vec{u}_{\text{fp}}$  and resembles the structure in Fig. 3.1(a). While the frequency analysis for all these tori produces  $(\nu_1, \nu_2) = (2/7, 1/7)$ , a frequency analysis using only every 7-th point of each orbit produces the frequencies  $(\nu'_1, \nu'_2)$  shown in Fig. 3.5(b) in



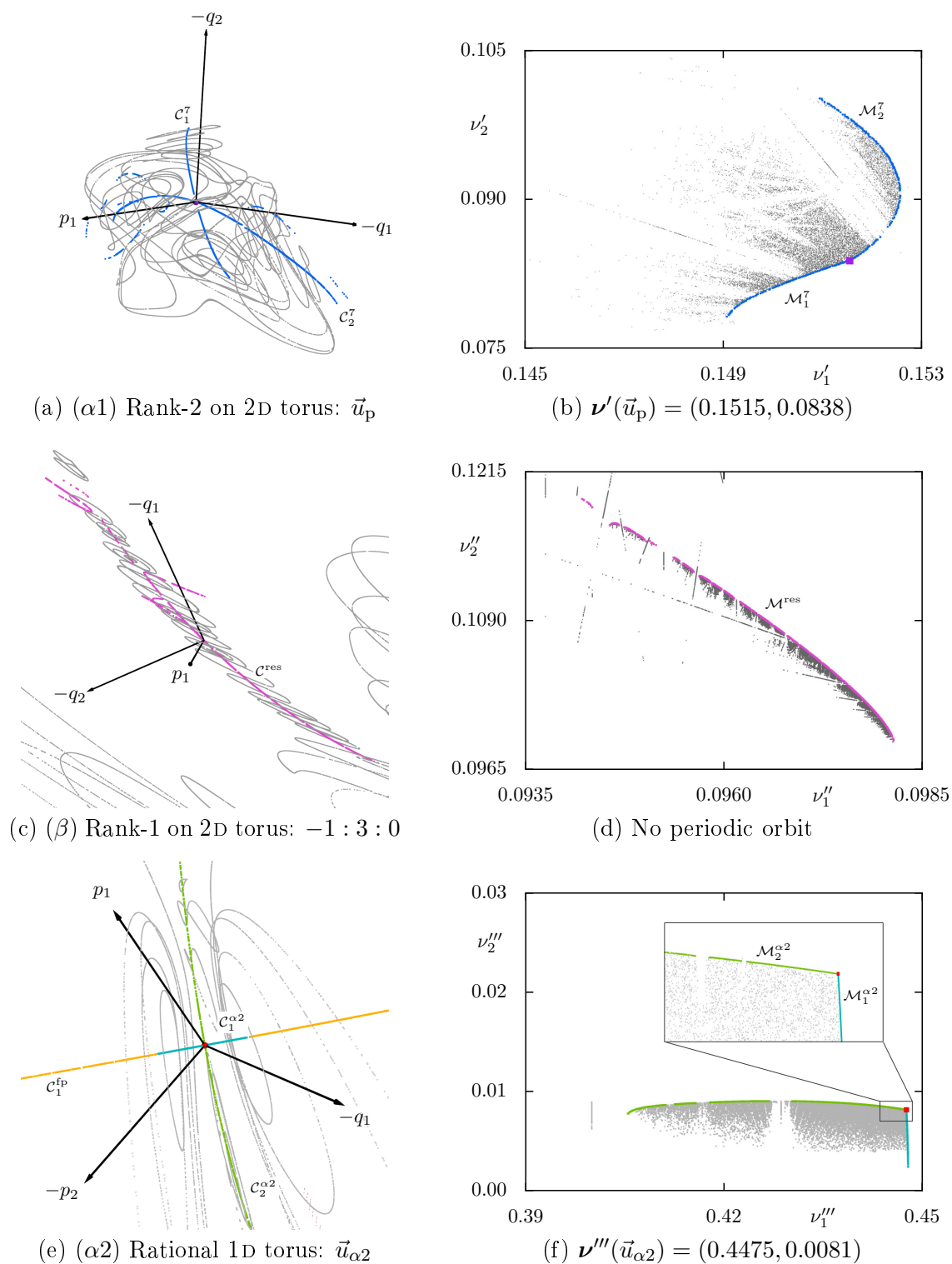


**Figure 3.5:** First level of the hierarchy with the three types  $(\alpha 1)$ ,  $(\beta)$ , and  $(\alpha 2)$  in (a), (c), (e) 3D phase-space slices and (b), (d), (f) adapted frequencies with 2D tori in gray. (a)  $\mathcal{C}^7$  around one point  $\vec{u}_p$  of the EE period-7 orbit, see Sec. 2.3, (c) one branch of  $\mathcal{C}^{\text{res}}$  of the  $-1 : 3 : 0$  resonance, and (e) central lines  $\mathcal{C}_1^{\alpha 2}$  (bright blue) and  $\mathcal{C}_2^{\alpha 2}$  (green) representing families of 1D tori  $\mathcal{M}_1^{\alpha 2}$  and  $\mathcal{M}_2^{\alpha 2}$  around one point  $\vec{u}_{\alpha 2} = (0.115287658, -0.141621338, 0.0, 0.0)$  of the EE period-7 chain. The slice conditions are (a), (c)  $|p_2| < 10^{-5}$  and (e)  $|q_2| < 10^{-6}$ . The coordinate system is shifted for each plot. The purple (red) point represents  $\vec{u}_p$  ( $\vec{u}_{\alpha 2}$ ) with adapted frequencies  $\nu'(\vec{u}_p)$  ( $\nu'''(\vec{u}_{\alpha 2})$ ). The two families emanating from  $\vec{u}_p$  (both blue) intersect in (b) with an angle close to  $\pi$ . [Modified from Ref. [138]]

corresponding colors. The families of elliptic 1D tori  $\mathcal{M}_1^7$  and  $\mathcal{M}_2^7$  shown in blue are located on the edges emanating from the periodic point  $\vec{u}_p$  in purple just as in the case of  $\mathcal{M}_1^{\text{fp}}$ ,  $\mathcal{M}_2^{\text{fp}}$ ,  $\vec{u}_{\text{fp}}$  in Fig. 3.1(b). The families from periodic orbits at resonance junctions seem to be embedded in the families of the crossing resonances, see Appendix A.4.

( $\beta$ ) In Fig. 3.5(c) one of the branches of the family  $\mathcal{M}^{\text{res}}$  in purple is magnified. While again the organization of the 2D tori around the family is visible, in this case only one family and no EE periodic point or fixed point is involved. While the frequency analysis for all these tori produces frequencies  $(\nu_1, \nu_2)$  on the resonance  $-1 : 3 : 0$ , choosing  $\nu_1'' = \nu_1/3 = \nu_2$  and calculating another independent frequency produces  $\nu_2''$ . In Fig. 3.5(d) the frequencies  $(\nu_1'', \nu_2'')$  shown in corresponding colors again display the family at one edge. Note that it is only one edge and not two in this case. It should be emphasized, that the direction along the resonance channel  $-1 : 3 : 0$ , expressed by  $\nu_1$  or  $\nu_2$  in Fig. 3.1(b), roughly corresponds to the direction along the family  $\mathcal{M}^{\text{res}}$ , expressed by the longitudinal frequency  $\nu_L = \nu_1''$  in Fig. 3.5(d). This correspondence is valid for all resonance channels.

( $\alpha_2$ ) In Fig. 3.5(e) a detail around one of the EE period-7 periodic points  $\vec{u}_{\alpha_2}$  from which the families  $\mathcal{M}_1^{\alpha_2}$  and  $\mathcal{M}_2^{\alpha_2}$  emanate is magnified. Note that  $\mathcal{M}_1^{\alpha_2}$  is denoted  $\mathcal{M}^{\alpha_2}$  in Figs. 3.1(b) and 3.3(a). Since only EH points of the chain are within the slice  $p_2 = 0$ , as seen in Fig. 3.1(c), the slice defined by  $q_2 = 0$  is used here. Additionally to the structures belonging to the red EE periodic point  $\vec{u}_{\alpha_2}$ , also the family  $\mathcal{M}_1^{\text{fp}}$  is included in orange, whose crossing with the resonance channel  $7 : 0 : 2$  is the cause for the periodic points, see Sec. 3.2.3. While this case looks similar to ( $\alpha_1$ ), there are a few peculiarities. The green family  $\mathcal{M}_2^{\alpha_2}$  emanating from the EE point  $\vec{u}_{\alpha_2}$  extends far away from the point. In contrast, the other family  $\mathcal{M}_1^{\alpha_2}$  shown in bright blue is embedded within the larger family  $\mathcal{M}_1^{\text{fp}}$ . The frequency analysis produces for the structures around the family  $\mathcal{M}_1^{\alpha_2}$  frequencies  $(\nu_1, \nu_2)$  on the resonance  $7 : 0 : 2$  and for structures around the family  $\mathcal{M}_1^{\alpha_2}$  in principle frequencies  $(\nu_1, \nu_2)$  at the intersection of the resonance and  $\mathcal{M}_1^{\text{fp}}$ , see Figs. 3.1(b) and 3.3(a). A frequency analysis as for ( $\alpha_1$ ) produces the frequencies  $(\nu_1''', \nu_2''')$  shown in Fig. 3.5(f) in corresponding colors. The only difference to ( $\alpha_1$ ) is the fact that the edge representing the embedded family  $\mathcal{M}_1^{\alpha_2}$  is much shorter and seems to approach to  $\nu_2''' = 0$ . The same behavior is observed for the crossing of the resonance  $17 : 0 : 5$  and the part of  $\mathcal{M}_1^{\text{fp}}$  belonging to the horseshoe. This might be interpreted as the frequencies of the embedded 1D tori of  $\mathcal{M}_1^{\alpha_2}$  getting closer to the separatrix. Note that the family  $\mathcal{M}_2^{\alpha_2}$  is considered to be a hybrid case of ( $\beta$ ) and ( $\alpha_2$ ), see Sec. 3.2.3. In particular, for  $\mathcal{M}_2^{\alpha_2}$  there is a direct relation between  $\nu_2$  and the longitudinal frequency  $\nu_L = \nu_1'''$  of  $\mathcal{M}_2^{\alpha_2}$  in Figs. 3.3(a) and 3.5(f), respectively, that is  $\nu_1''' = 1 - 7 \cdot \nu_2$ .

The similarity of the described cases  $(\alpha_1)$ ,  $(\beta)$ ,  $(\alpha_2)$  to their top class applies to all available resonances and junctions of this top class. Furthermore, for all cases resonance channels and junctions are visible in the frequency spaces in Fig. 3.5 as for the top class in Fig. 3.1(b). Consequently, the hierarchy can be continued in the same ways  $(\alpha_1)$ ,  $(\beta)$ ,  $(\alpha_2)$  along any of these resonances and junctions. For instance, the isolated gray points on the resonance  $5 : 0 : 2$ , that is the vertical line on the left of Fig. 3.5(f), correspond to the regular 2D tori at the junction of the resonances  $7 : 0 : 2$  and  $5 : -5 : 1$ . This even deeper class is illustrated in Fig. 3.4(a). Depending on the point of view, this deeper class is due to  $(\alpha_1)$  the junction or due to  $(\alpha_2)$  the crossing of the resonance  $5 : 0 : 2$  and  $\mathcal{M}_2^{\alpha_2}$ . An analogous example is the resonance  $21 : 0 : 2$  crossing  $\mathcal{M}^{\text{res}}$  in Fig. 3.5(d), which corresponds to the junction of the resonances  $-1 : 3 : 0$  and  $7 : 0 : 2$  in Fig. 3.3(a), and whose periodic orbits are shown in Fig. 3.3(e).

### 3.3.2 Frequency analysis along hierarchy

In order to explore the deeper classes of the hierarchy in the frequency space, it is necessary to perform the frequency analysis with respect to the organizing structures. A few examples for this are presented in Sec. 3.3.1. In particular, it is crucial to compute and predict the longitudinal frequency of the 1D tori of a deeper class, as most of the algorithms for computing 1D tori heavily depend on this frequency [72, 138, 156, 194–198]. One approach is to construct suitable normal forms to transform the motion, which is rather cumbersome [184, 185]. Instead, for  $(\alpha_1, \alpha_2)$  Lyapunov families this frequency can be estimated from the eigenvalues of the EE periodic orbits or computed numerically by taking into account the period of the orbit. In this section, a general way to obtain this frequency for  $(\beta)$  families of 1D tori due to a single, generic resonance is proposed. Also an expression for the period of the periodic orbits at a resonance junction is mentioned.

In order to illustrate the importance of the longitudinal frequency, the contraction algorithm for computing elliptic 1D tori is briefly discussed here. The main idea for this algorithm has been devised in Ref. [72] and the algorithm has been refined in later publications [138, 189, 199]. Consider an orbit  $\mathbf{x}_0(t)$  on a 2D torus  $T_0$  that is organized around an elliptic 1D torus. With respect to this 1D torus the frequencies  $(\nu_1, \nu_2)$  obtained from frequency analysis for the orbit  $\mathbf{x}_0(t)$  can be interpreted as longitudinal and normal frequency  $(\nu_L, \nu_N)$  of the torus  $T_0$ . The points  $\{\mathbf{x}_0(t_j)\}_j$  with  $\nu_L t_j \bmod 1 \approx 0$  are located at a similar longitudinal angle but have arbitrary normal angles. Approximating an initial point in the center of these points, e.g., by their geometric center, in general leads to an orbit  $\mathbf{x}_1(t)$  on a torus  $T_1$  with smaller radius in normal direction. This procedure is iterated until the resulting torus is close enough to a 1D torus, as

defined by some criteria. Despite the fact that this algorithm only works for elliptic 1D tori, it provides good initial guesses for elliptic 1D tori that are required by more sophisticated algorithms and continuation methods to find hyperbolic 1D tori [189]. The crucial step is to associate frequencies  $(\nu_1, \nu_2)$  with  $(\nu_L, \nu_N)$ . In case of families like  $\mathcal{M}_1^{\text{fp}}$  and  $\mathcal{M}_2^{\text{fp}}$  this is straightforward, as  $\nu_L = \nu_1$  and  $\nu_N = \nu_2$ , respectively. However, this is not true for families from generic resonances, like  $\mathcal{M}^{\text{res}}$  from the resonance  $-1 : 3 : 0$ .

As discussed in Sec. 2.1, the frequencies  $\boldsymbol{\nu} = (\nu_1, \nu_2)$  of any 2D torus are only defined up to unimodular transformations  $\mathcal{U} = (u_{ij})$  with  $i, j \in \{1, 2\}$ ,  $u_{ij} \in \mathbb{Z}$ , and  $\det \mathcal{U} = \mathbb{I}$ ,  $\mathbb{I} \in \{-1, 1\}$ . More precisely, a change in the angle coordinates  $\Theta' = \mathcal{U}\Theta$  causes new frequencies  $\boldsymbol{\nu}' = \mathcal{U}\boldsymbol{\nu}$ . If the frequencies  $\boldsymbol{\nu}$  fulfill a resonance condition  $k_1\nu_1 + k_2\nu_2 = k_3$ , without loss of generality  $k_2 \neq 0$ , then the transformed frequencies read

$$\boldsymbol{\nu}' = \begin{pmatrix} u_{11} & u_{12} \\ u_{21} & u_{22} \end{pmatrix} \begin{pmatrix} \nu_1 \\ \nu_2 \end{pmatrix} = \begin{pmatrix} u_{11} - \frac{k_1}{k_2}u_{12} \\ u_{21} - \frac{k_1}{k_2}u_{22} \end{pmatrix} \nu_1 + \begin{pmatrix} u_{12} \\ u_{22} \end{pmatrix} \frac{k_3}{k_2}. \quad (3.1)$$

It is possible to find a transformation  $\mathcal{U}$  such that for all frequencies  $\boldsymbol{\nu}$  on the resonance  $k_1 : k_2 : k_3$  one of the transformed frequencies is rational, without loss of generality  $\nu'_2 = n/m$  with  $n, m \in \mathbb{Z}$  and  $\gcd(m, n) = 1$ . In this new angle coordinates  $\Theta'$  all orbits on the 2D torus densely fill  $m$  disjoint lines which are described by  $\Theta'_1 \in [0, 2\pi)$  and  $\Theta'_2 = 2\pi \cdot i/m + \Theta_0$  with  $i \in \mathbb{N}$ ,  $0 \leq i < m$ , and some orbit specific offset  $\Theta_0 \in [0, 2\pi)$ . The previous arguments apply also if instead of a resonant 2D torus, a 1D torus originating from such a resonant 2D torus with resonance  $k_1 : k_2 : k_3$ , see Sec. 3.2.2, is considered. Then the period  $m$  and the frequency  $\nu'_1$  define the longitudinal frequency  $\nu_L$  of this 1D torus. More precisely, the 1D torus consists of  $m$  disjoint rings and the frequency on one of these rings, that is with respect to the  $m$ -th iterate, is  $\nu_L = m \cdot \nu'_1$ .

A suitable transformation is not uniquely defined, as there are four integers and the sign of  $\mathbb{I}$  to be determined and only two conditions for them. The condition  $\nu'_2 = n/m$  requires the  $\nu_1$  dependent term in Eq. (3.1) to vanish

$$u_{21} = \frac{k_1}{k_2}u_{22} = \frac{\tilde{k}_1}{\tilde{k}_2}u_{22} \quad (3.2)$$

with  $\gcd(\tilde{k}_1, \tilde{k}_2) = 1$ . Substituting  $u_{21}$  by Eq. (3.2) in the condition  $\det \mathcal{U} = \mathbb{I}$  leads to

$$\mathbb{I} = (u_{11}\tilde{k}_2 - u_{12}\tilde{k}_1) \frac{u_{22}}{\tilde{k}_2}. \quad (3.3)$$

A simple ansatz fulfilling both equations Eqs. (3.2) and (3.3) is  $u_{22} = \tilde{k}_2 l$  with  $l \in \mathbb{Z}$ . Choosing  $l = 1$  the remaining integers  $u_{11}$ ,  $u_{12}$ , and the sign of  $\mathbb{I}$  in Eq. (3.3) have to be determined by brute force. For a unimodular transformation  $\mathcal{U}$  is found the period  $m$  is determined by

$$\frac{n}{m} = \frac{k_3}{k_2} u_{22} = \frac{\mathbb{I} k_3}{u_{11} k_2 - u_{12} k_1}. \quad (3.4)$$

Once a suitable transformation  $\mathcal{U}$  is determined, the frequency analysis can be performed with respect to the resonance  $k_1 : k_2 : k_3$  for all 1D tori belonging to this resonance and their surrounding 2D tori. Firstly, for each of these objects the frequencies  $(\nu_1, \nu_2)$  are obtained straightforward from frequency analysis. Then, the longitudinal frequency  $\nu_L$  is computed by transformation. For 2D tori the second frequency is the next most relevant frequency obtained by frequency analysis, which is linearly independent of the other frequencies  $\nu_1, \nu_2$ , and  $\nu_L$ . Note that in time-continuous systems the normal frequencies can be obtained by averaging out the resonant motion [184, 185]. If there is a period  $m > 1$ , the frequency analysis has to be performed with respect to the  $m$ -th iterate, analogous to the frequency analysis with respect to EE periodic orbits. Note that there is a problem when straightforward frequency analysis is used for 2D tori surrounding periodic objects, i.e. which consist of several disjoint but dynamically connected 2D tori. When selecting regular orbits by a frequency criterion, see Eq. (2.17), these frequencies seem to be less stable in case of such 2D tori. More precisely, in the frequency space of the deeper class, which takes into account the period, stripes which are depleted of 2D tori appear. This numerical artifact is avoided by taking into account the period  $m$  already for the frequency criterion, i.e. using only every  $m$ -th iterate for the frequency analysis.

The junction of two resonances  $k_1^a : k_2^a : k_3^a$  and  $k_1^b : k_2^b : k_3^b$  is a point in frequency space  $(\nu_1, \nu_2) = (n_1/m_1, n_2/m_2)$  with  $\gcd(n_1, m_1) = \gcd(n_2, m_2) = 1$  and the period  $m$  of the resulting periodic orbits is  $m = \text{lcm}(m_1, m_2)$ . The point  $(\nu_1, \nu_2)$  is given by

$$\nu_1 = \frac{n_1}{m_1} = -\frac{k_2^a k_3^b - k_3^a k_2^b}{k_1^a k_2^b - k_2^a k_1^b} \quad \nu_2 = \frac{n_2}{m_2} = \frac{k_1^a k_3^b - k_3^a k_1^b}{k_1^a k_2^b - k_2^a k_1^b} \quad (3.5)$$

with one exception. If the denominator is zero  $k_1^a k_2^b - k_2^a k_1^b = 0$  and all the involved coefficients not, the two resonances are parallel. This expression works for any of the infinite resonances intersecting at a junction.

### 3.3.3 Hierarchy of regular tori

Based on the organization of 2D tori around families of elliptic 1D tori and the different origins of such families, a hierarchy of classes can be described analogous to the island-around-island hierarchy in 2D maps, see Sec. 2.4. In this section, the labeling of the classes analogous to 2D maps [139] is discussed. The basic principle is that an object has a deeper class or higher label than the object it is organized around. As an example the labeling is applied to the previously discussed families and their associated phase-space structures. The cases  $(\alpha_1, \beta, \alpha_2)$  introduced in Sec. 3.3.1 are used to mark the distinct possibilities. In addition, the meaning of trapping in a deeper class is discussed.

Consider an EE fixed point of class  $c$ . The two Lyapunov families originating from it are class  $c + 1$  and the 2D tori organized around these families are class  $c + 2$ .  $(\alpha_1)$  The periodic orbits present at each resonance junction within the set of 2D tori of class  $c + 2$  are also class  $c + 2$ . The labeling can be continued at each of the EE periodic orbits of class  $c + 2$  as for the EE fixed point of class  $c$ .  $(\beta)$  For each of the resonances crossing the set of class  $c + 2$  2D tori the associated families of elliptic and hyperbolic 1D tori also are class  $c + 2$ . The 2D tori organized around each of these families of elliptic 1D tori are class  $c + 3$ . The labeling can be continued for each class  $c + 2$  family of elliptic 1D tori as for one of the class  $c + 1$  Lyapunov families.  $(\alpha_2)$  The EE and EH periodic orbits that are present wherever the longitudinal frequency on the class  $c + 1$  Lyapunov families crosses a rational value are class  $c + 1$ . The labeling can be continued at the EE periodic orbit as in case  $(\alpha_1)$ .

In the 4D map  $F_{SC}$  the EE fixed point  $\vec{u}_{fp}$  is considered to be class 0. Thus, the families  $\mathcal{M}_1^{fp}$  and  $\mathcal{M}_2^{fp}$  are class 1,  $\mathcal{M}^{res}$  is class 2, the periodic orbit  $\vec{u}_p$  is class 2,  $\mathcal{M}^7$  are class 3, the EE periodic orbit  $\vec{u}_{\alpha_2}$  is class 1, and  $\mathcal{M}^{\alpha_2}$  are class 2. As predicted the families  $\mathcal{M}^{res}$ ,  $\mathcal{M}^7$ , and  $\mathcal{M}^{\alpha_2}$  represent a deeper class than  $\mathcal{M}_1^{fp}$  and  $\mathcal{M}_2^{fp}$ . Note the consistency of the labeling. For instance, the family  $\mathcal{M}_2^{\alpha_2}$  can be considered both a Lyapunov family of the EE periodic orbit  $\vec{u}_{\alpha_2}$  and the family of the resonance  $7 : 0 : 2$ . In both interpretations  $\mathcal{M}_2^{\alpha_2}$  is class 2.

As mentioned at the end of Sec. 3.2.2, the hierarchy of hyperbolic 1D tori is neglected for brevity, but the labeling works analogous. In particular, since trapping of chaotic orbits should refer to the trapping at regular structures, trapping in a deeper class denotes in the following chapters trapping at the elliptic structures of the deeper class. For example, trapping in the deeper class of a junction means trapping around the EE periodic orbit of the junction. Note the peculiarity of the proposed labeling in 4D maps: As presented in Secs. 4.4 and 4.5 an orbit within a sticky region of class  $c$  can get trapped in class  $c + 1$  of a resonance channel or class  $c + 2$  of a resonance junction.

For instance, a trapped orbit in the first sticky region of  $F_{\text{SC}}$ , i.e. at the central island, the outer ring, or the top tower, is class 2 like the KAM tori and can get trapped at the resonance  $-1 : 3 : 0$ , i.e. at the 2D tori surrounding  $\mathcal{M}^{\text{res}}$ , becoming class 3 or at the junction corresponding to  $\vec{u}_p$ , i.e. at the 2D tori surrounding  $\mathcal{M}^7$ , becoming class 4.

### 3.4 Bifurcations of families of elliptic 1D tori

After having established the origin and hierarchy of the families of 1D tori, it remains to discuss the features which occur along these families due to crossing resonances. According to Ref. [186] these features are explained by bifurcations of 1D tori. In this section, only some details of this joint work with Franziska Onken and co-workers [189] are outlined in order to establish the following: The horseshoe which is relevant for the power-law trapping in the 4D map  $F_{\text{SC}}$  is the deeper class of the resonance  $3 : 1 : 1$ .

In Ref. [186] it is explained how features of the families of elliptic 1D tori, including gaps, bends, and branches, see Fig. 3.1, are due to bifurcations of the families caused by crossing resonances. The families cross resonances since their normal and longitudinal frequencies vary smoothly along the families, e.g. see  $\mathcal{M}_1^{\text{fp}}$  and  $\mathcal{M}_2^{\text{fp}}$  in Fig. 3.1(b). While bifurcations are usually studied under parameter variation, this crossing of resonances allows to observe all stages of a bifurcation in a single phase space where the longitudinal frequency of the elliptic 1D tori plays the role of the bifurcation parameter. Using 2D projections of details of the 3D phase-space slices the remarkable resemblance of these bifurcations with bifurcations in 2D maps is shown, which is in agreement with analytical predictions [158, 159, 161]. In 2D maps the order  $|m|$  of the resonance  $\nu = n/m$  determines the type of bifurcation, like weak bifurcations  $|m| \geq 5$ , touch-and-go cases  $|m| \in \{4, 3\}$ , period-doubling  $|m| = 2$ , and saddle-node bifurcations  $|m| = 1$ . In 4D maps the coefficient  $|m_N|$  of the normal frequency of the resonance  $m_L\nu_L + m_N\nu_N = n$  determines similar types of bifurcation. The different values of  $|m_N|$  cause characteristic features in frequency space and phase space, e.g., branches  $|m_N| \geq 3$ , gaps  $|m_N| \in \{2, 0\}$  and bends  $|m_N| = 1$ . In contrast to 2D maps the special case  $m_N = 0$  is possible, see Sec. 3.2.2. This bifurcation is the only type possible for hyperbolic 1D tori as they have a Lyapunov exponent instead of a normal frequency.

In Ref. [186] it is also shown how the branches of a bifurcation, i.e. the families of hyperbolic and elliptic 1D tori, are the skeleton of the corresponding resonance channel. In particular, the 1D tori remaining from the break-up of 2D tori with a particular resonance as reviewed in Sec. 3.2.2 coincide with the branches from the corresponding bifurcation of the family of elliptic 1D tori. These two different perspectives on the branches explains the relations found between the elliptic branch and the hyperbolic

counterpart, see Sec. 3.2.3: The pairs of elliptic and hyperbolic 1D tori with same longitudinal frequency and similar actions are explained in terms of the break-up of 2D torus, while the match of their normal frequency and Lyapunov exponent is explained by the linearized dynamics around the bifurcation point.

Bifurcations of type  $|m_N| = 1$  are peculiar in terms of the frequency analysis on their deeper class [189], see also Sec. 3.3.2. For instance the prominent bend of the family  $\mathcal{M}_1^{\text{fp}}$  seen in Fig. 3.1(a) is caused by the resonance  $3 : 1 : 1$  which has  $|m_N| = 1$ , see Fig. 3.1(b). The bended part of  $\mathcal{M}_1^{\text{fp}}$  coincides to the remnant elliptic 1D tori resulting from the break-up due to the resonance. Thus, the 2D tori attached to the bended part of  $\mathcal{M}_1^{\text{fp}}$  belong to the deeper class of that resonance. However, they appear in the frequency space in Fig. 3.1(b) consistently with the close-by 2D tori of the higher class. This deeper class of the resonance  $3 : 1 : 1$  is denoted horseshoe in Sec. 2.6 and relevant for the trapping in the map  $F_{\text{SC}}$ . This resonance also explains the necessity of subtracting all harmonics up to order three, see Sec. 2.6.2, in order to resolve this region in frequency space.

## 3.5 Coupled twist maps

Based on the knowledge about the organization of the regular structures in a generic 4D symplectic map, as presented in the previous sections, a designed map is proposed in this section. This designed map consists of two 2D twist maps which are conveniently coupled. This 4D map exhibits all relevant characteristics of a generic system but at the same time has simple coordinates, which should allow for an accurate measurement of the chaotic transport. After an introduction of the map and a discussion of the parameters chosen, the statistics of Poincaré recurrences are presented along with trapped orbits in the frequency space. As for the generic map  $F_{\text{SC}}$  the statistics decay with a relatively straight power law and the chaotic orbits are trapped at the surface of the regular structures. The transport of the majority of the trapped orbits resembles the transport in the sticky region of the generic map  $F_{\text{SC}}$ , see Sec. 2.6.3. However, in Sec. 3.5.1 a region is identified which, due to the peculiar coupling, exhibits a distinctly different type of trapping mechanism. This mechanism is explained in Sec. 4.3 to be related to the trapping along the level hierarchy in 2D maps.



The designed map consists of two 2D twist maps with action–angle coordinates  $(I_k, \Theta_k)$  for  $k = 1, 2$  and linear functions  $\nu_k^0(I_k)$ ,

$$\begin{aligned} \tilde{I}_1 &= I_1 & \tilde{\Theta}_1 &= \Theta_1 + 2\pi\nu_1^0(I_1) \\ \tilde{I}_2 &= I_2 & \tilde{\Theta}_2 &= \Theta_2 + 2\pi\nu_2^0(I_2) \end{aligned} \quad (3.6)$$

leading to intermediate coordinates  $(\tilde{I}_k, \tilde{\Theta}_k)$ . They are symplectically coupled in position–momentum coordinates  $\tilde{p}_k = \sqrt{2\tilde{I}_k} \cos \tilde{\Theta}_k$ ,  $\tilde{q}_k = \sqrt{2\tilde{I}_k} \sin \tilde{\Theta}_k$ , via,

$$\begin{aligned} p'_1 &= \tilde{p}_1 - \xi \frac{dV(\tilde{q}_1, \tilde{q}_2)}{d\tilde{q}_1} & q'_1 &= \tilde{q}_1 \\ p'_2 &= \tilde{p}_2 - \xi \frac{dV(\tilde{q}_1, \tilde{q}_2)}{d\tilde{q}_2} & q'_2 &= \tilde{q}_2 \end{aligned} \quad (3.7)$$

with a coupling potential  $V(q_1, q_2) = q_1^3 q_2^3$  and a coupling strength  $\xi$ . Instead of the straightforward version expressed by Eqs. (3.6) and (3.7), a symmetric application of the coupling is chosen analogous to the half-kick version of the standard map. That is starting with an initial condition  $(I_1, I_2, \Theta_1, \Theta_2)$  the corresponding position–momentum coordinates  $(p_1, p_2, q_1, q_2)$  are computed and mapped according to Eq. (3.7) using half the coupling strength  $\xi/2$  leading to a point  $(p''_1, p''_2, q''_1, q''_2)$ . Then the twist according to Eq. (3.6) is applied to the corresponding action–angle coordinates  $(I''_1, I''_2, \Theta''_1, \Theta''_2)$  leading to  $(\tilde{I}_1, \tilde{I}_2, \tilde{\Theta}_1, \tilde{\Theta}_2)$ . Finally, the corresponding coordinates  $(\tilde{p}_1, \tilde{p}_2, \tilde{q}_1, \tilde{q}_2)$  are mapped again according to Eq. (3.7) using the other half of the coupling strength  $\xi/2$  leading to a point  $(p'_1, p'_2, q'_1, q'_2)$ . The final action–angle coordinates are then  $I'_k = (1/2)\sqrt{q_k'^2 + p_k'^2}$  and  $\Theta'_k = \arctan(p'_k/q'_k)$ . In the following, this map is referred to as coupled twist maps  $F_{\text{Twist}}$  with the parameters chosen in the following.

The coupling potential  $V(q_1, q_2)$  is chosen such that the planes  $I_1 = 0$  and  $I_2 = 0$  correspond to the uncoupled twist maps of Eq. (3.6) independently of any parameters. The exponents in the coupling potential are chosen to be three, which is the smallest exponent for which also the linearization around the uncoupled planes is independent of the coupling. This implies three major advantages of the map  $F_{\text{Twist}}$ , which are independent of the coupling strength  $\xi$ . Firstly, there is always an EE fixed point at  $I_1 = I_2 = 0$  and the uncoupled planes  $I_1 = 0$  and  $I_2 = 0$  represent its two Lyapunov families. Secondly, the action–angle coordinates of the uncoupled twist maps are a reasonable first approximation of the action–angle coordinates of the coupled maps even away from this Lyapunov families, see also Appendix A.5. Thirdly, the frequencies  $(\nu_1, \nu_2)$  of the regular tori are controllable: If one of the actions  $I_1$  or  $I_2$  is small, their frequencies are directly given by the frequencies  $\nu_1^0(I_1)$ ,  $\nu_2^0(I_2)$  of the uncoupled twist

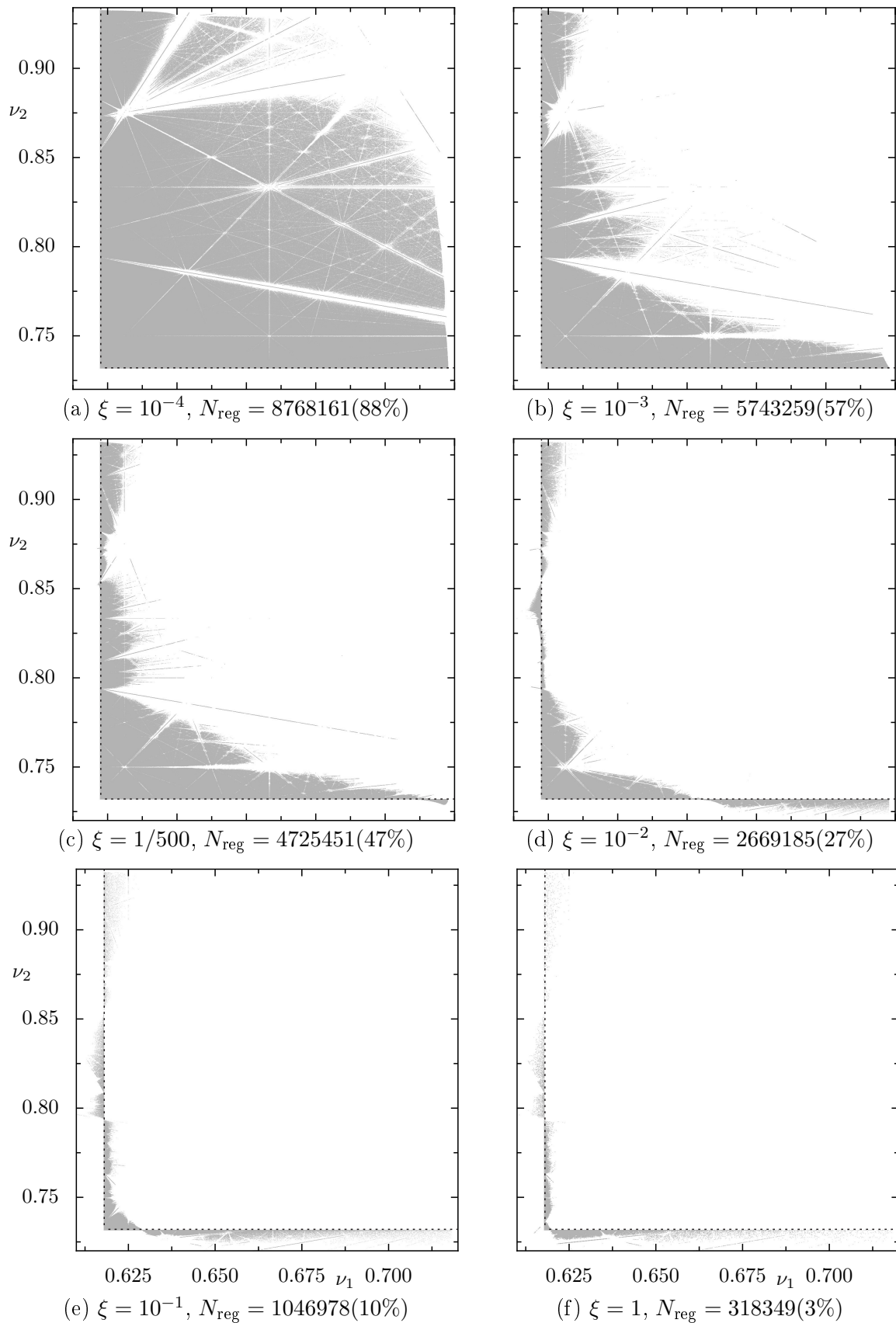


**Figure 3.6:** Frequencies of regular tori of the map Eq. (3.6)–Eq. (3.8) for different  $\xi$  shown in gray. Out of  $10^7$  initial points started uniformly in the phase space  $(I_1, I_2, \Theta_1, \Theta_2) \in [0, 10)^2 \times [-\pi, \pi)^2$  there are  $N_{\text{reg}}$  regular ones according to Eq. (2.17). The uncoupled twist maps Eq. (3.8) are indicated as dashed lines.

maps. In Fig. 3.6 the frequency space of the map  $F_{\text{Twist}}$  with regular tori in gray is shown for different coupling strengths  $\xi$ . In all cases the same linear functions  $\nu_k^0(I_k)$  are chosen

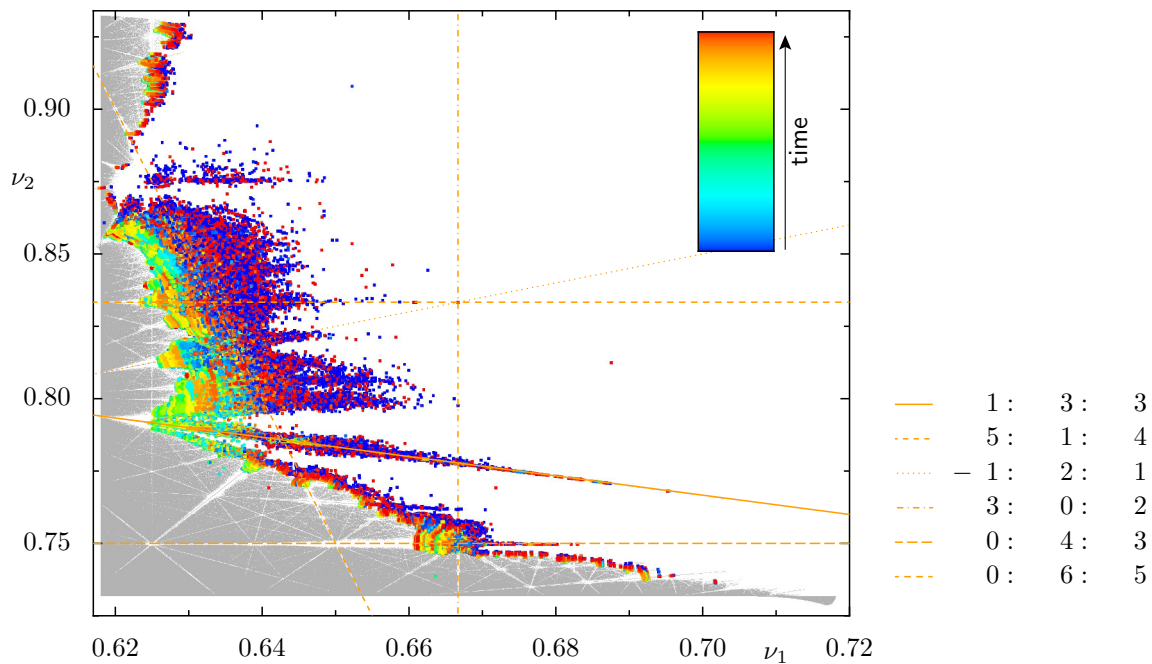
$$\nu_1^0(I_1) = (\sqrt{5} - 1)/2 + I_1/100 \qquad \nu_2^0(I_2) = \sqrt{3} - 1 + I_2/50 \qquad (3.8)$$

such that  $\nu_1 < \nu_2$  is guaranteed and the frequencies are away from the resonance  $-1 : 1 : 0$ . The frequencies corresponding to either  $I_1 = 0$  or  $I_2 = 0$  are indicated by two dashed lines. The edges in frequency space corresponding to the Lyapunov families nicely coincide with these dashed lines. In order to define Poincaré recurrences the phase space is chosen to be confined to  $(I_1, I_2, \Theta_1, \Theta_2) \in [0, 10]^2 \times [-\pi, \pi]^2$ . Thus, there are no regular tori at and beyond the upper and right borders of the frame shown in Fig. 3.6.

The frequency spaces of  $F_{\text{Twist}}$  in Fig. 3.6 look particularly simple in comparison with the frequency space for the generic map  $F_{\text{SC}}$  in Fig. 3.1(b). Nevertheless, all the generic features are present such as a chaotic region and resonance channels with an embedded part  $\mathcal{E}$  and an outer part  $\mathcal{O}$ . More precisely, with increasing coupling strength  $\xi$  the fraction of regular tori decreases and they get more confined to the vicinity of the Lyapunov families. In this sense the coupling also acts as a perturbation of the integrable twist maps. For  $\xi \geq 1/500$  folds become visible, i.e. regular tori with frequencies on the other side of the Lyapunov families. Such folds destroy the uniqueness of the frequencies, see also Appendix A.5. In order to both avoid them and ensure a sufficiently large chaotic sea, the coupling strength  $\xi = 1/500$  is chosen. The Poincaré recurrences are obtained for  $10^{11}$  initial conditions with uniformly distributed random actions  $I_1, I_2 \in [4.8, 9.2]$  and angles  $\Theta_1, \Theta_2 \in [-\pi, \pi)$ . The resulting 20775 chaotic orbits with recurrence times  $T > 10^6$  are shown in frequency space in Fig. 3.7 according to Sec. 2.6.2. Some important resonances are indicated with orange lines. The chaotic orbits are trapped at the surface of the regular region analogous to the observations for the two coupled standard maps  $F_{\text{SC}}$ , see Sec. 2.6. Moreover, the Poincaré recurrence statistics for the map  $F_{\text{Twist}}$ , shown in Fig. 3.9 in the next section, also exhibit a relatively straight power law.

### 3.5.1 Sticky regions

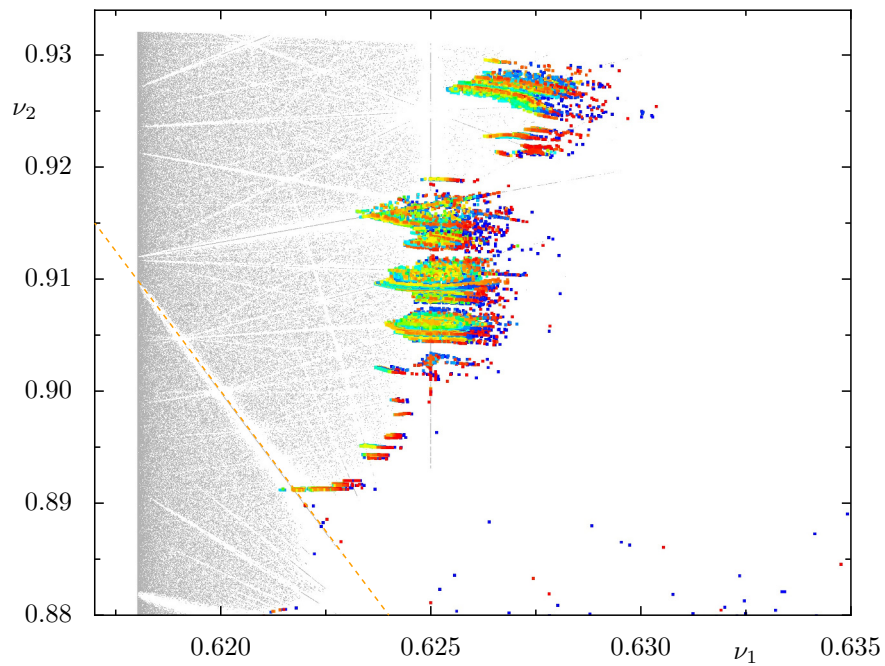
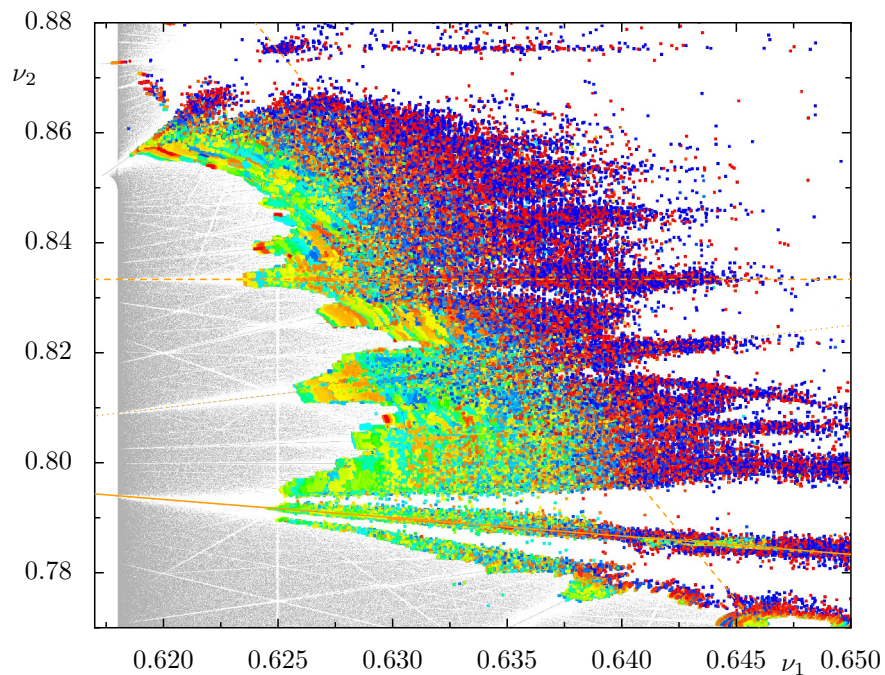
In this section, two regions A and B with different types of chaotic transport are distinguished within the coupled twist maps  $F_{\text{Twist}}$ , cf. Figs. 3.8(a) and 3.8(b). The region B exhibits the same characteristics as the sticky region of the generic map  $F_{\text{SC}}$ . It is explained how the region A resembles a 3D map due to the coupling. The Poincaré re-



**Figure 3.7:** Trapped orbits of the map  $F_{\text{Twist}}$  in frequency space with the iteration time  $t \in [0, T > 10^6]$  encoded in color for each of the 20775 orbits, as shown in Fig. 2.4(b) for a single orbit. For comparison the regular tori from Fig. 3.6(c) are shown in gray. Some important resonances  $m_1 : m_2 : n$  are indicated as orange lines.

currence statistics for the individual regions exhibits in both cases straight power laws similar to the statistics of the system, but region B is the dominant sticky region. The trapping mechanism for region A is sketched later in Sec. 4.3.

In Figs. 3.8(a) and 3.8(b) two disjoint regions of the frequency space in Fig. 3.7 are shown which are denoted in the following as region A and region B, respectively. The transport between these two regions is observed to be negligible. For both regions the chaotic orbits are trapped at the surface of the regular region represented by the regular tori in gray. However, the trapped orbits of region A in Fig. 3.8(a) seem to be almost exclusively transported in the direction of  $\nu_1$ , while the second frequency  $\nu_2$  hardly changes for these orbits. Note that since the surface of the regular region in Fig. 3.8(a) runs relatively parallel to the  $\nu_2$ -axis, the transport in  $\nu_1$  coincides with transport towards or away from the regular region. On the contrary, for region B in Fig. 3.8(b) the chaotic orbits are transported relatively fast along the surface of the regular region and much slower away from this region, as seen by the orientation of the colored bands. In this sense, region B resembles the sticky region of the horseshoe of the generic map  $F_{\text{SC}}$ , see Sec. 2.6. The difference between the two regions shown in Fig. 3.8 is supported by the observation, that the most relevant resonances affecting the trapped orbits run relatively parallel to the  $\nu_2$ -axis for region A, cf. Fig. 4.9(b), and somewhat away from the  $\nu_2$ -axis for region B.

(a) Region A:  $\nu_2 > 0.88$ (b) Region B:  $0.77 < \nu_2 \leq 0.88$ 

**Figure 3.8:** Sticky regions of the map  $F_{\text{Twist}}$  in frequency space. (a) and (b) are magnifications of Fig. 3.7 illustrating region A and region B, respectively. While the trapped orbits in (b) show the generic behavior known from the horseshoe of the two coupled standard maps  $F_{\text{SC}}$ , in (a) the orbits mainly propagate along  $\nu_1$  with  $\nu_2$  being approximately constant.

The region A is a special case due to the chosen coupling, while region B can be considered as a generic sticky region. The transport in region A can be understood from the kick term of Eq. (3.7) which maps  $(p_1, p_2, q_1, q_2)$  to  $(p'_1, p'_2, q'_1, q'_2)$

$$\delta p_j = p'_j - p_j = -\xi \frac{dV(q_1, q_2)}{dq_j} \quad \delta q_j = q'_j - q_j = 0$$

with  $j \in \{1, 2\}$ . In terms of one of the original uncoupled twist maps, the kick  $\delta p_j$  is a non-integrable propagation changing the action  $I_j$  and thus roughly translates to a transport  $\delta \nu_j \sim \delta p_j$  in the frequency  $\nu_j$ . For a coupling potential  $V(q_1, q_2) = q_1^{m_1} q_2^{m_2}$  this reads

$$\delta p_j = p'_j - p_j = -\xi \cdot m_j \frac{V(q_1, q_2)}{q_j}$$

and thus it follows for the case  $|q_1| \ll |q_2|$

$$|q_1| \ll |q_2| \quad \Leftrightarrow \quad \frac{1}{|q_1|} \gg \frac{1}{|q_2|} \quad \Rightarrow \quad |\delta p_1| \gg |\delta p_2| \quad \Rightarrow \quad |\delta \nu_1| \gg |\delta \nu_2|.$$

In region A the condition  $|q_1| \ll |q_2|$  holds on average as  $I_1 \ll I_2$ . An examination of the average ratio  $|\delta p_1 / \delta p_2|$  on the regular tori of each region confirms this, but is not shown here. This explains the very small transport in  $\nu_2$ . A model for the transport in region A would be the 3D map in the coordinates  $(I_1, \Theta_1, \Theta_2)$  resulting from setting  $\delta p_2 = 0$  in Eq. (3.7) as considered in Sec. 4.3. Note that the reverse situation  $I_1 \gg I_2$  is observed for trapped orbits with  $\nu_1 > 0.67$  in Fig. 3.7.

The Poincaré recurrence statistics for the map  $F_{\text{Twist}}$  are obtained from two differently large sets of initial conditions both with uniformly distributed random actions  $I_1, I_2 \in [4.8, 9.2]$  and angles  $\Theta_1, \Theta_2 \in [-\pi, \pi)$ . Note that the initial region is chosen differently from the exit region  $\Gamma = \{(I_1, I_2, \Theta_1, \Theta_2) : I_1, I_2 > 10\}$  for numerical advantages. While this technically means that escape times rather than recurrences  $T$  are computed, the latter notion is used in the following to avoid confusion when comparing the maps  $F_{\text{Twist}}$  and  $F_{\text{SC}}$ . For each trapped orbit  $\mathbf{x}(t)$  with very long recurrence time  $T$  the two frequencies  $(\nu_1, \nu_2)$  of the middle segment  $\{x(t_i)\}$  with  $t_i \in [(T - \Delta t)/2, (T + \Delta t)/2]$  are computed. These frequencies are used to assign each of these chaotic orbits to the region they are trapped at. The first set are  $10^{11}$  initial conditions and for the resulting 20775 chaotic orbits with recurrence times  $T > 10^6$  the two frequencies of the middle segment are computed. The second set are  $1.8 \cdot 10^{11}$  initial conditions and for the resulting 1652930 chaotic orbits with recurrence times  $T > 4 \cdot 10^4$ , including 37777 orbits with  $T > 10^6$ , the two frequencies of the middle segment are computed. As suggested by

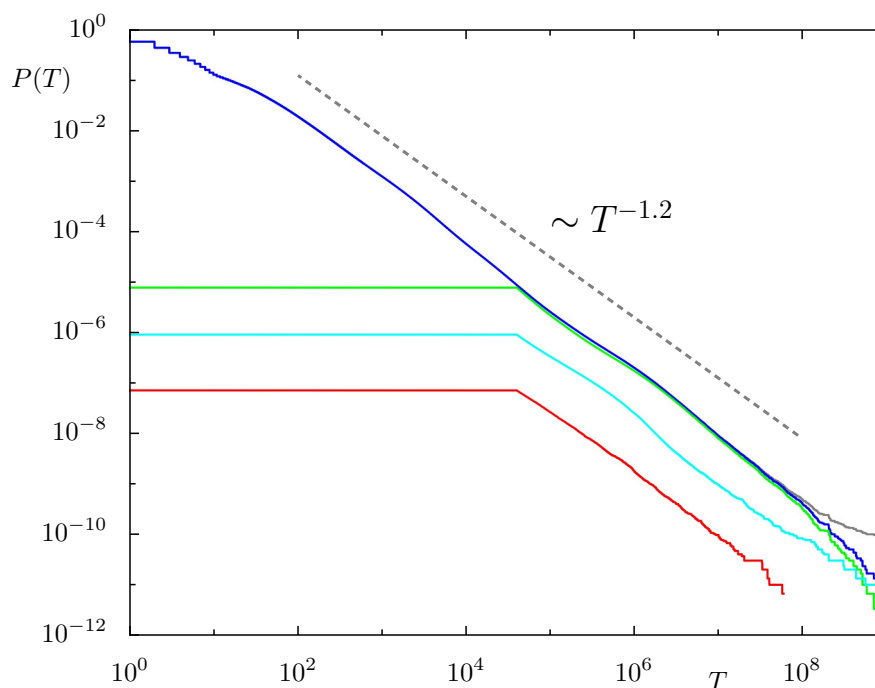


**Figure 3.9:** Statistics of Poincaré recurrences  $P(T)$  for the map  $F_{\text{Twist}}$ . The overall statistics is shown in blue. Orbits with  $T > 4 \cdot 10^4$  are assigned to regions A, B, and C giving corresponding statistics shown in red, green, and bright blue. The statistics for the individual sticky regions are normalized according to their share of all trapped orbits, i.e. their sum gives the overall statistics. The gray line behind the blue one is the overall statistics including 25 orbits which are most likely regular, see text. For the statistics a total of  $2.8 \cdot 10^{11}$  chaotic orbits started uniformly in  $(I_1, I_2, \Theta_1, \Theta_2) \in [4.8, 9.2]^2 \times [-\pi, \pi]^2$  are used with the exit region  $\Gamma = \{(I_1, I_2, \Theta_1, \Theta_2) : I_1, I_2 > 10\}$ , see text. For comparison the gray, dashed line represents a power-law  $P(t) \sim t^{-\gamma}$ , with  $\gamma = 1.2$ .

Fig. 3.8, orbits with  $\nu_2 > 0.88$  are considered to be trapped in region A and orbits with  $0.77 < \nu_2 \leq 0.88$  in region B and the region with  $\nu_2 \leq 0.77$  is denoted as region C. Note that for the first set of initial conditions eight orbits do not recur within  $10^9$  iterations and for the second set 17 orbits. The resulting statistics of Poincaré recurrences  $P(T)$  are presented in Fig. 3.9.

In Fig. 3.9 the statistics for the whole system are shown as gray line which is mostly covered by a blue line. The gray line includes the not recurred orbits, while they are ignored in case of the blue line. Without the not recurred orbits the statistics decays with a relatively straight power law. The frequencies of almost all of the not recurred orbits stay constant throughout  $10^9$  iterations with deviations less than  $10^{-6}$  and are thus considered to be regular tori within small regular islands which lie within the initial region. Judging from the frequencies  $(\nu_1, \nu_2)$ , see Eq. (3.5), these islands result from one of the junctions at  $(2/3, 5/6)$ ,  $(11/16, 13/16)$  and  $(115/174, 5/6)$ . In the following, the not recurred orbits are neglected. The statistics for the individual sticky regions

are included with different colors in Fig. 3.9. They are normalized according to their share of all trapped orbits, i.e. for all times  $T$  the sum of  $P(T)$  of the colored lines is equal to  $P(T)$  of the blue line. The decay for all three regions resembles the overall decay. However, the statistics for region B shown in green almost coincides with the blue line, implying that this region is the dominant sticky region of the map  $F_{\text{Twist}}$ . The region A shown in red contributes the least to the overall statistics, but exhibits a very straight power law. The remaining region C shown in blue contains regions of both kind, i.e. with transport resembling the transport observed for region A or region B. The majority of the transport in region C seems to be governed by the resonances  $1 : 3 : 3$ ,  $0 : 4 : 3$  and  $3 : 0 : 2$ , see Fig. 3.7. No major transport between region A and region C is observed. In conclusion, it is assumed that region A and region B are sufficient to understand the fundamental transport in the coupled twist maps  $F_{\text{Twist}}$  and thus region C is ignored. Thus, for better resolution the frequency space is only shown for  $\nu_1 < 0.67$  for the map  $F_{\text{Twist}}$  in the following.



# 4 Transport and trapping in 4D maps

Despite the importance of chaotic transport in the vicinity of regular structures many fundamental questions about the nature of this transport in higher-dimensional systems remain open. In particular, the mechanism of power-law trapping, while quite well understood for 2D maps, is completely unknown for higher-dimensional systems. In the preliminary work [72] this mechanism was traced back to sticky regions at the surface of the regular structures. In this chapter, the chaotic transport within this sticky region is shown to be organized by overlapping resonance channels. In particular, the chaotic transport is decomposed into four basic processes: escape from one resonance channel to another, trapping in a deeper class of hierarchy, transport at junctions of resonance channels, and transport along resonance channels. The escape from one resonance channel to another and the transport along the class hierarchy, discussed in the previous chapter, are shown to be governed by partial barriers. While the class hierarchy and resonance junctions turn out to be insignificant for the sticky region, the transport between resonance channels provides, in special cases, a mechanism for power-law trapping in higher-dimensional systems. However, the results suggest that the trapping in the generic sticky regions is governed by the transport along the resonance channels. A one-dimensional stochastic model of this transport including a drift along the channel is proposed. In principle, this model can not only explain the power-law trapping, but the proposed drift has general implications for the transport in the Arnold web. This transport is usually considered to be purely diffusive. The drift and the stochastic model have not been verified yet as the measurement of the transport along a resonance channel turned out to be extremely difficult. Nevertheless, the coupled twist maps  $F_{\text{Twist}}$  introduced in the last chapter appear to be a promising model to quantify this transport. All results presented in the following sections for this map are consistent with the corresponding results for the map  $F_{\text{SC}}$ , which demonstrates the generic dynamics of this designed system  $F_{\text{Twist}}$ .

In Sec. 4.1 it is shown that several sticky regions with different power laws exist for the map  $F_{\text{SC}}$ , but that the horseshoe is the dominant sticky region. Based on the coarse

quantification of transport properties within a sticky region open resonance channels are found to organize the chaotic transport in the sticky regions. In Sec. 4.2 this transport is decomposed into the four basic processes using time–frequency plots and signatures of partial barriers are identified. In Sec. 4.3 a possible mechanism for the power-law trapping based on the transport from one resonance channel to another is sketched. While the trapping in a special region of the twist map  $F_{\text{Twist}}$  is explained by this mechanism, it is ruled out for the generic sticky regions of  $F_{\text{Twist}}$  and  $F_{\text{SC}}$ . Likewise, in Secs. 4.4 and 4.5 trapping in the deeper classes of resonance channels and junctions is demonstrated to be insufficient as origin of the overall power-law decay. However, the escape statistics for the deeper classes exhibit power-law decays as expected from the self-similarity. Instead, in Sec. 4.6 a one-dimensional stochastic process with drift modeling the transport along a single resonance channel is proposed which generates the power-law decay. It is derived how such a drift may originate from the change of the volume of the stochastic layer along the resonance channel. This volume is computed for the resonance  $0 : 6 : 5$  of the map  $F_{\text{Twist}}$  and the measurement of the drift and diffusion coefficients is discussed in Appendix A.1.

## 4.1 Sticky region and resonance channels

Chaotic orbits in symplectic 4D maps get trapped in so called sticky regions at the surface of the regular structures, as discussed in Sec. 2.6. Since different regular regions can be distinguished as discussed in Sec. 2.6.2 and chapter 3 also their attached sticky regions should be differentiated. In fact, it is observed that trapped orbits only visit one of these sticky regions before returning to the chaotic sea [72]. In this section, individual power-law decays for the sticky regions of the two coupled standard maps  $F_{\text{SC}}$  are obtained by categorizing trapped orbits via frequency analysis. The results justify the assumption of Ref. [72] that the horseshoe is the most relevant sticky region of the system. A coarse grained inspection of the transport within the sticky regions of  $F_{\text{SC}}$  and the coupled twist maps  $F_{\text{Twist}}$  reveals that it is organized by the open resonance channels which pervade the sticky regions. Analytic results for the number and area of resonance channels of different order are presented in Appendix A.3.

First, the Poincaré recurrences of  $F_{\text{Twist}}$  are obtained as described in Sec. 2.6. Then, these recurrences are categorized analogously to the recurrences of the coupled twist maps  $F_{\text{SC}}$  in Sec. 3.5.1: For each orbit  $\mathbf{x}(t)$  of the  $3 \cdot 10^6$  trapped orbits with recurrence times  $T > 10^4$ , see Sec. 2.6, the two frequencies of the middle segment  $t \in [(T - \Delta t)/2, (T + \Delta t)/2]$  are computed and the orbit is assigned to the regular region which is closest to this segment in frequency space. The detailed mapping from areas in frequency

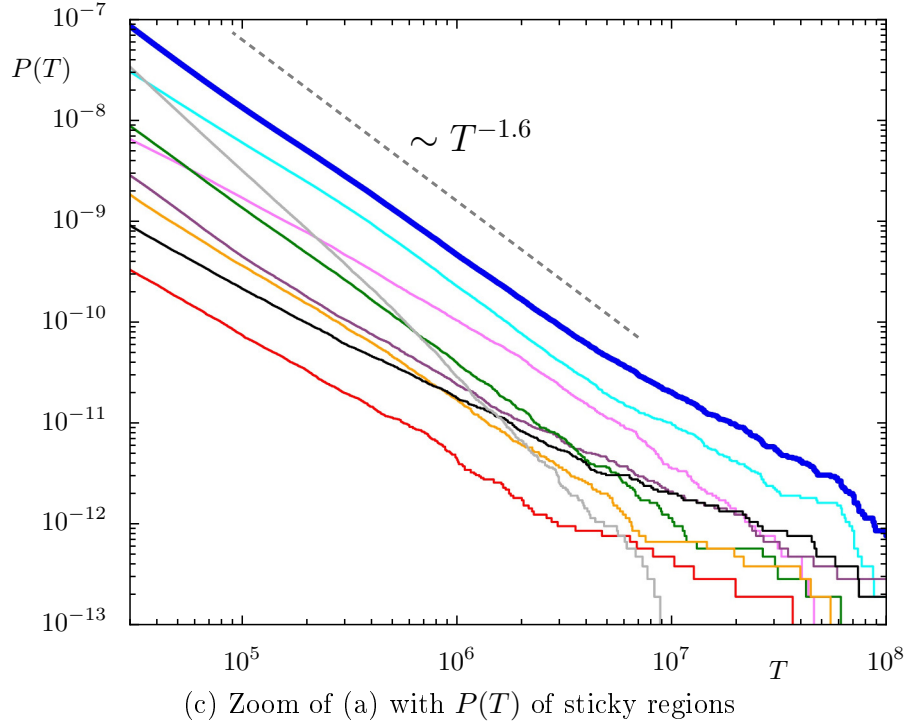
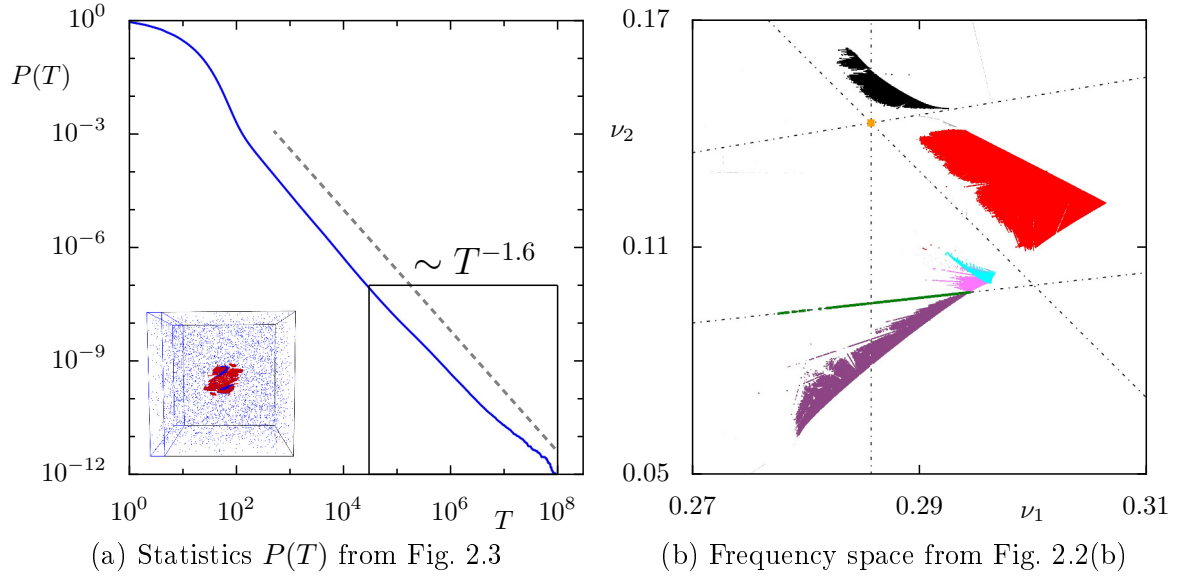


**Figure 4.1:** Statistics of Poincaré recurrences  $P(T)$  for the sticky regions of the map  $F_{\text{SC}}$ , analogous to Fig. 3.9. (c) Magnification as indicated by the black box in (a) with the overall statistics shown as thick, blue line and the statistics associated with individual regular regions shown as thin, colored lines. The statistics for the individual regions are normalized according to their share of all trapped orbits, i.e. their sum gives the overall statistics. The individual statistics are colored like their associated regular region in (b). The thin, gray line corresponds to orbits which could not be assigned. Only the 3354864 chaotic orbits with  $T > 4 \cdot 10^4$  are assigned to individual regions according to their middle frequency, see Appendix A.7. The exponents for the individual power laws  $P(T) \sim T^{-\gamma}$  range from  $\gamma \approx 1.6$  for the region around the resonance  $-1 : 3 : 0$  (green) to  $\gamma \approx 1.15$  for the outer ring (black).

space to regular regions is listed in Appendix A.7. As in Sec. 3.5.1, the transport between the sticky regions of most of these different regular regions is observed to be small. Thus, it is assumed that each chaotic orbit is only trapped in a single region before returning to the chaotic sea. The resulting statistics of Poincaré recurrences  $P(T)$  are presented in Fig. 4.1. Figure 4.1(a) shows again the statistics for the whole system as blue line. Figure 4.1(c) is a magnification of this statistics for longer times  $T$  as indicated by the black box in Fig. 4.1(a). The statistics for the individual sticky regions are included with different colors in Fig. 4.1(c). They are normalized according to their share of all trapped orbits, i.e. for all times  $T$  the sum of  $P(T)$  of the thin colored lines is equal to  $P(T)$  of the thick blue line. The colors of individual sticky regions in Fig. 4.1(c) match the colors of the associated regular regions in the frequency space in Fig. 4.1(b). These regions match the ones introduced in Sec. 2.6.2, except here it is further distinguished between the horseshoe and the inner end of the horseshoe, shown in bright blue and pink respectively in Fig. 4.1(b). Note that a gallery of chaotic orbits trapped at the different regular regions can be found in Ref. [72], Section 5.2. The gray line in Fig. 4.1(c) represents all trapped orbits which could not definitely be assigned to one of the big regular regions for various reasons. The share of these orbits decreases rapidly and can be neglected for longer times.

Figure 4.1(c) demonstrates that up to the considered time  $T < 10^9$  the statistics of Poincaré recurrences of  $F_{\text{SC}}$ , shown as thick blue line, is dominated by the sticky region at the horseshoe, shown in bright blue. The next most important contribution comes from the adjacent inner end of the horseshoe, shown in pink. All sticky regions in Fig. 4.1(c) exhibit power-law decays  $P(T) \sim T^{-\gamma}$  each with a slightly different exponent  $\gamma$ . For instance the outer ring, shown in black in Fig. 4.1(b), displays a slower decay of  $P(T)$  than the horseshoe and thus might well be the dominant sticky region for much longer times. In contrast, the region around the resonance  $-1 : 3 : 0$  has for shorter times  $T \sim 10^5 \dots 10^6$  a larger share of the overall decay than the outer ring but decays faster. While an explanation of the power-law decay in higher-dimensional maps ultimately has to address these different exponents, the following investigations for  $F_{\text{SC}}$  will focus on the dominant sticky region of the horseshoe.

In Ref. [72] the transport within the sticky region of the horseshoe is assumed to be locally a superposition of two stochastic processes in frequency space, which are perpendicular to each other, one roughly oriented along( $\leftrightarrow$ ) and the other away from( $\updownarrow$ ) the surface of the regular structure. Using ensembles of initial conditions within the sticky region, a normal diffusion along and a subdiffusion away from the regular structure is found with the spread along being much more rapid  $\sigma_{\leftrightarrow}^2/\sigma_{\updownarrow}^2 \approx 100$ . Also a small drift away from the regular structure is detected. However, these measurements use a single

manually estimated orientation of the stochastic processes and local distortions by the present open resonance channels are neglected.

In order to estimate the influence of the open resonance channels the distribution of several entities are obtained from the frequencies of the orbits which are trapped at the horseshoe. That is, for each of these orbits  $\mathbf{x}_i(\tilde{t})$  with  $i \in [0, N_{\text{horseshoe}})$ ,  $N_{\text{horseshoe}} = 61600$ ,  $\tilde{t} \in [0, T_i]$  and Poincaré recurrence times  $10^5 \leq T_i \leq 10^9$  the corresponding frequencies  $(\nu_{i,1}, \nu_{i,2})(t)$  with  $t \in [0, T_i)$  are computed, see Sec. 2.6.2. This gives a set  $\Omega_{\text{horseshoe}} = \{(\nu_{i,1}, \nu_{i,2})(t)\}_{i,t}$  of  $|\Omega_{\text{horseshoe}}| \approx 5 \cdot 10^6$  frequency pairs. The frequency space is divided into a grid of squares of width  $\Delta\nu = 5 \cdot 10^{-6}$  and for each square containing the frequency pairs

$$\Omega_{\nu_1, \nu_2} = \{(\omega_1, \omega_2) : \omega_j \in (\nu_j - \Delta\nu/2, \nu_j + \Delta\nu/2), j = 1, 2\} \cap \Omega_{\text{horseshoe}}$$

the density of the frequency pairs

$$\rho(\nu_1, \nu_2) = \frac{|\Omega_{\nu_1, \nu_2}|}{|\Omega_{\text{horseshoe}}|} \quad (4.1)$$

is calculated. Considering that each frequency pair  $(\nu_{i,1}, \nu_{i,2})(t) \in \Omega_{\text{horseshoe}}$  represents an orbit which escapes to the chaotic sea after  $T_i - t + \Delta T$  iterations with the finite resolution  $\Delta T \in [0, \Delta t)$ , the average escape time is calculated as

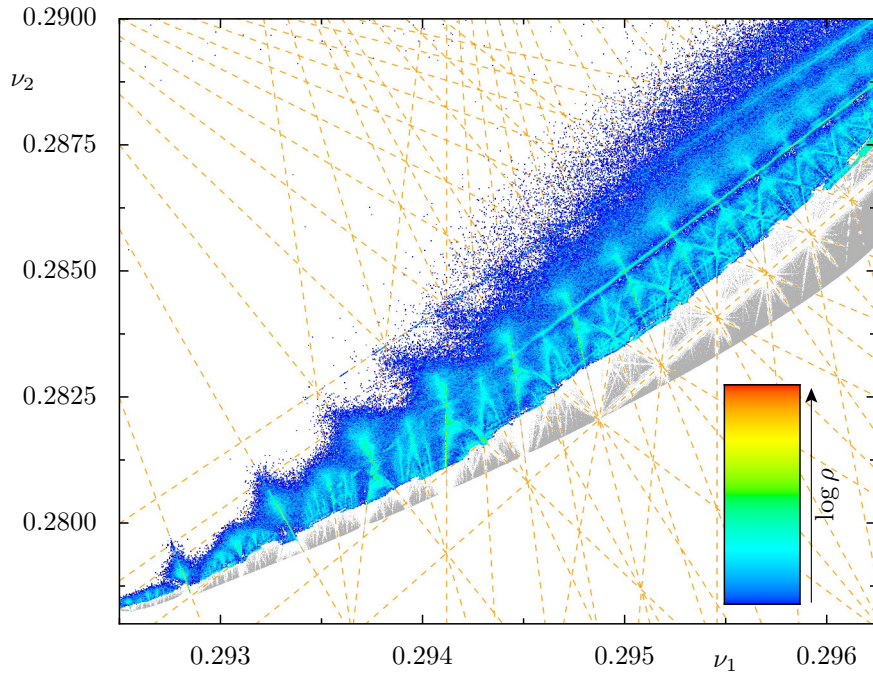
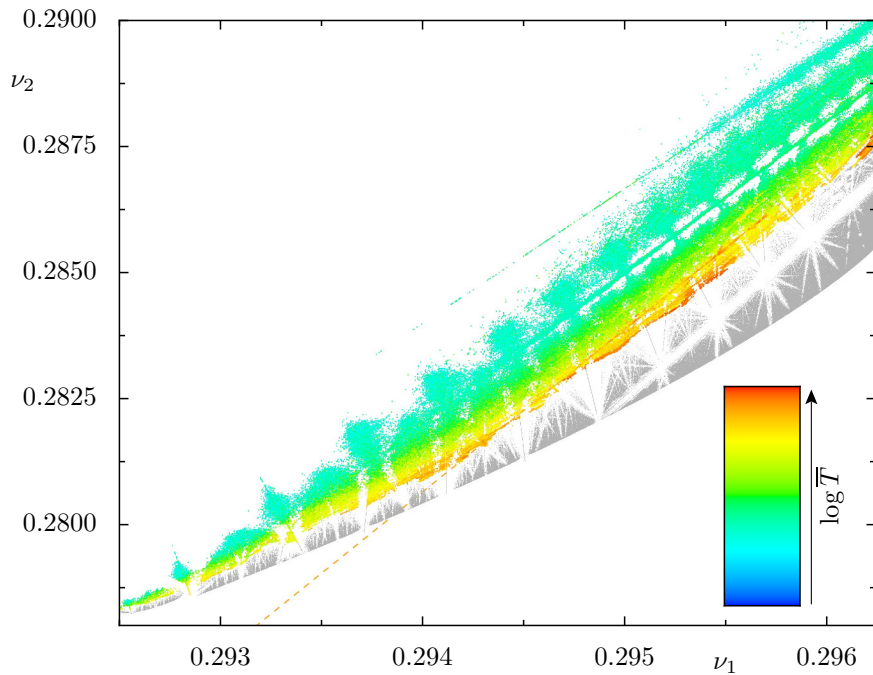
$$\bar{T}(\nu_1, \nu_2) = \frac{1}{|\Omega_{\nu_1, \nu_2}|} \sum_{(\nu_{i,1}, \nu_{i,2})(t) \in \Omega_{\nu_1, \nu_2}} (T_i - t). \quad (4.2)$$

Finally, the eigenvalues of the  $2 \times 2$  covariance matrix  $\text{Cov}_{k,l}(\nu_1, \nu_2)$  after one iteration  $t \mapsto t + \Delta t$  of the frequency pairs

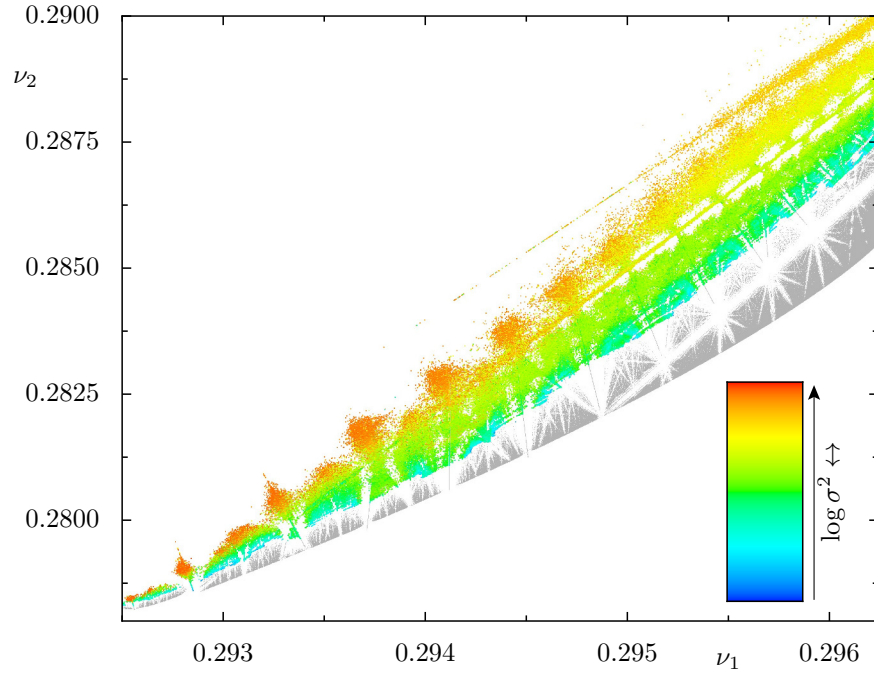
$$\begin{aligned} \text{Cov}_{k,l}(\nu_1, \nu_2) &= \mathbb{E}[\nu_{i,k}(t + \Delta t) \cdot \nu_{i,l}(t + \Delta t)]_{(\nu_{i,1}, \nu_{i,2})(t) \in \Omega_{\nu_1, \nu_2}} - \\ &\quad \mathbb{E}[\nu_{i,k}(t + \Delta t)]_{(\nu_{i,1}, \nu_{i,2})(t) \in \Omega_{\nu_1, \nu_2}} \cdot \mathbb{E}[\nu_{i,l}(t + \Delta t)]_{(\nu_{i,1}, \nu_{i,2})(t) \in \Omega_{\nu_1, \nu_2}} \end{aligned}$$

are calculated for each square of the grid, where the larger eigenvalue corresponds to  $\sigma_{\leftrightarrow}^2(\nu_1, \nu_2)$  and the smaller one to  $\sigma_{\downarrow}^2(\nu_1, \nu_2)$ . The results are shown in the frequency space in Figs. 4.2 and 4.3 where their values are encoded as color and the regular tori are included in gray. Squares with  $|\Omega_{\nu_1, \nu_2}| < 5$  or in the case of the density  $|\Omega_{\nu_1, \nu_2}| = 0$  are neglected and left white.

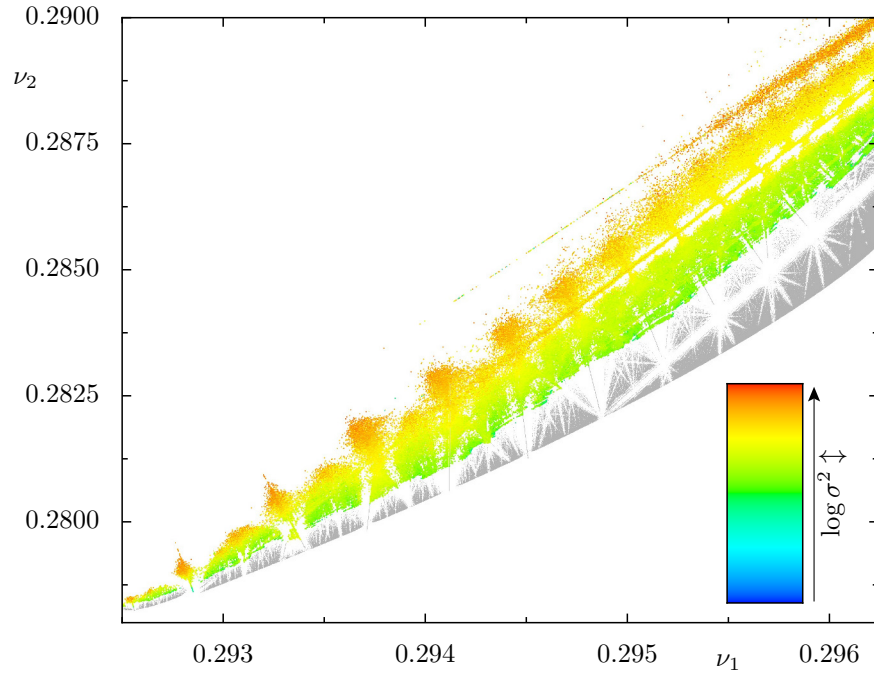
The distribution of densities  $\rho(\nu_1, \nu_2)$  in Fig. 4.2(a) shows pronounced peaks along several lines which match resonance lines. For comparison a set of the recognizable resonances are indicated by the orange dashed lines in the background. Going away

(a) Density  $\rho(\nu_1, \nu_2) \in [4 \cdot 10^{-7}, 2 \cdot 10^{-3}]$ (b) Average escape time  $\bar{T}(\nu_1, \nu_2) \in [5.5 \cdot 10^3, 7.9 \cdot 10^7]$ 

**Figure 4.2:** Distribution of the density  $\rho$  and the average escape time  $\bar{T}$  in frequency space for the 61600 chaotic orbits trapped at the horseshoe with  $T \geq 10^5$ , i.e. a total of  $|\Omega_{\text{horseshoe}}| \approx 5 \cdot 10^6$  frequency pairs. The values are encoded according to the color bars with limiting values given in the subcaptions. The resolution of the grid is  $\Delta\nu = 5 \cdot 10^{-6}$  and grid points are left white if less than (a) 1 or (b) 5 frequency pairs are at the grid point. For comparison the regular tori from Fig. 2.4(b) are shown in gray and some resonances are indicated in the background as orange, dashed lines, i.e. in (b) the resonance  $29 : -9 : 6$ .



(a) Large eigenvalue  $\sigma_{\leftrightarrow}^2(\nu_1, \nu_2) \in [4 \cdot 10^{-13}, 10^{-4}]$



(b) Small eigenvalue  $\sigma_{\downarrow}^2(\nu_1, \nu_2) \in [4 \cdot 10^{-21}, 7 \cdot 10^{-6}]$

**Figure 4.3:** Distribution of the eigenvalues  $\sigma_{\leftrightarrow}^2$ ,  $\sigma_{\downarrow}^2$  of the covariance matrix in frequency space, analogous to Fig. 4.2(b). Note that for a majority of the grid points the ratio  $\sigma_{\leftrightarrow}^2/\sigma_{\downarrow}^2 \approx 100$  is obtained which matches the observations in Ref. [72].

from any resonance the density decays rapidly as demonstrated by the logarithmic color scale in Fig. 4.2(a). Exceptions are the vicinity of some resonance junctions where cones of higher density exist between two of the intersecting resonances. This may be due to a strong overlap of these resonance channels at the junction. The highest values of density are observed right at the junctions but the peaks are so confined to the point of their junction that they are hardly visible in Fig. 4.2(a). An inspection in phase space of the orbit segments whose frequencies are located at junctions by 3D projections confirms that these points surround EE periodic orbits. The high density at resonances is partially caused by the fact that due to the periodicity a large region of the phase space is mapped to a single point by frequency analysis. Nevertheless, the distribution of densities demonstrates that chaotic orbits within the sticky region can be assigned to open resonance channels or junctions at almost all times.

The rapid decay of density away from resonances along with the requirement of at least five frequency pairs per square for the entities  $\bar{T}(\nu_1, \nu_2)$ ,  $\sigma_{\leftrightarrow}^2(\nu_1, \nu_2)$ , and  $\sigma_{\downarrow}^2(\nu_1, \nu_2)$  causes large white gaps around resonances in the remaining subfigures of Figs. 4.2 and 4.3. The distribution of escape times  $\bar{T}(\nu_1, \nu_2)$  in Fig. 4.2(b) shows almost no signs of resonances apart from these gaps. There is a peak of escape times at the resonance  $29 : -9 : 6$ , which is inserted as orange dashed line in Fig. 4.2(b), but otherwise the escape time decreases monotonously going away from the regular structure. This is consistent with the observation that the last frequency pair before the recurrence of any trapped orbit is situated in the area of the lowest escape times or even a further away from the regular structure. This area also hosts the first frequency pairs which are close to the regular structure. In conclusion, Fig. 4.2(b) demonstrates that the chaotic orbits enter and exit the vicinity of the horseshoe away from the regular structure and tend to get closer to it when they are trapped for longer times.

The eigenvalues  $\sigma_{\leftrightarrow}^2(\nu_1, \nu_2)$  and  $\sigma_{\downarrow}^2(\nu_1, \nu_2)$  of the covariance matrix in Fig. 4.3 should give some idea about the local stochastic transport in frequency space in the following sense. If the transport can be locally described by the superposition of two independent 1D diffusion processes which are perpendicular to each other, it is straightforward to prove that in the limit of infinite sample size the eigenvalues of the above defined covariance matrix are the variances resulting from these processes after one time step. The corresponding eigenvectors are oriented along the direction of the corresponding diffusion process. It turns out that the eigenvectors of the larger eigenvalue  $\sigma_{\leftrightarrow}^2(\nu_1, \nu_2)$  usually point along regular structures as expected from the previous observations of Ref. [72]. The only exception are again the vicinity of some junctions, mostly on the resonance  $15 : -5 : 5$ , where the directions of eigenvectors are spatially very unstable. The smaller eigenvalue  $\sigma_{\downarrow}^2(\nu_1, \nu_2)$  increases away from the regular structure without



---

very pronounced signatures of resonances. In contrast, the larger eigenvalue  $\sigma_{\leftrightarrow}^2(\nu_1, \nu_2)$  additionally exhibits some drops appearing in bright blue around resonances close to the regular structure in particular at larger  $\nu_1$ . Thus, while the overall escape  $\bar{T}(\nu_1, \nu_2)$  from the sticky region seems to be independent of resonance channels, the local, short time transport is organized by them.

The distributions for the entities  $\rho(\nu_1, \nu_2)$ ,  $\bar{T}(\nu_1, \nu_2)$ ,  $\sigma_{\leftrightarrow}^2(\nu_1, \nu_2)$ , and  $\sigma_{\downarrow}^2(\nu_1, \nu_2)$  are also computed for the coupled twist maps  $F_{\text{Twist}}$  with width  $\Delta\nu = 10^{-4}$ , based on the  $N_{\text{Twist}} = 20775$  trapped orbits with Poincaré recurrence times  $T \geq 10^6$  which lead to  $|\Omega_{\text{Twist}}| \approx 1.7 \cdot 10^7$  frequency pairs. The results are shown in Fig. 4.4. For region B, the major sticky region, and largely for region C observations analogous to Figs. 4.2 and 4.3 can be made. The region A exhibits ungeneric behavior as expected and is not discussed here.

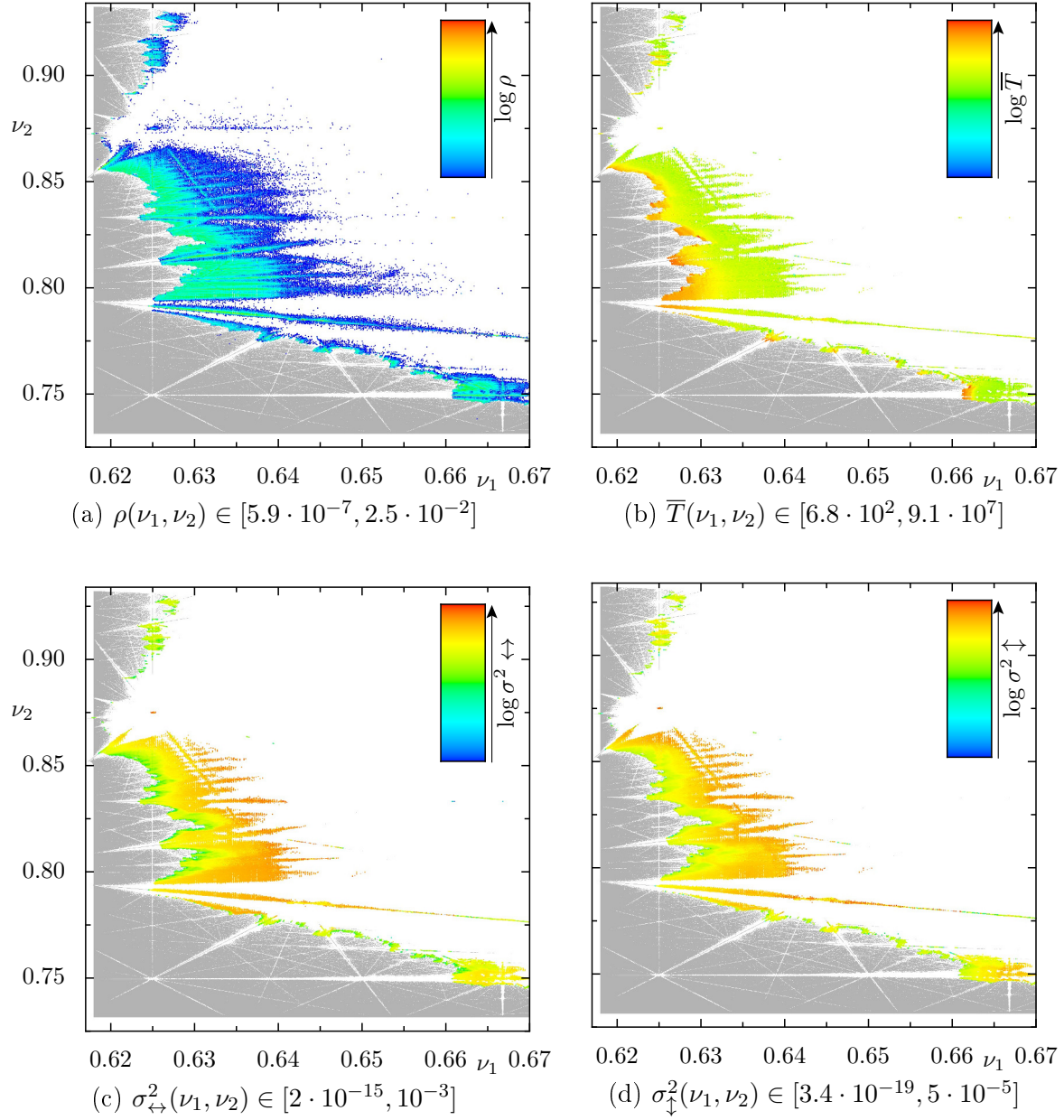


**Figure 4.4:** Distribution of  $\rho$ ,  $\bar{T}$ ,  $\sigma_{\leftrightarrow}^2$ ,  $\sigma_{\downarrow}^2$  in the frequency space for the coupled twist maps  $F_{\text{Twist}}$ , analogous to Figs. 4.2 and 4.3, based on the 20775 trapped orbits with  $T \geq 10^6$ , i.e. a total of  $|\Omega_{\text{Twist}}| \approx 1.7 \cdot 10^7$  frequency pairs. The resolution of the grid is  $\Delta\nu = 10^{-4}$ . For comparison the regular tori from Fig. 3.7 are shown in gray while only a detail of this frequency space is displayed. Note that for a majority of the grid points the ratio  $\sigma_{\leftrightarrow}^2/\sigma_{\downarrow}^2 \approx 100$  is obtained which matches the observations in Ref. [72].

## 4.2 Four transport processes in resonance channels (I–IV)

In the sticky region at the surface of the regular structures the chaotic transport is strongly governed by the web of open resonance channels. In the following, this transport is considered to be composed of the four basic transport phenomena present in an open resonance channel of a 4D map:

- I) Transport across a resonance channel
- II) Trapping in deeper class of hierarchy
- III) Trapping at a resonance junction
- IV) Transport along a resonance channel

The heuristic argument for this decomposition goes as follows: In principle, the 4D chaotic transport close to the regular structures can be described in the 2D frequency space. Thus, a possible, local coordinate system is given by the two directions I) across and IV) along a resonance channel. According to Sec. 3.3, an important phenomenon which is not properly displayed in frequency space is the trapping in a deeper class of the hierarchy. Deeper classes only appear as lines and points in frequency space, i.e. II) resonance lines and III) junctions. Note that at resonance junctions even more complicated dynamics occur. These dynamics are not considered here.

In order to examine the interplay of the four transport processes and to estimate their impact onto the overall chaotic transport, trapped orbits are examined in frequency space and time–frequency plots, see Sec. 2.6.2. While it turns out that the processes I) and II) resemble the transport due to partial barriers along the levels and classes in 2D maps, respectively, see Sec. 2.4, the processes III) and IV) are purely higher-dimensional phenomena. The features of time–frequency plots which are identified in this section for instance as signatures of partial barriers are also visible for other systems [41, 43, 44, 60] but have not been properly understood yet, emphasizing the relevance of the findings in this section.

Chaotic transport is usually studied in phase space. There partial barriers in 2D maps can be detected by drops in density of chaotic orbits iterated for a finite time, see Fig. 2.1 in Sec. 2.4. However, for 4D maps with a 4D phase space the 2D frequency space is more accessible. In order to understand chaotic transport also in the frequency space of a 4D map, at first trapped orbits of the 2D map  $F_{2D}$  with  $K = 2.25$  are considered in phase and frequency space. Figures 4.5(a) and 4.5(b) show a chaotic orbit that is mainly

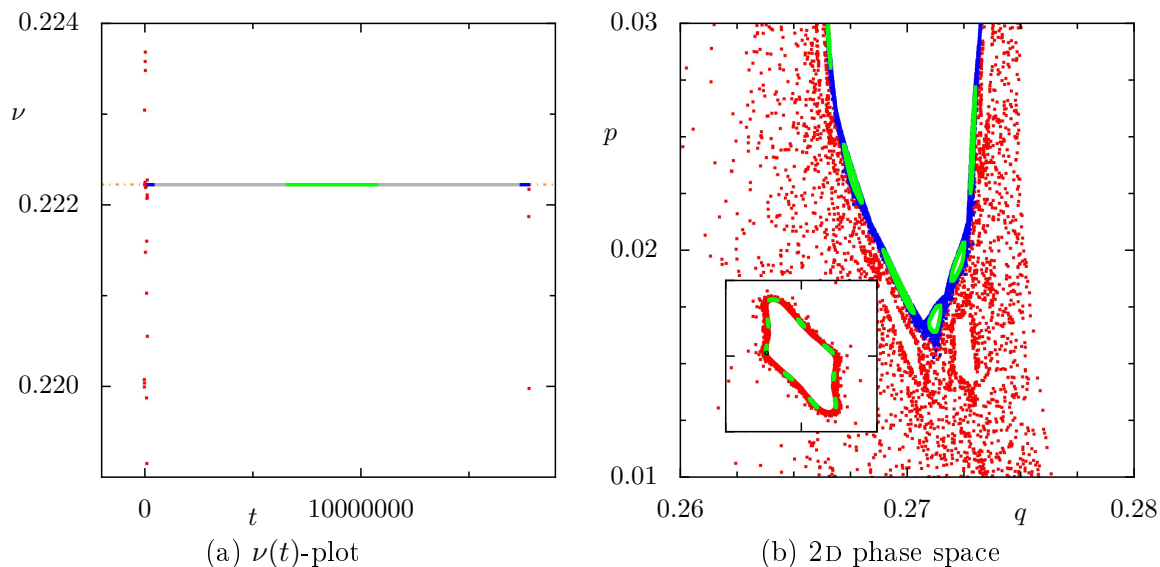


**Figure 4.5:** Trapped orbit of the 2D map  $F_{2D}$  with  $K = 2.25$ , mainly trapped in the class hierarchy, in (a) time–frequency plot and (b) phase space with iteration time  $t \in [0, T = 17763757]$ . The frequency analysis is performed on segments of length  $\Delta t = 4096$ , see Sec. 2.6.2. In (a) frequency intervals are chosen and points within the same interval are shown with the same color. The corresponding points in (b) are colored accordingly, see Eq. (2.18). Since in (b) the green, blue, and gray points are very dense, and the gray ones are plotted first, they are not visible. In (a) the resonance  $\nu = 2/9$  is indicated in the background as orange, dashed-dotted line. In (b) the inset shows the whole phase space  $(p, q) \in [-0.5, 0.5] \times [0, 1)$ . A black box indicating the magnification seen in (b) is hardly visible as black point.

trapped at the resonance  $\nu = 2/9$  in a time–frequency plot and phase space, respectively. In both figures the points of the orbit are colored correspondingly. Most points are gray but certain sets of points, which are chosen in frequency space, are highlighted in other colors. Note that due to the finite size of the points in the plots, highlighted points may cover other points if they are too close to each other. For instance there are no gray points visible in Fig. 4.5(b) and no blue points visible in the inset of Fig. 4.5(b). The central part of the orbit is colored green, highlighting nine islands of the resonance chain  $\nu = 2/9$  in phase space, which are visible in the inset of Fig. 4.5(b). The magnification at one of these islands shown in Fig. 4.5(b) reveals further green subislands. This implies that the orbit is trapped in the deeper classes of the resonance  $\nu = 2/9$ . The frequencies  $\nu(t)$  of the trapped orbit shown in corresponding colors in Fig. 4.5(a) are almost constant at  $\nu(t) = 2/9$  for the majority of the iterations  $t$ . Only the frequencies of the initial iterations and the last iterations before the recurrence of the orbit deviate from  $2/9$  and fluctuate strongly over time. These points are colored red, while the first and last iterations exhibiting an almost constant frequency are colored blue. There is a sharp transition between almost constant and strongly fluctuating frequency. In

the phase space in Fig. 4.5(b) the blue and red points are well separated from each other with a drop in density from the blue to the red points. As explained in Sec. 2.4, this transition corresponds to the crossing of the partial barrier belonging to the next deeper class around the islands of the resonance  $\nu = 2/9$ . Note that the frequency  $\nu(t)$  also fluctuates during the time the orbit is trapped in the deeper class. However, the amplitude is several orders of magnitude smaller than for the intervals colored in red.

In general, constant frequencies with a rational number  $\nu(t) = n/m$  correspond to the orbit being in a deeper class. The reason is that for an orbit trapped at an island chain, the corresponding rational frequency  $\nu = n/m$  is very dominant in the Fourier spectrum of this orbit. This is analogous to resonant frequencies obtained by frequency analysis in 4D maps, cf. Secs. 3.2.3 and 3.3.1. Within the deeper class the frequencies cannot resolve further details about the transport of the orbit. For instance, in Fig. 4.5(a) the blue and green points have the same frequency, but the phase space in Fig. 4.5(a) shows that the green points are in an even deeper class than the blue points. A further examination requires a frequency analysis for the points with constant frequency with respect to an island of the resonance, analogous to Secs. 3.3.1 and 3.3.2. In the time–frequency plots the point of transition from one class to the next can of course only be resolved up to the length  $\Delta t$  of the segments used for the frequency analysis. In particular, if the orbit crosses the partial barrier more than once within two segments  $\Delta t$ , e.g., for partial barriers with high flux, the transition cannot even be detected.

In the same fashion as Fig. 4.5, Fig. 4.6 shows a chaotic orbit that is mainly trapped along the levels of the hierarchy. In the magnification of the phase space in Fig. 4.6(b) there is a clear drop in point density between the region with the blue and red points and the gray stripe to the right. The island visible within the area of red and blue points belongs to the resonance  $\nu = 2/9$ . A further magnification of the the gray area, indicated by the box in Fig. 4.6(b), is shown in Fig. 4.6(d) with different colors. On this scale another drop in density is visible between the regions with colored points and the gray stripe to the right. A magnification of this stripe, indicated by the box in Fig. 4.6(d), is shown in Fig. 4.6(f) and reveals further details. The corresponding time–frequency plots in the left column of Fig. 4.6 display the same hierarchy of scales. In Fig. 4.6(a) a few initial and last iterations in red and blue, respectively, are scattered over a wide frequency interval. The rest of the iterations in gray are confined to a much smaller frequency interval, indicated by the box. The magnification of this interval in Fig. 4.6(c) reveals several frequency intervals to which the orbit seems to be confined for several consecutive iterations. These intervals are estimated manually by visual inspection and highlighted with different colors. The most pronounced intervals are the purple and upper gray one. The frequencies  $\nu(t)$  of the orbit jump twice

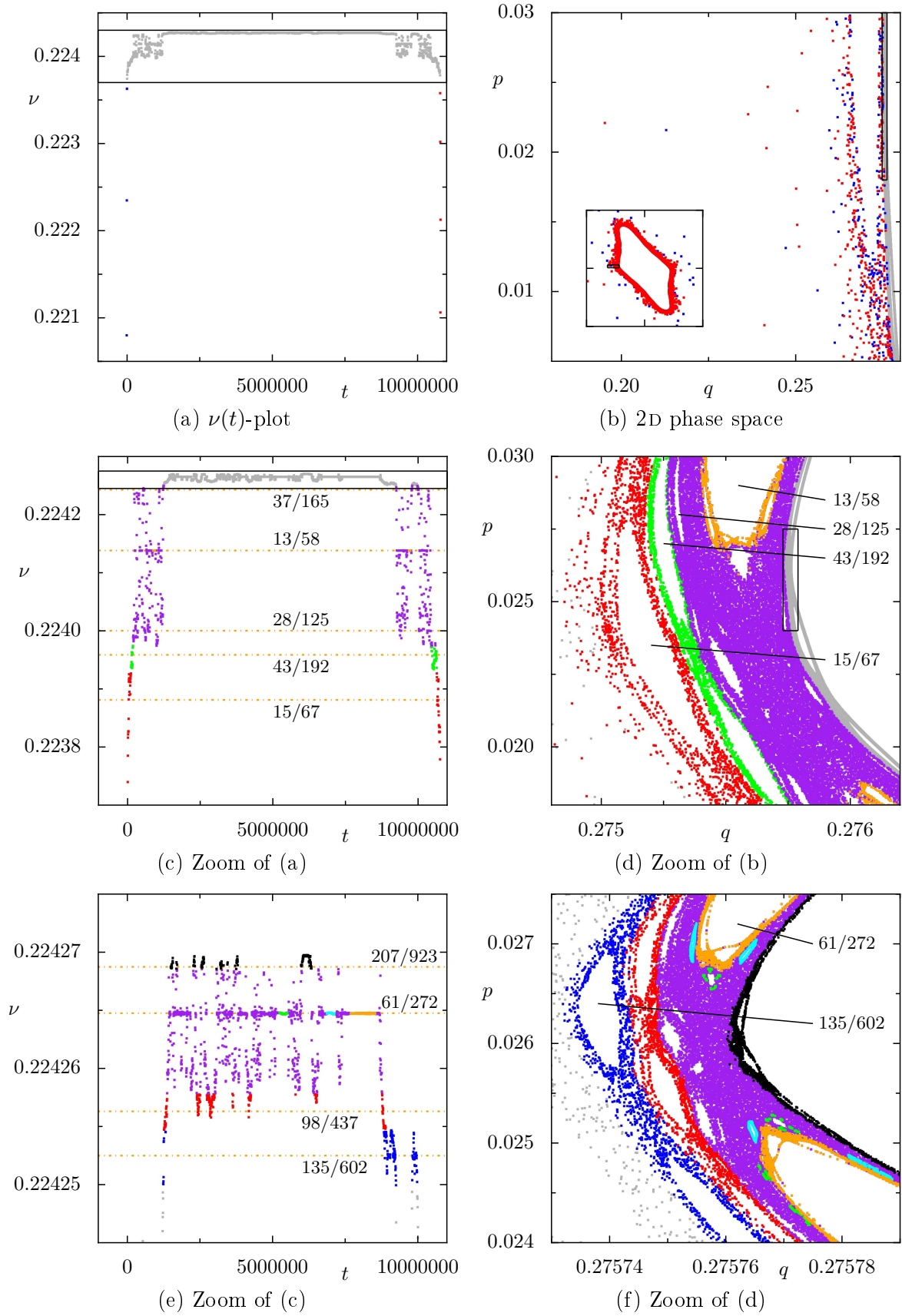


**Figure 4.6:** Trapped orbit of the map  $F_{2D}$  from Fig. 2.1(b), mainly trapped along the level hierarchy, displayed analogous to Fig. 4.5. Each row represents a magnification of the previous one, as indicated by the black boxes, with different sets of points being colored. Resonances are from top to bottom (c)  $\nu = \{37/165, 13/58, 28/125, 43/192, 15/67\}$  and (e)  $\nu = \{207/923, 61/272, 98/437, 135/602\}$ .

from the purple to the gray interval and back, once dwelling in the gray interval for several million iterations, once for less than one million iterations. The sudden transitions in the time–frequency plots are signatures of partial barriers. A comparison with the correspondingly colored points in phase space in Fig. 4.6(d) demonstrates that the frequency intervals represent stochastic layers of resonances. For instance the purple layer is caused by the resonances  $\nu = 37/165, 13/58, 28/125$  which are indicated by the orange dashed-dotted lines in Fig. 4.6(c). A comparison of the order of the red, green and purple layer in Figs. 4.6(c) and 4.6(d) also implies that for this map a higher frequency is equivalent to being closer to the central regular island. The magnification of the inner gray stripe indicated by boxes in Figs. 4.6(c) and 4.6(d) is shown in Figs. 4.6(e) and 4.6(f) and allows for highlighting even more stochastic layers. It should be emphasized that all these stochastic layers are identified by selecting intervals from time–frequency plots. While the frequencies of the orbit change chaotically within the frequency interval of the stochastic layer, for short time periods they exhibit trapping in a deeper class. An example are the points at the resonance  $\nu = 13/58$  highlighted in orange in Figs. 4.6(c) and 4.6(d) and the green, blue and orange points at the resonance  $\nu = 61/272$  in Figs. 4.6(e) and 4.6(f). The different highlighted island chains in the latter example in Fig. 4.6(f) illustrate again the ambiguity of frequencies when the orbit is in a deeper class.

In general, if frequencies are confined to some interval around resonances for some period of time with sudden jumps to adjacent intervals it means that the corresponding orbit is trapped in the stochastic layer of a fixed class of the hierarchy. In contrast to being trapped in a deeper class, the frequencies change chaotically within the interval representing the stochastic layer. As demonstrated with the example in Fig. 4.6, trapping along the levels of the hierarchy is well observable in time–frequency plots. Again the transitions from layer to layer can only be resolved up to  $\Delta t$ . In particular, the layers of different resonances may appear as overlapping, if the flux in between them is too big.

The orbit in Fig. 4.6 spends the majority of the iterations in the deeper levels of the hierarchy that it reaches, i.e. at  $\nu = 61/272$  and adjacent stochastic layers. This is the typical behavior predicted by the theory for orbits trapped mainly along the levels of the hierarchy, see Sec. 2.4. However, Fig. 4.7 shows a chaotic orbit that is trapped in the same system more than twice as long, but reaches at most  $\nu = 135/602$ , while spending most of the iterations in the purple layer around  $\nu = 13/58$ . In particular, the orbit frequently jumps to stochastic layers, which are even further away from the central regular island. Due to more points in these layers it is possible to resolve finer layers in Fig. 4.7 than in Fig. 4.6. It is interesting to acknowledge that also such kind

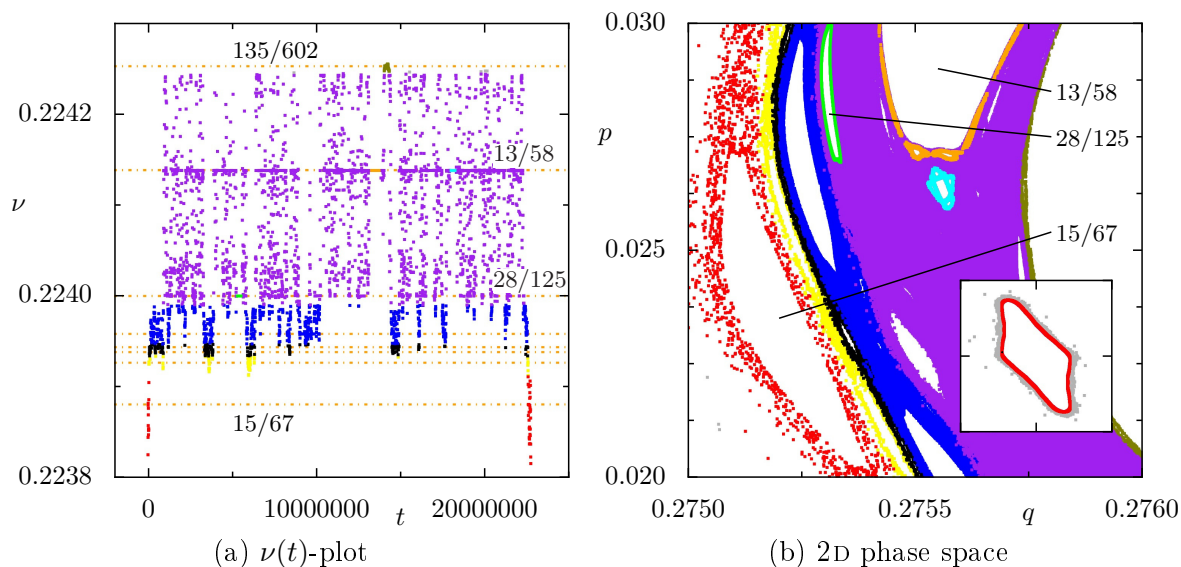


**Figure 4.7:** Trapped orbit of the map  $F_{2D}$  with  $K = 2.25$  and  $T = 22742154$ , frequently jumping between stochastic layers, displayed analogous to Fig. 4.5. The stochastic layers recognized from the frequencies  $\nu(t)$  are similar to the ones recognized in Figs. 4.6(c) and 4.6(d). The resonances are from top to bottom  $\nu = \{135/602, 13/58, 28/125, 43/192, 159/710, 58/259, 73/326, 15/67\}$ .

of orbits contribute to the power-law of the 2D map, because frequent jumps between resonances are generically observed for trapped orbits of 4D maps in the following.

The time–frequency signatures of deeper classes and stochastic layers are also observed for trapped orbits in 4D maps. It is convenient to demonstrate this for the coupled twist maps  $F_{\text{Twist}}$  as the original 2D twist maps are still recognizable in the coupled system and thus allow a direct comparison to the observations in 2D maps. Figure 4.8 shows a chaotic orbit of the coupled twist maps  $F_{\text{Twist}}$  trapped in region B. Figures 4.8(a) and 4.8(b) show the orbit in time–frequency  $(t, \nu_2)$  and frequency space  $(\nu_1, \nu_2)$  with points colored according to their iteration time. Several relevant resonances are indicated by dashed orange lines in Fig. 4.8(b). The horizontal line is the resonance  $0 : 6 : 5$  and the vertical line intersecting with it corresponds to  $8 : 0 : 5$ . Already the familiar signatures of partial barriers due to these resonances are visible in the course of  $\nu_2(t)$  in Fig. 4.8(a), that is sudden jumps between frequency intervals and periods of constant frequency. In order to observe the signatures of partial barriers also in phase space, thin slices in the angles  $|\Theta_1|, |\Theta_2| < 10^{-2}$  are projected to the  $(p_2, q_2)$ -,  $(p_1, q_1)$ -coordinates, respectively. Details of these slices for the chaotic orbit are shown in Figs. 4.8(d) and 4.8(f). As for the examples of the 2D map, several frequency intervals in  $\nu_2$  are highlighted with different colors in Fig. 4.8(c) and these points are colored accordingly in the slices and the  $(t, \nu_1)$ -plot in Fig. 4.8(e). This highlights different layers with relatively sharp borders in the  $\Theta_1$ -slice in Fig. 4.8(d), resembling stochastic layers of a



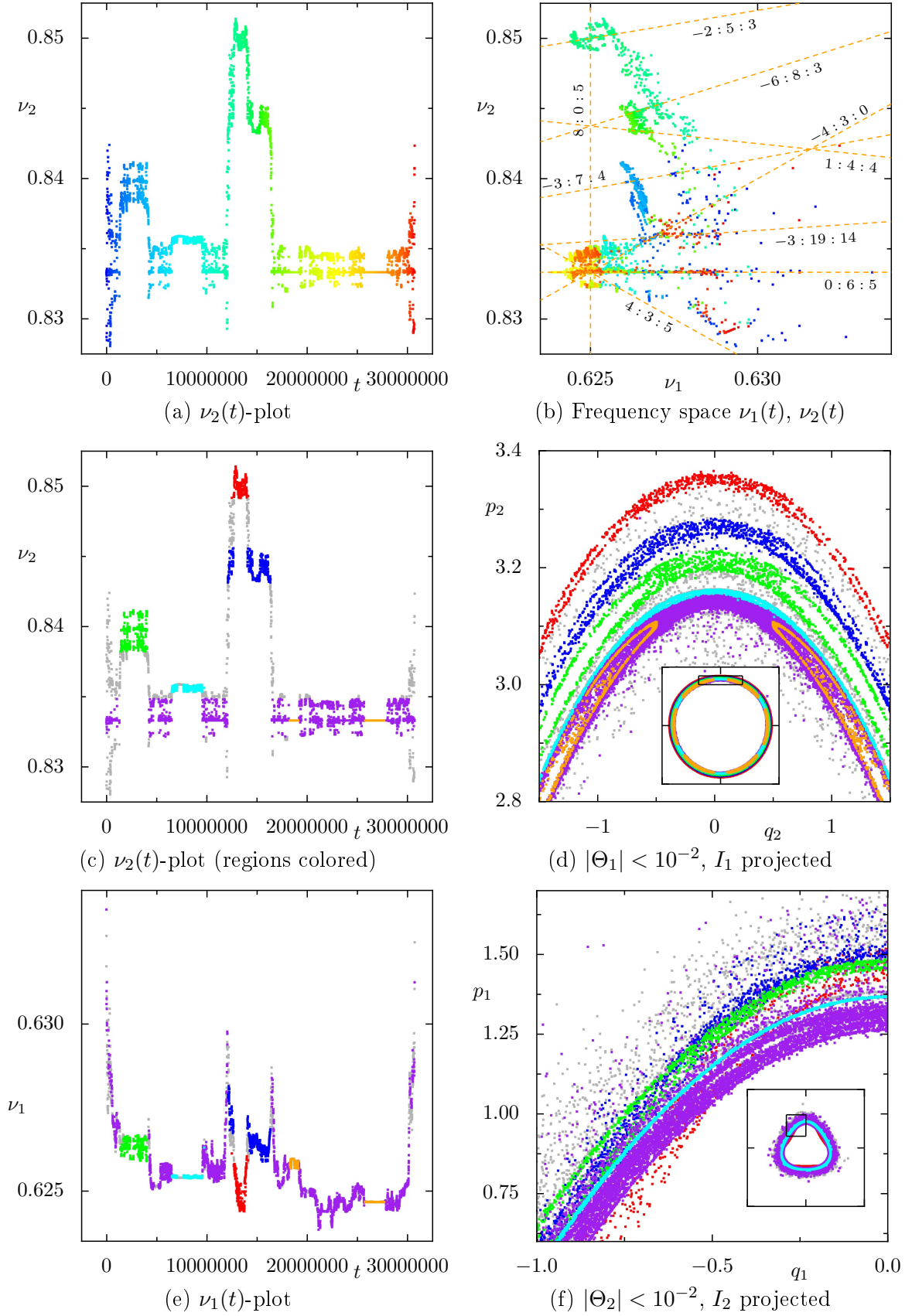


**Figure 4.8:** Chaotic orbit trapped in region B of the 4D map  $F_{\text{Twist}}$  displayed similar to Fig. 4.5. In (a), (b) the points are colored according to the iteration time  $t \in [0, T = 30665958]$ . The stochastic layers are recognized from  $\nu_2(t)$ , see (c), and all points in (c)–(f) are colored accordingly. The resonances associated with the layers of (c) are indicated in (b) as orange, dashed lines, i.e.  $-2 : 5 : 3$ ,  $8 : 0 : 5$  (red);  $-6 : 8 : 3$ ,  $1 : 4 : 4$  (blue);  $-3 : 7 : 4$  (green);  $-3 : 19 : 14$  (bright blue); and  $-4 : 3 : 0$ ,  $4 : 3 : 5$  (purple),  $6 : 0 : 5$  (orange). The insets in (d),(f) show  $p_1, q_1 \in [-3, 3]$ ,  $p_2, q_2 \in [-4, 4]$ .

2D phase space. Also Fig. 4.8(d) confirms that the pronounced intervals of constant frequency  $\nu_2 = 5/6$  ( $\sim 0 : 6 : 5$ ) colored orange in Fig. 4.8(c) correspond to the orbit being trapped at an island chain. More precisely, an island chain of period-six can be seen in the inset of Fig. 4.8(d) which shows a larger part of the slice. Note that for  $F_{\text{Twist}}$  by construction larger  $\nu_i$  correspond to points in phase space further away from the center  $(p_i, q_i) = (0, 0)$ , as suggested by the order of colors in Figs. 4.8(c) and 4.8(d).

While the resemblance of these plots and the according plots for 2D maps demonstrates the existence and impact of partial barriers in 4D maps, the additional degree of freedom complicates the proper identification and display of the stochastic layers. Firstly, the resonances in 4D maps are in general coupled, i.e. they involve two frequencies. Hence, except for the uncoupled resonance  $0 : 6 : 5$  the resonances responsible for the stochastic layers are not horizontal lines in the time–frequency plot in Fig. 4.8(c) anymore. Instead a resonance and the frequency interval of its affiliated stochastic layer have to be identified in the frequency space  $(\nu_1, \nu_2)$  rather than in the time–frequency plot of a single frequency  $\nu_2$ . Secondly, even if the relevant resonances were uncoupled, there is an additional dynamics in the non-resonant degree of freedom, i.e. the transport along the resonances. This dynamics is visible in the time–frequency plot  $(t, \nu_1)$  in Fig. 4.8(e). The development of  $\nu_1(t)$  reminds of a random walk with possibly time-dependent variance. Accordingly, the corresponding slice in Fig. 4.8(f) shows all colored points distributed relatively randomly over a common area. A time dependence of the variance could result from the different resonances the orbit visits over time, which each might have an individual transport rate. Likewise, the frequency interval of a stochastic layer may change along the corresponding resonance. For this reason the green and bright blue frequency intervals for  $\nu_2$  in Fig. 4.8(c) are confined to certain time intervals for which the corresponding frequencies  $\nu_1$  do not change much.

Besides transport along resonances, also junctions of resonances are only possible in higher-dimensional maps. An example is the junction of the resonances  $-2 : 5 : 3$  and  $8 : 0 : 5$  at  $(\nu_1, \nu_2) = (0.625, 0.85)$  in Fig. 4.8(b). Points in the vicinity of this junction are highlighted in red in Figs. 4.8(c) and 4.8(e). On closer inspection of Figs. 4.8(c) and 4.8(e), not shown here, it seems the orbit frequently jumps between the stochastic layers of the resonances  $-2 : 5 : 3$  and  $8 : 0 : 5$ . Also stochastic layers of other resonances meeting at this junction may be visible. This behavior may be due to the layers increasingly overlapping in the vicinity of the junction, entering the Chirikov regime, see Sec. 2.5. However, this behavior does not seem to be universal for the vicinity of junctions. A counterexample is the junction of the resonances  $0 : 6 : 5$ ,  $8 : 0 : 5$ ,  $-4 : 3 : 0$ , and  $4 : 3 : 5$  in Fig. 4.8(b). Despite the orbit being right at the junction, only the stochastic layer of the  $0 : 6 : 5$  resonance colored in purple in

Fig. 4.8(c) is visible with a random walk like behavior of  $\nu_1$  in Fig. 4.8(e). This might be due the low order of this resonance. Another phenomenon expected at a junction is trapping directly at the islands around the EE periodic orbits of the junction, see Sec. 3.3.3, which is not observed for this example. Note that the orange segment with seemingly constant frequencies  $\nu_1(t) = k$  in Fig. 4.8(e) is actually not at the junction  $k < 5/8 = 0.625$ .

In order to present a possible way to deal with the stochastic layers of uncoupled resonances in frequency space, Fig. 4.9 shows an example of a chaotic orbit of  $F_{\text{Twist}}$  trapped in region A. While the plots are essentially the same as in Fig. 4.8, there are a few adjustments. Firstly, since the relevant resonances are almost parallel to the  $\nu_2$ -axis, see Fig. 4.9(b), the stochastic layers are this time better visible in  $\nu_1(t)$  in Fig. 4.9(a). Secondly, the axes of the frequency space in Fig. 4.9(b) are switched to allow a better comparison with Fig. 4.9(a). Since the relevant resonances are not uncoupled, the stochastic layers are not easily identified in the time–frequency plot in Fig. 4.9(a). For instance, the most important resonance  $5 : 1 : 4$ , which is the resonance at lowest  $\nu_1$ -values in Fig. 4.9(b), appears as a non-straight line in Fig. 4.9(a). For a particular resonance the time–frequency plot can be improved by a transformation, e.g., a rotation, which maps the frequencies  $(\nu_1, \nu_2)$  to new coordinates  $(\tilde{\nu}_1, \tilde{\nu}_2)$  in which the resonance corresponds to a line parallel to one of the axes. The result for the resonance  $5 : 1 : 4$  is shown in Figs. 4.9(c) and 4.9(e). In the time–frequency plot in Fig. 4.9(c), where the resonance  $5 : 1 : 4$  appears now as a straight line, several stochastic layers can be recognized and are highlighted with different colors. The corresponding slice in Fig. 4.9(d) shows the expected signatures of stochastic layers, including the trapping at an island chain of period-five highlighted in orange, which corresponds to the resonance  $5 : 1 : 4$ . Note that these islands are actually one connected tube intersecting five times with the slice. A comparison of Figs. 4.9(c) and 4.9(d) with Fig. 4.7 shows a striking resemblance between one degree of freedom of a trapped orbit of a 4D map and a trapped orbit of a 2D map. The other coordinate  $\tilde{\nu}_2(t)$  resembles as expected a random walk with time dependent variance in Fig. 4.9(e). However, as implied by the different scales of frequencies in Fig. 4.9(b), this random walk is confined to a thin layer in the corresponding slice in Fig. 4.9(f).

Having established the general signatures of partial barriers, it is possible to examine trapped orbits of any generic 4D map in frequency space. An example of the two coupled standard maps  $F_{\text{SC}}$  is presented in Fig. 4.10 in the same way as for the coupled twist maps in Fig. 4.9. The orbit is trapped at the horseshoe around the resonance  $17 : 0 : 5$ . Since most of the relevant resonances in Fig. 4.10(b) are quite parallel to the  $\nu_2$ -axis, the axes are again switched to allow a better comparison with Fig. 4.10(a). Three major

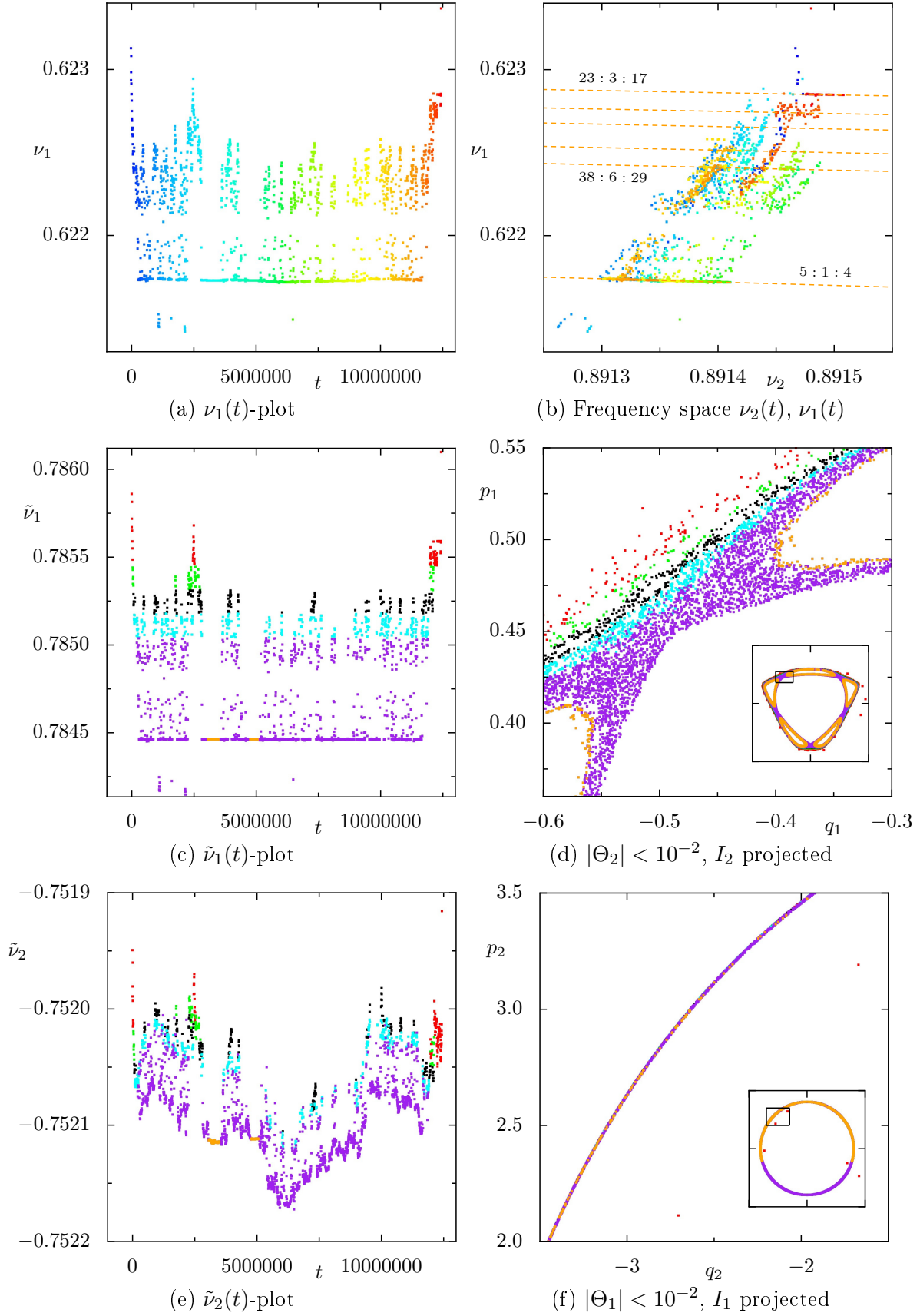


**Figure 4.9:** Chaotic orbit trapped in region A of the 4D map  $F_{\text{Twist}}$  with  $T = 12433054$  displayed similar to Fig. 4.8. For (c), (e) the frequencies  $(\nu_1, \nu_2)$  are transformed to  $(\tilde{\nu}_1, \tilde{\nu}_2)$  such that the resonance  $5 : 1 : 4$  is along the  $\tilde{\nu}_1$ -axis. The stochastic layers are recognized from  $\tilde{\nu}_1(t)$ , see (c). For (b) the axes are switched. The resonances in (b) are from top to bottom  $23 : 3 : 17$ ,  $51 : 7 : 38$ ,  $28 : 4 : 21$ ,  $33 : 5 : 25$ ,  $38 : 6 : 29$ ,  $5 : 1 : 4$ . The insets in (d),(f) show  $p_1, q_1 \in [-1, 1]$ ,  $p_2, q_2 \in [-5, 5]$ .

---

stochastic layers can be identified immediately in the time–frequency plot in Fig. 4.10(a) with fast transitions in between them, which shows the existence and impact of partial barriers in the generic 4D map  $F_{\text{SC}}$ . However, a closer examination in phase space by highlighting points selected from different layers in Fig. 4.10(c) is hardly possible. There is no trivial slice which effectively captures the relevant degree of freedom. A detail of the slice defined by  $|p_1| < 10^{-3}$  and a projection to the  $(p_2, q_2)$ -coordinates is shown in Fig. 4.10(d) as an example. The different stochastic layers highlighted in Fig. 4.10(c) lie all on top of each other. The only recognizable detail are the blue points being trapped at an period-five island chain. This chain corresponds to the resonance  $19 : 5 : 7$  and is actually a tube that intersects the slice five times at two positions, see also the inset of Fig. 4.10(d). Since the transport along the resonances is very slow and all but one resonance are coupled, the time–frequency plot for  $\nu_2(t)$  resembles the one for  $\nu_1(t)$ . On top of that the relevant resonances are not close to being parallel to each other. Hence, the transport along the resonances cannot easily be viewed in the frequency coordinates even after a transformation as suggested by the previous example of  $F_{\text{Twist}}$ . However, the frequency space should be sufficient to get a rough quantitative estimate about the dwell times and fluxes across the resonances.

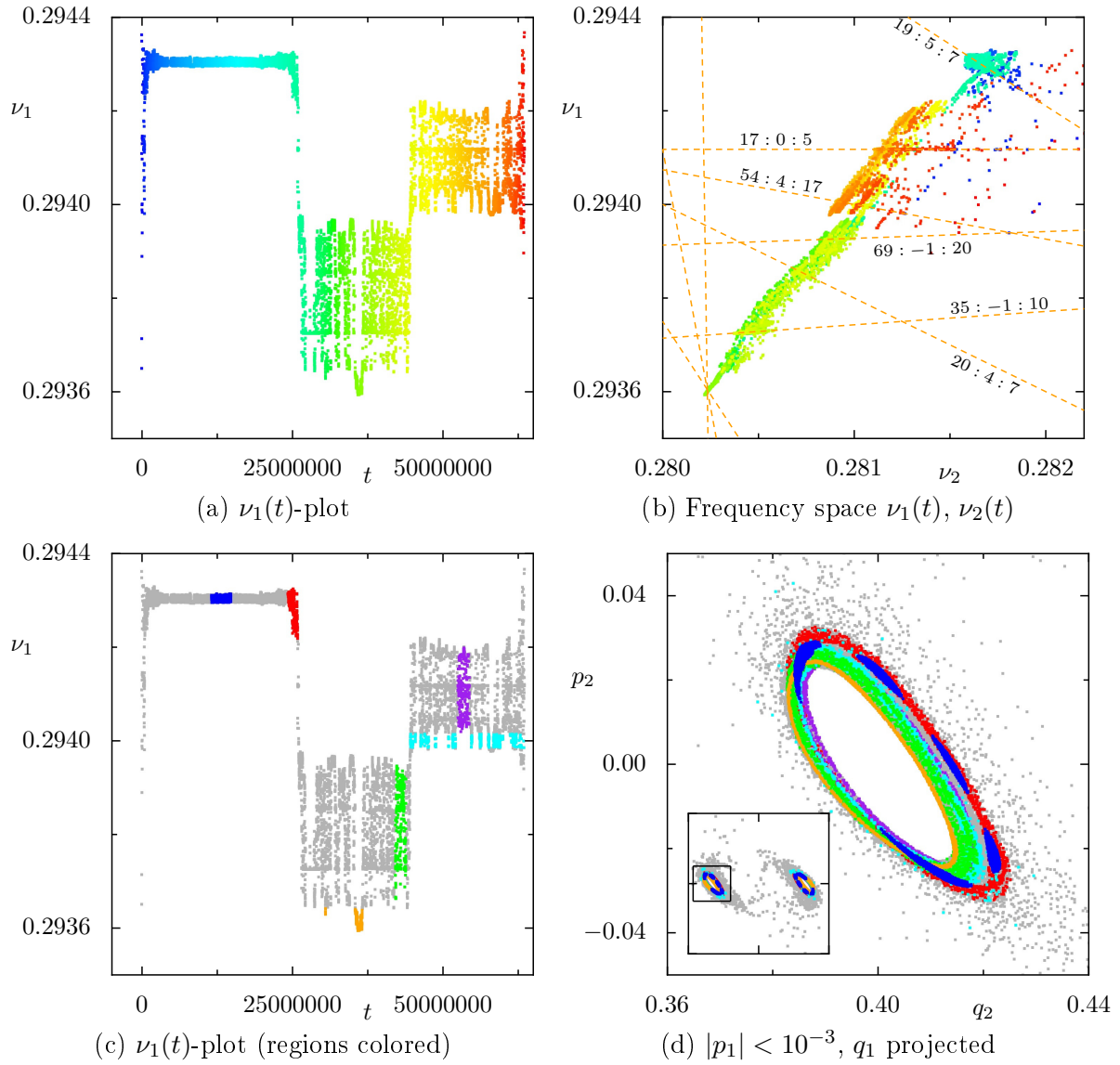


**Figure 4.10:** Chaotic orbit trapped at the horseshoe of the 4D map  $F_{SC}$  with  $T = 63524738$  displayed similar to Fig. 4.8. The stochastic layers are recognized from  $\nu_1(t)$ , see (c). For (b) the axes are switched. The resonances associated with the layers of (c) are indicated in (b) as orange, dashed lines, i.e.  $19 : 5 : 7$  (blue, red);  $17 : 0 : 5$  (purple);  $54 : 4 : 17$  (bright blue);  $69 : -1 : 20$ ,  $20 : 4 : 7$ ,  $35 : -1 : 10$  (green);  $34 : 75 : 31$ ,  $2 : 55 : 16$ ,  $32 : 20 : 15$  (orange). The inset in (d) shows  $p_2 \in [-0.2, 0.2]$ ,  $q_2 \in [0.35, 0.65]$ .

### 4.3 I) Transport across a resonance channel

The chaotic transport across the open resonance channels provides a possible mechanism for the observed trapping with the very straight power law as sketched in the following. This mechanism is analogous to the model for trapping in 2D maps of Ref. [114]. A comparison with a 3D map demonstrates that this transport across resonance channels is responsible for the trapping in region A of the twist map  $F_{\text{Twist}}$ . However, the same mechanism is ruled out for the generic sticky regions of  $F_{\text{Twist}}$  and  $F_{\text{SC}}$  by using the average escape time  $\bar{T}(\nu_1, \nu_2)$  from Sec. 4.1 as a measure for the distance to the regular region. Instead, the course of the isolines of this distance suggests that the trapping is governed by the transport along the resonance channels.

The relevant resonances in region A of the coupled twist maps  $F_{\text{Twist}}$  are almost parallel to the surface of the regular region in frequency space, as discussed in Sec. 3.5.1 and demonstrated by the example in Fig. 4.9. Thus, transport of a chaotic orbit across the resonance channels directly affects its distance to the regular region. This transport is similar to the transport along the levels of the hierarchy of a 2D map, since the action  $I_2$  and likewise  $\nu_2$  of a chaotic orbit in region A do not alter much over time. This similarity is illustrated by the resemblance of slices in  $\Theta_2$ , as shown in Fig. 4.9(d), and phase space pictures of 2D maps. One interpretation is that the coordinate  $I_2$  acts as a perturbation parameter, similar to the kicking strength  $K$  of the standard map, defining a 2D mixed phase space the chaotic orbit is confined to for short time scales. In this case the trapping mechanism could be described by trapping in a 2D map with a slowly diffusing perturbation parameter, which modulates position and fluxes of the partial barriers. Such a model should give similar results as the models discussed in Ref. [114]. For instance, a straight power-law decay with universal exponent  $\gamma \approx 1.5$  is obtained by averaging the survival probabilities of 100 2D symplectic maps. This is remarkable as the power-law decays of the individual maps still show the characteristic oscillations on logarithmic scale. In order to demonstrate that the trapping in region A works analogously, an additional 3D map  $F_{\text{3D}}$  is introduced which matches the coupled twist maps  $F_{\text{Twist}}$  as defined in Eq. (3.6)ff. but with an integrable second degree of freedom. That is, instead of Eq. (3.7) the perturbation of the 3D map is defined by

$$\begin{aligned} p'_1 &= \tilde{p}_1 - \xi \frac{dV(\tilde{q}_1, \tilde{q}_2)}{d\tilde{q}_1} & q'_1 &= \tilde{q}_1 \\ p'_2 &= \tilde{p}_2 & q'_2 &= \tilde{q}_2 . \end{aligned}$$

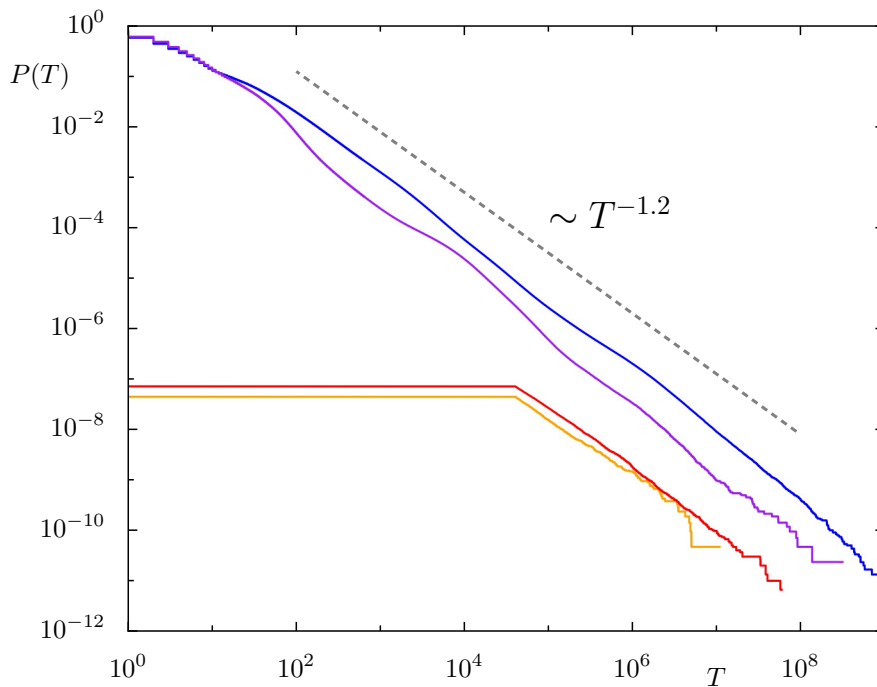


**Figure 4.11:** Comparison of the statistics of Poincaré recurrences  $P(T)$  for the 4D map  $F_{\text{Twist}}$  and the 3D map  $F_{3\text{D}}$ . The blue and red line correspond to the statistics of the map  $F_{\text{Twist}}$  and its region A, respectively, see Fig. 3.9. The purple and orange line are the analogous statistics for the map  $F_{3\text{D}}$  with initial region  $(I_1, I_2, \Theta_1, \Theta_2) \in [6.1, 9.2]^2 \times [-\pi, \pi]^2$ , exit region  $\Gamma = \{(I_1, I_2, \Theta_1, \Theta_2) : I_1, I_2 > 10\}$  and  $2 \cdot 10^{10}$  chaotic orbits.

While all parameters match the ones of  $F_{\text{Twist}}$ , the initial region  $\Gamma$  for the Poincaré recurrence is chosen to be  $\Gamma = \{(I_1, I_2, \Theta_1, \Theta_2) : I_1, I_2 \in [6.1, 9.2]\}$ .

The statistics of Poincaré recurrences  $P(T)$  of the maps  $F_{3\text{D}}$  and  $F_{\text{Twist}}$  are compared in Fig. 4.11. The statistics for  $F_{\text{Twist}}$  and its region A, shown in blue and red, respectively, are the same as in Fig. 3.9. The result for the 3D map  $F_{3\text{D}}$  shown in purple is a little bit below the one for  $F_{\text{Twist}}$  but the decay is very similar. The results for region A of  $F_{\text{Twist}}$  and  $F_{3\text{D}}$ , in red and orange, respectively, almost coincide, which confirms that the back-coupling is negligible for  $F_{\text{Twist}}$  in this region. The time–frequency plots for chaotic orbits of  $F_{3\text{D}}$  trapped at region A exhibit the same signatures of partial barriers as observed for  $F_{\text{Twist}}$  in Fig. 4.9. From these observations it can be inferred that the trapping mechanism of the maps  $F_{\text{Twist}}$  and  $F_{3\text{D}}$  is essentially the same in region A. However, chaotic orbits of the 3D map  $F_{3\text{D}}$  have constant action  $I_2$  set by their initial condition  $I_2 \in [6.1, 9.2]$  and thus can only get trapped at the regular region by transport in  $I_1$ . This implies that also the trapping in region A of the 4D map  $F_{\text{Twist}}$  depends solely on the transport in  $I_1$ . Furthermore, the 3D map  $F_{3\text{D}}$  allows to examine the statistics for individual actions  $I_2$  as shown in Fig. 4.12. The five thin, colored lines depict  $P(T)$  for different initial  $I_2 \in [6.5, 9.0]$  corresponding to both rational and irrational



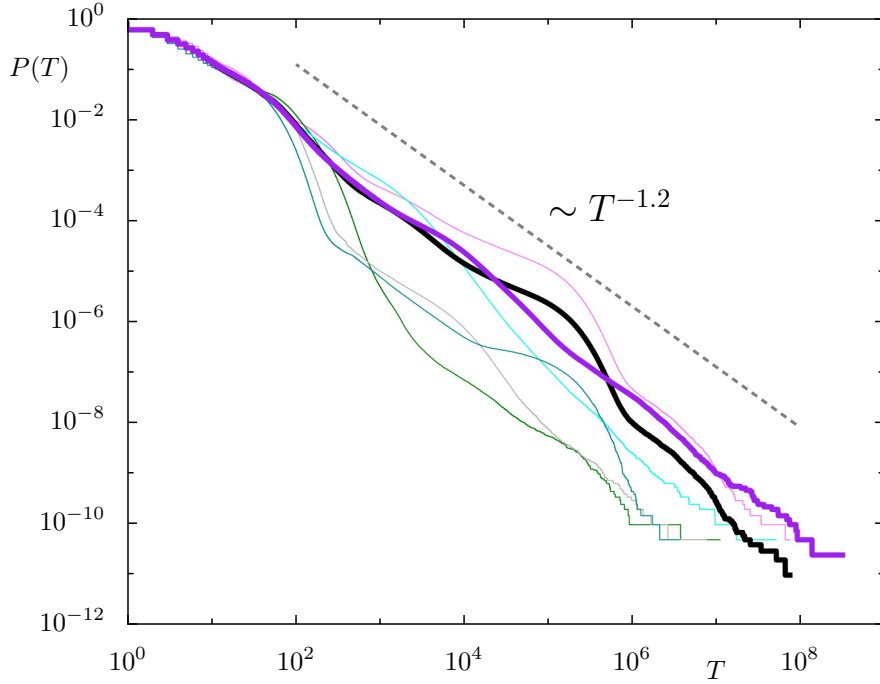
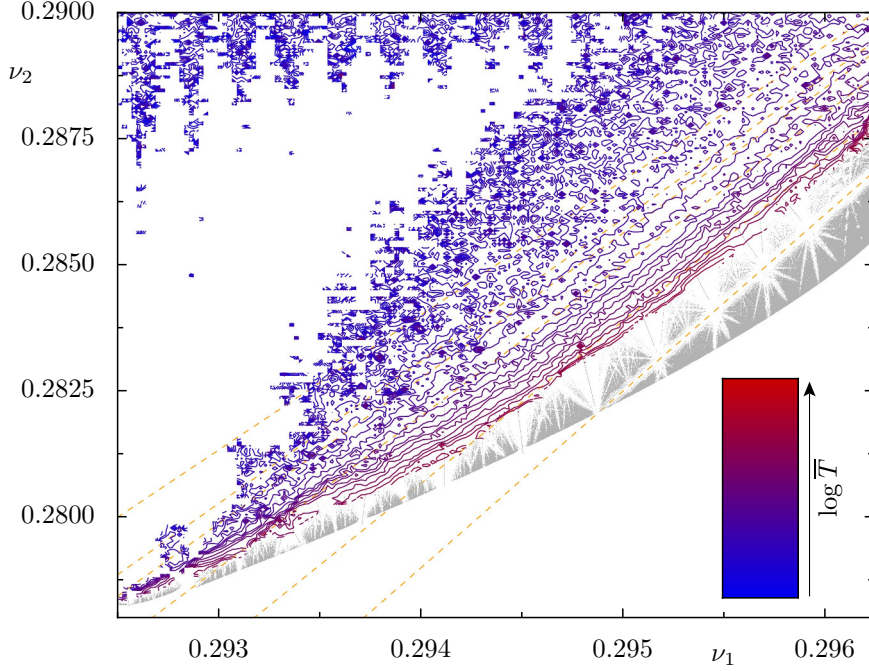
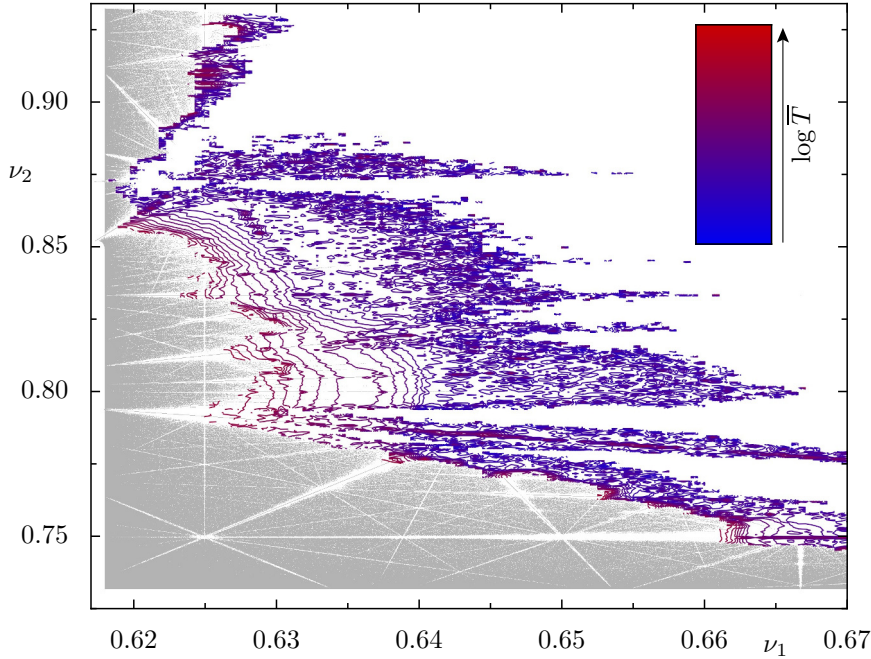


**Figure 4.12:** Statistics of Poincaré recurrences  $P(T)$  for particular actions  $I_2 = I_2^0$  of the 3D map  $F_{3D}$ . The statistics  $P(T)$  for  $F_{3D}$  are shown as thick, purple line as in Fig. 4.11. The thin lines correspond to the statistics  $P(T)$  for  $F_{3D}$  with the initial regions  $(I_1, I_2, \Theta_1, \Theta_2) \in [6.1, 9.2] \times I_2^0 \times [-\pi, \pi]^2$  with the constant  $I_2^0 = \{6.5, 7.5, 7.1475, 7.8419, 9.0\}$  (pink, green, bright blue, gray, dark cyan) which corresponds approximately to  $\nu_2 = \{0.8621, 0.8821, 7/8, 8/9, 0.9121\}$ , see Eq. (3.8). In each case  $2 \cdot 10^{10}$  chaotic orbits are used. The average of these five statistics shown as thick black line exhibits a much straighter power-law similar to the overall statistics of  $F_{3D}$ .

frequencies  $\nu_2$ . These individual decays exhibit much stronger fluctuations over time than the relatively straight power-law decay of the overall statistics shown again as thick, purple line. Only the average of the individual decays included as thick black line in Fig. 4.12 results in a similarly straight power-law decay. The averaged decay converges by construction to the overall decay by including an increasing number of individual decays, but even for the five actions considered the black line already almost coincides with the purple one for small times  $T < 10^4$ . This suggests that trapping with straight power-law decay of  $P(T)$  in a 3D map  $F_{3D}$  and consequently in region A of the 4D map  $F_{\text{Twist}}$  can be explained analogous to the straight power-law decay discussed in Ref. [114]. Of course the outlined argument is just a rough sketch and a more careful, quantitative analysis is required to rigorously link the trapping in 4D maps caused by transport across open resonance channels to the models of Ref. [114]. Note that the one-parameter stacking of 2D maps plus a rotation is not an uncommon model for 4D maps [11, 161].



(a)  $\nu_1 \in [0.2923, 0.297]$ ,  $\Delta\nu_1 = 2.4 \cdot 10^{-5}$ ;  $\nu_2 \in [0.278, 0.291]$ ,  $\Delta\nu_2 = 2.7 \cdot 10^{-4}$



(b)  $\nu_1 - (\sqrt{5} - 1)/2 \in [0, 0.1]$ ,  $\Delta\nu_1 = 5 \cdot 10^{-4}$ ;  $\nu_2 - (\sqrt{3} - 1) \in [0, 0.2]$ ,  $\Delta\nu_2 = 5 \cdot 10^{-4}$

**Figure 4.13:** Isolines of the average escape time  $\bar{T}(\nu_1, \nu_2)$ , see Eq. (4.2), for the maps (a)  $F_{\text{SC}}$  and (b)  $F_{\text{Twist}}$ . The isolines are based on the sets of frequency pairs from trapped orbits discussed in Sec. 4.1, i.e. (a)  $|\Omega_{\text{horseshoe}}| \approx 10^7$  frequency pairs obtained from  $N_{\text{horseshoe}} = 938384$  trapped orbits of  $F_{\text{SC}}$  with recurrence times  $10^4 \leq T_i \leq 10^9$  and (b)  $|\Omega_{\text{Twist}}| \approx 9 \cdot 10^7 = (1.7 + 7.3) \cdot 10^7$ ,  $N_{\text{Twist}} = 20775 + 1652930$  trapped orbits of  $F_{\text{Twist}}$  with  $10^4 \leq T_i \leq 10^9$  and  $4 \cdot 10^4 \leq T_i \leq 10^9$ . The distribution  $\bar{T}(\nu_1, \nu_2)$  is evaluated on a grid with resolutions  $\Delta\nu_1, \Delta\nu_2$ , see subcaptions. The factor between the escape times  $\bar{T}$  of two adjacent isolines is 1.61 and the value  $\bar{T}$  is encoded in color according to the colorbars with the limiting values  $10^3$  (blue) and  $10^9$  (red). For comparison the regular tori from (a) Fig. 2.4(b) and (b) Fig. 3.6(c) are shown in gray. In (a) some resonances are indicated as orange, dashed lines, i.e. from top to bottom  $16 : -6 : 3$ ,  $31 : -11 : 6$ ,  $46 : -16 : 9$ ,  $15 : -5 : 3$ ,  $29 : -9 : 6$ ,  $14 : -4 : 3$ .

While the trapping mechanism described above produces straight power-law decays and explains the trapping in region A of the map  $F_{\text{Twist}}$ , it requires that the chaotic orbits mainly escape from the sticky region by transport across resonance channels. In this case there is a fixed order in which a chaotic orbit from the chaotic sea reaches each resonance. This order can be considered as levels, i.e. an orbit has to pass the resonance of level  $n$  to get to the resonance of level  $n + 1$ . Certain recurrence times of chaotic orbits should on average coincide with certain levels reached by the orbits just like for trapping along the levels of the hierarchy of 2D maps [100,102]. Thus, one might expect that the isolines of the average escape time  $\bar{T}(\nu_1, \nu_2)$  as defined in Eq. (4.2) do not cross the relevant resonance lines in frequency space but rather are directed along them. However, a depiction of these isolines for the generic sticky regions of the maps  $F_{\text{SC}}$  and  $F_{\text{Twist}}$  in Fig. 4.13 is in stark contrast to this. For Fig. 4.13(a) some isolines are computed based on  $|\Omega_{\text{horseshoe}}| \approx 10^7$  frequency pairs obtained from  $N_{\text{horseshoe}} = 938384$  trapped orbits of  $F_{\text{SC}}$  with recurrence times  $10^4 \leq T_i \leq 10^9$ , see Sec. 4.1. The colors of the isolines indicate the value of  $\bar{T}(\nu_1, \nu_2)$  on them as in Fig. 4.2(b). The lines run more or less parallel to each other along the surface of the regular region. Some relatable resonances are included as orange, dashed lines in Fig. 4.13(a). They are all crossed by the isolines, even at larger values of  $\nu_1$  where the isolines seem to be relatively straight. The independence of the isolines from resonances become even more apparent for the coupled twist maps  $F_{\text{Twist}}$  in Fig. 4.13(b). For Fig. 4.13(b) some isolines are computed based on  $|\Omega_{\text{Twist}}| \approx 9 \cdot 10^7 = (1.7 + 7.3) \cdot 10^7$  frequency pairs obtained from  $N_{\text{Twist}} = 20775 + 1652930$  trapped orbits of  $F_{\text{Twist}}$  with recurrence times  $10^4 \leq T_i \leq 10^9$  and  $4 \cdot 10^4 \leq T_i \leq 10^9$ , respectively. The isolines clearly adapt to the surface of the regular region of region B and their pattern do not resemble the grid of resonance lines.

In addition to the isolines of the average escape time also the distribution of densities  $\rho(\nu_1, \nu_2)$  for orbits with recurrence times  $T_i$  in intervals with constant width on log-scale are examined, i.e.  $T_i \in [t_j, 2t_j]$  with  $t_j = a^j t_0$ ,  $j \in \mathbb{N}$ , and, e.g.,  $a = 1.2$ ,  $t_0 = 10^4$ , but not shown here. The distribution of these densities looks like it continuously advances towards the regular region with increasing  $j$  and exhibits no jumps at resonances. In cooperation with Matthias Wagner and Prof. Padberg-Gehle the isolines and resonances of Fig. 4.13(a) are also compared with eigenstates of the transfer operator for one time step  $\Delta t = 4096$  in frequency space in order to find related almost invariant sets [200]. However, no relevant signatures of such sets are found in this frequency space. Note however that in Appendix A.1 the resonances  $0 : 6 : 5$  and  $4 : 3 : 0$  of the coupled twist maps  $F_{\text{Twist}}$  are discussed in between which jumps are observed that may cause transport towards the chaotic sea. This is despite the fact that these resonances are directed along the surface of the regular region. In order to investigate this one might

use the isolines introduced above as coordinate system to measure transport towards the chaotic sea during jumps between resonances.

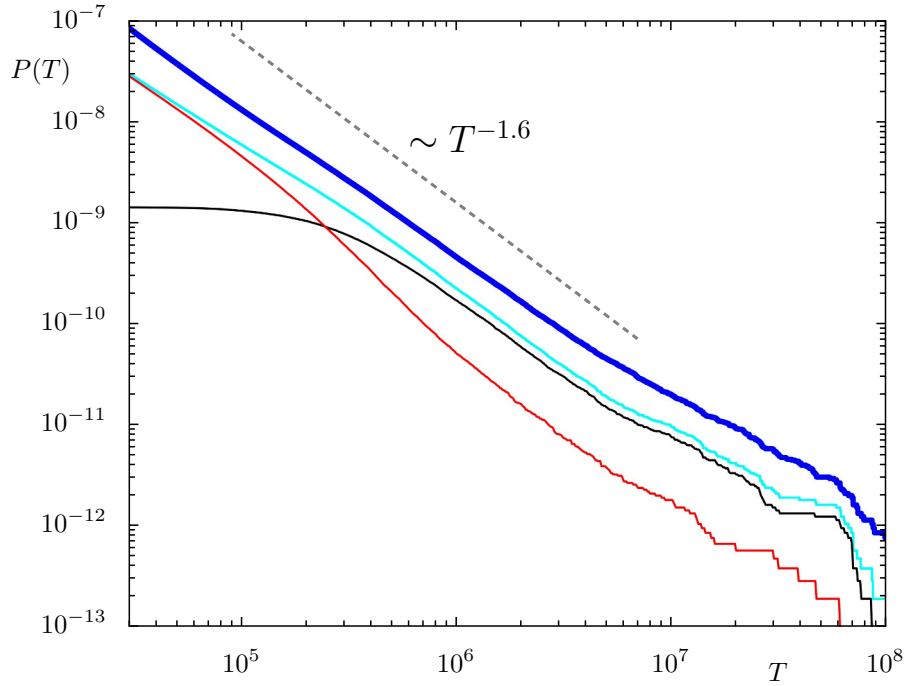
## 4.4 II) Trapping in deeper class of hierarchy

In Sec. 3.3.3 the hierarchy of classes in 4D maps is explained in analogy to 2D maps. The trapping of chaotic orbits in deeper classes of this hierarchy is established in Sec. 4.2. In particular, this trapping exhibits signatures of partial barriers as in 2D maps. In this section however, it is estimated that chaotic orbits are only trapped for short time periods in deeper classes and reach only a couple of consecutive classes. Thus, this type of trapping can not explain the power-law trapping. The escape times from deeper classes exhibit power-law decays with different exponents as expected due to the self-similarity of the regular structures along the hierarchy: The escape from the regular region of a deeper class to the stochastic layer of the corresponding resonance channel should be governed by the same mechanisms as the escape from the major sticky region of a system to its chaotic sea. In this sense, understanding the power-law trapping for a generic 4D map automatically implies understanding the trapping at the regular structures which are present in any resonance channel within the Arnold web. Finally, the impact of transport within the deeper class on transport along resonance channels is discussed in this section.

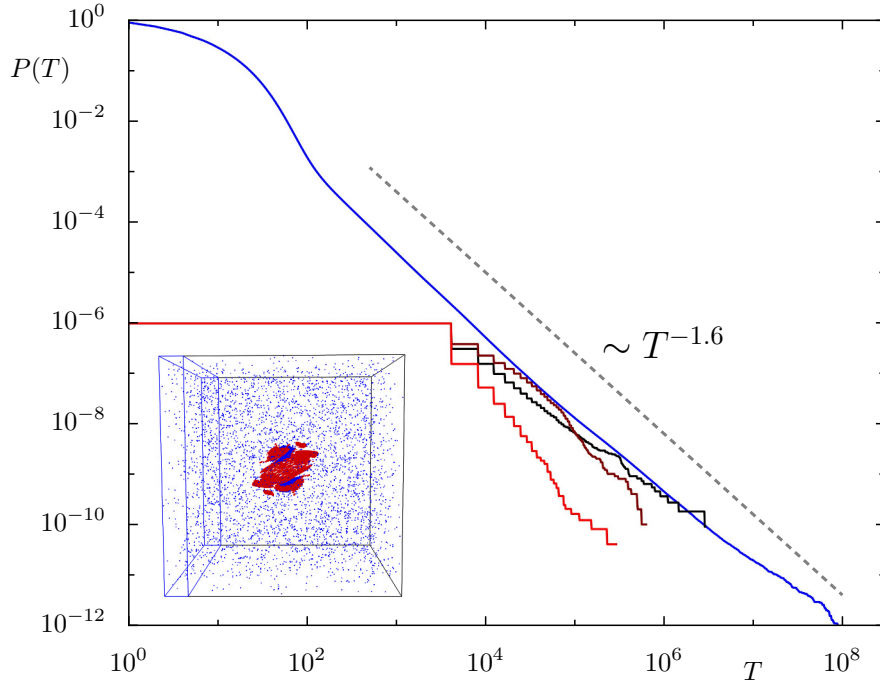
To determine numerically whether a chaotic orbit is trapped in a deeper class, e.g., at the regular structures of a resonance channel or a junction, is not straightforward. The comparison of time–frequency plots and 2D phase-space slices in Sec. 4.2 suggests that a sufficient criterion is the sudden confinement of the frequencies of the orbit to a thin stripe around the resonance line. However, being within this stripe of half-width  $\Delta\nu$  is only a necessary condition. For instance, some chaotic orbits of the twist map show a sudden change from a confinement  $\Delta\nu \sim 10^{-3}$  due to the stochastic layer of the resonance to  $\Delta\nu \sim 10^{-6} \dots 10^{-7}$  due to the deeper class. But also during the time span in which the orbit is in the stochastic layer and explicitly not trapped in the deeper class the fluctuating frequencies are frequently within the thin stripe  $\Delta\nu \sim 10^{-6} \dots 10^{-7}$  around the resonance line. This can be inferred from the pronounced densities  $\rho(\nu_1, \nu_2)$  at resonances discussed in Sec. 4.1 and seen in the time–frequency plots in Sec. 4.2. This behavior is an artifact of the frequency analysis, which averages over  $\Delta t$  iterates of an orbit, and thus can assign near resonant frequencies to an orbit which is in the stochastic layer around a resonant island. One way to verify that the points of the chaotic orbit are indeed trapped in the deeper class is to compare their positions with the corresponding elliptic 1D tori of the resonance in a 3D projection. However, this

is only checked for a few examples and not shown here. A more detailed discussion of the frequency fluctuations at resonances and widths of resonance channels can be found in Appendix A.3. In short, the frequencies of a chaotic orbit being within a stripe of half-width  $\Delta\nu \ll 1$  around a resonance line is a necessary condition for this orbit to be trapped in the corresponding deeper class. This condition is used in the following to assess the relevance of the deeper classes for the overall power-law trapping. Whenever the frequencies  $(\nu_1, \nu_2)(t)$  of a chaotic orbit are within a stripe of half-width  $\Delta\nu = 10^{-6}$  or  $\Delta\nu = 10^{-7}$  around a resonance line of the maps  $F_{\text{SC}}$  and  $F_{\text{Twist}}$ , respectively, for  $t \in [t_0 + 1, t_0 + T]$  and outside for  $t = t_0$  and  $t = t_0 + T + 1$  the orbit is considered to be trapped in the deeper class with an escape time  $T$ . Only the resonances with the most frequency pairs trapped in their deeper class are considered, that is  $17 : 0 : 5$ ,  $16 : 1 : 5$ , and  $15 : -5 : 3$  for  $F_{\text{SC}}$  and  $0 : 6 : 5$ ,  $5 : 1 : 4$ ,  $1 : 3 : 3$ , and  $-1 : 2 : 1$  for  $F_{\text{Twist}}$ . Note that the chosen condition for being trapped in the deeper class of a resonance does not distinguish between the resonance and junctions on it. However, the separate discussion of the junctions in Sec. 4.5 reveals that the junctions are even less relevant than the trapping in the deeper class of resonances. The following results are based on the same frequency pairs  $\Omega_{\text{horseshoe}}$  and  $\Omega_{\text{Twist}}$  as in Sec. 4.3.

The results for the horseshoe of the two coupled standard maps  $F_{\text{SC}}$  are depicted in Fig. 4.14. In Fig. 4.14(a) the statistics of Poincaré recurrences  $P(T)$  for the horseshoe and the whole system  $F_{\text{SC}}$  are shown in bright and dark blue, respectively, as in Fig. 4.1(c). Additionally, the statistics for the orbits trapped at the horseshoe are divided into two groups: Orbits that are trapped at any time in the deeper class of any of the resonances  $17 : 0 : 5$ ,  $16 : 1 : 5$  or  $15 : -5 : 3$  (black) and the remaining orbits (red). These statistics are normalized according to their share of all trapped orbits, i.e. for all times  $t$  the sum of  $P(T)$  of the black and red line is equal to  $P(T)$  of the bright blue line. Figure 4.14(a) shows that the majority of the orbits that get trapped in the deeper class of the resonances have longer recurrence times, since the red line has higher  $P(T)$  for  $T < 2 \cdot 10^5$ . However, almost any trapped orbit with recurrence time  $T > 10^6$  has been trapped at least once in a deeper class of the resonances, as seen by the proximity of the black and bright blue line in the double logarithmic plot. Nevertheless, the three lines have the same decay for  $T > 3 \cdot 10^6$  meaning that the observed power-law trapping does not require the trapping in a deeper class. In addition, only about 1% of all frequency pairs  $|\Omega_{\text{horseshoe}}|$ , see Sec. 4.3, are trapped in a deeper class of the considered resonances. This small fraction of trapping in deeper classes may also be deduced from the time–frequency plots in Sec. 4.2. In conclusion, these observations confirm the presence of trapping in deeper classes but depict this mechanism as not essential for the power-law trapping.



(a) Orbits (bright blue) divided into trapped at resonances (black) and rest (red)



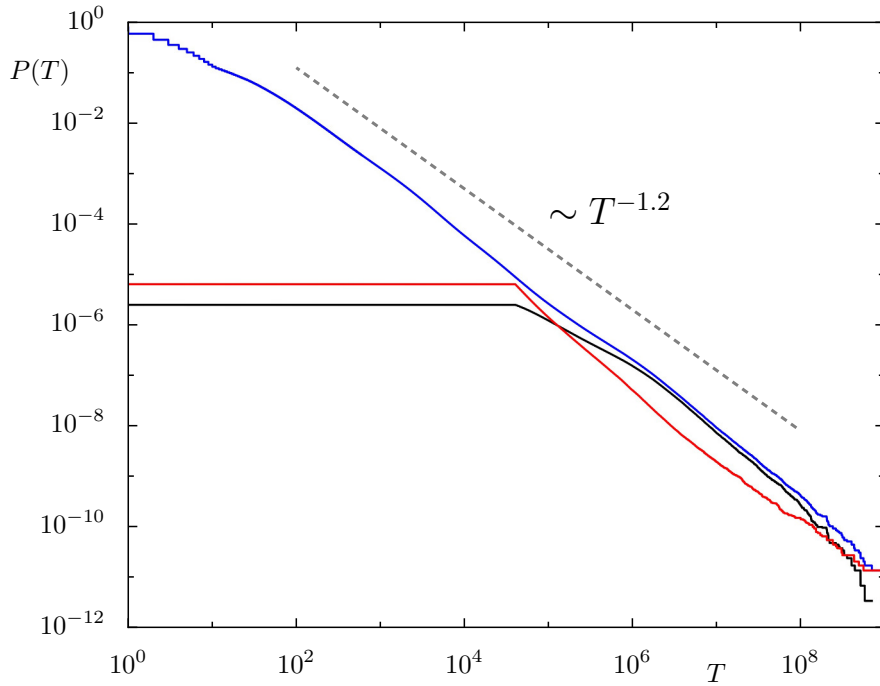
(b) Statistics of individual resonances (black to red)

**Figure 4.14:** Statistics of escape times  $P(T)$  for individual resonances of the horseshoe of the map  $F_{SC}$ . For comparison the statistics of Poincaré recurrences  $P(T)$  for the whole map  $F_{SC}$  (blue) and just the horseshoe (bright blue) from Fig. 4.1 is shown. A chaotic orbit is considered to be trapped for  $T$  at a resonance, whenever its frequencies  $(\nu_1, \nu_2)(t)$  are within a stripe of half-width  $\Delta\nu = 10^{-6}$  around the resonance line for  $t \in [t_0+1, t_0+T]$  and outside for  $t = t_0$  and  $t = t_0 + T + 1$ . In (b) the resulting statistics  $P(T)$  for the resonances  $17:0:5$ ,  $16:1:5$ ,  $15:-5:3$  (black to red) are shown with a factor  $10^{-6}$  for visibility. In (a) the statistics  $P(T)$  of the horseshoe (bright blue) is additionally divided into orbits trapped at least once at one of the three resonances (black) and the remainder (red). All results are based on the set  $\Omega_{\text{horseshoe}}$  of frequency pairs from Fig. 4.13.

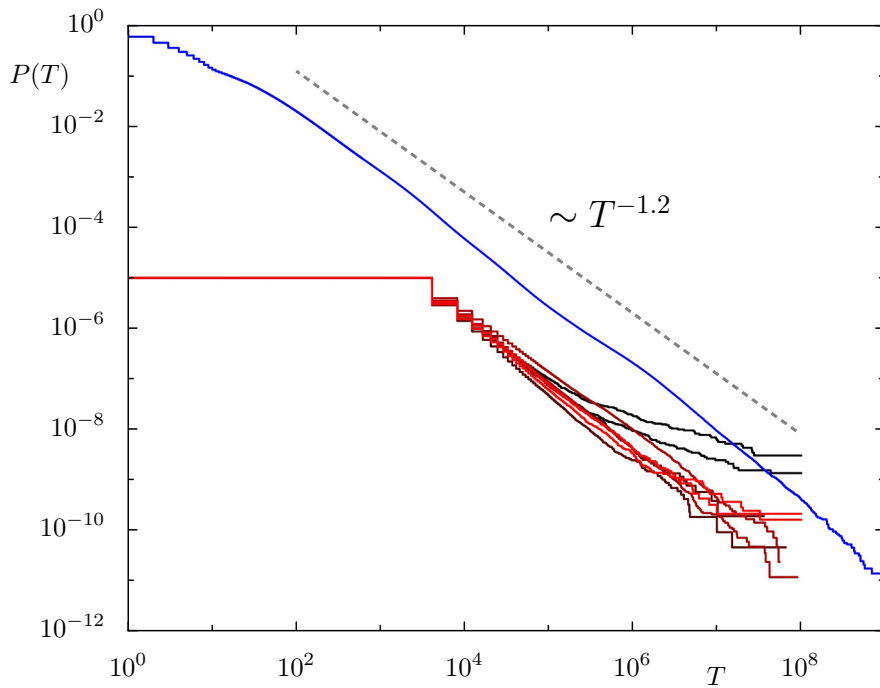
The statistics of escape times  $P(T)$  for the classes of the resonances  $17 : 0 : 5$ ,  $16 : 1 : 5$  and  $15 : -5 : 3$  are shown in Fig. 4.14(b) along with the statistics for the whole system  $F_{\text{SC}}$  in blue. Due to the frequency analysis the escape times  $T$  for the resonances are only determined up to  $\Delta t = 4096$  iterations and thus their decay only starts for longer times. In order to facilitate the comparison with the decay of the whole system, the statistics of the resonances are shifted along the  $P(T)$  axis. For each resonance the statistics  $P(T)$  exhibits an individual power-law decay with exponents both bigger and smaller than the exponent of the whole system. This is in agreement with the fact that the deeper class of a resonance or junction is a generic regular region and thus is expected to exhibit power-law trapping. Note that the horseshoe itself represents the deeper class of the resonance  $3 : 1 : 1$  as explained in Sec. 3.4. In this sense, the statistics for the resonances  $17 : 0 : 5$ ,  $16 : 1 : 5$ , and  $15 : -5 : 3$  are analogous to the statistics for resonance  $-1 : 3 : 0$ , the junction  $(\nu_1, \nu_2) = (2/7, 1/7)$ , and the horseshoe representing the resonance  $3 : 1 : 1$ , which are shown in Fig. 4.1 in dark green, orange, and bright blue, respectively. The only difference is that deeper classes of the resonances  $17 : 0 : 5$ ,  $16 : 1 : 5$  and  $15 : -5 : 3$  represent already the next deeper classes of the hierarchy of the map  $F_{\text{SC}}$ . Taking into account that the first classes of the system are observed to trap orbits for up to  $\sim 10^8$  iterations, see Fig. 4.1(c), while the next deeper classes trap for only up to  $\sim 10^6$  iterations, see Fig. 4.14(b), it seems unlikely that orbits reach an even deeper class within the observed time span. Note that there is an argument in 2D maps, i.e. if the power-law trapping was majorly caused by the class hierarchy, certain recurrence times should be related to certain classes reached by the trapped orbits [100, 105].

In Fig. 4.15 the results for the most important resonances  $0 : 6 : 5$ ,  $5 : 1 : 4$ ,  $1 : 3 : 3$ , and  $-1 : 2 : 1$  of the coupled twist maps  $F_{\text{Twist}}$  are presented analogous to Fig. 4.14. The results are in principle in agreement with the results discussed above for the horseshoe of the generic map  $F_{\text{SC}}$ . However, about 10% of all frequency pairs  $|\Omega_{\text{Twist}}|$ , see Sec. 4.3, are trapped in a deeper class of the map  $F_{\text{Twist}}$ , which are ten times more than for the horseshoe. Also the deeper classes of the map  $F_{\text{Twist}}$  are observed to trap chaotic orbits up to  $\sim 10^7 \dots 10^8$  iterations, one to two orders of magnitude longer than the deeper classes of the horseshoe. These scale differences are attributed to the fact that the horseshoe is already a deeper class of the map  $F_{\text{SC}}$ .

The above estimates about the relevance of trapping in the deeper class of a resonance are interesting for the transport along resonance channels. The transport along the surface of the regular region of the deeper class coincides with the transport along the corresponding resonance channel, as pointed out in Sec. 3.3.1 for the resonance  $-1 : 3 : 0$ . Another example is the transport along the surface of the horseshoe, which



(a) Orbits (blue) divided into trapped at resonances (black) and rest (red)



(b) Statistics of individual resonances (black to red)

**Figure 4.15:** Statistics of escape times  $P(T)$  for individual resonances of the map  $F_{\text{Twist}}$  analogous to Fig. 4.14. For comparison the statistics of Poincaré recurrences  $P(T)$  for the map  $F_{\text{Twist}}$  (blue) from Fig. 3.9 is shown. The half-width of the resonances is chosen  $\Delta\nu = 10^{-7}$ . In (b) the resulting statistics  $P(T)$  for the resonances  $0 : 6 : 5$ ,  $5 : 1 : 4$ ,  $1 : 3 : 3$ ,  $-1 : 2 : 1$  (black to red) are shown with a factor  $10^{-5}$  for visibility. All results are based on the set  $\Omega_{\text{Twist}}$  of frequency pairs from Fig. 4.13.

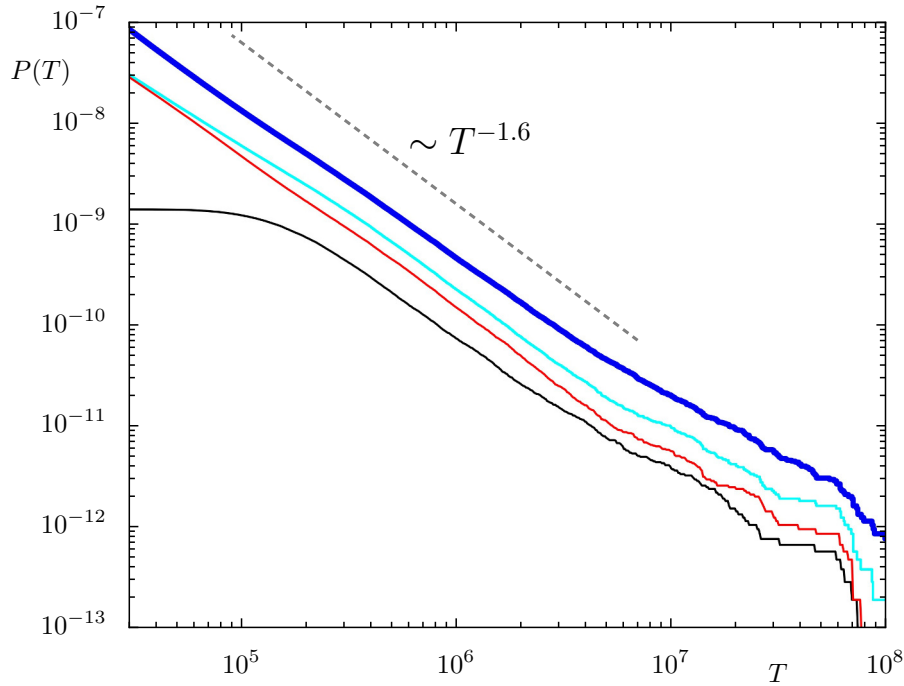


corresponds to transport along the resonance channel  $3 : 1 : 1$ , see Sec. 3.4. In Sec. 4.3 the former transport is suspected to be described by the transport across the resonance channels of the horseshoe governed by partial barriers. In this sense, a fraction of the chaotic transport along resonance channels can be explained by the transport across a set of partial barriers. However, this fraction is estimated above to be rather small. On top of that, the transport rate along the surface of the regular region is known to increase away from the region [72], see also the discussion of  $\sigma_{\leftrightarrow}^2(\nu_1, \nu_2)$  in Sec. 4.1. From this one may infer that the transport rate along the resonance channel is bigger for chaotic orbits within the stochastic layer than for orbits trapped in its deeper class. In conclusion, the transport due to partial barriers of the deeper class can probably be neglected as mechanism for transport along the Arnold web.

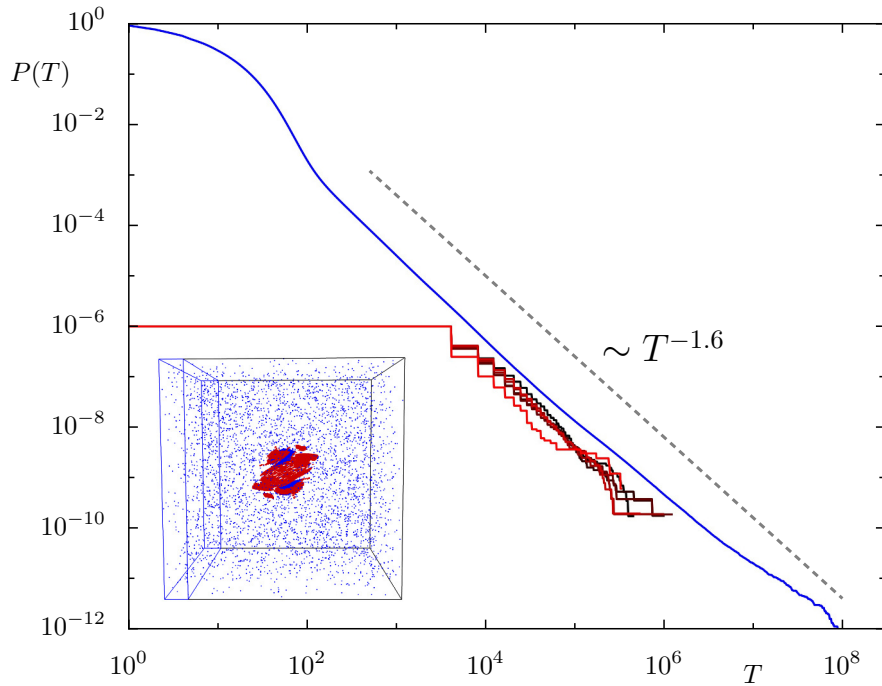
## 4.5 III) Trapping at a resonance junction

The transport at junctions of resonances is crucial in the closed part of the Arnold web, as chaotic orbits can switch from one resonance channel to another only in the vicinity of the junctions. A junction of resonance channels in 4D maps has an intricate phase-space structure containing periodic orbits, regular 2D tori, families of 1D tori and invariant manifolds, see Sec. 3.2.2. Consequently, the dynamics at a junction are complicated, supposedly governed by several intertwined transport mechanisms, as mentioned in Sec. 2.5. As the power-law trapping is governed by open resonance channels, only junctions of open resonance channels are considered here. An examination of the most prominent junctions yields results analogous to the trapping at resonances, see Sec. 4.4. Hence, the junctions can be neglected for the power-law trapping. For the escape times from the junctions power-law decays are observed as expected from the self-similarity of the regular structures along the class hierarchy.

A chaotic orbit is considered to be trapped at a junction when its corresponding frequencies  $(\nu_1, \nu_2)(t)$  are within a square of half-width  $\Delta\nu$  for  $t \in [t_0 + 1, t_0 + T]$  and outside for  $t = t_0$  and  $t = t_0 + T + 1$ , with  $T$  denoting the escape time  $T$ . Only the junctions with the most frequency pairs trapped at them are considered. The analogous statistics obtained for resonances in Sec. 4.4 are now obtained for junctions. The results for the generic map  $F_{\text{SC}}$  are shown in Fig. 4.16 for which  $\Delta\nu = 10^{-5}$  is chosen, which is ten times the half-width used for the resonances. The six considered junctions, see caption of the figure, all lie on the resonance  $15 : -5 : 3$ . In Fig. 4.16(a) the black line, representing orbits that are trapped at least once at any of the junctions, is well below the red line which represents the remaining orbits. Thus, even for times up to  $T = 10^8$  over 50% of the orbits trapped at the horseshoe are not trapped even once at



(a) Orbits (bright blue) divided into trapped at junctions (black) and rest (red)

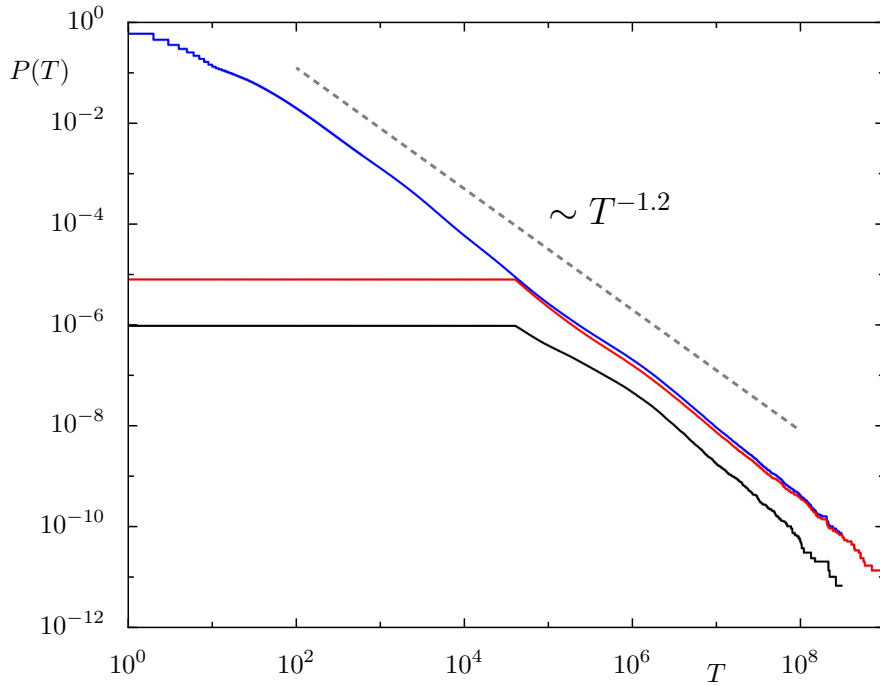


(b) Statistics of individual junctions (black to red)

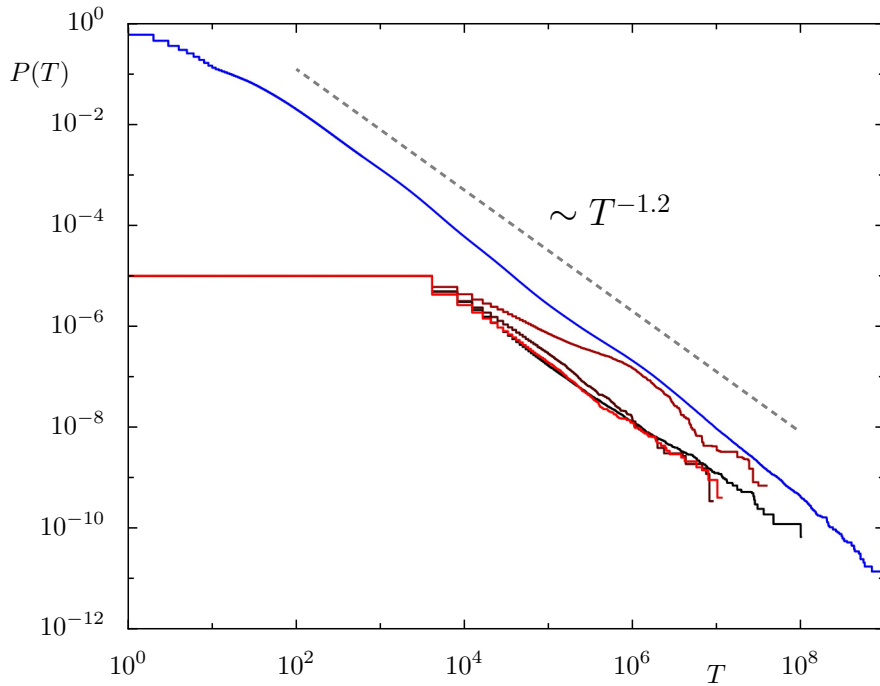
**Figure 4.16:** Statistics of escape times  $P(T)$  for individual resonance junctions of the map  $F_{\text{SC}}$  similar to Fig. 4.14. As vicinity of the junctions  $(\nu_1, \nu_2) = (n_1/m_1, n_2/m_2)$  a square of half-width  $\Delta\nu = 10^{-5}$  is chosen. In (b) the resulting statistics  $P(T)$  for the junctions  $(5/17, 24/85)$ ,  $(53/180, 17/60)$ ,  $(28/95, 27/95)$ ,  $(59/200, 57/200)$ ,  $(31/105, 2/7)$ ,  $(13/44, 63/220)$  (black to red) are shown with a factor  $10^{-6}$  for visibility.

one of most relevant junctions. Only about 0.5% of all frequency pairs  $|\Omega_{\text{horseshoe}}|$ , see Sec. 4.3, are trapped at any of these junctions. This puts the high densities observed at these junctions in Sec. 4.1 into perspective. On top of that, the decays for both groups of chaotic orbits resemble the decay for the horseshoe shown as bright blue line. In conclusion, just like the deeper classes of resonances the junctions do not seem to be essential for the power-law trapping. The statistics of the escape times  $T$  from the individual junctions are shown in Fig. 4.16(b). Again power-law decays are observed with similar but distinct exponents and orbits are trapped up to  $\sim 10^6$  iterations, as for the resonances in Sec. 4.4. For both maps these power-law decays are attributed to the regular region around the EE periodic orbit present at each junction. This could be verified by 3D projections of the trapped points along with the EE periodic orbit. As in the previous section, this is only checked for a few examples and not shown here. The regular regions around the EE periodic orbit represent the deeper class of the junction and are expected to be subject to the same transport mechanisms as any regular region.

In Fig. 4.17 the results for the four most important junctions of the coupled twist maps  $F_{\text{Twist}}$  are presented analogous to Fig. 4.16. The half-width  $\Delta\nu = 10^{-6}$  is again chosen ten times bigger than for the resonances in Fig. 4.15. The results are in principle in agreement with the results discussed above for the horseshoe of the generic map  $F_{\text{SC}}$ . In Fig. 4.17 the fraction of orbits being trapped at least once at any of the junctions is about 10% at all times. The higher fraction in case of the horseshoe in Fig. 4.16 may be caused by the fact that the  $15 : -5 : 3$  runs along the surface of the horseshoe and closer towards the chaotic sea. Due to this, chaotic orbits have to pass this resonance when approaching the horseshoe and may be more likely to get trapped at the junctions on it. About 6% of all frequency pairs  $|\Omega_{\text{Twist}}|$ , see Sec. 4.3, are trapped at any of the junctions considered for the map  $F_{\text{Twist}}$  and these junctions are observed to trap chaotic orbits up to  $\sim 10^7 \dots 10^8$  iterations. This means a difference in scale to the results of the horseshoe, which is also observed for the resonances in Sec. 4.4.



(a) Orbits (blue) divided into trapped at junctions (black) and rest (red)



(b) Statistics of individual junctions (black to red)

**Figure 4.17:** Statistics of escape times  $P(T)$  for individual resonance junctions of the map  $F_{\text{Twist}}$  similar to Fig. 4.15. As vicinity of the junctions  $(\nu_1, \nu_2) = (n_1/m_1, n_2/m_2)$  a square of half-width  $\Delta\nu = 10^{-6}$  is chosen. In (b) the resulting statistics  $P(T)$  for the junctions  $(9/14, 11/14, 6)$ ,  $(7/11, 9/11, 6)$ ,  $(2/3, 7/9, 6)$ ,  $(2/3, 3/4, 6)$  (black to red) are shown with a factor  $10^{-5}$  for visibility.

## 4.6 IV) Transport along a resonance channel

The previous sections conclude that transport across resonance channels and trapping in deeper classes of the hierarchy is deficient to generate the observed power-law trapping. The remaining transport phenomenon is transport along the resonance channels, which is exclusive to higher-dimensional maps. Several mechanisms have been proposed in the literature in order to describe the details of this transport mainly in terms of Arnold diffusion [48, 49, 52, 54, 55, 201]. A useful paradigm for the transport along a resonance channel in 4D maps is the chaotic layer of a resonance in one degree of freedom driving the action of the other degree of freedom, while the back-coupling to the chaotic layer is negligible [62, 66]. More precisely, the coordinates in the first degree of freedom are located in the layer of the resonance and thus are mapped chaotically. Due to the coupling this induces a transport in the second degree of freedom, even if this degree of freedom is integrable in the uncoupled case. The chaotic layer of the resonance is often treated as a stochastic driving and usually called stochastic layer. While the following sections also rely on this simplification, note that a chaotic layer is not always sufficiently modeled by a stochastic layer [66].

In this section, the transport along a single channel is simply viewed as a one-dimensional stochastic process with local diffusion and drift coefficients. Using an absorbing barrier along the channel to simulate the escape to the chaotic sea allows to investigate the survival probabilities and compare them to the statistics of Poincaré recurrences from the 4D maps. While a trapped orbit of a 4D map visits many channels, here it is surmised that the stochastic model for each channel results in a similar power-law, thus the mechanism of the power-law trapping can be reduced to a single channel. A relation between drift and diffusion coefficients is proposed which can generate the desired power-law decay. Furthermore, a drift which satisfies this relation is conjectured based on the change of the volume of the stochastic layer along the channel.

Numerical studies are performed on the resonance channel  $0 : 6 : 5$  of the coupled twist maps  $F_{\text{Twist}}$  with uncoupled coordinates  $(I_1, I_2, \Theta_1, \Theta_2)$ . For this channel the 4D transport can be separated into the stochastic layer of a 2D map  $\sim (I_2, \Theta_2)$ , a rotation  $\sim \Theta_1$ , and the transport along the channel  $\sim I_1$ . The goal is to numerically extract the local drift and diffusion coefficients in order to verify the proposed relation between these coefficients and to reproduce the observed exponent  $\gamma$  of the power-law decay  $P(T) \sim T^{-\gamma}$  predicted by the corresponding stochastic model. However, the measurement of the coefficients turns out to be extremely difficult. Within the framework of this thesis several ideas to overcome these difficulties are discussed. The extraction of the local drift and diffusion coefficients remains a subject for future studies.

In Sec. 4.6.1 the decay of survival probabilities for several relevant, one-dimensional stochastic processes are reviewed. Based on this review, the necessity of a non-zero drift is conjectured in order to obtain a power-law decay with the desired exponents. A stochastic model generating these exponents is presented. In Sec. 4.6.2 two possible physical origins of such a drift are presented, i.e. one known effect which is due to the curvature of the regular tori and one newly proposed effect, which is related to the volume of the stochastic layer. In Sec. 4.6.3 the volume of the layer along the resonance channel  $0 : 6 : 5$  of the map  $F_{\text{Twist}}$  is measured, revealing a strong increase of this volume towards the chaotic sea. The measurement of the drift and diffusion coefficients along the channel is discussed in Appendix A.1.

### 4.6.1 Stochastic processes and power-law escape

Chaotic dynamics are often modeled as stochastic Markovian processes, i.e. using a Fokker-Planck equation [66, 202]. For the chaotic transport along a resonance channel such a stochastic process should be one-dimensional with an absorbing barrier representing the escape to the chaotic sea. Possibly a reflecting barrier can be added which simulates the finite length of the resonance channel, i.e. its intersection with the central family of elliptic 1D tori, see Sec. 3.1. Furthermore, the discussion of the eigenvalues of the local covariance matrix in frequency space in Sec. 4.1 suggests that the diffusion coefficient should increase towards the absorbing barrier. In the following, some analytic concepts for stochastic processes are introduced including the survival probability which is comparable to the statistics of the Poincaré recurrences used for the symplectic maps. These statistics are discussed for several possible one-dimensional stochastic processes. Two types of processes are considered: Firstly, heterogeneous processes, i.e. with non-constant functions for the drift and diffusion coefficients of the Fokker-Planck equation, and, secondly, processes with anomalous diffusion, like continuous time random walks and fractional Brownian motion. The goal is to find a process for which the survival probability exhibits a power-law decay  $P(T) \sim T^{-\gamma}$  with a sufficiently large exponent  $\gamma > 1$ , as expected from Secs. 3.5.1 and 4.1 and Ref. [37]. It is conjectured that a drift towards the chaotic sea is required to generate such a power-law. In particular, a relation between drift and diffusion coefficients is proposed which is shown to produce a wide range of power-law decays. A physical motivation for this relation is given in the next section.

For one dimension, the Fokker-Planck equation of the probability density  $\rho(x, t)$  at point  $x \in \mathbb{R}$  and time  $t$  reads [203]

$$\frac{\partial \rho(x, t)}{\partial t} = -\frac{\partial}{\partial x} J(x, t) = \left( -\frac{\partial}{\partial x} v(x, t) + \frac{\partial^2}{(\partial x)^2} D(x, t) \right) \rho(x, t) \quad (4.3)$$

where  $J(x, t)$  denotes the probability current,  $v(x, t)$  is the drift defined by the expectation value over possible continuous paths  $x(t)$

$$v(x, t) = \lim_{\Delta t \rightarrow 0} \frac{1}{\Delta t} \mathbb{E}[x(t + \Delta t) - x(t)]_{x(t)=x}, \quad (4.4)$$

and analogously  $D(x, t)$  is the diffusion coefficient defined by

$$D(x, t) = \lim_{\Delta t \rightarrow 0} \frac{1}{2\Delta t} \mathbb{E}[(x(t + \Delta t) - x(t))^2]_{x(t)=x}. \quad (4.5)$$

An absorbing barrier at  $x_a$  is realized by the condition

$$\rho(x_a, t) = 0$$

and a reflecting barrier at  $x_r$  by

$$J(x_r, t) = v(x_r, t)\rho(x_r, t) - \frac{\partial}{\partial x} D(x_r, t)\rho(x_r, t) = 0.$$

The survival probability  $S(t)$  for a process in an interval  $x \in [x_A, x_E]$  is defined by the probability within the interval

$$S(t) = \int_{x_A}^{x_E} dx \rho(x, t).$$

The standard setup is  $S(0) = 1$  with at least one of the boundaries  $x_A$  or  $x_E$  being an absorbing barrier such that  $S(t)$  decreases over time. Basically,  $S(t)$  corresponds to the statistics of Poincaré recurrences  $P(T)$  except that for  $S(t)$  usually the initial condition is within the interval  $[x_A, x_E]$ . Note that in case of the Poincaré recurrences starting chaotic orbits outside of the recurrence region results in the same power-law decay at large times, as long as the orbits start far away from regular structures. For a transformation to a coordinate  $y(x)$  the Fokker-Planck equation Eq. (4.3) transforms

to

$$\begin{aligned} \frac{\partial \tilde{\rho}(y, t)}{\partial t} &= \left( -\frac{\partial}{\partial y} (v(x(y), t)y' + D(x(y), t)y'') + \frac{\partial^2}{(\partial y)^2} D(x(y), t) \cdot (y')^2 \right) \tilde{\rho}(y, t) \\ &= \left( -\frac{\partial}{\partial y} \tilde{v}(y, t) + \frac{\partial^2}{(\partial y)^2} \tilde{D}(y, t) \right) \tilde{\rho}(y, t) \end{aligned} \quad (4.6)$$

where  $y'$  and  $y''$  are the first and second derivatives of  $y(x)$ . Such a transformation does not change the time scales meaning that the survival probabilities for the processes of Eq. (4.3) and Eq. (4.6) with corresponding barriers and initial conditions are identical. Thus, the survival probability  $S(t)$  for a particular setup of drift  $v(x, t)$  and diffusion coefficients  $D(x, t)$ , initial conditions  $\rho(x, 0)$  and barriers  $x_A, x_E$  applies to a whole class of setups  $\tilde{v}(y, t), \tilde{D}(y, t), \tilde{\rho}(y, 0) = \rho(x(y), 0)/y', y(x_A), y(x_E)$  connected by transformations  $y(x)$  according to Eq. (4.6). As only autonomous processes are of interest here, the time dependence of the coefficients is dropped in the following and for brevity the coordinate  $x$  is assumed to be unitless.

The survival probabilities for some common setups are presented in the following. For a random walk  $v(x) = 0, D(x) = D$  with initial condition  $\rho(x, 0) = \delta(x - x_0)$ , an absorbing barrier at  $x_A = 0 < x_0$  and  $x_E = \infty$  follows [204, Section 3.2.2.1] [205, page 21]

$$S(t) = \operatorname{erfc} \left( \frac{x_0}{\sqrt{4Dt}} \right) \stackrel{t \gg \frac{x_0^2}{4D}}{\sim} \frac{|x_0 - x_A|}{\sqrt{\pi D}} \cdot t^{-\frac{1}{2}} \sim t^{-\frac{1}{2}}. \quad (4.7)$$

The Sparre-Andersen theorem states that this asymptotic of  $S(t)$  applies to a wide class of random walkers [206]. Consequently, a  $N$ -dimensional random walk has  $S(t) \sim t^{-N/2}$ . For instance, the statistics of residence times  $P(T)$  in the Arnold web has been observed to decay like a one- or two-dimensional random walk yielding  $P(T) \sim T^{-1/2}$  or  $P(T) \sim T^{-1}$  which is attributed to transport just along resonance channels or transport along and across channels, respectively [64, 125]. In case of a finite interval, i.e.  $x_E = L < \infty$ , the decay of  $S(t)$  is faster [204, Sections 2.2.1.1 and 2.2.2.1] [207]. If there is a reflecting barrier at  $x_E$  for the above random walk, then this barrier becomes relevant at times  $\tau$  and the current  $J(x_A, t)$  at the absorbing barrier exhibits an exponential cut-off

$$J(x_A, t) \sim t^{-\frac{3}{2}} \exp \left( -\frac{t}{\tau} \right) \quad \tau \sim L^2/D.$$



A second absorbing barrier at  $x_E$  causes also an exponential cut-off at large times

$$S(t) \sim \exp\left(-\frac{D\pi^2 t}{L^2}\right).$$

For a random walk with  $v(x) = v$ ,  $D(x) = D$ , an initial condition  $\rho(x, 0) = \delta(x - x_0)$ , an absorbing barrier at  $x_A = 0 < x_0$ , and  $x_E = \infty$  follows for a drift towards the absorbing barrier  $v < 0$  [143] [204, Section 3.2.2.2]

$$S(t) = \frac{1}{2} \left( \operatorname{erfc}\left(T - \frac{\beta}{T}\right) - \exp(4\beta) \operatorname{erfc}\left(T + \frac{\beta}{T}\right) \right)$$

with  $\beta = -\frac{x_0 v}{4D} > 0$   $T = \sqrt{\frac{v^2 t}{4D}}$

and for a drift away from the absorbing barrier  $v > 0$ , see Ref. [204] and own calculations,

$$S(t) = (1 - \exp(4\beta)) - \frac{1}{2} \left( \operatorname{erfc}\left(T - \frac{\beta}{T}\right) - \exp(4\beta) \operatorname{erfc}\left(T + \frac{\beta}{T}\right) \right)$$

with  $\beta, T$  as before. Note that in the latter case  $\int_0^\infty dt J(0, t) < 1$ . For large times  $t \gg 1$  it is estimated [143, 204]

$$S(t) \sim \begin{cases} 1 - \exp\left(-\frac{vx_0}{D}\right) = \text{const.} > 0 & v > 0 \\ \frac{\exp(2\beta)x_0}{v^2} \sqrt{\frac{4D}{\pi}} \exp\left(-\frac{v^2 t}{4D}\right) t^{-\frac{3}{2}} & v < 0 \end{cases} \quad (4.8)$$

Note that according to Eq. (4.6) this survival probability also applies to the transformed process  $y = \exp(x)$  with  $\tilde{v}(y) = (v + D)y$ ,  $\tilde{D}(y) = Dy^2$  and corresponding interval boundaries and initial conditions [143]. In particular, choosing  $v + D = 0$  this is a stochastic process with no drift and a diffusion coefficient increasing quadratic away from the absorbing barrier square. Furthermore, if there is a second absorbing barrier at  $x_E = L < \infty$  then the survival probability  $S(t)$  of the above random walk with drift exhibits an exponential cut-off at large times [204, Section 2.2.1.2.]

$$S(t) \sim \exp\left(-\frac{t}{\tau}\right) \quad \tau = \frac{L^2}{D\pi^2} \frac{1}{1 + \left(\frac{vL}{2\pi D}\right)^2} \stackrel{v \gg 1}{\approx} \frac{4D}{v^2}$$

regardless of the direction of the drift. For a stochastic process with linearly increasing diffusion coefficient  $D(x) = x$ , an absorbing barrier at  $x_A = 0$ , as well as  $v(x) = 0$ ,

$x_0 > 0$ ,  $x_E < \infty$  leads to [208]

$$S(t) = 1 - \exp\left(-\frac{x_0}{t}\right) \stackrel{t \gg 1}{\sim} t^{-1}. \quad (4.9)$$

Note that  $x_A$  is a so called natural barrier, i.e. the chosen coefficients  $v(x)$ ,  $D(x)$  themselves cause a propagation of the probability density  $\rho(x, t)$  which simulates an absorption at  $x_A$  [208]. According to Eq. (4.6) this survival probability also applies to the transformed process  $y = 2\sqrt{x}$  with  $\tilde{v}(y) = -1/y$ ,  $\tilde{D}(y) = 1$  and corresponding interval boundaries and initial conditions. The transformed process is a random walk with a drift towards the absorbing barrier which increases as this barrier is approached. For a process

$$\frac{\partial \rho(x, t)}{\partial t} = \frac{\partial}{\partial x} x^\alpha \frac{\partial \rho(x, t)}{\partial x} = -\frac{\partial}{\partial x} \alpha x^{\alpha-1} \rho(x, t) + \frac{\partial^2}{(\partial x)^2} x^\alpha \rho(x, t) \quad (4.10)$$

with  $v(x) = \alpha x^{\alpha-1}$ ,  $D(x) = x^\alpha$ ,  $\alpha > 2$  with initial condition  $\rho(x, 0) = \delta(x - x_0)$ , a natural boundary at  $x_A = 0 < x_0$  and an absorbing barrier at some large  $x_E > x_0$  follows for large times [209]

$$S(t) \sim t^{-\gamma} \quad \gamma = \frac{\alpha - 1}{\alpha - 2}$$

with an exponent  $\gamma \in (1, \infty)$ . The drift and diffusion coefficients increase towards the absorbing barrier. The survival probability also applies to the transformed process  $y = -x^{-(\alpha-1)}/(\alpha-1)$ , which has no drift  $\tilde{v}(y) = 0$ ,  $\tilde{D}(y) = ((1-\alpha)y)^{\alpha/(\alpha-1)}$  and corresponding interval boundaries  $y(x_A) = -\infty$ ,  $y(x_E) < 0$  and initial conditions. However, the diffusion coefficient of this process increases away from the absorbing barrier at  $y(x_E)$  with an exponent  $\tilde{D}(y) \sim y^\beta$ ,  $\beta \in (1, 2)$ . Simulations using the Euler-Maruyama scheme for exponential or quadratic spatial dependence of the diffusion coefficient roughly show power-law decays  $S(t) \sim t^{-\gamma}$  with  $\gamma \approx 1/2$ . These calculations are not shown here but see Appendix A.2 for the basic procedure. Exponential, power-law and logarithmic dependencies of the diffusion coefficient are known to lead to anomalous diffusion [210–212] and for the latter the survival probability  $S(t) \sim t^{-1/2}$  is observed [212]. Anomalous diffusion, i.e.  $\mathbb{E}[x^2(t)] \sim t^\alpha$  with  $\alpha \neq 1$ , is often modeled by continuous time random walks (CTRW) and fractional Brownian motion. For  $0 < \alpha < 2$  a Levy-type CTRW yields  $S(t) \sim t^{-\alpha/2}$  and fractional Brownian motion  $S(t) \sim t^{\alpha/2-1}$  [213], see also Refs. [214, 215]. These exponents  $\gamma \in [0, 1]$  for  $S(t) \sim t^{-\gamma}$  are insufficient to explain the power laws observed for the trapping in 4D maps.

In conclusion, most of the reviewed one-dimensional stochastic processes do either not lead to a power-law decay of the survival probability  $S(t)$  or to power-law decays  $S(t) \sim t^{-\gamma}$  with exponents that are too small, i.e.  $\gamma \leq 1$ . In particular, processes without drift seem to require a diffusion coefficient that decreases towards the absorbing barrier to generate a power-law with a sufficiently large exponent  $\gamma > 1$ , e.g., more than linearly or less than quadratically increasing, see the processes of Eqs. (4.8) and (4.9) and the transformed process of Eq. (4.10). This is opposite to what is expected for the transport along a resonance channel. The most promising process has both drift and diffusion coefficients increasing towards the absorbing barrier, see Eq. (4.10). More precisely, the coefficients fulfill

$$D(x, \alpha) = x^\alpha \qquad v(x, \alpha) = \frac{\partial D(x, \alpha)}{\partial x} = \alpha \frac{D(x, \alpha)}{x}$$

from which an exponent  $\gamma$  follows which is governed by the parameter  $\alpha > 2$ . This process is generalized in the following to

$$D(x, \alpha) = x^\alpha \qquad v(x, \alpha) = \delta \frac{D(x, \alpha)}{x} \qquad (4.11)$$

with two independent parameters  $\alpha > 2$ ,  $\delta > 1$ . Choosing the same parameters as for Eq. (4.10), i.e.  $x_A = 0$ ,  $x_A < x_0 < x_E$  and the transformation

$$y(x) = -\frac{x^{1-\frac{\alpha}{2}}}{1-\frac{\alpha}{2}}$$

leads according to Eq. (4.6) to  $\tilde{D}(y) = 1$  and

$$\tilde{v}(y) = -\frac{b}{y} \qquad b = \frac{2\delta - \alpha}{\alpha - 2} \qquad (4.12)$$

with  $y \in [-\infty, 0]$ , i.e. the absorbing barrier being at  $y(x_E) \leq 0$ . Guessing an ansatz for the probability density from numerical simulations for  $t \gg 1$

$$\tilde{\rho}(y, t \gg 1) = \frac{y}{2t^c} \exp\left(-\frac{y^2}{4t}\right) \qquad (4.13)$$

it is obtained  $c = (b + 3)/2$  from the Fokker-Planck equation Eq. (4.3). For  $x_E \rightarrow \infty$  follows  $y(x_E) \rightarrow 0$  and for the survival probability for large times

$$S(t \gg 1) = \int_0^\infty dy \tilde{\rho}(y, t) = t^{-\gamma} \qquad \gamma = \frac{\delta - 1}{\alpha - 2} \qquad (4.14)$$

with  $\alpha > 2$ ,  $\delta > 1$ , and  $\gamma \in (0, \infty)$ . Not only is this range of the exponent  $\gamma$  for the generalized process Eq. (4.11) wider than for the process Eq. (4.10), but also the generalized process is capable of generating this range of exponents for any chosen  $\alpha > 2$ . There are some special cases for  $\alpha$  and  $\delta$ . The transformation  $z(y) = y^{b+1}/(b+1)$  leads to a process without drift

$$\tilde{v}(z) = 0 \qquad \tilde{D}(z) = (2\gamma z)^d \qquad d = \frac{2\delta - \alpha}{\delta - 1}$$

with  $d \in (-\infty, 2)$ . For  $\alpha = 2\delta$  it follows  $d = 0$  and  $\gamma = 1/2$ , i.e. the random walk Eq. (4.7) is a special case of the generalized process Eq. (4.11). For  $\alpha = \delta + 1$  it follows  $d = 1$  and  $\gamma = 1$ , i.e. the process Eq. (4.9) is a special case of Eq. (4.11).

### 4.6.2 Origin of drift along resonances

According to the previous section a drift is required to generate the desired power-law trapping from the transport along a single resonance channel. In particular, a power-law increase of the diffusion coefficient towards the chaotic sea and a special relation between drift and diffusion coefficient is suggested, see Eq. (4.11). It is worth mentioning that even if the local diffusion coefficients along a channel are very precisely determined, the long-term transport along the channel can not be explained [66]. This may also hint towards the presence of a drift, which has been neglected so far. In the following, two possible physical origins of such a drift are presented. Firstly, the drift due to the curvature of the regular tori is reviewed [143, 144, 216]. Secondly, a drift due to the change of the volume of the chaotic layer along the resonance channel is proposed and discussed. This also provides an argument for the increase of the diffusion coefficient of the transport along the channel towards the chaotic sea.

A drift due to the non-zero curvature of the tori has been quantified for stochastically perturbed 2D maps [143] and its existence has been rigorously proven for a setting directly related to the transport along resonance channels [216]. As before, consider the transport along a resonance channel as the stochastic layer of a resonance in the first degree of freedom driving a transport in the second degree of freedom due to a coupling. Assume that without the coupling this driven degree of freedom is essentially a free rotor. In this case the driving due to the first degree of freedom may be modeled by white noise. More precisely, the Ito differential equation [203]

$$d\mathbf{x} = \mathbf{v}(\mathbf{x}, t)dt + \boldsymbol{\sigma}(\mathbf{x}, t)d\mathbf{W}$$

which is equivalent to the multi-dimensional Fokker-Planck equation

$$\frac{\partial \rho(\mathbf{x}, t)}{\partial t} = \left( - \sum_i \frac{\partial}{\partial x_i} v_i(\mathbf{x}, t) + \sum_{i,j} \frac{\partial^2}{\partial x_i \partial x_j} \sigma_{ik}(\mathbf{x}, t) \sigma_{jk}(\mathbf{x}, t) \right) \rho(\mathbf{x}, t)$$

and which transforms to  $y(\mathbf{x})$  according Ito's formula

$$\begin{aligned} dy(\mathbf{x}) = & \left( \sum_i v_i(\mathbf{x}, t) \frac{\partial y(\mathbf{x})}{\partial x_i} + \sum_{i,j} \sigma_{ik}(\mathbf{x}, t) \sigma_{jk}(\mathbf{x}, t) \frac{\partial^2 y(\mathbf{x})}{\partial x_i \partial x_j} \right) dt \\ & + \sigma_{ij}(\mathbf{x}, t) \frac{\partial y(\mathbf{x})}{\partial x_i} dW_j \end{aligned} \quad (4.15)$$

with vectors  $\mathbf{x}, \mathbf{v} \in \mathbb{R}^N$ , the  $N \times N$  matrix  $\boldsymbol{\sigma}$  and the differential of an  $N$ -dimensional Wiener process  $d\mathbf{W}$ , reads for the driven degree of freedom

$$d\mathbf{x} = f(\mathbf{x}, t) d\mathbf{W} \quad (4.16)$$

with some functional  $f(\mathbf{x}, t)$  and  $N = 2$ . The vector  $\mathbf{x} = (p, q)$  are the momentum-position coordinates in the free rotor. As only the transport in the action  $I = (p^2 + q^2)/2 = r^2/2$  is of interest and thus assuming  $f(\mathbf{x}, t) = f(r, t)$ , the Ito differential equation for the radius  $r$  follows from transforming Eq. (4.16) according to Eq. (4.15)

$$dr = \frac{f(r, t)^2}{2r} dt + f(r, t) dW = v(r, t) dt + \underbrace{\sigma(r, t)}_{\sqrt{2D(r, t)}} dW \quad (4.17)$$

where

$$dW = \frac{p}{r} dW_p + \frac{q}{r} dW_q = \sin \Theta dW_p + \cos \Theta dW_q$$

is a Wiener process. From Eq. (4.17) a relation between drift and diffusion coefficients is extracted

$$v(r, t) = \frac{D(r, t)}{r} . \quad (4.18)$$

This drift towards bigger radius  $r$  is due to the curvature  $1/r$  with  $v(r, t) \rightarrow 0$  for  $r \rightarrow \infty$ . In particular, in a system without curved regular tori, e.g.,  $I = p$ , there is no drift. As  $r = 0$  corresponds in this setting to an elliptic fixed point in the driven degree of freedom, the drift described by Eq. (4.18) points essentially towards the chaotic sea. For a power-law increase  $D(r, t) = r^\alpha$  the drift of Eq. (4.18) corresponds to the limiting

case  $\delta = 1$  of the generalized process Eq. (4.11). Another interpretation of Eq. (4.18) is that the drift arises from the fact that there is more volume at bigger radius [143]. The volume of a circular ring of width  $\Delta r$  is  $V(r) = 2\pi r \Delta r$  with the derivative  $V'(r) = 2\pi \Delta r$ . Thus, Eq. (4.18) may be expressed with respect to the relative volume change

$$v(r, t) = \frac{V'(r)}{V(r)} D(r, t). \quad (4.19)$$

It is worth mentioning that for a 4D map in which the curvature of the tori is suppressed, i.e. a 4D version of the designed map of Ref. [28], in some cases an intermediate power-law trapping  $P(T) \sim t^{-\gamma}$  with  $\gamma = 1$  is observed, which is a much slower decay than for generic 4D maps. However, this power law is only observed for two orders of magnitude while a faster power-law decay takes over for longer times and thus the results are not shown here.

While the drift described by Eq. (4.19) is essentially due to a volume change in the driven degree of freedom, there might be also a drift due to a volume change of the chaotic layer of the driving degree of freedom. Consider the resonance channel of an uncoupled resonance  $0 : m : n$  in action space  $(I_1, I_2)$ , where  $I_1$  is the driven action along the channel and  $I_2$  the driving action that describes the fluctuations perpendicular to the channel. Denoting the action corresponding to the rational frequency  $\nu_2 = n/m$  as  $I_{n/m}$  and assuming a symmetric resonance channel around the resonance line, the borders of the resonance channel are  $I_2 \in [I_{n/m} - b(I_1), I_{n/m} + b(I_1)]$ . Assuming further that for the minimal time step  $\Delta t$  an ensemble of chaotic initial conditions  $\{(I_1, I_2) : I_1 = I_1^0, I_2 \in [I_{n/m} - b(I_1^0), I_{n/m} + b(I_1^0)]\}$  is uniformly mapped into the region  $\{(I_1, I_2) : |I_1 - I_1^0| \leq \Delta I_1(I_1^0), I_2 \in [I_{n/m} - b(I_1), I_{n/m} + b(I_1)]\}$  a drift  $v(I_1^0)$  along the channel according to Eq. (4.4) follows

$$v(I_1^0) = \frac{1}{\Delta t} \mathbb{E}[I_1 - I_1^0]_{I_1} = \frac{\int_{I_1^0 - \Delta I_1(I_1^0)}^{I_1^0 + \Delta I_1(I_1^0)} dI_1 (I_1 - I_1^0) \int_{I_{n/m} - b(I_1)}^{I_{n/m} + b(I_1)} dI_2}{\Delta t \int_{I_1^0 - \Delta I_1(I_1^0)}^{I_1^0 + \Delta I_1(I_1^0)} dI_1 \int_{I_{n/m} - b(I_1)}^{I_{n/m} + b(I_1)} dI_2} \quad (4.20)$$

which reads for  $\Delta I_1(I_1^0) \ll 1$  using the approximation  $b(I_1) \approx b(I_1^0) + b'(I_1^0)(I_1 - I_1^0)$

$$v(I_1^0) = \frac{b'(I_1^0)}{b(I_1^0)} \frac{\Delta I_1(I_1^0)^2}{3\Delta t}. \quad (4.21)$$

Taking into account that the diffusion coefficient  $D(I_1^0)$  reads according to Eq. (4.5)

$$D(I_1^0) = \frac{1}{2\Delta t} \mathbb{E}[(I_1 - I_1^0)^2]_{I_1} = \frac{\Delta I_1 (I_1^0)^2}{6\Delta t} \quad (4.22)$$

and the width  $V(I_1^0)$  of the channel at  $I_1^0$  is  $V(I_1^0) = 2b(I_1^0)$  with the derivative  $V'(I_1^0) = 2b'(I_1^0)$ , one can write Eq. (4.21) analogously to Eq. (4.19)

$$v(I_1^0) = 2 \frac{V'(I_1^0)}{V(I_1^0)} D(I_1^0) . \quad (4.23)$$

Note that the derivative in Eq. (4.19) is with respect to the radius  $r$  and not the action  $I$ . The expression of Eq. (4.23) is valid for all channels independently of the dimensionality of the volume  $V(I_1^0)$ , as the corresponding term in Eq. (4.20) can be expressed by an arbitrary volume

$$\int_{I_{n/m}-b(I_1)}^{I_{n/m}+b(I_1)} dI_2 \mapsto V(I_1) \approx V(I_1^0) + V'(I_1^0)(I_1 - I_1^0) .$$

Note that for  $b'(I_1^0) = 0$  a zero drift  $v(I_1^0) = 0$  follows while the diffusion coefficient  $D(I_1)$  is independent of the shape and width of the channel, i.e. Eq. (4.22) is consistent with the variance of a uniform distribution. The numerics confirm that Eq. (4.23) not only applies for uniform distributions, but also for Gaussian distributions and  $\Delta t \rightarrow 0$ , see Appendix A.2 for details. Also the drift for the case of finite transport in  $I_2$ , i.e.  $\Delta I_2(I_1^0) < b(I_1^0)$  is derived and the transition to Eq. (4.23) for  $\Delta I_2(I_1^0) > 2b(I_1^0)$  is shown.

The width of the channel is related to the volume of the chaotic layer of the driving degree of freedom. This volume is not constant as the width of the layer or the size of the regular islands embedded in the layer vary along the channel. It is reasonable to assume that the width of the layer increases and the size of the islands decreases on average towards the chaotic sea with local fluctuations due to crossing resonance channels. Thus, Eq. (4.23) describes a drift towards the chaotic sea. As the layer volume  $V(I_1)$  is essentially determined by the width of the layer and this width is proportional to the amplitude of the driving [62], the diffusion coefficient  $D(I_1)$  should roughly follow the course of the volume  $V(I_1)$  and increase towards the chaotic sea.

### 4.6.3 Numerical results

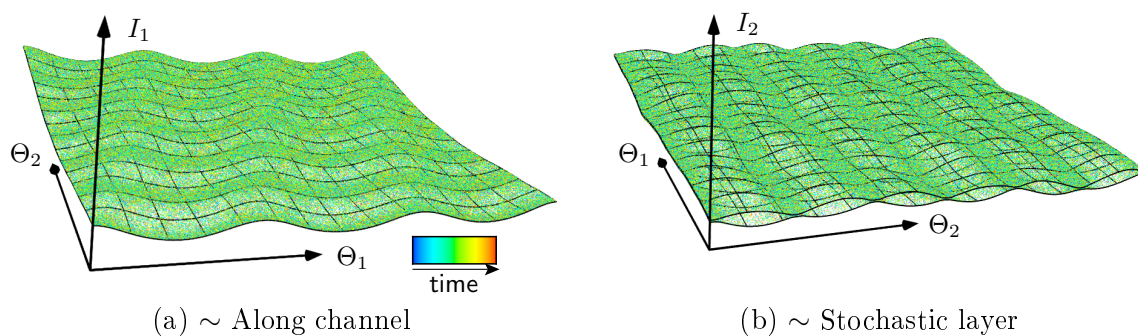
In the previous section, the presence of a drift along resonance channels is proposed based on the change of volume of the stochastic layer of the driving degree of freedom. As demonstrated with the stochastic model in Sec. 4.6.1 such a drift could explain the power-law trapping by the transport along a single resonance channel. In this section, the volume of the stochastic layer along the resonance channel  $0 : 6 : 5$  of the coupled twist maps  $F_{\text{Twist}}$  is numerically computed using a new method. Overall, this volume is found to increase towards the chaotic sea faster than exponentially, which implies considerable drift coefficients in terms of Eq. (4.23). Due to the inhomogeneity of the volume and the limited accuracy with which the transport can be measured, the presence of this proposed drift could not be verified numerically. In Appendix A.1 the attempts to measure the drift and diffusion coefficients along the channel are discussed in detail.

As announced in Sec. 3.5 the coupled twist maps  $F_{\text{Twist}}$  are used for the measurements. The measurements focus for the uncoupled resonance channel  $0 : 6 : 5$  from the generic region B also visible in Figs. 3.7 and 3.8(b). This resonance occurs roughly speaking in the second uncoupled degree of freedom  $(I_2, \Theta_2)$  and thus the transport along the channel roughly corresponds to transport along the uncoupled action  $I_1$ . In order to focus on the transport along the channel and perform the volume measurements the escape from the resonance channel as described in Secs. 4.2 and 4.3 should be avoided. Hence, the measurements are restricted to the closed part of the channel, e.g., in terms of the frequency space  $\nu_1 < 0.625$ . As mentioned in Sec. 3.4 a resonance channel contains a family of hyperbolic and a family of elliptic 1D tori. In the vicinity of hyperbolic 1D tori along the channel initial regions  $\Omega(I_1^0) \in [0, 10)^2 \times [-\pi, \pi)^2$  are defined which give rise to chaotic orbits, i.e.

$$\begin{aligned} \Omega(I_1^0) &= \{(I_1, I_2, \Theta_1, \Theta_2) : I_1 = I_1^0, \quad I_2 = 50 \cdot (5/6 - \sqrt{3} + 1) + 10^{-3} \cdot \Delta(I_1^0), \\ &\quad |\Theta_1 - \pi/2| < 10^{-2}, \quad |\Theta_2 - 0.01| < 10^{-3}\} \\ \Delta(I_1^0) &= \{3.8, 4.6, 4.6, 5, 6, 8, 8.5, 9, 9\} \\ \text{for } I_1^0 &= \{0.3, 0.325, 0.35, 0.4, 0.45, 0.5, 0.55, 0.6, 0.605\} \end{aligned} \tag{4.24}$$

where  $\Delta(I_1^0)$  for intermediate actions  $I_1^0$  follows from interpolation. Figure 4.18 shows the uncoupled coordinates  $(I_1, \Theta_1, \Theta_2)$  and  $(I_2, \Theta_2, \Theta_1)$  of several chaotic orbits with initial conditions at  $I_1^0 = 0.6$  according to Eq. (4.24). The chaotic orbits appear to be scattered on surfaces  $I_1(\Theta_1, \Theta_2)$ ,  $I_2^\pm(\Theta_1, \Theta_2)$ . These surfaces are indicated by the black grids and can be approximated as explained in a moment. The action along the channel  $\sim I_1$  is described by a single surface  $I_1(\Theta_1, \Theta_2)$ , see Fig. 4.18(a). In contrast, in

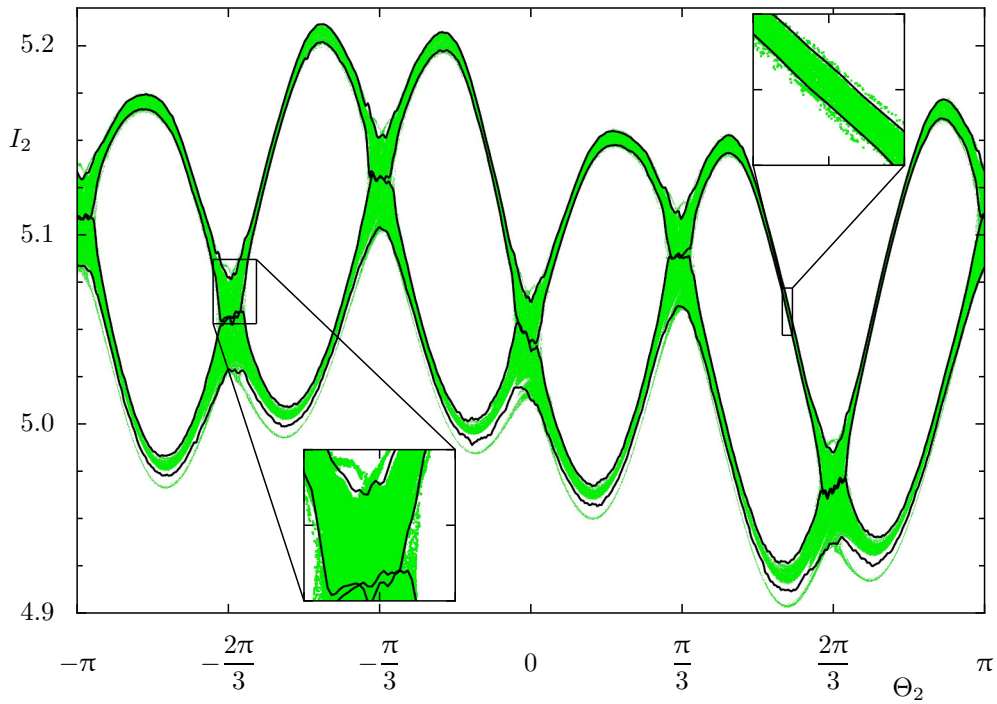
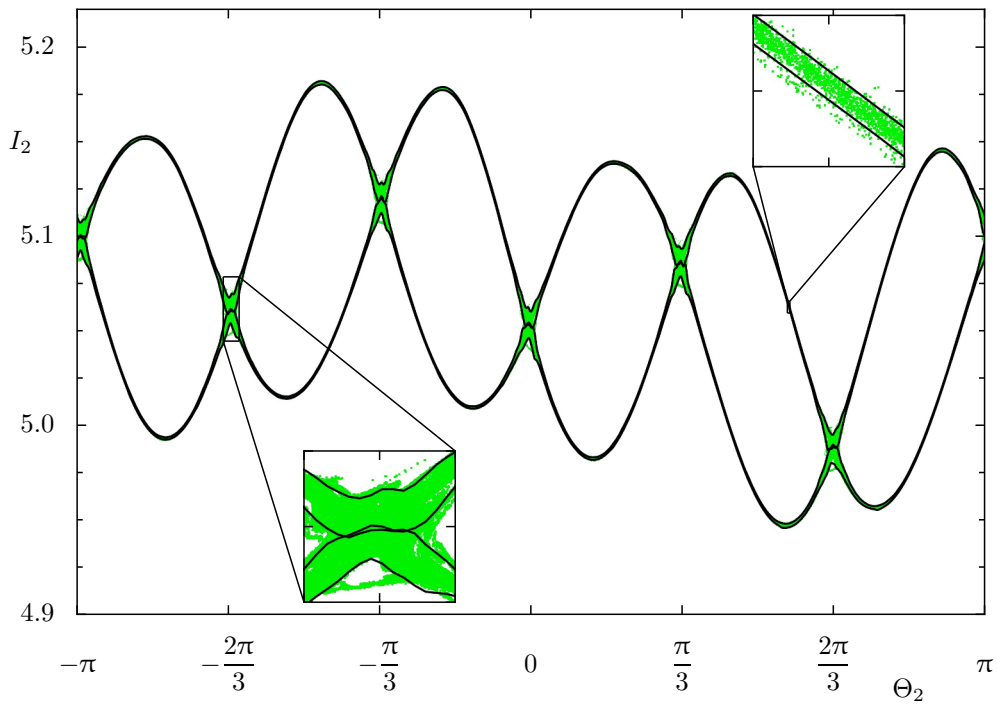




**Figure 4.18:** Chaotic orbits within the resonance channel  $0 : 6 : 5$  of the coupled twist maps  $F_{\text{Twist}}$  in 3D projections. The 100 orbits from the initial region  $\Omega(I_1^0 = 0.6)$ , see Eq. (4.24), are projected to the uncoupled action–angle coordinates (a)  $(I_1, \Theta_1, \Theta_2)$  and (b)  $(I_2, \Theta_1, \Theta_2)$  with the iteration time  $t \in [0, 6000]$  encoded in color. Approximations (a)  $I_2(\Theta_1, \Theta_2)$  and (b)  $I_2^\pm(\Theta_1, \Theta_2)$  of the layers are indicated as a black grids, see text. The coordinate axes are at (a)  $(0.2, -\pi, -\pi)$  and (b)  $(4.75, \pi/4, -\pi)$  (in (b)  $\Theta_1$ -axis is inverted).

Fig. 4.18(b) a period-6 island chain is visible along the  $\Theta_2$ -coordinate as expected for the resonance  $0 : 6 : 5$ . Thus, the other action  $I_2$  requires at least an upper  $I_2^+(\Theta_1, \Theta_2)$  and a lower surface  $I_2^-(\Theta_1, \Theta_2)$  with  $I_2^+(\Theta_1, \Theta_2) > I_2^-(\Theta_1, \Theta_2)$  for all  $\Theta_1, \Theta_2$ . In order to resolve more details, a slice  $|\Theta_1 - \pi/4| < \pi/800$  of Fig. 4.18(b) is shown in Fig. 4.19(a) with many more chaotic orbits in green. This slice corresponds to the front of Fig. 4.18(b). In this representation the resonance resembles the stochastic layer of a period-6 island chain of a 2D symplectic map. In this sense, the 4D map has two additional dimensions: a rotation  $\sim \Theta_1$  and the dimension along the resonance channel  $\sim I_1$ . Thus, the width or volume of the resonance channel discussed in Sec. 4.6.2 corresponds to the 3D volume of the stochastic layer in the coordinates  $(I_2, \Theta_2, \Theta_1)$ .

The volume of the stochastic layer is changing considerably along the resonance channel as illustrated by a comparison of slices with chaotic orbits at  $I_1^0 = 0.6$  and  $I_1^0 = 0.5$  shown in Figs. 4.19(a) and 4.19(b), respectively. Despite this, the chaotic orbits in the slice in Fig. 4.19(a) demonstrate the two main problems of the estimation of the volume of this layer. Firstly, the volume of a layer is ill defined as chaotic orbits which started in the stochastic layer explore adjacent island chains or go deeper into the island-around-island hierarchy for longer iterations. For instance, at the bottom of the island chain in Fig. 4.19(a) another thin island chain corresponding to the resonance  $-4 : 3 : 0$  is surrounded by chaotic orbits and another island chain is magnified in the left inset. As the escape to other island chains is governed by partial barriers as shown in Sec. 4.2, the density of chaotic points drops considerably outside the stochastic layer of the resonance  $0 : 6 : 5$ . This is well visible in the right inset in Fig. 4.19(a). Secondly, the width of the layer is varying over several orders of magnitude along the angle  $\Theta_2$ . This is illustrated

(a)  $I_1^0 = 0.6$ ,  $N_{pts} = 2279340$ (b)  $I_1^0 = 0.5$ ,  $N_{pts} = 2649046$ 

**Figure 4.19:** Stochastic layer of the resonance channel  $0 : 6 : 5$  of the map  $F_{\text{Twist}}$  displayed in a 2D slice  $|\Theta_1 - \pi/4| < \pi/800$  ( $I_1$  projected) with  $N_{pts}$  points of chaotic orbits shown in green. The layer is shown for two positions  $I_1^0 \in \{0.6, 0.5\}$  along the channel, i.e. (a) corresponds to the front of Fig. 4.18(b). The estimated borders of the stochastic layer with  $N = 800$  and  $\hat{t} = 3000$ , see text, are indicated as black lines. The insets magnify details of the layers.

by comparison of the width in between the islands and the width magnified in the right insets in Fig. 4.19. This fact makes a simple box-count approach unfeasible for the volume estimate. It should be pointed out that the estimation of the layer volume for 2D maps faces the same problems.

In the following, a new procedure is presented which gives an estimate of the upper and lower borders of the stochastic layer based on the chaotic orbits. These estimates are included as black lines for both examples in Fig. 4.19 to demonstrate how well the two mentioned problems are addressed: On the one hand the estimated borders ignore outer regions and islands chains with less chaotic points. On the other hand the width of the layer is well approximated both for thick and thin parts of the layer. In order to obtain the borders, firstly a grid in the angle coordinates with resolution  $N$  is chosen. For each grid point  $\Omega_{ij}$ ,  $i, j \in \{0, 1, \dots, N-1\}$  with

$$\Omega_{ij} = \left\{ \Theta_1, \Theta_2 \in [-\pi, \pi) : |\Theta_1 + \theta_i| < \frac{\pi}{N}, |\Theta_2 + \theta_j| < \frac{\pi}{N}, \right. \\ \left. \theta_k = \pi \left( \frac{2k+1}{N} - 1 \right) \right\} \quad (4.25)$$

the mean action  $\mathbb{E}[I_2]$  of the layers, the mean actions  $\mathbb{E}[I_2^{\text{up}}]$  and  $\mathbb{E}[I_2^{\text{lo}}]$  of the upper and lower layer, and the standard deviation  $\sigma^{\text{up,lo}}$  of each of these layers are obtained in three consecutive steps. Each step uses an individual set  $\Omega_{ij}^1, \Omega_{ij}^2$ , and  $\Omega_{ij}^3$  of chaotic orbits. For each step at the chosen position  $I_1^0$  along the resonance channel chaotic orbits are iterated up to  $\hat{t}$ . The first third of the iterations is considered to scatter the chaotic orbits uniformly over the stochastic layer and is therefore neglected. Chaotic orbits are started until at each grid point  $\Omega_{ij}$  for each average at least 100 points of the orbits are available. In the first step, the uncoupled action  $I_2$  of all points at a grid point  $\Omega_{ij}^1$  are averaged giving  $\mathbb{E}[I_2]_{\Omega_{ij}^1}$ . In the second step, all points at a grid point  $\Omega_{ij}^2$  are separated into upper  $I_2 \geq \mathbb{E}[I_2]_{\Omega_{ij}^1}$  and lower points  $I_2 < \mathbb{E}[I_2]_{\Omega_{ij}^1}$ . The average of the uncoupled action  $I_2$  for each set gives  $\mathbb{E}[I_2^{\text{up}}]_{\Omega_{ij}^2}$  and  $\mathbb{E}[I_2^{\text{lo}}]_{\Omega_{ij}^2}$ , respectively. In the third step, all points at a grid point  $\Omega_{ij}^3$  are separated again into upper and lower points and for each set the corresponding standard deviation is computed

$$\sigma_{\Omega_{ij}^3}^{\text{up}} = \sqrt{\mathbb{E}[(I_2 - \mathbb{E}[I_2^{\text{up}}]_{\Omega_{ij}^2})^2]_{\Omega_{ij}^3}} \quad \sigma_{\Omega_{ij}^3}^{\text{lo}} = \sqrt{\mathbb{E}[(I_2 - \mathbb{E}[I_2^{\text{lo}}]_{\Omega_{ij}^2})^2]_{\Omega_{ij}^3}}. \quad (4.26)$$

Based on the presence of partial barriers, it is assumed that at each grid point  $\Omega_{ij}$  the points of the chaotic orbits are distributed uniformly within the borders of the stochastic layer. As a one-dimensional, uniform distribution over finite interval of length  $2L$  has

the variance  $\sigma^2 = L^2/3$ , it follows for the borders of the stochastic layer

$$|I_2(\theta_i, \theta_j) - \mathbb{E}[I_2^{\text{up}}]_{\Omega_{ij}^2}| \leq \sqrt{3}\sigma_{\Omega_{ij}^3}^{\text{up}} \quad \text{or} \quad |I_2(\theta_i, \theta_j) - \mathbb{E}[I_2^{\text{lo}}]_{\Omega_{ij}^2}| \leq \sqrt{3}\sigma_{\Omega_{ij}^3}^{\text{lo}} \quad (4.27)$$

where for intermediate values of the angles linear interpolation is used. The resulting borders for the examples in Fig. 4.19 are shown as black lines. Note that all the described averages can in principle be obtained from the same set of chaotic orbits. However, by dividing the procedure into three steps memory problems are avoided as not all chaotic orbits but only the number of points and one sum at each grid point has to be stored. The volume measurement is discussed in more detail in Appendix A.1 including a comparison with results for a 2D map.

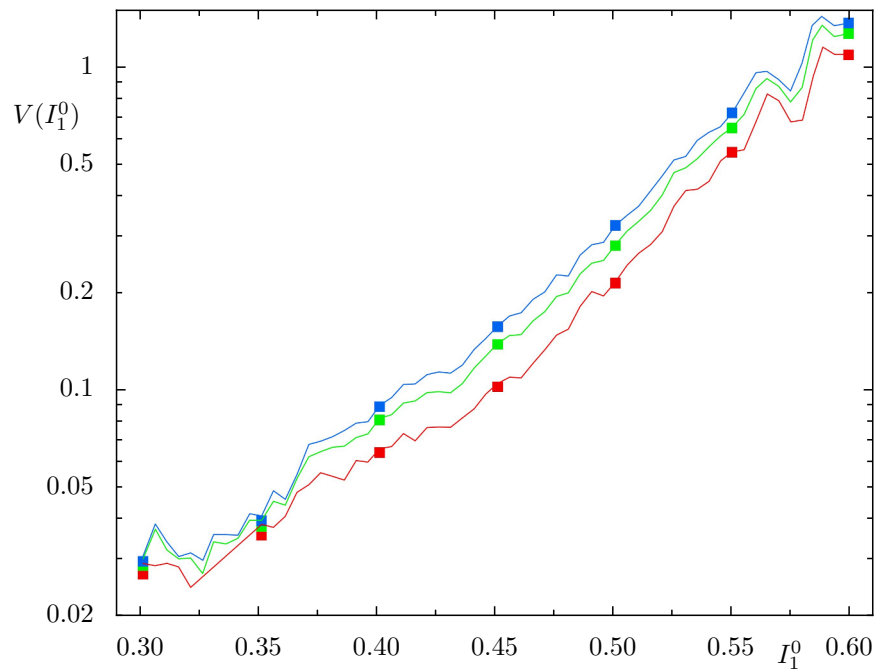
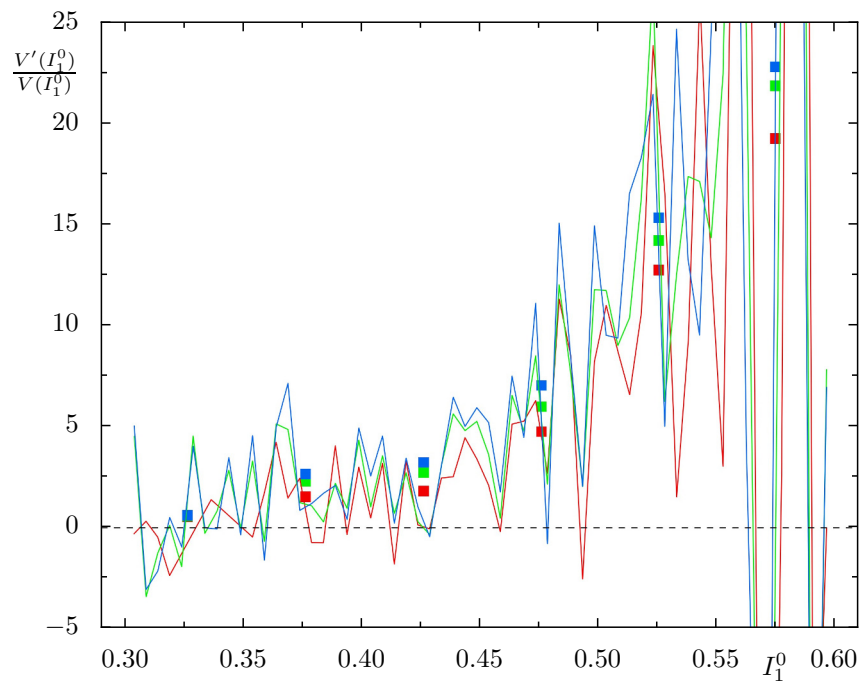
The volume  $V(I_1^0)$  of the stochastic layer at  $I_1^0$  follows from its borders according to Eqs. (4.25) and (4.27)

$$V(I_1^0) = 2\sqrt{3} \left( \frac{2\pi}{N} \right)^2 \sum_{i,j=0}^{N-1} \left( \sigma_{\Omega_{ij}^3}^{\text{up}}(I_1^0) + \sigma_{\Omega_{ij}^3}^{\text{lo}}(I_1^0) \right). \quad (4.28)$$

The volume  $V(I_1^0)$  is computed along the channel  $I_1^0 \in [0.3, 0.6]$  for a step size  $\Delta I_1^0 = 5 \cdot 10^{-3}$  with  $N = 500$ , for a step size  $\Delta I_1^0 = 5 \cdot 10^{-2}$  with  $N = 800$ , and  $\hat{t} = \{3000, 6000, 9000\}$ . The results are displayed in Fig. 4.20(a), where for  $N = 800$  large squares are shown and for  $N = 500$  the points are connected with lines as guide to the eye. The colors red, green and blue correspond to the different iteration times  $\hat{t}$ . While the volume increases with the times  $\hat{t}$ , the overall trend of the volume  $V(I_1^0)$  along the channel appears to be relatively independent of them. Also the results for the different resolutions  $N$  are consistent. The volume  $V(I_1^0)$  increases relatively smooth towards the chaotic sea apart from major distortions at small actions  $I_1^0 < 0.37$  and at  $I_1^0 \sim 0.56$ . As suggested by Eq. (4.23) the relative volume change in between two adjacent points along the channel  $\hat{I}_1^0 > \check{I}_1^0$  is computed according to

$$\begin{aligned} I_1^0 &= \frac{1}{2} \left( \hat{I}_1^0 + \check{I}_1^0 \right) & dI_1^0 &= \left( \hat{I}_1^0 - \check{I}_1^0 \right) \\ \frac{V'(I_1^0)}{V(I_1^0)} &= \frac{2}{V(\hat{I}_1^0) + V(\check{I}_1^0)} \frac{V(\hat{I}_1^0) - V(\check{I}_1^0)}{dI_1^0}. \end{aligned} \quad (4.29)$$

The results obtained from the data of Fig. 4.20(a) are depicted in Fig. 4.20(b) in corresponding fashion. For  $N = 500$  the relative volume change  $V'(I_1^0)/V(I_1^0)$  fluctuates considerably on small spatial scales with increasing amplitude towards the chaotic sea. Even the sign of  $V'(I_1^0)/V(I_1^0)$  flips frequently. In particular, at the distortion  $I_1^0 \sim 0.56$  the values range from  $-38$  up to  $135$ . Nevertheless, overall the relative volume change

(a) Volume  $V(I_1^0)$  along channel(b) Relative volume change  $V'(I_1^0)/V(I_1^0)$  of (a)

**Figure 4.20:** (a) Volume  $V(I_1^0)$  of the stochastic layer along the resonance channel  $0 : 6 : 5$  of the map  $F_{\text{Twist}}$  according to Eq. (4.28). The volume is estimated for  $\hat{t} \in \{3000, 6000, 9000\}$  (red, green, blue) and  $N = 500$  (lines) or  $N = 800$  (squares without lines). (b) Relative volume change  $V'(I_1^0)/V(I_1^0)$  computed from (a) according to Eq. (4.29). Zero is indicated by the dashed line.

$V'(I_1^0)/V(I_1^0)$  increases which is confirmed by the squares representing the values for  $N = 800$  with lower resolution along the channel. This implies according to Eq. (4.23) an overall drift towards the chaotic sea. Further, the squares for  $N = 800$  demonstrate that the values of  $V'(I_1^0)/V(I_1^0)$  increase faster than linear along the channel, implying that the volume  $V(I_1^0)$  increases faster than  $\sim \exp(I_1^0)^2$ . This is worth pointing out as common assumptions for the width or size of the stochastic layer are  $\sim \exp(-A/\sqrt{\epsilon})$  [62] or  $\sim \sqrt{\epsilon}$  [39, 40], where  $\epsilon$  denotes the perturbation strength. In the case of the resonance  $0 : 6 : 5$  of the coupled twist maps  $F_{\text{Twist}}$  this perturbation may be asserted, see Sec. 3.5.1, as  $\epsilon \sim q_1^3 q_2^2 \sim I_1^{3/2}$ . Thus, it seems that the common assumptions used for near-integrable settings severely underestimate the volume increase along a generic resonance channel. Rapidly widening resonance channels can also be seen in the figures of Ref. [38].

The relative volume change displayed in Fig. 4.20(b) predicts according to Eq. (4.23) the relation between the local drift and diffusion coefficients for the transport along the resonance channel. However, all attempts to test this relation so far failed as the measurement of the local coefficients is very difficult. This has two major reasons: On the one hand, the fluctuations of the volume of the stochastic layer implies corresponding fluctuations of the drift and diffusion coefficients. As these rapid changes of the coefficients appear on very small spatial scales, a very precise measurement of the transport for very short times is required. On the other hand, the correct coordinates to measure the transport are not available. Substitutes approximating these coordinates like the uncoupled action  $I_1$  or the frequency  $\nu_1$  always have finite precision. Thus, the transport in these coordinates has to be measured for longer iteration times to diminish the influence of these errors. Basically, these two competing time-scales inhibit a numerical confirmation of the stochastic process transport proposed in Sec. 4.6.2. In Appendix A.1 some approaches to quantify the transport along the channel are outlined including insights gained from these approaches. Further, it is explained that  $\Delta I_1^0 = 5 \cdot 10^{-3}$  is the minimal resolution achieved for the described setting and that the volume increases with  $\hat{t}$ , i.e.  $V(I_1^0) \sim \log \hat{t}$ . Finally, note that for the position along the channel instead of  $I_1^0$  from Eq. (4.24) the average uncoupled action  $I_1$ , i.e.  $\mathbb{E}[\mathbb{E}[I_1]_{\Omega_{ij}^1}]_{ij}$  for  $\hat{t}$  iterations using the initial conditions  $\Omega(I_1^0)$ , is used. However, due to the choice of the initial regions  $\Omega(I_1^0)$  these two values match very well  $I_1^0 \approx \mathbb{E}[\mathbb{E}[I_1]_{\Omega_{ij}^1}]_{ij}$  and for brevity they are not explicitly distinguished in Fig. 4.20.

# 5 Summary and outlook

In this thesis the chaotic transport near regular structures in generic 4D symplectic maps is investigated. Such 4D maps serve as a prototype for higher-dimensional Hamiltonian systems as they are the lowest dimensional maps which exhibit Arnold diffusion. The organization and hierarchy of the regular structures is explained. A power-law decay of the statistics of Poincaré recurrences is observed and attributed to chaotic orbits being trapped in sticky regions at the surface of the regular structures. The chaotic transport within such sticky regions is found to be moderated by a set of overlapping resonance channels. The transport across resonance channels and deeper into the hierarchy is shown to be governed by partial transport barriers similar to 2D maps. For the transport along resonance channels a drift is conjectured, which however could not be verified numerically due to technical difficulties. For the transport both across and along resonance channels models are proposed which can explain the power-law trapping in 4D maps. A part of the results has already been published [138, 182, 186].

The regular 2D tori are shown to be organized around a skeleton consisting of families of elliptic 1D tori [138]. The origins of these families are explained and it is demonstrated how they form a hierarchy similar to the island-around-island hierarchy in 2D maps. In particular, such families are present in any resonance channel centering the regular structures of the channel around them [186]. Analogously, these families occur at any resonance junction.

Two coupled standard maps are investigated as an example for a generic 4D symplectic map with a large chaotic sea. Using a combination of 3D phase-space slices [182] and frequency analysis a sticky region at the surface of the regular structures is identified. The chaotic transport in this region is found to be governed by a set of overlapping resonance channels which reach far out into the chaotic sea. The dynamics is locally decomposed into four phenomena, namely I) transport across resonance channels, II) trapping deeper into the hierarchy at resonances, III) trapping at resonance junctions, and IV) transport along resonance channels. Using time–frequency plots it is demonstrated how the transport processes I), II), and III) are regulated by partial transport barriers similar to 2D maps. In contrast to 2D maps, the trapping deeper in the hierarchy turns out to be insignificant for the power-law trapping. Instead, the transport

across resonance channels is shown to generate a power-law decay similar to the averaging over many 2D maps. However, the trapping in the generic sticky regions seems to be rather regulated by IV) the transport along resonance channels. For this transport the presence of a drift due to the geometry and change of width along the channel is proposed and it is demonstrated how such a drift could generate a power-law decay of recurrence times. Despite the use of a new designed map which facilitates the quantification of the chaotic transport, the slow dynamics along the channel could not be measured precisely enough to verify the drift.

It should be emphasized that due to the self-similarity of the mentioned hierarchy the generic power-law trapping has an impact on the transport along any resonance channel even in the near-integrable regime. That is chaotic orbits within any resonance channel can get trapped at the regular structures by the same mechanism and thus inhibit the transport along the channel. Also the proposed drift along resonance channels has general implications for the transport in the Arnold web as this transport is usually considered to be purely diffusive.

While the question about the mechanism of the power-law trapping is not definitely answered in this thesis, the comprehensive picture obtained for the dynamics of the 4D phase space and the used methods may guide future studies. In particular, the transport across and along resonance channels has to be described quantitatively. For the former this may be accomplished using time–frequency plots, which make the partial barriers, which are complicated objects in phase space, recognizable in the frequency space. Furthermore, the isolines of the local escape time from the sticky region could serve as a global coordinate system in the frequency space. By this the impact of the jumps between resonances on the escape from the sticky region could be determined. The introduced coupled twist maps  $F_{\text{Twist}}$  provide a promising system which should facilitate the measurement of the transport along resonance channels. After the extraction of the relevant stochastic properties of the chaotic transport, their origins in terms of invariant phase-space structures should be determined. This includes among others the computation of stable and unstable manifolds composing the partial transport barriers and the calculation of the 4D volumes enclosed by their intersections. Focus should be put on the understanding of 4D maps. Since all higher-dimensional systems share the crucial property that regular tori are no barriers in phase space, the results obtained for 4D maps should be generalizable to even higher-dimensional systems with reasonable effort. For instance, the hierarchy of the regular tori can in principle be constructed analogously in a  $2N$ -dimensional map with  $N > 2$  by taking into account that the frequencies on a  $k$ -dimensional regular torus with  $0 < k \leq N$  are able to fulfill  $i \in \{1, 2, \dots, k\}$  resonance conditions and thus can break up into tori of dimension  $k - i$ .



# A Appendix

## A.1 Measuring transport along resonance channels

In Sec. 4.6 the transport along a resonance channel is discussed in terms of a 1D heterogeneous stochastic process. In particular, a drift due to the change of the volume of the stochastic layer along the channel is proposed. Based on such a drift a model is presented which could explain the observed power-law trapping in 4D maps. However, it remains to demonstrate the validity of this model by verifying the relation predicted for the drift and diffusion coefficient Eq. (4.23) numerically. While the volume along the channel is computed in Sec. 4.6.3, the estimate of the drift and diffusion coefficient proves to be very difficult. In this section, some approaches to obtain these coefficients are discussed. The transport along the channel is monitored both in adapted action coordinates and frequencies. Some statistical insights about this chaotic transport and problems of its quantification are outlined. Note that the adapted action coordinates are a by-product of the computation of the layer volume from Sec. 4.6.3 and some details of this procedure are presented here including a comparison to a 2D map. The discussions in this section may guide future investigations to a successful description of the transport along resonance channels. As in Sec. 4.6.3 all following discussions focus on the example of the resonance  $0 : 6 : 5$  of the coupled twist maps  $F_{\text{Twist}}$ .

One approach is to measure the chaotic transport along the resonance channel via the adapted action coordinates introduced in Sec. 4.6.3. More precisely, local action coordinates  $I_2(\Theta_1, \Theta_2)$  are obtained by iterating ensembles  $\Omega(I_1^0)$  of chaotic orbits, see Eq. (4.24), up to times  $\hat{t}$  by averaging their action  $I_2$  on a  $N \times N$  grid of the angles  $(\Theta_1, \Theta_2) \in [-\pi, \pi]^2$ . In this sense, the average position  $I_2(\Theta_1, \Theta_2)$  of the stochastic layer at a certain position  $I_1^0$  along the resonance channel is approximated. The result at  $I_1^0 = 0.6$  is shown as black grid in Fig. 4.18(b). Analogously, for the transport along the channel the average position  $I_1(\Theta_1, \Theta_2)$  is used, e.g., the result at  $I_1^0 = 0.6$  is shown as black grid in Fig. 4.18(a). This approximation for  $I_1$  is displayed by a slice at  $\Theta_1 = \pi/4$  in Fig. A.1(a), analogously to the slice shown for the approximation of  $I_2$  in Fig. 4.19(a). In Fig. A.1(a) the points of the chaotic orbits from the ensemble  $\Omega(I_1^0 = 0.6)$  are shown in green and the approximation  $I_1(\Theta_1, \Theta_2)$  as black line. While

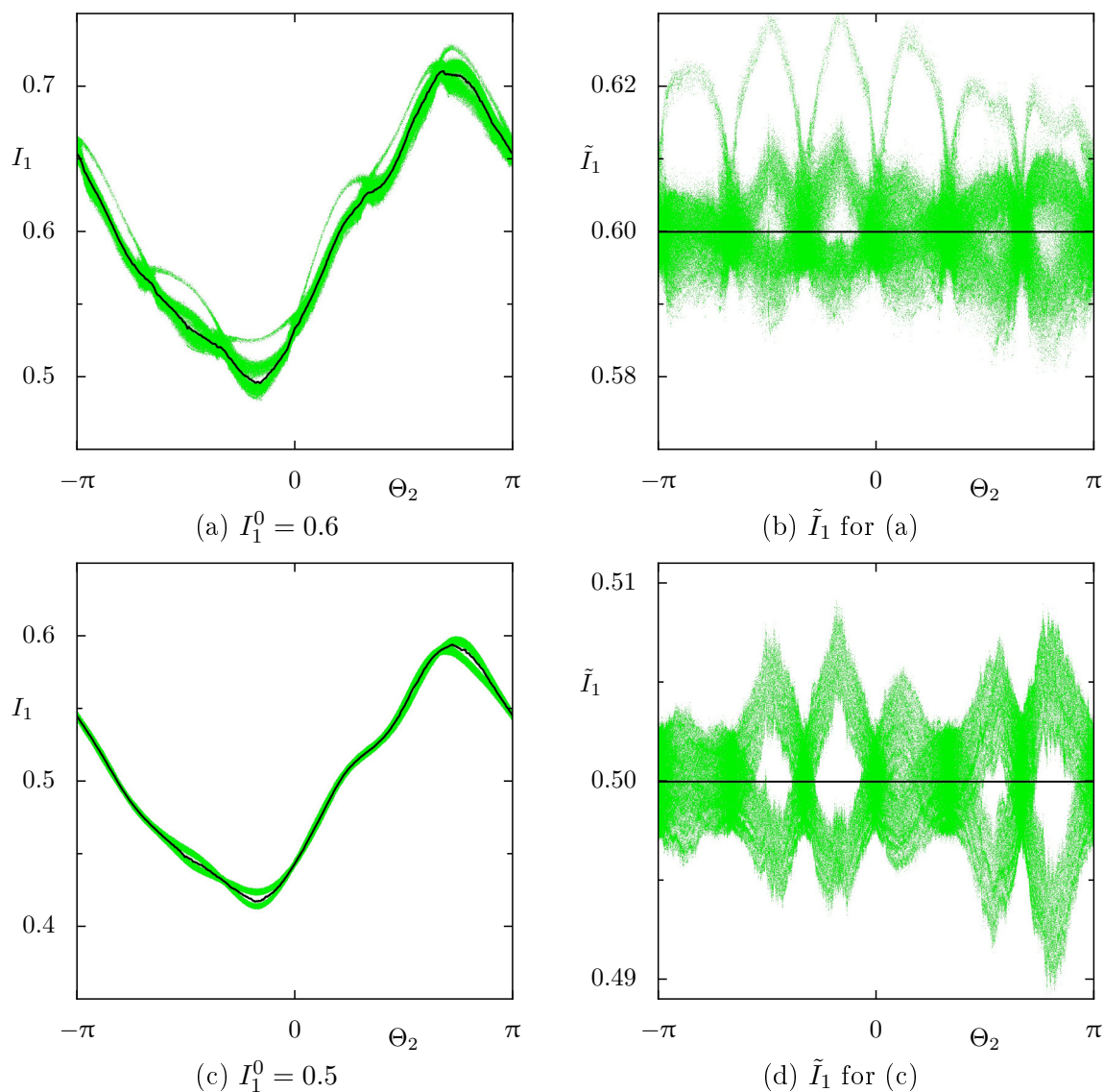


**Figure A.1:** Resonance channel  $0 : 6 : 5$  of the map  $F_{\text{Twist}}$  displayed in a 2D slice  $|\Theta_1 - \pi/4| < \pi/800$  ( $I_2$  projected) with the chaotic orbits from Fig. 4.19 shown in green. In (a),(c) the channel is shown for two positions  $I_1^0 \in \{0.6, 0.5\}$  along the channel. The approximations for constant action along the channel with  $N = 800$  and  $\hat{t} = 3000$ , see text, are indicated as black lines. In (b),(d) the same points are shown in the corresponding adapted action  $\tilde{I}_1$ , see Eq. (A.1). While the fluctuations along  $\Theta_2$  are decreased by an order of magnitude, period-6 island-like patterns are visible. Additionally, in (b) another island chain is visible above this pattern which is due to the resonance  $-4 : 3 : 0$  and also appears in Fig. 4.19(a) below the islands.

each chaotic orbit is only iterated up to  $\tilde{t} = 3000$  iterations and thus all his points remain approximately at the same position along the channel, the uncoupled action coordinate  $I_1$  of the points varies strongly  $dI_1 \sim 2 \cdot 10^{-1}$ . Thus, the slow transport along the channel is not measured in  $I_1$  but rather with respect to the approximation

$$\tilde{I}_1 = (I_1 - I_1(\Theta_1, \Theta_2)) + I_1^0. \quad (\text{A.1})$$

In Fig. A.1(b) the points of Fig. A.1(a) are presented in this new coordinate  $\tilde{I}_1$ . While this coordinate seems to be an order of magnitude less sensitive to the angle coordinates, i.e.  $d\tilde{I}_1 \sim 2 \cdot 10^{-2}$ , it reveals signatures of the resonance  $0 : 6 : 5$ , i.e. a period-6 island-chain-like distribution of the points along the  $\Theta_2$  coordinate. This feature is even more pronounced in Figs. A.1(c) and A.1(d) which show the analogous slices for  $I_1^0 = 0.5$ . In Fig. A.1(d) six intervals can be distinguished, i.e. at  $|\Theta_2| \sim \{0, \pi/3, 2\pi/3, \pi\}$ , at which the range of  $\tilde{I}_1$  is much more confined than in between these intervals, where islands with no chaotic points appear. These features resemble the island chain visible in Figs. 4.19(a) and 4.19(b) and suggest that the uncoupled degree of freedoms  $(I_1, \Theta_1)$  and  $(I_2, \Theta_2)$  do not sufficiently separate the stochastic layer from the direction along the resonance channel. This implies a lower bound for how accurate the coordinate  $\tilde{I}_1$  can express the position along the channel. More precisely, the distribution  $\rho(\tilde{I}_1)$  of  $\tilde{I}_1$  for an initial ensembles of chaotic orbits  $\Omega(I_1^0)$ , see in principle Fig. A.3(c), shows that the minimal achieved resolution along the channel is  $\Delta\tilde{I}_1 = 5 \cdot 10^{-3}$ . Note that the shift by  $I_1^0$  in the definition of  $\tilde{I}_1$  in Eq. (A.1) is added in order to enable a distinction of this local coordinate  $\tilde{I}_1$  for different positions along the channel. Furthermore, instead of  $I_1^0$  from Eq. (4.24) the average uncoupled action of the approximation  $I_1(\Theta_1, \Theta_2)$ , i.e.  $\mathbb{E}[I_1(\Theta_1, \Theta_2)]_{\Theta_1, \Theta_2}$  for  $\hat{t}$  iterations using the initial region  $\Omega(I_1^0)$ , is used. Due to the choice of the initial regions  $\Omega(I_1^0)$  these two values match very well  $I_1^0 \approx \mathbb{E}[I_1(\Theta_1, \Theta_2)]_{\Theta_1, \Theta_2}$  and for brevity they are not explicitly distinguished in this thesis.

Another approach is to measure the chaotic transport along the resonance channel via frequency analysis. In Fig. A.2 a detail of the resonance channel  $0 : 6 : 5$  in frequency space is shown. The resonance line lies at  $\nu_2 = 5/6$  and the channel is ultimately confined to the top and the bottom by regular tori as indicated by the gray points. Also the frequencies of two ensembles of chaotic orbits started at  $I_1^0 = 0.5$  and  $I_1^0 = 0.6$  are shown as points colored according to the iteration time  $t$  of each orbit, according to Sec. 2.6.3. The first segments  $t \in [0, \Delta t)$  of the chaotic orbits are approximately at  $\nu_1 = 0.623$  and  $\nu_1 = 0.624$ , respectively, as seen by the location of the dark blue points in Fig. A.2. In principle, the frequency  $\nu_2$  of the orbits varies rapidly and corresponds

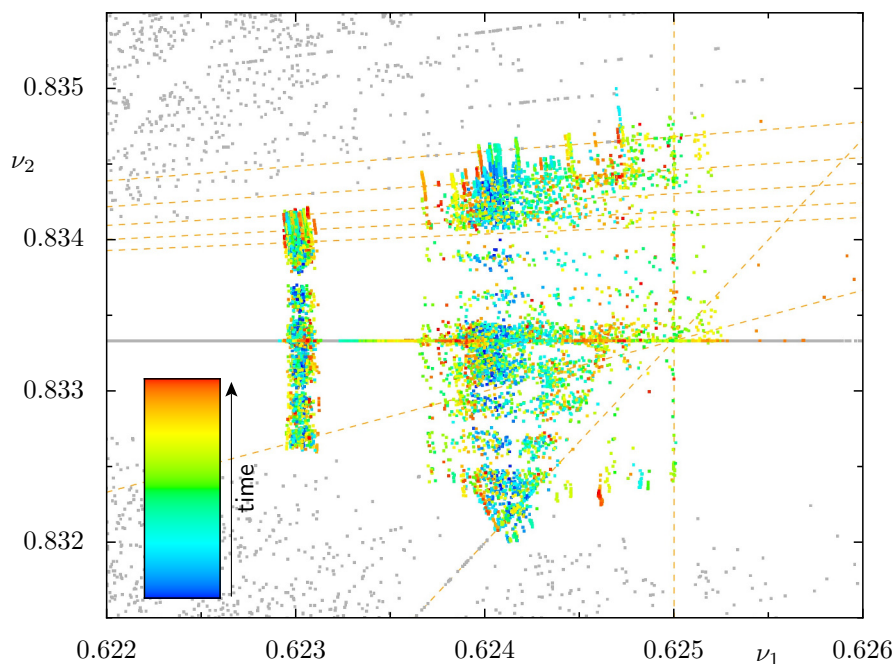


**Figure A.2:** Resonance channel  $0 : 6 : 5$  of the map  $F_{\text{Twist}}$  in frequency space. The regular tori from Fig. 3.6(c) are shown as gray points. At each of the two positions  $I_1^0 \in \{0.5, 0.6\}$ , see Eq. (4.24), which translates roughly to frequencies  $\nu_1 \in \{0.623, 0.624\}$ , 30 chaotic orbits are iterated  $t \in [0, 513 \cdot 4096)$  and shown in frequency space each orbit colored according to its iteration time. Some relevant resonances indicated by orange dashed lines are from top to bottom at  $\nu_1 = 0.624 - 3 : 31 : 24, -3 : 37 : 29, -3 : 49 : 39, -3 : 55 : 44, -8 : 24 : 15, -3 : 43 : 34, -4 : 3 : 0$ , plus the vertical resonance  $8 : 0 : 5$ . The channel of the resonance  $-4 : 3 : 0$  is well visible at the bottom with gray points on the resonance line.

roughly to the transport within the stochastic layer, while the frequency  $\nu_1$  varies much less and corresponds roughly to the transport along the channel. The different expansion of each ensemble already illustrates the change of the transport rates along the channel. The left ensemble, from  $I_1^0 = 0.5$ , is further away from the chaotic sea, which is to the right of Fig. A.2. The ensemble is confined along  $\nu_2$  due to the width of the channel, while it is even more confined along  $\nu_1$  due to the slow transport along the resonance channel. The right ensemble, from  $I_1^0 = 0.6$ , expands slightly more along  $\nu_2$  as the width of the channel increases towards the chaotic sea, see also Sec. 4.6.3. At the same time this right ensemble spreads an order of magnitude more along  $\nu_1$  than the left ensemble demonstrating the considerably increased transport rate along the channel. It is important to point out that the considered channel is not exclusively spanned by the resonance  $0 : 6 : 5$  as higher order resonances, shown as orange dashed lines in Fig. A.2, are frequently visited by the chaotic orbits. These resonances correspond to the adjacent island chains discussed in the context of Fig. 4.19. For instance, the resonance  $-4 : 3 : 0$  appears in the  $(I_2, \Theta_2)$ -plot of Fig. 4.19(a) as the period-6 island chain below the island

chain of the resonance  $0 : 6 : 5$ . This resonance appears likewise as the period-6 island chain above the black line in the  $(I_1, \Theta_2)$ -plots in Figs. A.1(a) and A.1(b). Note that the position of this islands chain is consistent with its position in the frequency space in Fig. A.2 as for the coupled twist maps  $F_{\text{Twist}}$  bigger/smaller  $I_1, I_2$  roughly correspond to bigger/smaller  $\nu_1, \nu_2$ , respectively. An advantage of the frequency space is that the additional, higher order resonances are well separated from the main resonance  $0 : 6 : 5$ . For instance, one might assume only frequencies with  $0.833 < \nu_2 < 0.83375$  are located at the resonance  $0 : 6 : 5$  and thus avoiding other resonances. A coarse transformation between actions and frequencies is obtained by averaging over the frequencies of the initial segments  $t \in [0, \Delta t)$  of chaotic orbits at  $I_1^0$  giving  $\nu_1(I_1^0) \approx (\sqrt{5} - 1)/2 + I_1^0/100$  for  $I_1^0 \in [0.3, 0.6]$ , in accordance with Eq. (3.8). While the first approach is to measure the transport along the channel via  $\nu_1$ , the frequencies  $(\nu_1, \nu_2)$  are not independent of each other within the channel. This is for instance visible in the vicinity of the  $-4 : 3 : 0$  resonance in Fig. A.2 around  $(\nu_1, \nu_2) \approx (0.624, 0.832)$ . There the fast motion is not directed along  $\nu_2$  anymore but rather perpendicular to the resonance line  $-4 : 3 : 0$ . Thus, the fast motion in this region affects both frequencies. Note that the transition from the resonance  $0 : 6 : 5$  to  $-4 : 3 : 0$  is again governed by transport across partial barriers, see Sec. 4.2. It should be emphasized that in this particular case this transition also causes higher frequencies  $\nu_1$ , i.e. seemingly a transport along the resonance channel towards the chaotic sea. This is also seen in the action coordinates  $I_1$  and  $\tilde{I}_1$  in Figs. A.1(a) and A.1(b), where the resonance  $-4 : 3 : 0$  appears as a period-6 island chain above the black line. This observation introduces the possibility that the trapping mechanism described in Sec. 4.3 might also explain the trapping in the generic sticky regions.

The general problem of measuring the transport along the channel is the inhomogeneity of the coefficients in combination with the limited accuracy of the measurement as discussed at the end of Sec. 4.6.3. In the following some numerical results for the transport along the resonance channel  $0 : 6 : 5$  are outlined in order to highlight these challenges. The calculations have been performed for several positions along the channel but the discussion uses only one position as prototypical example. The initial region at  $I_1^0 = 0.52$  is chosen, see Eq. (4.24), as the drift coefficient fluctuates less at this position and is exclusively positive according to Fig. 4.20(b). In order to allow a comparison between the frequency and action coordinates, the actions are averaged over segments of length  $\Delta t$  like the frequencies, see Eq. (2.18). The first segment  $t \in [0, \Delta t)$  is considered to scatter the chaotic orbits uniformly over the stochastic layer and therefore neglected. The next segment  $t \in [\Delta t, 2\Delta t)$  is considered to be the initial condition with  $t = 0$ . In Figs. A.3 and A.4 the results are shown for  $\Delta t = 1024$  and  $\Delta t = 4096$ ,

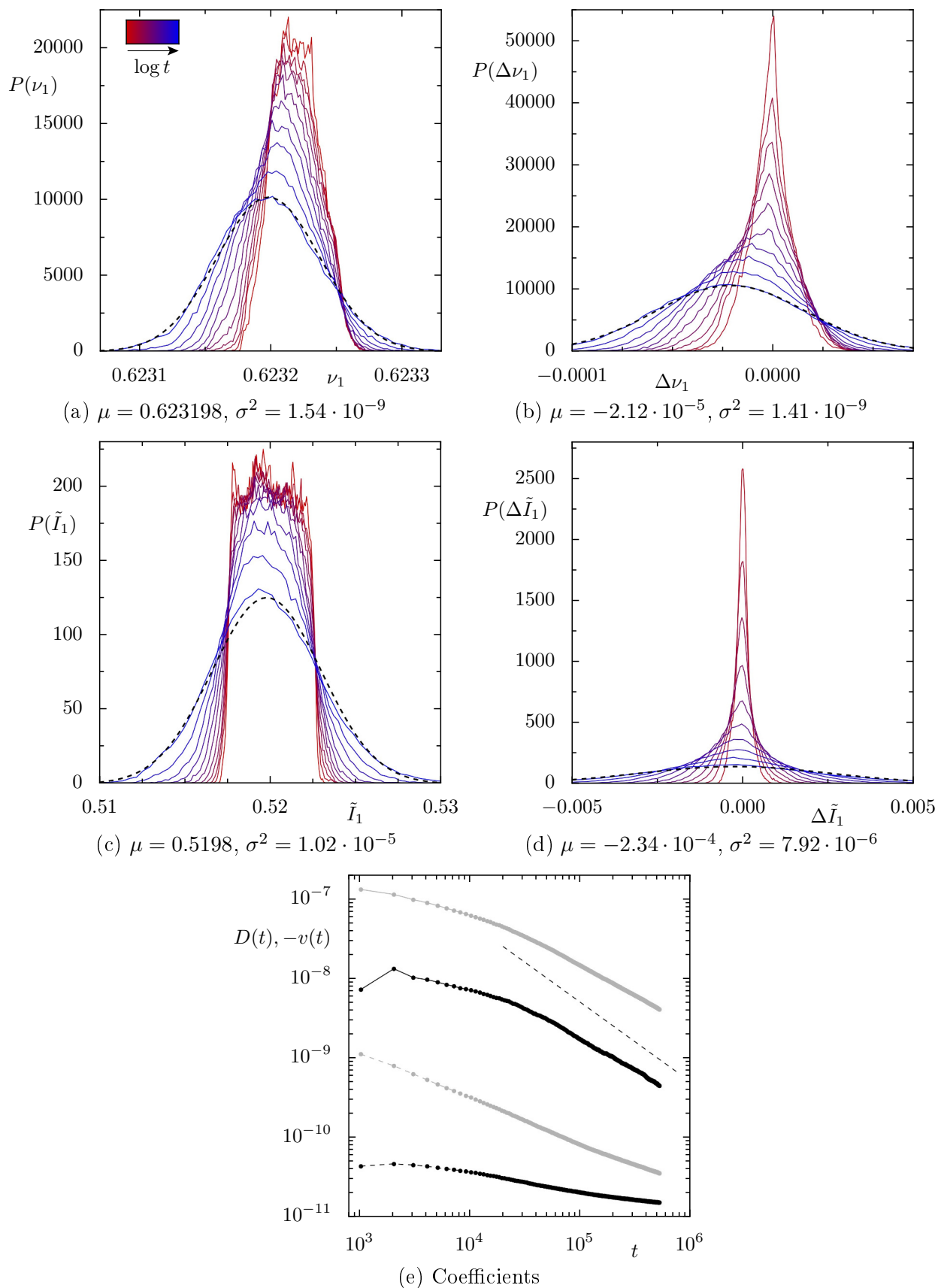


**Figure A.3:** Transport along resonance channel  $0 : 6 : 5$  at  $I_1^0 = 0.52$  for 100020 chaotic orbits iterated  $\Delta t$  in advance and then  $t \in [0, 524287)$ , each decomposed into segments of length  $\Delta t = 1024$ . (a)-(d) Distributions at times  $t = i\Delta t$ ,  $i \in \{0, 1, 2, 4, \dots, 512\}$  (or  $i \in \{1, \dots, 512\}$ , red to blue) with  $\Delta x(t) = x(t) - x(0)$ ,  $x \in \{\nu_1, \tilde{I}_1\}$  (continue on Fig. A.4).

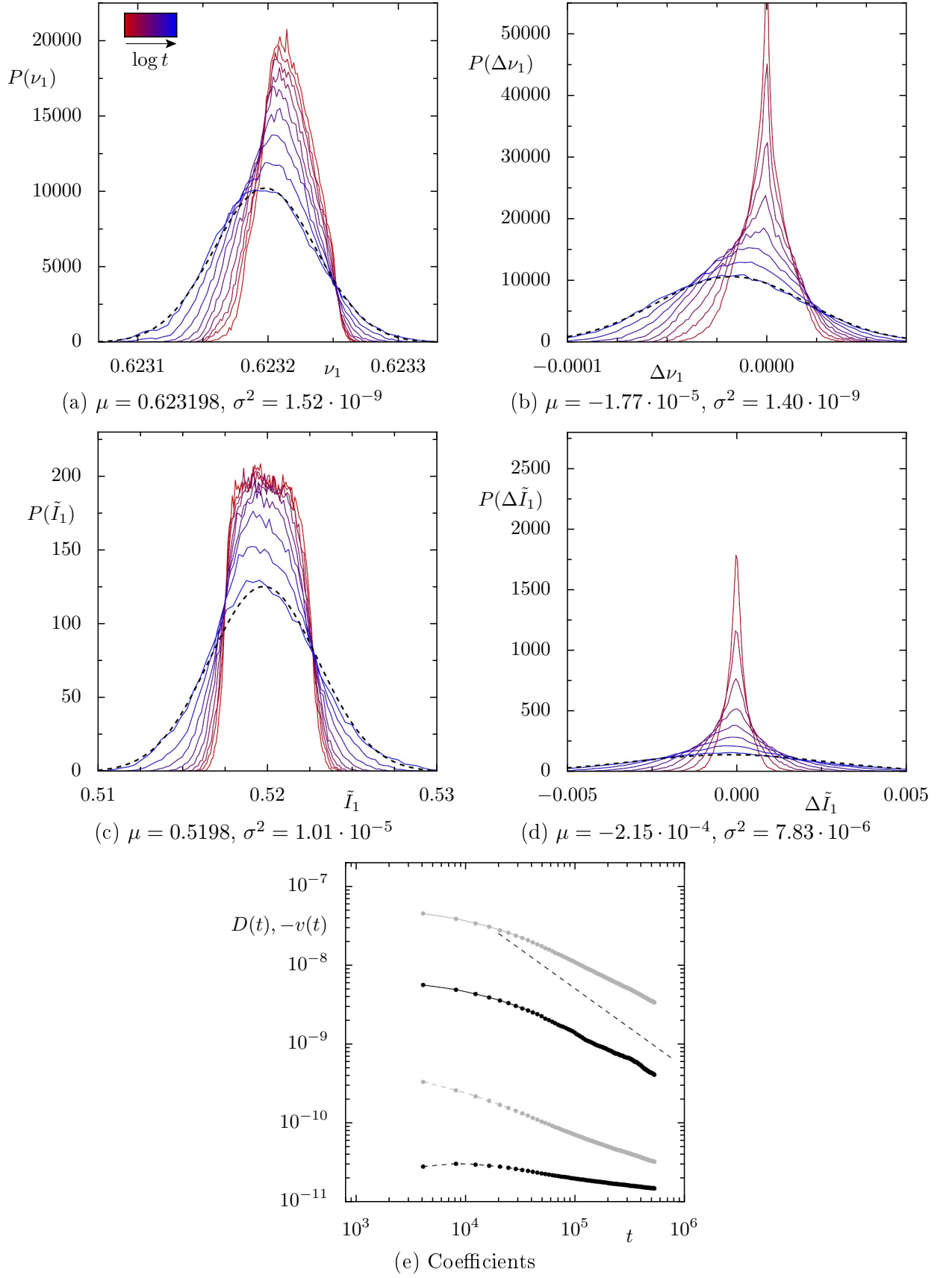


**Figure A.4:** Analogous to Fig. A.3 with  $\Delta t = 4096, i \leq 128$ , i.e. same final time for both Figs. A.3 and A.4. (continue from Fig. A.3) Distributions normalized. Gaussian with mean  $\mu$  and variance  $\sigma^2$  from final segment shown as dashed line. (e) Diffusion  $D(t)$  (dashed line) and negative drift  $-v(t)$  (solid line) Eq. (A.2) for  $\tilde{I}_1$  (black) and  $\nu_1$  (gray, additional factor 100,  $100^2$  for  $v, D$ ). The dashed straight line represents  $\sim t^{-1}$ .

respectively. The results are similar in both cases demonstrating that the measurement is relatively independent of  $\Delta t$ . In Figs. A.3(a) and A.3(b) the distributions  $P(\nu_1)$ ,  $P(\Delta\nu_1)$  for the frequency  $\nu_1(t)$  and the frequency change  $\Delta\nu_1(t) = \nu_1(t) - \nu_1(0)$  are displayed. The corresponding iteration time  $t$  is encoded in color as indicated by the color bar in Fig. A.3(a). In Figs. A.3(c) and A.3(d) the analogous results for the adapted action  $\tilde{I}_1$  are shown. Most of the time the distributions are not Gaussian. Especially at short times the distributions in Figs. A.3(a) and A.3(c) look like plateaus with widths  $d\nu_1 \approx 5 \cdot 10^{-5}$  and  $d\tilde{I}_1 \approx 5 \cdot 10^{-3}$ , respectively. The factor 100 between these widths is consistent with Eq. (3.8). The reason for this finite spatial resolution is discussed for  $\tilde{I}_1$  in the context of Fig. A.1, i.e. the incomplete decoupling of the two degrees of freedom. However, it is unclear how this affects the frequency  $\nu_1$  as the frequencies should decouple for an uncoupled resonance  $0 : 6 : 5$ . In any case, the drift  $v$  and diffusion coefficients  $D$  can only be computed according to Eqs. (4.4) and (4.5) for  $t > 0$

$$v(t) = \frac{1}{t} \mathbb{E}[x(t) - x(0)] \quad D(t) = \frac{1}{2t} \mathbb{E}[(x(t) - x(0))^2] . \quad (\text{A.2})$$

with  $x = \nu_1, \tilde{I}_1$ , if the distributions are Gaussian. Nevertheless as a demonstration, the coefficients are computed with respect to the initial segment and displayed in Fig. A.3(e). The results for  $\tilde{I}_1$  and  $\nu_1$  are displayed with black and gray points, respectively, where the results for the drift coefficient are connected with solid lines and for the diffusion coefficient with dashed lines. In particular, the coefficients  $D$  and  $v$  for the frequency  $\nu_1$  are multiplied with  $100^2$  and  $100$ , respectively, to relate them to the actions according to Eq. (3.8). Despite this, the coefficients obtained from actions and frequencies differ up to an order of magnitude. Note however, that for some reason multiplying the drift for the frequency only with 10 makes the drift results almost coincide. All coefficients have in common that they are not constant over time but decrease with increasing distance to the initial segment. For comparison the power-law decay  $\sim t^{-1}$  is indicated as dashed line. In case the measured transport is a sum of a time-constant error, e.g., due to the finite precision of the coordinates, and the actual transport, the coefficients should decay with this power law and converge to the correct values over time. Such a  $t^{-1}$ -decay has been observed at other position along the channel. Of course already the non-Gaussian shape of the initial distributions makes the meaning of the obtained coefficients questionable. In particular, the drift is negative, i.e. directed away from the chaotic sea and opposite to the prediction in Sec. 4.6.3. In case of the frequency this drift is even visible in the distributions. The distributions for the adapted action have a slight asymmetry which seems to cause the negative drift. However, for long times this drift is regularly observed change to a positive drift, see for instance Fig. A.5(e) in



the following. In particular, for measurements closer to the chaotic sea  $I_1^0 \in [0.6, 1.0]$  positive drifts are also obtained for shorter times.

At longer times all distributions seem to approach Gaussian form. This is illustrated by the Gaussian fits of the final distribution at  $t = 512 \cdot 1024 = 128 \cdot 4096 = 524288$  indicated by the dashed curve. The corresponding mean  $\mu$  and variance  $\sigma^2$  written in the subcaptions match very well between Figs. A.3 and A.4 demonstrating the independence of the results from  $\Delta t$ . In Fig. A.5 the transport is measured in principle by using the final distribution of Fig. A.4 as initial ensemble. More precisely, about  $10^6$  chaotic orbits from  $I_1^0 = 0.52$  iterated for 524288 are used as initial ensemble. While the distributions in Figs. A.5(a) and A.5(c) resemble Gaussians, the distributions of  $\Delta\nu_1$  and  $\Delta\tilde{I}_1$  in Figs. A.5(b) and A.5(d) on which the transport coefficients are based, look considerably different. For all times they exhibit sharp peaks around 0 which reach for short times up to ten times the height of the figures. Such peaks are already visible for the setup of Figs. A.3 and A.4. For some positions along the channel chaotic orbits whose frequencies stay close to the resonance line  $0.833 < \nu_1(t) < 0.83375, \forall t$  are observed to produce distributions without such peaks, while the remaining orbits still exhibit this feature. Thus, the peaks are attributed to the fact that the chaotic orbits regularly visit adjacent higher-order resonances, see Fig. A.2, at which the transport along the channel is much slower than at the resonance  $0 : 6 : 5$ . The diffusion coefficients in Fig. A.5(e) are very similar to the ones in Fig. A.4(e). The magnitude of the drift coefficients however is much smaller. In particular, the drift for the action  $\tilde{I}_1$  is positive and increasing over time, while the dip at the end of the still negative drift for the frequency  $\nu_1$  indicates that also this value is about to change sign for longer times. While these indications of a drift towards the chaotic sea are closer to the predictions of Fig. 4.20, the results are still very problematic. Firstly, both diffusion and drift coefficients are far from being constant over time. Secondly, the used distributions in Figs. A.5(b) and A.5(d) are still not Gaussian. Thirdly, the ensemble in Fig. A.5 is spread so far along the channel that according to Fig. 4.20 a superposition of many different transport coefficients is expected anyway. Due to the last point longer iteration times are not a real option to improve the measurement. Also other positions along the channel do not seem to solve this problem as slower transport allows for longer iteration times, but requires also more accurate measurements. Designing another convenient, near-integrable system to measure the transport in is non-trivial as its channels still have to exhibit the generic widening towards the chaotic sea. However, systems allowing a semi-analytical estimate of the transport coefficients might be a solution [66] or measuring the transport with novel normal form approaches [39]. The adjacent resonances should be easily identified by frequency analysis in case they pose a problem. In order to make the frequency analysis

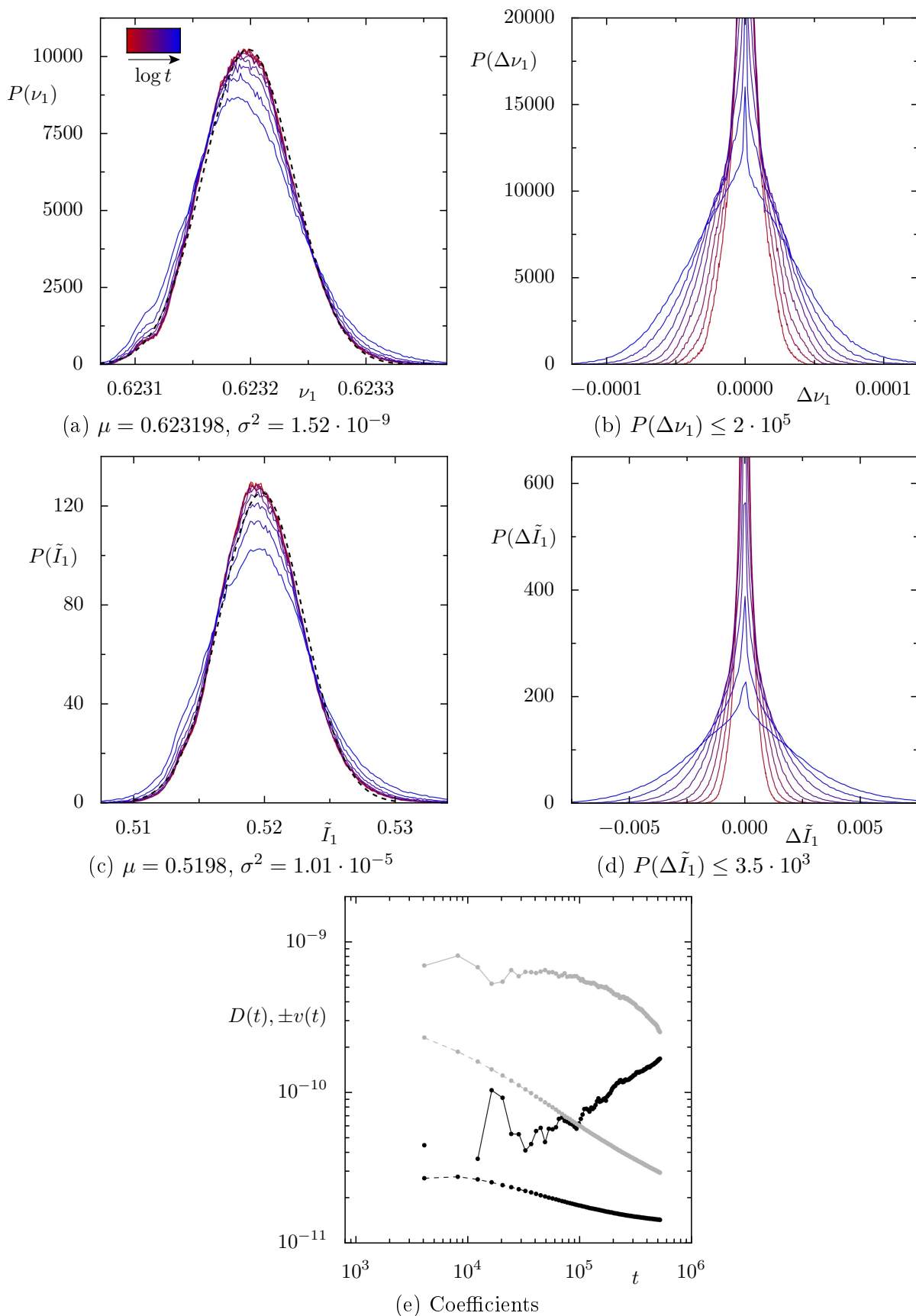


**Figure A.5:** Transport along resonance channel  $0 : 6 : 5$  analogous to Figs. A.3 and A.4 for 1000020 chaotic orbits with  $\Delta t = 4096$  with are iterated initially for  $128\Delta t$ , i.e. the initial distributions in (a), (b) correspond to the final ones of Fig. A.4 (a), (b). Note that in (e) the drift for  $\nu_1$  is negative and for  $\tilde{I}_1$  positive.

more reliable for measuring transport, its accuracy for diffusing chaotic orbits should be investigated using designed time series. The issue of the heterogeneity of the transport coefficients may be overcome by examining designed heterogeneous stochastic processes, i.e. comparing their probability distributions and coefficients in terms of Eq. (A.2) to the results within the channel.

Finally, some numerical features of the measurement of the volume  $V(I_1^0)$  of the stochastic layer, presented in Sec. 4.6.3, are outlined in the following. In Figs. A.6(a) and A.6(b) the dependence of the estimated volume  $V(I_1^0)$  on the resolution  $N$  of the used grid and on the iteration time  $\hat{t}$  of the chaotic orbits, respectively, is shown. In Fig. A.6(a) the estimated volume at  $I_1^0 = 0.3$  is marked with colored points connected by a solid line. The colors red, green, and blue correspond to the used iteration time  $\hat{t} = \{3000, 6000, 9000\}$ . For all of these three cases, the volume  $V(N)$  quickly converges from above to a finite value for increasing  $N$ . However, note that the volume still slowly decreases with increasing  $N$ , e.g., for  $\hat{t} = 3000$  the volume  $V(N)$  decreases from  $N = 1100$  to  $N = 1500$  seemingly linear by 1.7%. Also the volume  $V(N)$  increases with  $\hat{t}$  for constant  $N$ . In Fig. A.6(b) the volume  $V(\hat{t})$  is shown for  $I_1^0 = 0.4$  and  $N = 500$  with black points connected by a solid line. In the half-logarithmic plot these points almost lie on a straight line suggesting a logarithmic dependence  $V(\hat{t}) \sim \log \hat{t}$ . The slope of this line is observed to depend on  $I_1^0$  and not shown here. For comparison the method described in Sec. 4.6.3 is used to estimate the volume of the stochastic layer of the resonance  $\nu = 2/3$  for the 2D standard map with  $K = 0.7$ . In contrast to Sec. 2.3 the domains are  $p \in [0, 1)$  and  $q \in [-0.5, 0.5)$ , the initial points are uniformly chosen in  $\{(p, q) : p = 4.412/(2\pi), |q| < 5 \cdot 10^{-3}\}$ , and the resulting 2D volume is multiplied by  $2\pi$  to make it comparable to the 3D stochastic layer from the 4D map  $F_{\text{Twist}}$ . The results of the 2D map are shown in Figs. A.6(a) and A.6(b) as points connected by a dashed line. Features analogous to the case of the 4D map are observed. In particular, the increase of  $V(\hat{t})$  for the stochastic layer of the 2D map looks very close to being logarithmic. In Figs. A.6(c) and A.6(d) the distribution of the volume of the stochastic layer over the two angles is shown for different positions  $I_1^0$  along the resonance channel  $0 : 6 : 5$  of the map  $F_{\text{Twist}}$ . The volume  $V(\Omega_{ij})$  at each grid point  $\Omega_{ij}$  is known from Eq. (4.28)

$$V(\Omega_{ij}) = 2\sqrt{3} \left( \frac{2\pi}{N} \right)^2 \left( \sigma_{\Omega_{ij}^3}^{\text{up}}(I_1^0) + \sigma_{\Omega_{ij}^3}^{\text{lo}}(I_1^0) \right) . \quad (\text{A.3})$$

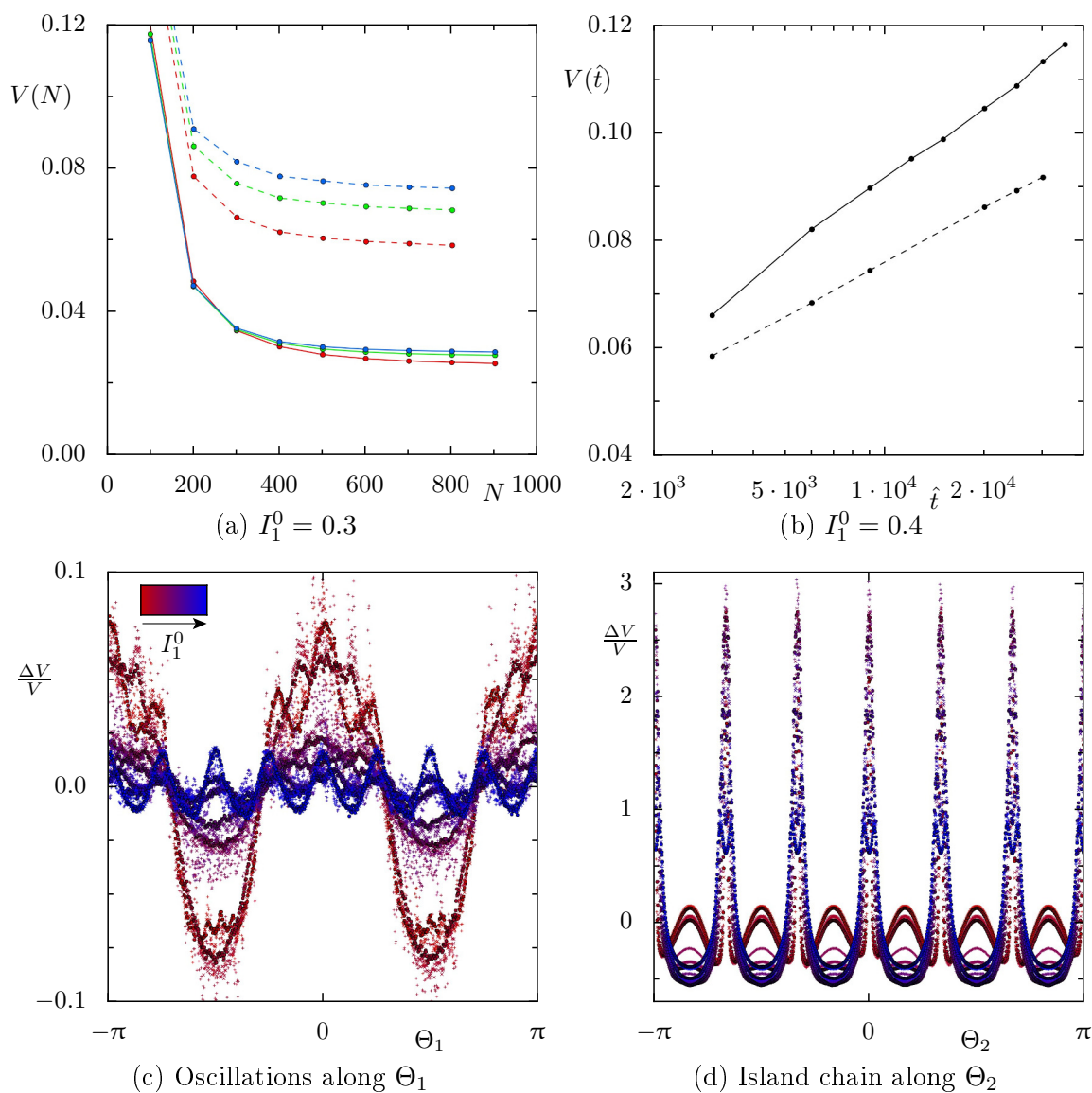


**Figure A.6:** Sensitivity of 3D volume  $V(I_1^0)$  of the stochastic layer of a resonance channel on parameters of algorithm, see Sec. 4.6.3, for the resonance channel  $0 : 6 : 5$ . In (a),(b) additionally the results for the resonance  $\nu = 2/3$  of the 2D standard map with  $K = 0.7$ , see text, are shown as points connected by dashed lines. (a)  $V(N)$  for resolution  $N$  of the grid with  $I_1^0 = 0.3$  and  $\hat{t} \in \{3000, 6000, 9000\}$  (red, green, blue). (b)  $V(\hat{t})$  for the maximal iteration time  $\hat{t}$  with  $I_1^0 = 0.4$  and  $N = 500$  ( $N = 800$  for 2D map). (c), (d) Relative deviation from the average volume per angle  $\Delta V/V$ , see Eq. (A.5), along  $\Theta_1$ ,  $\Theta_2$ . The position along the channel  $I_1^0 \in \{0.3, 0.35, 0.4, 0.45, 0.5, 0.55, 0.6\}$  is encoded by color (red to blue), and for  $\hat{t} \in \{3000, 6000, 9000\}$  the symbols  $+$ ,  $\times$ ,  $\circ$  are used of which mostly the last one is visible as dark dots.

and can be summed up over one of the angles, e.g.,

$$V(\Theta_1 = \theta_i) = \sum_{j=0}^{N-1} V(\Omega_{ij}) . \quad (\text{A.4})$$

For the distributions in Figs. A.6(c) and A.6(d) the relative deviation from the average volume per angle is used, e.g.,

$$\frac{\Delta V}{V}(I_1^0, \Theta_1 = \theta_i) = \frac{N \cdot V(\Theta_1 = \theta_i) - V(I_1^0)}{V(I_1^0)} \quad (\text{A.5})$$

with  $V(I_1^0)$  from Eq. (4.28). In both figures the points are colored according to their position  $I_1^0$  along the channel according to the colorbar displayed in Fig. A.6(c) and for the used iteration time  $\hat{t} = \{3000, 6000, 9000\}$  the symbols +, ×, and circle are used, respectively. The points for all three iteration times appear so close to each other in Fig. A.6(d) that they are not distinguishable in the plot. In Fig. A.6(c) the symbols + and × appear as small points scattered around the big circles for  $\hat{t} = 9000$ . These circles reveal oscillations of the volume along the angle  $\Theta_1$  whose phase and period change along the channel and are not yet understood. The amplitude of these oscillations decreases towards the chaotic sea but is overall small with 2 – 8%. In contrast, Fig. A.6(d) displays peaks with up to 300% coinciding with the approximate position of the hyperbolic 1D tori at  $|\Theta_2| \sim \{0, \pi/3, 2\pi/3, \pi\}$  in between the islands. These peaks seem to be relatively independent of the position  $I_1^0$  along the channel. In contrast, the values for the intervals in between vary, ranging from –60 to 10%. Similar results are obtained for the example of the resonance  $\nu = 2/3$  of the 2D map, where three peaks are observed with amplitudes up to 1000% and values in between the peaks as low as –40%. In conclusion, the distribution of the volume of the stochastic layer along the angle  $\Theta_2$  affected by the resonance shows the same features as for the 2D map. Along the other angle  $\Theta_1$  the volume is relatively evenly distributed with some oscillations.

## A.2 Model for channel transport

In Sec. 4.6.2 the drift and diffusion for transport along a 2D channel with varying width are derived as one model for the drift along a resonance channel. In this section, the drift for the case of finite transport perpendicular to the channel is derived and the consistency with Eq. (4.23) for this transport being large is shown. These results are confirmed numerically using an Euler-Maruyama-scheme. It is also numerically shown

that the expression for the drift Eq. (4.23), derived in Sec. 4.6.2 assuming a single, finite time step  $\Delta t$  with a uniform distribution, works for  $\Delta t \rightarrow 0$  and for a Gaussian distribution. In particular, for the setting of Sec. 4.6.2 drift and probability distributions are discussed for more than one time step. While the numerical results are omitted for brevity the method to obtain them is outlined.

The setting is a symmetric channel  $\Omega \subset \mathbb{R}^2$  in action space, i.e.

$$\Omega = \{(I_1, I_2) : I_2 \in [-b(I_1), b(I_1)]\} .$$

For a time step  $\Delta t$  an initial condition  $(I_1^0, I_2^0) \in \Omega$  is uniformly mapped into the region

$$\begin{aligned} \Omega_{\Delta t}(I_1^0, I_2^0) &= \Omega_{\Delta t}^0(I_1^0, I_2^0) \cap \Omega \\ \Omega_{\Delta t}^0(I_1^0, I_2^0) &= \{(I_1, I_2) : |I_1 - I_1^0| \leq \Delta I_1(I_1^0), |I_2 - I_2^0| \leq \Delta I_2(I_1^0)\} . \end{aligned}$$

A reasonable assumption for such a channel is small transport along the channel  $\Delta I_1(I_1^0) \ll 1$ , such that the approximation  $b(I_1) \approx b(I_1^0) + b'(I_1^0)(I_1 - I_1^0)$  can be used. Without loss of generality it is assumed  $b'(I_1^0) > 0$ . Furthermore, a broad channel  $\Delta I_2(I_1^0) \ll b(I_1^0)$  whose width is slowly varying  $b'(I_1^0) \leq \Delta I_2(I_1^0)/\Delta I_1(I_1^0)$  is assumed. Thus, within an ensemble of chaotic initial conditions  $\Omega_0(I_1^0) \subset \Omega$

$$\Omega_0(I_1^0) = \{(I_1, I_2) : I_1 = I_1^0\} \cap \Omega$$

there are three kind of distinct initial conditions  $(I_1^0, I_2^0) \in \Omega_0(I_1^0)$ . Due to the symmetry of the channel, only points with  $I_2^0 > 0$  are discussed: Firstly, for points for which  $\Omega_{\Delta t}^0(I_1^0, I_2^0) \subset \Omega$  the corresponding drift  $v_1(I_1^0, I_2^0)$  is zero according to Eq. (4.4)

$$v_1(I_1^0, I_2^0) = \frac{\int_{I_1^0 - \Delta I_1(I_1^0)}^{I_1^0 + \Delta I_1(I_1^0)} dI_1 (I_1 - I_1^0) \int_{I_2^0 - \Delta I_2(I_1^0)}^{I_2^0 + \Delta I_2(I_1^0)} dI_2}{V(\Omega_{\Delta t}^0(I_1^0, I_2^0))\Delta t} = 0$$

where  $V(\tilde{\Omega})$  denotes the area of a set  $\tilde{\Omega}$ . Secondly, points for which the edge of the channel intersects with the edges of  $\Omega_{\Delta t}^0(I_1^0, I_2^0)$  at the two points

$$\begin{aligned} (I_1^{c1}, b(I_1^{c1})) &= (b^{-1}(I_2^0 + \Delta I_2(I_1^0)), I_2^0 + \Delta I_2(I_1^0)) \\ (I_1^{c2}, b(I_1^{c2})) &= (I_1^0 - \Delta I_1(I_1^0), b(I_1^0 - \Delta I_1(I_1^0))) . \end{aligned}$$

For such points the corresponding drift  $v_2(I_1^0, I_2^0)$  reads

$$v_2(I_1^0, I_2^0) = \left( \int_{I_1^0 - \Delta I_1(I_1^0)}^{I_1^{c1}} dI_1 (I_1 - I_1^0) \int_{I_2^0 - \Delta I_2(I_1^0)}^{b(I_1)} dI_2 \right. \\ \left. + \int_{I_1^{c1}}^{I_1^0 + \Delta I_1(I_1^0)} dI_1 (I_1 - I_1^0) \int_{I_2^0 - \Delta I_2(I_1^0)}^{I_2^0 - \Delta I_2(I_1^0)} dI_2 \right) \\ / (V(\Omega_{\Delta t}(I_1^0, I_2^0))\Delta t) .$$

Thirdly, points for which the edge of the channel intersects with the edges of  $\Omega_{\Delta t}^0(I_1^0, I_2^0)$  at the two points

$$(I_1^{s1}, b(I_1^{s1})) = (I_1^0 + \Delta I_1(I_1^0), b(I_1^0 + \Delta I_1(I_1^0))) \\ (I_1^{s2}, b(I_1^{s2})) = (I_1^0 - \Delta I_1(I_1^0), b(I_1^0 - \Delta I_1(I_1^0))) .$$

For such points the corresponding drift  $v_3(I_1^0, I_2^0)$  reads

$$v_3(I_1^0, I_2^0) = \frac{\int_{I_1^0 - \Delta I_1(I_1^0)}^{I_1^0 - \Delta I_1(I_1^0)} dI_1 (I_1 - I_1^0) \int_{I_2^0 - \Delta I_2(I_1^0)}^{b(I_1)} dI_2}{V(\Omega_{\Delta t}(I_1^0, I_2^0))\Delta t} .$$

The drift  $v(I_1^0)$  for the ensemble of initial conditions  $\Omega_0(I_1^0)$  then reads

$$v(I_1^0) = 2 \left( \int_{b(I_1^0 - \Delta I_1(I_1^0)) - \Delta I_2(I_1^0)}^{b(I_1^0 + \Delta I_1(I_1^0)) - \Delta I_2(I_1^0)} dI_2^0 v_2(I_1^0, I_2^0) \right. \\ \left. + \int_{b(I_1^0 + \Delta I_1(I_1^0)) - \Delta I_2(I_1^0)}^{b(I_1^0)} dI_2^0 v_3(I_1^0, I_2^0) \right) / (2b(I_1^0)) \\ = v_2(I_1^0) + v_3(I_1^0) \tag{A.6}$$

After a cumbersome but straightforward evaluation of this expression, it is obtained for the term  $v_2(I_1^0)$  due to the contribution of  $v_2(I_1^0, I_2^0)$

$$v_2(I_1^0) = -\frac{1}{3b\Delta t} (4b'\Delta I_1^2 - 4\Delta I_1\Delta I_2 \ln(1 - B) \\ + 3\sqrt{2b'\Delta I_1^3\Delta I_2} \ln\left(\frac{1 - \sqrt{B}}{1 + \sqrt{B}}\right)) \tag{A.7}$$

and for the term  $v_3(I_1^0)$  due to the contribution of  $v_3(I_1^0, I_2^0)$

$$v_3(I_1^0) = \frac{b' \Delta I_1^2}{3b \Delta t} \ln(2(1 - B)) \quad (\text{A.8})$$

where

$$B = \frac{b' \Delta I_1}{2 \Delta I_2} \quad (\text{A.9})$$

and the  $I_1^0$  dependence of the entities  $b(I_1^0)$ ,  $b'(I_1^0)$ ,  $\Delta I_1(I_1^0)$ , and  $\Delta I_2(I_1^0)$  is dropped for brevity. For  $\Delta I_2(I_1^0) \gg \Delta I_1(I_1^0)$ , i.e.  $B \ll 1$ , these expressions are in lowest order

$$v_2(I_1^0) = -\frac{1}{3b \Delta t} (4b' \Delta I_1^2 + 2b' \Delta I_1^2 - 6b' \Delta I_1^2) = 0 \quad (\text{A.10})$$

$$v_3(I_1^0) = \frac{b' \Delta I_1^2}{3b \Delta t} \ln(2) \quad (\text{A.11})$$

While the limit  $\Delta I_2(I_1^0) \gg b(I_1^0)$  is equivalent to the setting in Sec. 4.6.2, the drift here  $v(I_1^0) = v_3(I_1^0)$  has in comparison with Eq. (4.21) an additional factor  $\ln(2)$ . This deviation can be explained by the fact that the above expression is only valid up to  $\Delta I_2(I_1^0) \sim b(I_1^0)$ , i.e. when initial conditions  $(I_1^0, I_2^0) \in \Omega_0(I_1^0)$  start to exist for which  $\Omega_{\Delta t}^0(I_1^0, I_2^0)$  is intersected by both borders of the channel. On the other hand, Eq. (4.21) is only beginning to be valid around  $\Delta I_2(I_1^0) \sim 2b(I_1^0)$ , when for all initial conditions  $\Omega_{\Delta t}^0(I_1^0, I_2^0)$  is intersected by both borders of the channel. The numerics nicely show the transition between these two domains. The transition is even visible for a Gaussian distribution with the same diffusion coefficient as the uniform distribution, i.e. for the corresponding Euler-Maruyama-scheme.

In the following the performed but for brevity not presented numerics are outlined. A stochastic process as described by a Fokker-Planck equation Eq. (4.3) is numerically realized by the Euler-Maruyama-scheme for which the Ito stochastic differential equation corresponding to Eq. (4.3) reads [203]

$$dx = v(x, t)dt + \sqrt{2D(x, t)}dW \quad (\text{A.12})$$

with the differential  $dW$  of a Wiener process, and is used to map a point  $x(t)$  over a finite time step  $\Delta t$  to a point  $x(t + \Delta t) = x(t) + \Delta x(t)$  with

$$\Delta x(t) = v(x(t), t)\Delta t + \sqrt{2D(x(t), t)\Delta t} \mathcal{N}(0, 1) \quad (\text{A.13})$$



where  $\mathcal{N}(0, 1)$  is a normal random variable with expectation value zero and variance one. Using Eq. (A.13) the stochastic process can be performed on an ensemble of initial conditions. Then, stochastic properties, like the probability distribution, diffusion, and drift, can be extracted from the ensemble in order to double-check the analytical solutions of the Fokker-Planck equation. An absorbing barrier is realized by removing members of the ensemble when they cross this barrier. It always has to be checked that for a fixed target time  $t_{\max} > t$ ,  $t_{\max} = n \cdot \Delta t$ ,  $n \in \mathbb{N}$  these numerical results are stable for  $\Delta t \rightarrow 0$ . For a uniform distribution, e.g., as assumed for the derivation of Eq. (4.23), the second term in Eq. (A.13) is replaced by  $\Delta I_i \mathcal{U}([-1, 1])$ ,  $i \in \{1, 2\}$ , using the notation of this section, with a uniform random  $\mathcal{U}([-1, 1])$  variable in the interval  $[-1, 1]$ . By using the diffusion coefficient  $D_i(I_1^0) = \Delta I_i(I_1^0)^2 / (6\Delta t)$  from Eq. (4.22) this term reads  $\sqrt{6D_i(I_1^0)\Delta t} \Delta \mathcal{U}([-1, 1])$ . In order to simulate the finite channel, every time a point of the ensemble would be mapped to the outside of the channel, this point is not mapped but instead the uniform random variable is drawn again. By this the prediction for the transition of the drift mentioned above for  $I_2(I_1^0) \rightarrow \infty$  is numerically confirmed for a single iteration of the Ito stochastic differential equation. This transition is also observed with the Gaussian distribution Eq. (A.13) with the same diffusion coefficients  $D_i(I_1^0) = \Delta I_i(I_1^0)^2 / (6\Delta t)$ ,  $i = 1, 2$ .

For the setting of Sec. 4.6.2 and Eq. (4.21) also the probability distribution after the first and second time step  $\Delta t$ ,  $2\Delta t$  is presented and it is analytically shown that the drift stays the same after two time steps. The initial probability density along the channel is  $\rho_0(I_1) = \delta(I_1 - I_1^0)$  and consequently after the first time step  $\Delta t$  it is

$$\rho_{\Delta t}(I_1) = \frac{2b(I_1)}{2 \int_{I_1^0 - \Delta I_1(I_1^0)}^{I_1^0 - \Delta I_1(I_1^0)} d\tilde{I}_1 b(\tilde{I}_1)} \mathbb{I}_{\Omega_{\Delta t}} = \frac{b(I_1^0) + b'(I_1^0)(I_1 - I_1^0)}{2b(I_1^0)\Delta I_1(I_1^0)} \mathbb{I}_{\Omega_{\Delta t}}. \quad (\text{A.14})$$

Furthermore, for a sufficiently slow transport along the channel one may assume a constant derivative  $b'(I_1) = b'(I_1^0)$  and a constant transport  $\Delta I_1(I_1) = \Delta I_1(I_1^0) = \Delta I_1$ . Hence, while the drift  $v_{\Delta t}(I_1^0)$  after the first time step is expressed by Eq. (4.21), the

drift  $v_{2\Delta t}(I_1^0)$  after the second time step reads

$$\begin{aligned}
v_{2\Delta t}(I_1^0) &= \frac{1}{2\Delta t} \int dI_1 (v_{\Delta t}(I_1)\Delta t + I_1 - I_1^0) \Delta t \rho_{\Delta t}(I_1) \\
&= \frac{\int_{I_1^0 - \Delta I_1}^{I_1^0 + \Delta I_1} dI_1 \left( \frac{1}{3} b'(I_1^0) \Delta I_1^2 + b(I_1^0)(I_1 - I_1^0) + (I_1 - I_1^0)^2 b'(I_1^0) \right)}{4b(I_1^0)\Delta I_1\Delta t} \\
&= \frac{b'(I_1^0)}{b(I_1^0)} \frac{\Delta I_1^2}{3\Delta t}
\end{aligned} \tag{A.15}$$

which is the same as  $v_{\Delta t}(I_1^0)$ . The probability density  $\rho_{2\Delta t}(I_1)$  after the second time step reads with  $|I_1 - I_1^0| \leq 2\Delta I$

$$\begin{aligned}
\rho_{2\Delta t}(I_1) &= \int_{I_1 - \Delta I_1}^{I_1 + \Delta I_1} d\tilde{I}_1 \rho_{\Delta t}(\tilde{I}_1) \text{prob}(\tilde{I}_1 \rightarrow I_1) \\
&= \int_{I_1 - \Delta I_1}^{I_1 + \Delta I_1} d\tilde{I}_1 \rho_{\Delta t}(\tilde{I}_1) \left( \frac{b(\tilde{I}_1) + (I_1 - \tilde{I}_1)b'(I_1^0)}{2b(\tilde{I}_1)\Delta I_1} \right) \\
&= \frac{b(I_1^0) + (I_1 - I_1^0)b'(I_1^0)}{2b(I_1^0)\Delta I_1} \left( 1 - \frac{|I_1 - I_1^0|}{2\Delta I_1} \right).
\end{aligned} \tag{A.16}$$

The probability for one time step Eq. (A.14) can be used to simulate the transport along the channel numerically, i.e. to map an initial condition  $I_1^0$  to  $I_1$  after one time step. For this a transformation is employed which maps a uniform distribution  $\rho_{\mathcal{U}([0,1])}(x) = 1$ ,  $x \in [0, 1]$  to  $\rho_{\Delta t}(I_1)$ . According to

$$\rho_{\Delta t}(I_1)dI_1 = \rho_{\mathcal{U}([0,1])}(x)dx = x'(I_1)dI_1$$

the derivative  $x'(I_1) = dx(I_1)/dI_1$  is

$$x'(I_1) = \rho_{\Delta t}(I_1) = \frac{b(I_1^0) + b'(I_1^0)(I_1 - I_1^0)}{2b(I_1^0)\Delta I_1(I_1^0)} \mathbb{I}_{\Omega_{\Delta t}}$$

from which follows by integration

$$x(I_1) = \frac{2b(I_1^0)I_1 + b'(I_1^0)(I_1 - I_1^0)^2}{4b(I_1^0)\Delta I_1(I_1^0)} + C$$

where the constant  $C$  is obtained from the condition  $x(I_1^0 + \Delta I_1) = 1$  (or  $x(I_1^0 - \Delta I_1) = 0$ )

$$C = 1 - \frac{2b(I_1^0)(I_1^0 + \Delta I_1) + b'(I_1^0)\Delta I_1^2}{4b(I_1^0)\Delta I_1}. \quad (\text{A.17})$$

Consequently, for a point at position  $I_1^0$  along the channel a new position  $I_1$  after one time step  $\Delta t$  is obtained by drawing a uniform random variable  $x = \mathcal{U}([0, 1])$  and transform this by

$$I_1(x) = -A \pm \sqrt{A^2 - (I_1^0)^2 + \frac{4b(I_1^0)\Delta I_1 y(x)}{b'(I_1^0)}} \quad (\text{A.18})$$

$$A = \frac{b(I_1^0) - b'(I_1^0)I_1^0}{b'(I_1^0)}$$

with  $y(x) = x - C$ . Choosing the positive sign for the corresponding numerical simulations, the distributions Eqs. (A.14) and (A.16) are checked. Furthermore, it is found that for even more iterations  $n \in N$  and rescaled time, i.e. setting the squared step width for  $n$ -steps  $\Delta I^2(n) = \Delta I^2(n=1)/n$ , the distribution quickly converges to a Gaussian distribution with mean  $\mathbb{E}[I_1(n\Delta t) - I_1^0] \approx b'(I_1^0)/b(I_1^0) \cdot \Delta I_1^2(n)n/(3\Delta t)$ , variance  $\mathbb{E}[(I_1(n\Delta t) - \mathbb{E}[I_1(n\Delta t)])^2] \approx \Delta I_1^2(n)n/3 - \mathbb{E}[I_1(n\Delta t) - I_1^0]^2$  and  $\mathbb{E}[(I_1(n\Delta t) - I_1^0)^2] \approx \Delta I_1^2(n)n/3$ . This implies that the expressions for the diffusion and drift Eqs. (4.22) and (4.23) are valid for  $\Delta t \rightarrow 0$ . Note that for the simulation it has to be ensured that the chosen parameters prevent the ensemble from reaching the tip of the channel, i.e. where the walls meet, as this causes artifacts.

### A.3 Resonances

Resonance channels govern the chaotic dynamics in the vicinity of regular structures, see Sec. 4.1. In particular, the sticky regions of 4D maps consist of a large set of overlapping resonance channels. In view of the relevance of such sets of resonances, some of their number-theoretic properties are presented in this section. An estimate for both the number of resonances and the area covered by their channels is derived with respect to the order of the resonances. These analytic results are shown to describe the numerical results very well. An application of the latter result is illustrated, i.e. to assess up to which order resonances are relevant for the chaotic transport of a system. Moreover, the distances between numerically obtained frequencies and a certain resonance are examined. It is discussed to what extent they contain information about trapping in the deeper class of the resonance.

A resonance condition  $k_1\nu_1 + k_2\nu_2 = k_3$  is defined by the three coefficients  $k_1 : k_2 : k_3$  or  $\mathbf{k} = (k_1, k_2, k_3) \in \mathbb{Z}^3$  with order  $k = |k_1| + |k_2|$ . Two resonance conditions  $\mathbf{k}^1, \mathbf{k}^2 \in \mathbb{Z}^3$  are considered to be equal, if  $\exists c \in \mathbb{Z} : \mathbf{k}^1 = c\mathbf{k}^2$ , see also Appendix A.4. Thus, any resonance condition  $\mathbf{k} \in \mathbb{Z}^3$  is assumed to be reduced to  $\gcd(k_1, k_2, k_3) = 1$ . In this sense, an estimate for the number  $N(k)$  of distinct resonances in the frequency space  $(\nu_1, \nu_2) \in [0, 1) \times [0, 1)$  for a fixed order  $k$  is derived in the following. For brevity of the derivation assume  $k_1, k_2 \neq 0$ , while analogous results are obtained for the special cases  $k_1 = 0$  and  $k_2 = 0$ . A resonance line  $k_1 : k_2 : k_3$  in frequency space can then be expressed by

$$\nu_2(\nu_1) = \frac{k_3}{k_2} - \frac{k_1}{k_2}\nu_1. \quad (\text{A.19})$$

There is a whole set of resonances with identical  $k_1$  and  $k_2$  but distinct  $k_3$ . In order for a resonance to intersect with the frequency space  $(\nu_1, \nu_2) \in [0, 1) \times [0, 1)$  on a non-zero set the following conditions have to be fulfilled

$$\left. \begin{array}{l} \frac{k_1}{k_2} \geq 0 : \quad \left. \begin{array}{l} \nu_2(0) > 0 \rightarrow \frac{k_3}{k_1} > 0 \\ \nu_2(1) < 1 \rightarrow \frac{k_3 - k_2}{k_1} < 1 \end{array} \right\} \rightarrow \left\{ \begin{array}{l} k_2 > 0 : \quad 0 < k_3 < k_1 + k_2 \\ k_2 < 0 : \quad 0 > k_3 > k_1 + k_2 \end{array} \right. \\ \frac{k_1}{k_2} < 0 : \quad \left. \begin{array}{l} \nu_2(0) < 1 \rightarrow \frac{k_3}{k_1} < 1 \\ \nu_2(1) > 0 \rightarrow \frac{k_3 - k_2}{k_1} > 0 \end{array} \right\} \rightarrow \left\{ \begin{array}{l} k_2 > 0 : \quad k_1 < k_3 < k_2 \\ k_2 < 0 : \quad k_1 > k_3 > k_2 \end{array} \right. \end{array} \right\} \quad (\text{A.20})$$

Note that intersection with a non-zero set implies that resonances which only intersect with the frequency space at its corners are not included. The above inequalities can be adjusted to a frequency space  $(\nu_1, \nu_2) \in [0, 1] \times [0, 1]$  which includes the corners by replacing  $<, >$  with  $\leq, \geq$ . The number  $N(k_1, k_2)$  of possible  $k_3$  values for fixed  $k_1, k_2$  are inferred from the inequalities Eq. (A.20)

$$\left. \begin{array}{l} \frac{k_1}{k_2} \geq 0 : \quad N(k_1, k_2) = |k_1 + k_2| - 1 \\ \frac{k_1}{k_2} < 0 : \quad N(k_1, k_2) = |k_1 - k_2| - 1 \end{array} \right\} \boxed{N(k_1, k_2) = |k_1| + |k_2| - 1}. \quad (\text{A.21})$$

From Eq. (A.21) an upper bound for the number  $N(k)$  of resonances of a certain order  $k \geq 1$  can be estimated as

$$\begin{aligned} N_{\max}(k) &= \sum_{k_2=-k+1}^k N(k - |k_2|, k_2) = \sum_{k_2=-k+1}^k (k - 1) = 2k(k - 1) \\ &\Rightarrow \boxed{N(k) \leq 2\delta_{k,1} + 2k(k - 1)} \end{aligned} \quad (\text{A.22})$$

including the Kronecker delta for the two resonances  $1 : 0 : 0$  and  $0 : 1 : 0$ . Note that the upper bound  $N_{\max}(k)$  includes resonances with  $|\gcd(k_1, k_2, k_3)| > 1$ . In particular, any resonance  $k_1 : k_2 : k_3$  with order  $k$  is also included as resonance  $k_1 l : k_2 l : k_3 l$  with order  $kl$  for all  $l \in \mathbb{N}$ . Thus, from the upper bound  $N_{\max}(k)$  the contributions  $N(k')$  with  $k = k'l$ ,  $l \geq 2$  have to be subtracted

$$N(k) = N_{\max}(k) - \sum_{\substack{k' \in \mathbb{N}: \\ \exists l \in \mathbb{N}, l \geq 2: \\ k = k'l}} N(k') . \quad (\text{A.23})$$

The function  $N(k)$  can be computed from Eq. (A.23) in an iterative manner for increasing  $k$ . An obvious lower bound for  $N(k)$  which can be written explicitly is

$$N(k) \geq N_{\max}(k) - \sum_{\substack{k' \in \mathbb{N}: \\ \exists l \in \mathbb{N}, l \geq 2: \\ k = k'l}} N_{\max}(k') .$$

Consider that every resonance of order  $k'$  with  $k = k'l$  where  $l$  is not a prime number, i.e.  $l = l'l''$  with  $l', l'' \geq 2$ , is also considered in  $N_{\max}(k'')$  with  $k'' = k'l''$  since  $k = k'l = k''l''$ . Thus, for a refinement of the lower bound only prime numbers should be considered for  $l$ , i.e. if the prime factorization of  $k$  reads  $k = l_1 l_2 \cdots l_{\max}$  with  $l_i \leq l_j$  for  $i \leq j$

$$\boxed{N(k) \geq N_{\max}(k) - \sum_{\substack{l \text{ prime number} \\ 2 \leq l \leq l_{\max}}} N_{\max}\left(\frac{k}{l}\right)} . \quad (\text{A.24})$$

In Fig. A.7 the upper bound from Eq. (A.22), shown in red, and the lower bound from Eq. (A.24), shown up to different prime numbers, are compared with the actual number  $N(k)$  of resonances, shown by green points, for  $1 \leq k \leq 100$ . The green points are connected by green lines as guide to the eye. It seems that for the lower bound already  $l_{\max} = 2$  or  $l_{\max} = 3$  is sufficient to describe  $N(k)$  up to large orders.

Each resonance line in a 4D symplectic map is surrounded by a resonance channel in which the chaotic transport takes place. Thus, an interesting quantity is the area in frequency space  $(\nu_1, \nu_2) \in [0, 1) \times [0, 1)$  covered by resonance channels of a certain order. The area  $A_{[0,1) \times [0,1)}(\mathbf{k})$  covered by a resonance channel of the resonance  $\mathbf{k} = (k_1, k_2, k_3) \in \mathbb{Z}^3$  can be expressed in terms of the length of the resonance line  $L_{[0,1) \times [0,1)}(\mathbf{k})$  within the frequency space and the width  $2\epsilon(\mathbf{k}, \boldsymbol{\nu})$  of the channel. Assuming  $\epsilon(\mathbf{k}, \boldsymbol{\nu}) = \epsilon(\mathbf{k})$  the

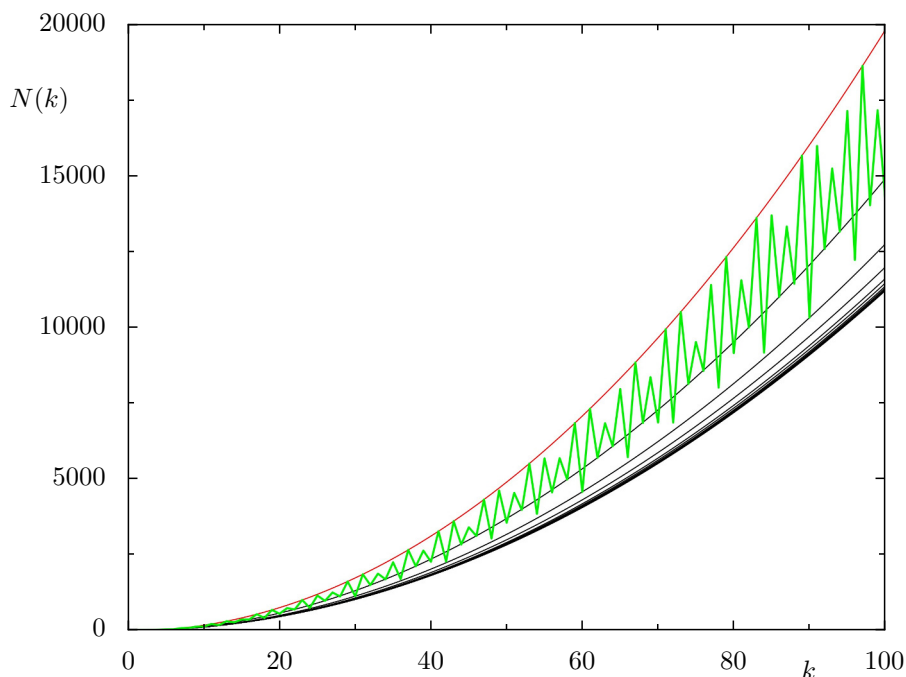


**Figure A.7:** Number  $N(k)$  of unique resonances  $k_1 : k_2 : k_3$  per order  $k = |k_1| + |k_2|$  shown as points connected by green lines for visibility. The upper estimate is shown as red line, see Eq. (A.22). Some lower estimates are shown as black lines for  $l_{\max} \in \{2, 3, 5, 7, \dots, 29\}$  (top to bottom) see Eq. (A.24).

area reads

$$A_{[0,1) \times [0,1)}(\mathbf{k}) = 2\epsilon(\mathbf{k})L_{[0,1) \times [0,1)}(\mathbf{k}) \quad (\text{A.25})$$

From Eqs. (A.19) and (A.20) follows that for any fixed  $k_1, k_2$  a resonance  $\mathbf{k} = (k_1, k_2, k_3)$  within the frequency space exists such that

$$\frac{k_1}{k_2} \geq 0, k_3 = k_2 : \nu_2(0) = 1 \quad \text{or} \quad \frac{k_1}{k_2} < 0, k_3 = 0 : \nu_2(0) = 0 .$$

For brevity only the first case is discussed, while the arguments apply analogously to the second one. Also assume initially  $\gcd(k_1, k_2) = 1$ . Taking into account the periodicity of the frequency space the line defined by  $\nu_2(\nu_1)$  according to Eq. (A.19) with the resonance  $\mathbf{k}$  closes itself for  $\nu_1^{\max}$

$$\begin{aligned} \nu_2(\nu_1^{\max}) &= 1 - \frac{k_1}{k_2} \nu_1^{\max} = n \in \mathbb{Z} \\ \Rightarrow \nu_1^{\max} &= |k_2| \quad \nu_2(\nu_1^{\max}) = 1 - |k_1| . \end{aligned}$$

Without the periodicity of the frequency space the length of this line is determined by

$$L(\mathbf{k}) = \left\| \begin{pmatrix} \nu_1^{\max} \\ \nu_2(\nu_1^{\max}) \end{pmatrix} - \begin{pmatrix} 0 \\ \nu_2(0) \end{pmatrix} \right\| = \sqrt{k_1^2 + k_2^2}. \quad (\text{A.26})$$

Due to the periodicity of the frequency space this line is folded back into  $[0, 1) \times [0, 1)$ . This implies that the segments of this line appear as resonances with identical slope  $-k_1/k_2$  and different offset  $k'_3/k_2$  with  $k'_3 \neq k_3$ , see Eq. (A.19). More precisely, the original line in  $(\nu_1, \nu_2) \in [1 - k_1, 1) \times [0, k_2)$  is decomposed into  $\tilde{N}(\mathbf{k})$  segments. This number of segments is equal to the number of unit squares within a rectangle of size  $|k_1| \times |k_2|$  which are intersected by the diagonal on a non-zero set. As  $|k_1| - 1$  horizontal and  $|k_2| - 1$  vertical boundaries of such unit squares are crossed by the diagonal this gives, including the initial square,

$$\tilde{N}(\mathbf{k}) = |k_1| + |k_2| - 1.$$

This number matches with the number of possible resonances  $N(k_1, k_2) = \tilde{N}(\mathbf{k})$  for fixed  $k_1, k_2$ , cf. Eq. (A.21), which implies that the segments coincide with these resonances. Hence, the accumulated length  $L(k_1, k_2)$  of all resonances for fixed  $k_1, k_2$  is given by  $L(\mathbf{k})$

$$\boxed{L(k_1, k_2) = L(\mathbf{k}) = \sqrt{k_1^2 + k_2^2} = |\mathbf{k}|}. \quad (\text{A.27})$$

For the case  $\text{gcd}(k_1, k_2) = n > 1$  one obtains analogously

$$L(\mathbf{k}) = \sqrt{k_1'^2 + k_2'^2} \quad \tilde{N}(\mathbf{k}) = |k_1'| + |k_2'| - 1$$

with  $k_i = k_i' n$ . As  $\tilde{N}(\mathbf{k}) < N(k_1, k_2)$ , this leaves some resonances  $\mathbf{k}' = (k_1, k_2, k_3')$  with  $\nu_2(0) \in [0, 1)$ , in the sense of Eq. (A.19), which are not segments of the resonance  $\mathbf{k}$  which has  $\nu_2(0) = 1$ . For a resonance  $\mathbf{k}'$  arguments analogous to  $\mathbf{k}$  apply. However, since such resonance  $\mathbf{k}'$  is shifted away from the corner of the unit square in contrast to  $\mathbf{k}$  one more square is crossed by the corresponding diagonal. Thus, one obtains

$$L(\mathbf{k}') = \sqrt{k_1'^2 + k_2'^2} \quad \tilde{N}(\mathbf{k}') = |k_1'| + |k_2'|.$$

The resonances corresponding to the segments of  $\mathbf{k}$  and  $\mathbf{k}'$  are disjoint, since a single coincidence implies the coincidence of the complete resonance lines  $\mathbf{k}$  and  $\mathbf{k}'$ . As there are  $N(k_1, k_2) = |k_1| + |k_2| - 1 = n(|k_1'| + |k_2'|) - 1$  resonances for fixed  $k_1, k_2$  within

the frequency space  $(\nu_1, \nu_2) \in [0, 1) \times [0, 1)$  there have to be  $n - 1$  pairwise disjoint resonances of the type of  $\mathbf{k}'$ . The accumulated length of all these resonance lines is

$$L(k_1, k_2) = n\sqrt{k_1'^2 + k_2'^2} = \sqrt{k_1^2 + k_2^2}$$

confirming Eq. (A.27) also for  $\gcd(k_1, k_2) > 1$ . Using Eqs. (A.25) and (A.27) and assuming  $\epsilon(\mathbf{k}) = \epsilon(k_1, k_2)$  an upper bound for the area  $A(k)$  in frequency space covered by resonance channels of a certain order  $k$  reads

$$A(k) \leq \sum_{\substack{\mathbf{k}=(k_1, k_2, k_3): \\ k=|k_1|+|k_2|}} A_{[0,1) \times [0,1)}(\mathbf{k}) = \sum_{k_2=-k+1}^k A(\underbrace{k - |k_2|}_{k_1}, k_2) \quad (\text{A.28})$$

$$= \sum_{k_2=-k+1}^k 2\epsilon(k_1, k_2)L(k_1, k_2) . \quad (\text{A.29})$$

This expression is only an upper bound, as there are areas due to junctions on which the resonance channels overlap. This fact is neglected so far and hence these areas are added multiple times.

Note that there appear two norms of  $\mathbb{Z}^2$  in Eq. (A.28), i.e. the order  $k = |k_1| + |k_2|$  and the euclidean distance  $|\mathbf{k}| = \sqrt{k_1^2 + k_2^2}$ . All norms in  $\mathbb{R}^2$  are equivalent, i.e.

$$\frac{k}{\sqrt{2}} \leq |\mathbf{k}| \leq k \quad |\mathbf{k}| \leq k \leq \sqrt{2}|\mathbf{k}| .$$

A further evaluation of Eq. (A.28) requires further assumptions about the width  $2\epsilon(k_1, k_2)$  of a resonance channel. The width defines the resonance channel in the sense that all points belong to the resonance channel whose distance to the resonance line is smaller than  $\epsilon(k_1, k_2)$ . Usually, the distance  $d$  of a point  $(\nu_1, \nu_2)$  to a resonance  $\mathbf{k} = (k_1, k_2, k_3)$  is expressed by how well this point fulfills the resonance condition  $d(\boldsymbol{\nu}, \mathbf{k}) = |k_1\nu_1 + k_2\nu_2 - k_3|$ , see the diophantine condition below or, e.g., Ref. [125]. This distance  $d(\boldsymbol{\nu}, \mathbf{k})$  can be related to the euclidean distance  $D(\boldsymbol{\nu}, \mathbf{k})$  between the point  $(\nu_1, \nu_2)$  and the resonance line of Eq. (A.19) by considering that the point lies on a parallel line with a third coefficient  $k_3' \in \mathbb{R}$ . A sketch of the situation demonstrates the relation with the



angle  $\phi$  between the  $\nu_2$ -axis and the resonance line  $\mathbf{k}$

$$\begin{aligned}
D(\boldsymbol{\nu}, \mathbf{k}) &= \frac{|k'_3 - k_3|}{|k_2|} \sin(\phi) = \frac{|k_1\nu_1 + k_2\nu_2 - k_3|}{|k_2|} \frac{d\nu_1}{\sqrt{d\nu_1^2 + \left(\frac{d\nu_2(\nu_1)}{d\nu_1}d\nu_1\right)^2}} \\
&= \frac{d(\boldsymbol{\nu}, \mathbf{k})}{|k_2|} \frac{d\nu_1}{\sqrt{d\nu_1^2 + \left(\frac{k_1}{k_2}d\nu_1\right)^2}} = \frac{d(\boldsymbol{\nu}, \mathbf{k})}{|k_2|} \frac{|k_2|}{\sqrt{k_2^2 + k_1^2}} \\
\Rightarrow D(\boldsymbol{\nu}, \mathbf{k}) &= \frac{d(\boldsymbol{\nu}, \mathbf{k})}{|\mathbf{k}|} = \frac{|k_1\nu_1 + k_2\nu_2 - k_3|}{\sqrt{k_1^2 + k_2^2}}. \tag{A.30}
\end{aligned}$$

A simple assumption for the half-width of a resonance channels is  $\epsilon(k_1, k_2) = \epsilon_0/k$  [49, Eq. (3.36)]. Assuming exponentially decaying Fourier coefficients  $V_{\mathbf{k}} \sim \exp(-\sigma k)$  in the Fourier representation of the non-integrable perturbation of an integrable Hamiltonian leads to  $\epsilon(k_1, k_2) = \epsilon_0 \exp(-\sigma k)$  [39, 62], see also [49, Eq. (4.65)]. The diophantine condition  $|\sum_i k_i \nu_i| > \gamma/k^\tau$  from the KAM-theorem for  $(n+1)$  degrees of freedom with  $i \in \{0, 1, \dots, n\}$ ,  $\tau > n-1$ , and  $\gamma$  proportional to the square of the perturbation strength, cf. Ref. [40], suggests  $\epsilon(k_1, k_2) = \gamma/k$  in terms of the distance  $d(\boldsymbol{\nu}, \mathbf{k})$ . In terms of the euclidean distance  $D(\boldsymbol{\nu}, \mathbf{k})$  this means  $\tilde{\epsilon}(k_1, k_2) = \gamma/(k|\mathbf{k}|)$ . Finally, a constant half-width  $\epsilon(k_1, k_2) = \epsilon_0$  in terms of  $d(\boldsymbol{\nu}, \mathbf{k})$  is equal to  $\tilde{\epsilon}(k_1, k_2) = \epsilon_0/|\mathbf{k}|$  in terms of  $D(\boldsymbol{\nu}, \mathbf{k})$ . The evaluation of Eq. (A.28) for some of these cases reads

$$A(k) \leq 4\epsilon_0 \cdot \begin{cases} k^2 & \text{for } \epsilon(k_1, k_2) = \epsilon_0 \\ k & \text{for } \epsilon(k_1, k_2) = \frac{\epsilon_0}{|\mathbf{k}|} \text{ or } \epsilon(k_1, k_2) = \frac{\epsilon_0}{k} \\ 1 & \text{for } \epsilon(k_1, k_2) = \frac{\epsilon_0}{k|\mathbf{k}|} \end{cases} \tag{A.31}$$

where  $|\mathbf{k}| \leq k$  is used. For the accumulated area  $A(k \leq K)$  up to a certain order  $K$  follows

$$A(k \leq K) \leq \sum_{k=1}^K A(k) \leq 4\epsilon_0 \cdot \begin{cases} \frac{K(K+1)(2K+1)}{6} & \sim K^3 \\ \frac{K(K+1)}{2} & \sim K^2 \\ K & \sim K \end{cases} \tag{A.32}$$

The resonances that are considered several times in the expressions in Eqs. (A.31) and (A.32) can be corrected analogously to the lower bound in Eqs. (A.23) and (A.24). In the following the corrections due to junctions are discussed. At the junction of two resonances  $\mathbf{k}, \mathbf{k}'$  the corresponding channels with half-widths  $\epsilon(\mathbf{k}), \epsilon(\mathbf{k}')$  overlap on a

parallelogram with area

$$A(\mathbf{k} \times \mathbf{k}') = \frac{4\epsilon(\mathbf{k})\epsilon(\mathbf{k}')}{\sin \sphericalangle(\mathbf{k}, \mathbf{k}')} = 4\epsilon(\mathbf{k})\epsilon(\mathbf{k}') \frac{|\mathbf{k}||\mathbf{k}'|}{|k_1 k'_2 - k'_1 k_2|} \quad (\text{A.33})$$

where  $\sphericalangle(\mathbf{k}, \mathbf{k}')$  denotes the angle between the two resonance lines. For two perpendicular resonances it is obtained  $A(\mathbf{k} \times \mathbf{k}') = 4\epsilon(\mathbf{k})\epsilon(\mathbf{k}')$  and there is the pathological case  $\mathbf{k} \rightarrow \mathbf{k}'$  with  $A(\mathbf{k} \times \mathbf{k}') \rightarrow \infty$  which is ruled out. An upper bound for the number  $N((k_1, k_2) \times (k'_1, k'_2))$  of junctions between all resonances with fixed  $k_1, k_2$  and  $k'_1, k'_2$  is given by the case that each resonance intersects with every other, i.e. using Eq. (A.22)

$$N((k_1, k_2) \times (k'_1, k'_2)) \leq (|k_1| + |k_2| - 1)(|k'_1| + |k'_2| - 1) \leq kk'$$

which implies for the overlap  $A((k_1, k_2) \times (k'_1, k'_2))$  of all resonance channels of fixed  $k_1, k_2$  and  $k'_1, k'_2$

$$\begin{aligned} A((k_1, k_2) \times (k'_1, k'_2)) &= N((k_1, k_2) \times (k'_1, k'_2))A(\mathbf{k} \times \mathbf{k}') \\ &\leq 4\epsilon(\mathbf{k})\epsilon(\mathbf{k}') \frac{|\mathbf{k}||\mathbf{k}'|kk'}{|k_1 k'_2 - k'_1 k_2|} \\ &\leq 4\epsilon(\mathbf{k})\epsilon(\mathbf{k}') \frac{k^2 k'^2}{|k_1 k'_2 - k'_1 k_2|} \end{aligned} \quad (\text{A.34})$$

For finite angles  $0 \ll \sphericalangle(\mathbf{k}, \mathbf{k}') \leq \pi/2$  this gives  $\sim \epsilon(\mathbf{k})\epsilon(\mathbf{k}')kk'$  for the upper bound of  $A((k_1, k_2) \times (k'_1, k'_2))$ . Depending on the choice of the half-width according to Eq. (A.31) this upper bound ranges from  $\sim \epsilon_0^2 kk'$  to  $\sim \epsilon_0^2$ . The overlap  $A(k \times k)$  of all resonances of the same order  $k$  is estimated by

$$A(k \times k) \leq \frac{1}{2} \sum_{k_2=-k+1}^k \sum_{\substack{k'_2=-k+1 \\ k'_2 \neq k_2}}^k A((k - |k_2|, k_2) \times (k - |k'_2|, k'_2)) .$$

Hence, the correction terms to Eq. (A.31) due to junctions have an upper bound ranging from  $\sim \epsilon_0^2 k^4$  to  $\sim \epsilon_0^2 k^2$ . Thus, for small half-widths  $\epsilon_0$  and small orders  $k$  these corrections are negligible.

An application of Eq. (A.31) is to estimate up to which order resonances are relevant for the observed dynamics. This is illustrated in Fig. A.8, showing the fraction of  $A(k)$  of frequencies at resonances of order  $k$ . For Figure A.8(a)  $10^6$  random frequency pairs  $(\nu_1, \nu_2)$  are drawn uniformly distributed over a quarter of the frequency space  $(\nu_1, \nu_2) \in [0, 0.5]^2$ . For each frequency pair the lowest order resonance  $\mathbf{k}$  with  $k < 90$  is determined such that  $d((\nu_1, \nu_2), \mathbf{k}) < \epsilon_0$  with  $\epsilon_0 = 10^{-5}$ . The fraction of frequency

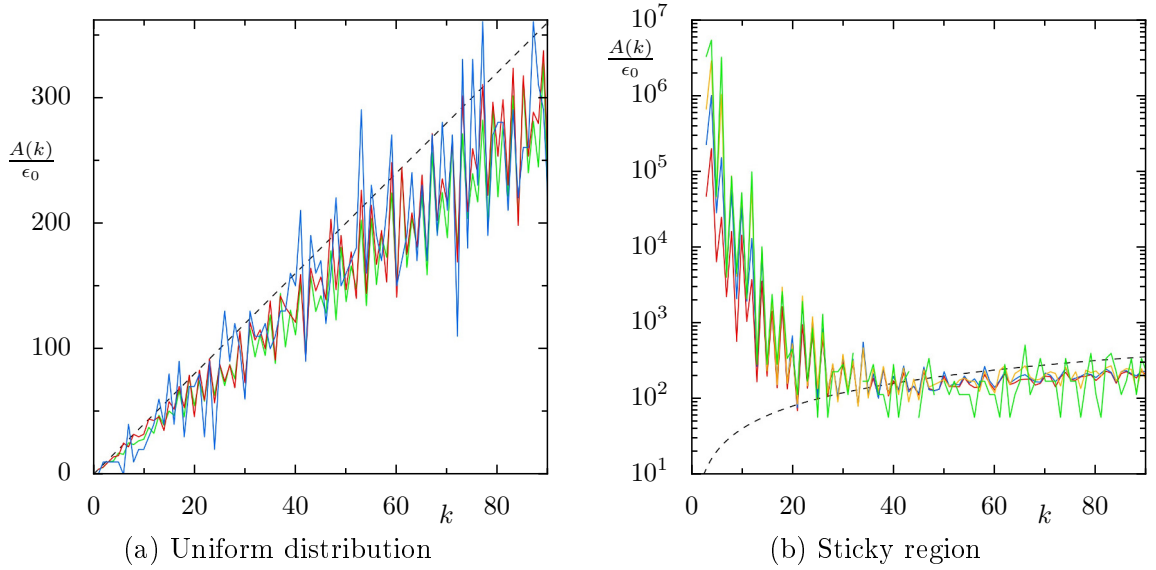


**Figure A.8:** Fraction  $A(k)$  of frequencies at resonances of order  $k$  with width  $2\epsilon_0$ , see text. For (a)  $10^6$  uniformly random distributed frequency pairs  $(\nu_1, \nu_2) \in [0, 0.5]^2$  are used with  $\epsilon_0 \in \{10^{-5}, 10^{-6}, 10^{-7}\}$  (green, red, blue). For (b) the 20775 trapped orbits of  $F_{\text{Twist}}$  with  $T \geq 10^6$ , i.e. a total of  $|\Omega_{\text{Twist}}| \approx 1.7 \cdot 10^7$  frequency pairs, from Sec. 3.5.1 and Fig. 4.4 are used with  $\epsilon_0 \in \{10^{-6}, 10^{-7}, 10^{-8}, 10^{-9}\}$  (red, blue, orange, green). The estimate  $A(k) \sim 4k$  is indicated in both cases as dashed line, see second row of Eq. (A.31).

pairs assigned in this fashion to resonances of a certain order  $k$  is an approximation for the area  $A(k)$  covered by resonances of this order with width  $2\epsilon_0$ . Using the same assigned resonances as above, this area is additionally estimated for smaller widths  $\sim \epsilon_0 = 10^{-6}, 10^{-7}$ . Finally, these estimates are rescaled with the considered  $\epsilon_0$  and shown by differently colored points connected by lines as guide to the eye. In Fig. A.8(a) the behavior of  $A(k)/\epsilon_0$  is linear over three orders of magnitude of the width and nicely follows the upper bound given by Eq. (A.31). This upper bound is sometimes surpassed indicating a numerical artifact which is expected to disappear for larger number of random points. In Fig. A.8(b) analogously obtained results for trapped orbits of the coupled twist maps  $F_{\text{Twist}}$  are shown. While again the scaling of the area  $A(k)$  with the width  $\sim \epsilon_0$  is confirmed for large orders  $k$ , the results disagree considerably with the upper bound for small orders. This is due to the dynamics of the real system, which is dominated by low order resonance channels accumulating trapped orbits in their vicinity. Since the upper bound shown as dashed line represents a uniform distribution of points, it is reasonable to assume that for orders  $k$  at which  $A(k)/\epsilon_0$  is in agreement with the bound no dynamics but numerical artifacts are resolved. In the present case at most resonance up to order  $k = 50$  can be considered relevant for the observed dynamics.

The discussion of the width of a resonance channel in frequency space is linked to the problem of detecting whether orbits are within the deeper class of a resonance,

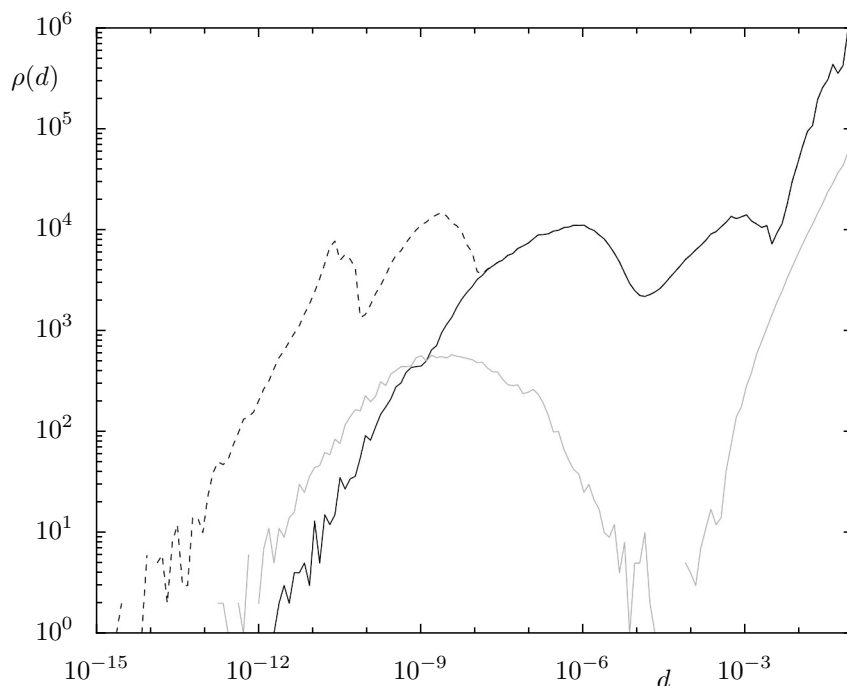


**Figure A.9:** Distribution  $\rho(d)$  of frequencies over the distance  $d$  to the resonance  $k_1 : k_2 : k_3 = 0 : 6 : 5$  of  $F_{\text{Twist}}$ . For the regular tori from Fig. 3.7 the gray curve is obtained, with a peak around  $d \sim 10^{-9}$  from points on the resonance line and the right tongue from the other KAM tori. For the trapped orbits from Fig. A.8(b) the dashed line behind the black one is obtained. By excluding segments of trapped orbits with  $\nu_1 \geq 0.66064$  the black line is obtained, i.e. the two left peaks of the dashed line result from resonance junctions  $(\nu_1, \nu_2) = (n_1/m_1, 5/6)$ . The peak at  $d \sim 10^{-12}$  results from  $\nu_1 = 2/3$  and the peak at  $d \sim 10^{-9}$  from  $\nu_1 \in \{329/498, 261/395, 115/174\}$ . The distance  $d = |k_1\nu_1 + k_2\nu_2 - k_3|$  is used, see discussion of Eq. (A.30).

see Sec. 4.4. It is reasonable to ask whether this can be inferred from the frequencies themselves. In Fig. A.9 a profile  $\rho(d)$  of the number of frequency segments with respect to their distance  $d$  to the resonance  $0 : 6 : 5$  of  $F_{\text{Twist}}$  is displayed in a log-log scale. While this profile is for a particular resonance, equivalent profiles are obtained for other resonances not shown here. Firstly, the gray line represents the regular tori also shown in Fig. 3.6(c). The regular tori seem to be separated sharply into a peak close to the resonance  $10^{-12} < d < 10^{-5}$  and tori further away from the resonance  $d > 10^{-4}$ , which are the majority. An inspection of the geometry of the regular tori within the peak by 3D projections reveals that these 2D tori belong to the deeper class of the resonance as expected from Sec. 3.3.1. Such a sharp separation is not observed for the segments of the trapped orbits of  $F_{\text{Twist}}$  represented by the black dashed line, which coincides with the black solid line for  $d > 10^{-8}$ . At larger distance  $d > 10^{-3}$  a rapidly increasing number of segments is observed which analogous to the regular tori can be considered to be outside of the resonance channel or at most in the stochastic layer of it.

Closer to the resonance four characteristic peaks can be identified. This suggests that the distribution is a superposition of four broad peaks resulting from four dynamical regimes with respect to the resonance. The inner two peaks can be associated to explicit junctions on the resonance. Segments of the innermost peak are trapped at the junction with  $\nu_1 = 2/3$  and the next peak is a superposition of segments trapped at the junctions with  $\nu_1 = 329/498, 261/395, 115/174$ . Due to this junctions the distribution reaches as close as  $d \sim 10^{-14}$  to the resonance, even closer than most of the regular tori of the deeper class. After excluding the segments at the junctions from the set of trapped orbits, the black solid line remains, which just has two peaks and decays at smaller  $d$  in a similar fashion as the peak of the regular tori. From comparison with this peak it may be inferred that the outer peak is due to the stochastic layer of the resonance channel and the inner peak is due to the deeper class. However, a careful comparison of segments from each peak, for instance in phase space by 3D projections, is necessary to affirm this conjecture and is left for future studies.

## A.4 Resonance module and junctions

Resonance junctions are essential to the global transport within the Arnold web as reviewed in Sec. 2.5.1. At each junction infinitely many resonances are crossing composing the so called resonance module. As the order of a resonance is relevant for its transport properties, see Appendix A.3, it is interesting to know the lowest order resonances at a junction. In this section, an effective, semi-analytical procedure is derived to obtain the lowest order resonances for a junction  $(n_1/m_1, n_2/m_2)$  of a 4D map. As a possible application the orientation of Lyapunov families of EE periodic orbits at junctions with respect to the crossing resonances is discussed.

The resonance module  $L$  at a point  $(\nu_1, \nu_2)$  in frequency space of a 4D map is the set of all resonance conditions fulfilled at that point

$$L(\nu_1, \nu_2) = \{\mathbf{k} \in \mathbb{Z}^3 : k_1\nu_1 + k_2\nu_2 = k_3\} .$$

It is easy to show that the resonance module is a vector space with respect to integer superposition, i.e.  $\forall \mathbf{k}^1, \mathbf{k}^2 \in L(\nu_1, \nu_2) : \forall a, b \in \mathbb{Z} : a\mathbf{k}^1 + b\mathbf{k}^2 \in L(\nu_1, \nu_2)$ . In this sense, the dimension of the resonance module is zero, one or two according to the rank of the resonance condition, see Sec. 3.2.2. However, here two resonance conditions  $\mathbf{k}^1, \mathbf{k}^2 \in L$  are considered to be equal  $\mathbf{k}^1 = \mathbf{k}^2$ , if  $\exists c \in \mathbb{Z} : \mathbf{k}^1 = c\mathbf{k}^2$ , since these conditions are fulfilled on the same set of frequencies. Without loss of generality it is therefore assumed that  $\gcd(k_1, k_2, k_3) = 1$  for  $\mathbf{k} \in L(\nu_1, \nu_2)$ . In this sense, the

dimension of the resonance module is only non-zero at a resonance junction, i.e. for rank-2. More precisely, at a resonance junction  $(\nu_1, \nu_2) = (n_1/m_1, n_2/m_2)$  with  $n_i, m_i \in \mathbb{Z}$  and  $\gcd(n_i, m_i) = 1$ ,  $0 \leq n_i < m_i$ , the module  $L(n_1/m_1, n_2/m_2)$  is spanned by any two linearly independent elements of the module, i.e.  $\forall \mathbf{k}^1, \mathbf{k}^2 \in L(n_1/m_1, n_2/m_2)$   $\mathbf{k}^1 \neq \mathbf{k}^2$  ( $\nexists c \in \mathbb{Z} : \mathbf{k}^1 = c\mathbf{k}^2$  or  $\mathbf{k}^2 = c\mathbf{k}^1$ ) :  $\forall \mathbf{k}^3 \in L(n_1/m_1, n_2/m_2) \exists a, b, c \in \mathbb{Z} : a\mathbf{k}^1 + b\mathbf{k}^2 = c\mathbf{k}^3$  which are given by

$$\frac{a}{c} = -\frac{k_1^2 k_2^3 - k_2^2 k_1^3}{k_1^1 k_2^2 - k_2^1 k_1^2} \quad \frac{b}{c} = \frac{k_1^1 k_2^3 - k_2^1 k_1^3}{k_1^1 k_2^2 - k_2^1 k_1^2} \quad (\text{A.35})$$

These expressions for  $a/c$  and  $b/c$  can be directly verified for the first two components  $k_1^3, k_2^3$  and for the third component  $k_3^3$  by identifying  $n_1/m_1, n_2/m_2$  using Eq. (3.5).

It should be pointed out that in a normal form analysis two resonances  $\mathbf{k}^1, \mathbf{k}^2 \in L$  with  $\mathbf{k}^1 = c\mathbf{k}^2$ ,  $c \in \mathbb{Z}$  are not equal. In particular, the different orders of these resonances may lead to different kind of normal forms and thus dynamics [61]. In this sense, not all pairs of linearly independent resonances of a resonance module span the module, but only so called minimal generators. For such generators the denominator in Eq. (A.35), which is the determinant of the Matrix  $(k_i^j)_{i,j \in \{1,2\}}$ , has to fulfill a certain condition [61, Corollary 3.9] also called minimal representation [183].

In any case, a characterizing property of a junction  $(n_1/m_1, n_2/m_2)$  is lowest order  $k^0$  of the crossing resonances  $\mathbf{k} \in L(n_1/m_1, n_2/m_2)$  which is given by  $k^0 = \min\{k : \mathbf{k} \in L(n_1/m_1, n_2/m_2)\}$  with the order  $k = |k_1| + |k_2|$ . This order  $k^0$  has an trivial upper bound  $k^0 \leq k_{\max}$  deduced from the two uncoupled resonances of the module  $\mathbf{k}^1 = (m_1, 0, n_1)$  and  $\mathbf{k}^2 = (0, m_2, n_2)$ , i.e.  $k_{\max} \leq \min\{m_1, m_2\}$ . This implies that the number of resonance conditions  $\mathbf{k} \in L(n_1/m_1, n_2/m_2)$  that have to be compared by a brute force algorithm in order to find  $k^0$  are at most  $\sum_{j=1}^{k_{\max}} 2 \sum_{i=0}^j = k_{\max}(k_{\max} + 3)$ . Other helpful restrictions for such a brute force algorithm may be found in Ref. [61], Lemma 3.4 and following Corollary. However, a more efficient and direct way to obtain  $k^0$  is derived in the following. Any resonance  $\mathbf{k} \in L(n_1/m_1, n_2/m_2)$  can be expressed by the two uncoupled resonances  $\mathbf{k}^1, \mathbf{k}^2$  using Eq. (A.35) which leads to the condition

$$\boxed{k_3 = \frac{n_1}{m_1} k_1 + \frac{n_2}{m_2} k_2 = \frac{m_2 n_1 k_1 + m_1 n_2 k_2}{m_1 m_2} = \frac{x k_1 + y k_2}{z}} \quad (\text{A.36})$$

with  $x, y, z \in \mathbb{Z}$  and  $\gcd(x, y, z) = 1$ . In order to determine  $k^0$ , a solution  $k_1, k_2 \in \mathbb{Z}$  to the diophantine equation

$$z k_3 = Z = x k_1 + y k_2 \quad (\text{A.37})$$

has to be found for which  $k = |k_1| + |k_2|$  is minimal. For a diophantine equation like Eq. (A.37) it is straightforward to see that

$$\forall k_1, k_2 \in \mathbb{Z} : \exists l \in \mathbb{Z} : xk_1 + yk_2 = l \operatorname{gcd}(x, y) . \quad (\text{A.38})$$

In particular  $|\operatorname{gcd}(x, y)|$  is the smallest absolute value possible for  $Z$ . Also one can decompose

$$xy = \operatorname{gcd}(x, y)\operatorname{lcm}(x, y) . \quad (\text{A.39})$$

Note that the solution of Eq. (A.37) for a particular  $Z$  is ambiguous as

$$xk_1 + yk_2 = xk_1 + lxy + yk_2 - lxy = x(k_1 + ly) + y(k_2 - lx) = x\tilde{k}_1 + y\tilde{k}_2 \quad (\text{A.40})$$

with  $l \in \mathbb{Z}$ . A generic way to obtain a solution of Eq. (A.37) is Euclid's algorithm reviewed in Ref. [217]. However, this algorithm can produce very large  $k_1, k_2$ . Instead, a continued fraction procedure which produces minimal solutions [217] is more appropriate for the purpose here. This algorithm is briefly reviewed in the following.

At first assume  $\operatorname{gcd}(x, y) = 1$  in Eq. (A.37). The case  $\operatorname{gcd}(x, y) > 1$  can be transformed to new parameters  $x', y', Z'$  by  $x = x' \operatorname{gcd}(x, y)$ ,  $y = y' \operatorname{gcd}(x, y)$  and  $Z = Z' \operatorname{gcd}(x, y) = zk'_3 \operatorname{gcd}(x, y)$ , where  $Z' \in \mathbb{Z}$  according to Eq. (A.38). Adapt the notation for the iterative algorithm

$$\boxed{Z' = x'k_1 + y'k_2 \quad \rightarrow \quad c_0 = b_0x_1 + b_1x_0} \quad (\text{A.41})$$

where without loss of generality  $|b_0| \geq |b_1|$  is assumed. A solution to Eq. (A.41) is obtained iterative by

$$\boxed{c_i = b_i x_{i+1} + b_{i+1} x_i \quad |b_i| \geq |b_{i+1}|} \quad (\text{A.42})$$

where the new coefficients result from a decomposition

$$\boxed{\begin{array}{l} b_i = q_{i+1} b_{i+1} + b_{i+2} \quad \text{with} \quad |b_{i+2}| \leq \frac{1}{2} |b_{i+1}| \\ c_i = g_{i+1} b_{i+1} + c_{i+1} \quad \text{with} \quad |c_{i+1}| \leq \frac{1}{2} |b_{i+1}| \end{array}} \quad (\text{A.43})$$

from which follows in combination with Eq. (A.42)

$$x_i = \frac{c_i - b_i x_{i+1}}{b_{i+1}} \stackrel{\text{Eq. (A.43)}}{=} g_{i+1} - q_{i+1} x_{i+1} + \frac{c_{i+1} - b_{i+2} x_{i+1}}{b_{i+1}}$$

$$\boxed{x_i = g_{i+1} - q_{i+1} x_{i+1} + x_{i+2}}$$
 (A.44)

with all parameters being integers, in particular  $x_{i+2} \in \mathbb{Z}$ . The combination of Eq. (A.42) with Eqs. (A.43) and (A.44) results in the next step of the iteration

$$c_{i+1} = b_{i+1} x_{i+2} + b_{i+2} x_{i+1} \quad |b_{i+1}| \geq |b_{i+2}|$$

as predicted by Eq. (A.42). The procedure is iterated until

$$\boxed{\begin{aligned} 0 < |c_i| < \frac{1}{2}|b_i| \quad \forall i \in 1, \dots, n-1 \\ \text{and either (a) } c_n = 0 \quad b_n \neq 0 \\ \text{or (b) } c_n = \pm \frac{1}{2} b_n \quad b_n \neq 0 \end{aligned}}$$
 (A.45)

In these cases the final equation of Eq. (A.42) reads

$$(a) \quad b_n x_{n+1} + b_{n+1} x_n = 0$$

$$(b) \quad b_n x_{n+1} + b_{n+1} x_n = \pm \frac{1}{2} b_n$$

with the trivial solutions

$$\boxed{\begin{aligned} (a) \quad x_n = x_{n+1} = 0 \\ (b) \quad x_n = \pm \frac{1}{2} b_n \quad x_{n+1} = \mp \frac{1}{2} (b_{n+1} - 1) . \end{aligned}}$$
 (A.46)

Note that  $b_{n+1}$  in case (b) in Eq. (A.46) is odd due to  $b_n$  being even the first line of Eq. (A.43). Using the solutions of Eq. (A.46) the preceding values  $x_{i < n}$  are obtained by solving Eq. (A.44) backwards.

The solution of the described algorithm is minimal in the following sense [217]. A solution  $(x_0, x_1)$  of Eq. (A.41) with  $|b_0| \geq |b_1|$  is called minimal solution with respect to  $x_1$  if  $|x_1| < |b_1|/2$  and is the only such solution, except when the equality holds. A solution of Eq. (A.41) is called definitely least solution, if and only if both  $|x_1| \leq |b_1|/2$  and  $|x_0| \leq |b_0|/2$ . The algorithm gives a minimal solution with respect to  $x_1$ . Either a solution from the algorithm  $(x_0, x_1)$  is only minimal with respect to  $x_1$  or there is just one other and then  $(x_0, x_1)$  is the one in which  $|x_0|$  is smaller. This implies that if a definitely



least solution exists and is unique, this solution is obtained by the algorithm. There is a statement about the uniqueness of the definitely least solution (d.l.s.). Consider  $b_0 > 0$ ,  $b_1 > 0$  odd,  $\gcd(b_0, b_1) = 1$  and  $c_0 \geq 0$ , then  $\exists L, R \in \mathbb{Z}$ ,  $L < R$  defined by

$$\begin{cases} L = \frac{1}{2}(b_0 + b_1) & R = b_0b_1 - \frac{1}{2}(b_0 + b_1) & : & b_0 \text{ odd} \\ L = \frac{1}{2}b_0 + b_1 & R = b_0b_1 - \frac{1}{2}b_0 & : & b_0 \text{ even} \end{cases}$$

such that

$$\forall c_0 < L : \exists \text{ d.l.s.}$$

$$\forall c_0 > R : \nexists \text{ d.l.s.}$$

$$\forall L \leq c_0 \leq R : \exists \text{ d.l.s. for half the values of } c_0, \text{ i.e.}$$

$$\forall c, c', c + c' = L + R : \exists \text{ d.l.s. for exactly one } c_0 \in \{c, c'\}$$

$$\text{e.g. } c_0 = R \rightarrow \exists \text{ d.l.s.} \quad c_0 = L \rightarrow \nexists \text{ d.l.s.}$$

Once a solution  $(x_0, x_1)$  of Eq. (A.41) is obtained by the algorithm any other solution  $(\tilde{x}_0, \tilde{x}_1)$  automatically follows from

$$\boxed{\begin{aligned} \tilde{x}_0 &= x_0 + l \frac{\text{lcm}(b_0, b_1)}{b_1} \stackrel{\text{Eq. (A.39)}}{=} x_0 + l \frac{b_0}{\gcd(b_0, b_1)} \stackrel{\gcd(b_0, b_1)=1}{=} x_0 + lb_0 \\ \tilde{x}_1 &= x_1 - l \frac{\text{lcm}(b_0, b_1)}{b_0} \stackrel{\text{Eq. (A.39)}}{=} x_1 - l \frac{b_1}{\gcd(b_0, b_1)} \stackrel{\gcd(b_0, b_1)=1}{=} x_1 - lb_1 \end{aligned}} \quad (\text{A.47})$$

with  $l \in \mathbb{Z}$ . This is a sufficient condition for  $(\tilde{x}_0, \tilde{x}_1)$  being a solution, cf. Eq. (A.40). In the following, it is proven that Eq. (A.47) is also a necessary condition. Consider an arbitrary other solution  $(\tilde{x}_0, \tilde{x}_1)$  of Eq. (A.41). It is always possible to write

$$c_0 = b_0\tilde{x}_1 + b_1\tilde{x}_0 = b_0(x_1 + \Delta_1) + b_1(x_0 + \Delta_0)$$

with  $\Delta_i \in \mathbb{Z}$ ,  $\Delta_i = \tilde{x}_i - x_i$ . This implies

$$b_1\Delta_0 = -b_0\Delta_1$$

such that both  $b_0\Delta_1$  and  $b_1\Delta_0$  are multiple of both  $b_0$  and  $b_1$ . Thus, both terms can be expressed by

$$b_1\Delta_0 = -b_0\Delta_1 = l \cdot \text{lcm}(b_0, b_1)$$

with  $l \in \mathbb{Z}$ . This proves that Eq. (A.47) is a necessary condition.

According to Eq. (A.47), in order to obtain a solution  $(x_0, x_1)$  for Eq. (A.41) with minimal order  $x$  the minimum of

$$x(l) = |\tilde{x}_0| + |\tilde{x}_1| = |x_0 + lb_0| + |x_1 - lb_1|$$

has to be found. Since  $(x_0, x_1)$  is already the minimal or definitely least solution, the solution  $(\tilde{x}_0, \tilde{x}_1)$  with minimal order is expected to be in the neighborhood of  $(x_0, x_1)$ . To find the actual solution with minimal order of Eq. (A.41) the solutions  $(\tilde{x}_0, \tilde{x}_1)$  have to be obtained for every  $Z' = zk'_3$ ,  $k'_3 \in [0, k_3^{\max}]$  and the minimal order has to be found among these solutions. The boundary  $k_3^{\max}$  is determined according to the following considerations. Let  $x_{\min}(k''_3 - 1)$  be the minimal order obtained for  $k'_3 \in [0, k''_3 - 1 < k_3^{\max}]$ ,  $k''_3 \in \mathbb{N}$ . For  $b_0x_1 + b_1x_0 = zk''_3$  the order  $x(k''_3)$  has a lower boundary

$$x(k''_3) \geq \frac{|zk''_3|}{\max(|b_0|, |b_1|)} = \frac{|zk''_3|}{|b_0|}$$

and since the search can be stopped once this lower boundary is bigger or equal than  $x_{\min}(k''_3 - 1)$ , it is obtained that

$$\boxed{k_3^{\max} \leq \frac{|b_0|}{|z|} x_{\min}(k''_3)} . \quad (\text{A.48})$$

The upper bound  $k_3^{\max}$  is successively updated with increasing  $k''_3$  until  $k_3^{\max} \leq k''_3$ . Then the solution corresponding to the order  $x_{\min}(k''_3)$  is the solution of Eq. (A.41) with minimal order. In an analogous fashion the solutions with second, third, ... smallest order can be additionally computed. The case  $k'_3 = 0$  in Eq. (A.41) does not require the algorithm, because the minimal solution is obviously  $x_0 = x_1 = 0$ . However, this solution does not represent a valid resonance. Thus, for the case  $k'_3 = 0$  according to Eq. (A.47) the solution with minimal order is  $(\tilde{x}_0, \tilde{x}_1) = (b_0, b_1)$  with order  $x_{\min}(0) = |b_0| + |b_1|$  from which the initial upper bound is estimated  $k_3^{\max} \leq |b_0|/|z| \cdot (|b_0| + |b_1|)$ . Note that an initial solution for an arbitrary  $Z' = zk'_3$  is trivially given by multiplying the solution for  $Z' = 1$  with  $zk'_3$ . This solution can be optimized by Eq. (A.47).

As an example the resonances with lowest order are computed for two junctions present in the two coupled standard maps  $F_{\text{SC}}$ . The first example is the junction  $(\nu_1, \nu_2) = (2/7, 2/21)$  at the crossing of the resonances  $-1 : 3 : 0$  and  $7 : 0 : 2$ . In this case, Eq. (A.36) reads

$$k_3 = \frac{2}{7}k_1 + \frac{2}{21}k_2 = \frac{6k_1 + 2k_2}{21} .$$

Since  $\gcd(6, 2) = 2$  the left side is substituted  $k_3 = 2k'_3$  and Eq. (A.41) reads

$$21k'_3 = 3k_1 + 1k_2 .$$

For  $k'_3 = 0$  the solution with minimal order is  $(k_1, k_2) = (1, -3)$  with order  $x_{\min}(0) = 4$  from which according to Eq. (A.48) the upper bound  $k'_3 \leq k_3^{\max} \leq 12/21 < 1$  follows. Thus, the resonance  $-1 : 3 : 0$  is indeed the resonance with the smallest order at the junction and is the only resonance with that order.

The second example is the junction  $(\nu_1, \nu_2) = (2/7, 3/35)$  at the crossing of the resonances  $7 : 0 : 2$  and  $5 : -5 : 1$ . In this case, Eq. (A.36) reads

$$k_3 = \frac{2}{7}k_1 + \frac{3}{35}k_2 = \frac{10k_1 + 3k_2}{35} .$$

For  $k_3 = 0$  the solution with minimal order is  $(k_1, k_2) = (3, -10)$  with order  $x_{\min}(0) = 13$  from which according to Eq. (A.48) the upper bound  $k_3 \leq k_3^{\max} \leq 10 \cdot 13/35 < 4$  follows. For  $k_3 = 1$  the steps of the algorithm read

$$k_2 = \frac{35 - 10k_1}{3} = 12 - 3k_1 - \underbrace{\frac{1 + k_1}{3}}_w$$

$$k_1 = -1 - 3w \rightarrow w = 0 \quad k_1 = -1 \quad k_2 = 15 .$$

Using Eq. (A.47) the minimal order is found

	$l$	$k_1$	$k_2$	$ k_1  +  k_2 $
	0	-1	15	16
→	1	2	5	7
	2	5	-5	10

for the resonance  $2 : 5 : 1$  with order  $x_{\min}(1) = 7$ . According to Eq. (A.48) this implies the upper bound  $k_3 \leq k_3^{\max} \leq 10 \cdot 7/35 = 2$ . Thus, the case  $k_3 = 2$  has to be considered, which can be done by three different ways. Firstly, the steps of the algorithm for this case read

$$k_2 = \frac{70 - 10k_1}{3} = 23 - 3k_1 + \underbrace{\frac{1 - k_1}{3}}_w$$

$$k_1 = -1 - 3w \rightarrow w = 0 \quad k_1 = 1 \quad k_2 = 20 .$$

Using Eq. (A.47) the minimal order is found

	$l$	$k_1$	$k_2$	$ k_1  +  k_2 $
	0	1	20	21
	1	4	10	14
→	2	7	0	7
	3	10	-10	20

for the resonance  $7 : 0 : 2$  with order  $x_{\min}(2) = 7$ . Secondly, one might use the algorithm to find the solution minimized with respect to  $k_2$

$$k_1 = \frac{70 - 3k_1}{10} = 7 - \frac{3k_2}{10} \rightarrow k_2 = 0 \quad k_1 = 7$$

and realize according to Eq. (A.47) that this solution has the minimal order. Thirdly, one might multiply the solution for  $k_3 = 1$  with two, which leads to the resonance  $4 : 10 : 2$ . While this resonance is equivalent to  $2 : 5 : 1$ , such reductions do not have to be considered, since the resulting resonance is already included in the cases  $k_3 < 2$ . From the resonance  $4 : 10 : 2$  according to Eq. (A.47) the resonance  $7 : 0 : 2$  is found to have the minimal order. In conclusion, there are two resonances with minimal order at the junction that is  $7 : 0 : 2$  and  $2 : 5 : 1$ .

Knowing the resonances with the lowest order at a resonance junction is interesting, as these resonances may determine the orientation of the Lyapunov families of the junction: In Sec. 3.3.1 it is demonstrated that for  $(\alpha_2)$  the EE periodic orbit from a broken resonant elliptic 1D torus one of the emanating Lyapunov families is embedded in the original family of elliptic 1D tori. At  $(\alpha_1)$  a resonance junction also an EE periodic orbit with two Lyapunov families is present and additionally the elliptic and hyperbolic families of 1D tori of all the intersecting resonances. More precisely, the junction represents a gap in the families of the resonances in which the periodic orbits are located. Thus, it is reasonable to expect the Lyapunov families of the EE periodic orbit to be embedded in one of these families as in the case  $(\alpha_2)$ . Indeed, it is observed that one of the Lyapunov families of the EE periodic orbit at the junction  $\nu = (2/7, 3/35)$  is embedded within the elliptic family of the resonance  $7 : 0 : 2$ . As there is an infinite number of resonances at each junction the question is in which two of them the Lyapunov families are embedded. One conjecture is that these two resonances are the ones of lowest order. For the junction  $\nu = (2/7, 3/35)$  these are the resonances  $7 : 0 : 2$  and  $2 : 5 : 1$  and for  $\nu = (2/7, 2/21)$  one is  $-1 : 3 : 0$  as calculated above.

Another idea is that the resonances are selected by the order of the uncoupled resonance which represents the junction in the frequency space of the resonances, see Sec. 3.3.2. In detail, the periodic orbits at a junction can be interpreted as the remnants of the break-up of resonant 1D tori from the families of the resonances. For

instance, the junction  $\boldsymbol{\nu} = (2/7, 3/35)$  corresponds in the frequencies of the resonance  $7 : 0 : 2$  to  $\nu_L = \nu_1''' = 7 \cdot 3/35 = 1 - 2/5$  which represents the resonance  $5 : 0 : 2$ . Indeed, in Fig. 3.5(f) all the points from the junction fall on this resonance. In case of the resonance  $5 : -5 : 1$  using the unimodular transformation  $\mathcal{U} = ((0, 1), (-1, 1))$ , see Sec. 3.3.2, the junction corresponds to  $\nu_L = 5 \cdot 3/35 = 3/7$ , i.e.  $7 : 0 : 3$ . For the resonance  $2 : 5 : 1$  using  $\mathcal{U} = ((1, 2), (2, 5))$  the junction corresponds to  $\nu_L = 16/35$ , i.e.  $35 : 0 : 16$ . Likewise, the junction  $\boldsymbol{\nu} = (2/7, 2/21)$  in terms of the resonance  $7 : 0 : 2$  corresponds to  $\nu_L = 7 \cdot 2/21 = 1 - 1/3$  which is not within Fig. 3.5(f) anymore. The same junction in terms of the resonance  $-1 : 3 : 0$  using  $\mathcal{U} = ((0, 1), (1, -3))$  corresponds to  $\nu_L = \nu_1'' = 2/21$ , i.e.  $21 : 0 : 2$ , which is visible in Fig. 3.5(d). Which resonance in fact governs the orientation of the Lyapunov families is left for future studies.

## A.5 Action space

For generic symplectic maps with a mixed phase space it is challenging to find the local action–angle coordinates as introduced in Sec. 2.1. In this section, the method for computing the actions for 4D symplectic maps from Ref. [38] is reviewed by generalizing the crucial equation to arbitrary dimensions. The method is used to present regular tori and a trapped orbit of the two coupled standard maps  $F_{\text{SC}}$  in action space, which demonstrates that the edges in frequency space indeed correspond to the families of 1D tori, see Sec. 3.1. While the action computation only works for non-resonant tori, a method for estimating the actions on resonances is proposed. It is also explained how actions of regular tori can be zero and even negative in higher-dimensional maps. Finally, a comparison with the action space for the coupled twist maps  $F_{\text{Twist}}$  illustrates the generic nature of this map.

In Ref. [38] the Fourier coefficients of orbits on regular 2D tori in 4D symplectic maps are used to compute the actions of these tori. In the following, the method is reviewed by generalizing it to arbitrary dimensions. Consider a  $2N$ -dimensional symplectic map with an orbit  $\boldsymbol{x}(t)$  on a regular torus in momentum–position coordinates  $\boldsymbol{x}(t) = (\boldsymbol{p}, \boldsymbol{q})(t) \in \mathbb{R}^{2N}$  and corresponding action–angle coordinates  $(\boldsymbol{I}, \boldsymbol{\Theta}(t)) \in \mathbb{R}^N \times \mathbb{T}^N$  and frequencies  $\boldsymbol{\nu}(\boldsymbol{I}) = \boldsymbol{\nu} \in [0, 1)^N$ , i.e.  $\boldsymbol{\Theta}(t) = 2\pi\boldsymbol{\nu}t$ . The Fourier series of the signal  $\boldsymbol{z}(t)$  also used for the frequency analysis, see Sec. 2.6.2 reads

$$\begin{aligned} \boldsymbol{z}(t) &= \boldsymbol{q}(t) - i\boldsymbol{p}(t) = \sum_{\boldsymbol{k}} \boldsymbol{a}_{\boldsymbol{k}} \exp(i2\pi\boldsymbol{\nu}\boldsymbol{k}t) \\ \Rightarrow \boldsymbol{z}(\boldsymbol{\Theta}) &= \sum_{\boldsymbol{k}} \boldsymbol{a}_{\boldsymbol{k}} \exp(i\boldsymbol{k}\boldsymbol{\Theta}) \end{aligned}$$

with integer vectors  $\mathbf{k} \in \mathbb{Z}^N$  and Fourier coefficients  $\mathbf{a}_{\mathbf{k}} \in \mathcal{C}^N$ . From this follows for Fourier series of the momentum–position coordinates

$$\begin{aligned} \mathbf{q}(\Theta) &= \frac{1}{2}(\mathbf{z}(\Theta) + \bar{\mathbf{z}}(\Theta)) = \frac{1}{2} \sum_{\mathbf{k}} (\mathbf{a}_{\mathbf{k}} \exp(i\mathbf{k}\Theta) + \bar{\mathbf{a}}_{\mathbf{k}} \exp(-i\mathbf{k}\Theta)) \\ \mathbf{p}(\Theta) &= -\frac{1}{2i}(\mathbf{z}(\Theta) - \bar{\mathbf{z}}(\Theta)) = -\frac{1}{2i} \sum_{\mathbf{k}} (\mathbf{a}_{\mathbf{k}} \exp(i\mathbf{k}\Theta) - \bar{\mathbf{a}}_{\mathbf{k}} \exp(-i\mathbf{k}\Theta)) . \end{aligned}$$

The actions  $\mathbf{I}$  can than be calculated using Eq. (2.4) over the closed paths  $\gamma_j$  with constant angles  $\Theta_{m \neq j}$

$$I_j = \frac{1}{2\pi} \int_0^{2\pi} \sum_{l=1}^N p_l \frac{dq_l}{d\Theta_j} d\Theta_j = \sum_{l=1}^N \frac{1}{2\pi} \int_0^{2\pi} p_l \frac{dq_l}{d\Theta_j} d\Theta_j .$$

Using the Fourier series of the coordinates from above one obtains for single term

$$\begin{aligned} \frac{1}{2\pi} \int_0^{2\pi} d\Theta_j p_l \frac{dq_l}{d\Theta_j} &= \frac{1}{2\pi} \int_0^{2\pi} d\Theta_j \left( -\frac{1}{4} \right) \sum_{\mathbf{k}, \mathbf{k}'} k'_j \\ &\quad \times (a_{l, \mathbf{k}} \exp(i\mathbf{k}\Theta) - \bar{a}_{l, \mathbf{k}} \exp(-i\mathbf{k}\Theta)) \\ &\quad \times (a_{l, \mathbf{k}'} \exp(i\mathbf{k}'\Theta) - \bar{a}_{l, \mathbf{k}'} \exp(-i\mathbf{k}'\Theta)) \\ &= \frac{1}{2\pi} \int_0^{2\pi} d\Theta_j \left( -\frac{1}{4} \right) \sum_{\mathbf{k}, \mathbf{k}'} k'_j \times \\ &\quad (a_{l, \mathbf{k}} a_{l, \mathbf{k}'} \exp(i\Theta(\mathbf{k} + \mathbf{k}')) + \bar{a}_{l, \mathbf{k}} \bar{a}_{l, \mathbf{k}'} \exp(-i\Theta(\mathbf{k} + \mathbf{k}')) \\ &\quad - a_{l, \mathbf{k}} \bar{a}_{l, \mathbf{k}'} \exp(i\Theta(\mathbf{k} - \mathbf{k}')) - \bar{a}_{l, \mathbf{k}} a_{l, \mathbf{k}'} \exp(-i\Theta(\mathbf{k} - \mathbf{k}')))) . \end{aligned}$$

The crucial step is to realize that the calculation of the action is independent of the coordinates of the remaining angles  $\Theta_{m \neq j}$ . Thus, it does not affect the result to average the equation over these angles, i.e. replace

$$\frac{1}{2\pi} \int_0^{2\pi} d\Theta_j \rightarrow \prod_{m=1}^N \frac{1}{2\pi} \int_0^{2\pi} d\Theta_m .$$

Using the Fourier representation of the Kronecker delta

$$\frac{1}{2\pi} \int_0^{2\pi} d\Theta \exp(\pm i\Theta(k - k')) = \delta_{kk'}$$

the action term reads then

$$\frac{1}{2\pi} \int_0^{2\pi} d\Theta_j p_l \frac{dq_l}{d\Theta_j} = \left(\frac{1}{4}\right) \sum_{\mathbf{k}} k_j (a_{l,\mathbf{k}} a_{l,-\mathbf{k}} + \bar{a}_{l,\mathbf{k}} \bar{a}_{l,-\mathbf{k}} + 2|a_{l,\mathbf{k}}|^2)$$

where the first two terms vanish over the sum as

$$\sum_{\mathbf{k}} k_j a_{l,\mathbf{k}} a_{l,-\mathbf{k}} = \sum_{\substack{\mathbf{k} \in K \\ \forall \mathbf{k}, \mathbf{k}' \in K: \mathbf{k} \neq -\mathbf{k}'}} (k_j a_{l,\mathbf{k}} a_{l,-\mathbf{k}} + (-k_j) a_{l,-\mathbf{k}} a_{l,\mathbf{k}}) = 0 .$$

Thus, for the actions  $\mathbf{I}$  follows

$$\boxed{I_j = \frac{1}{2} \sum_{l=1}^N \sum_{\mathbf{k}} k_j |a_{l,\mathbf{k}}|^2} . \quad (\text{A.49})$$

In order to compute the action for a regular torus, an orbit  $\mathbf{x}(t)$  on this torus is required from which using frequency analysis, see Sec. 2.6.2, the fundamental frequencies  $\boldsymbol{\nu}$  and Fourier coefficients  $\mathbf{a}_{\mathbf{k}}$  up to some maximal order  $k_{\max} = \sum_{i=1}^N |k_i|$  are obtained. Depending on how deformed the regular torus is this order has to be quite large in order to approximate the torus sufficiently well, see Ref. [189] and references therein. From these coefficients the actions are obtained according to Eq. (A.49).

Note that for resonant frequencies this method does not work as an orbit on a resonant torus is restricted to a closed lines and thus the averaging over all angles is not possible. However, as mentioned in Secs. 2.1 and 3.2.3, the action along such a closed line is a superposition of the fundamental actions. For instance, in a 4D map for a torus with the resonance  $k_1^a : k_2^a : k_3^a$  this action is  $I^a = k_2^a I_1 + k_1^a I_2$ . In a non-integrable system this action can be computed from the 1D tori remnant from the family of broken resonant 2D tori and extrapolated beyond gaps due to junctions, for examples see Sec. 3.2.1 or Refs. [186, 189]. At such a junction another independent equation  $I^b = k_2^b I_1 + k_1^b I_2$  from the crossing resonance  $k_1^b : k_2^b : k_3^b$  exists. Consequently, the fundamental actions at the junction can be computed by

$$I_1 = \frac{k_1^a I^b - k_1^b I^a}{k_1^a k_2^b - k_1^b k_2^a} \quad I_2 = -\frac{k_2^a I^b - k_2^b I^a}{k_1^a k_2^b - k_1^b k_2^a} . \quad (\text{A.50})$$

which resembles Eq. (3.5). Knowing the fundamental actions at sufficiently enough junctions may then allow to interpolate the actions on the resonances.

In Fig. A.10 the action space for the maps  $F_{\text{SC}}$  and  $F_{\text{Twist}}$  is shown with some regular tori in gray and a trapped orbit colored by its iteration time. For all calculations

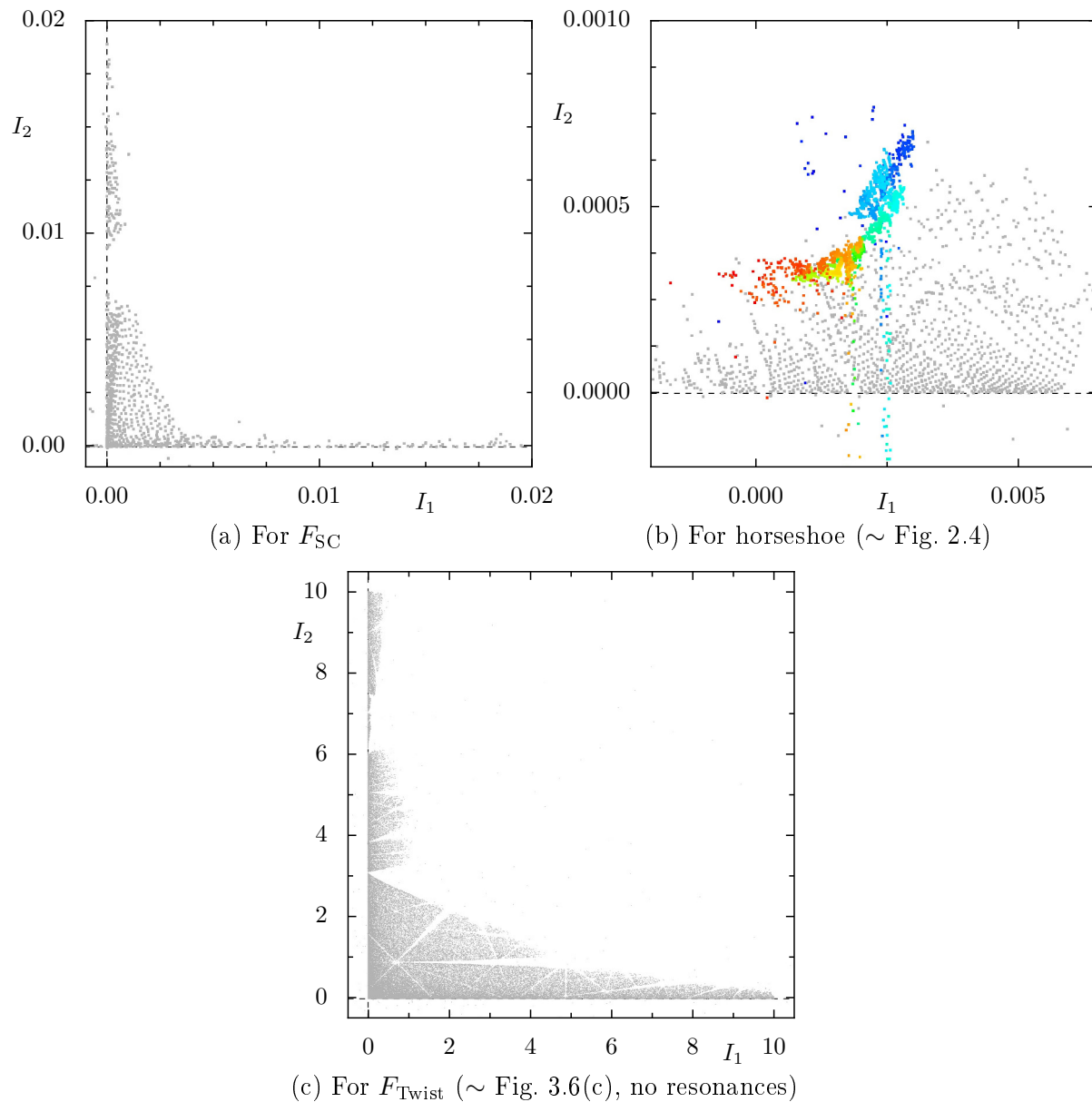


**Figure A.10:** Action space for (a) map  $F_{\text{SC}}$ , (b) horseshoe of  $F_{\text{SC}}$ , and (c) map  $F_{\text{Twist}}$  computed by Eq. (A.49) up to order  $k = |k_1| + |k_2| \leq 20$  with regular tori in gray and the trapped orbit from Fig. 2.4 in color. For (a), (b) the regular tori from Ref. [72] are used and for (c) the ones from Fig. 3.6(c), from which the most important resonances are sorted out. In (a),(c) the lines  $I_1 = 0$ ,  $I_2 = 0$  are indicated as dashed lines in the background (only  $I_2 = 0$  for (b)).



the maximal order  $k_{\max}$  is used. In Fig. A.10(a) the actions of the regular tori used in Ref. [72] excluding the horseshoe are shown. The two sharp edges known from the frequency space and corresponding to the families of 1D tori  $\mathcal{M}_1^{\text{fp}}$  and  $\mathcal{M}_2^{\text{fp}}$  nicely coincide with the lines  $I_2 = 0$  and  $I_1 = 0$ , respectively. This confirms the explanations from Sec. 3.1 according to which the edges correspond to either one of the two actions going to zero. The EE fixed point  $\vec{u}_{\text{fp}}$  corresponds to the tip  $I_1 = I_2 = 0$  in Fig. A.10(a). In Fig. A.10(b) the actions for the regular tori of the horseshoe of Ref. [72] including the trapped orbit from Fig. 2.4 are shown. Again, the edge known from the frequency space coincides with the  $I_2 = 0$  line. Several segments, mostly blue green and orange, of the trapped orbit are scattered at positions which are not expected from the arrangement in frequency space. The frequencies of these segments are too close to resonances and their actions are numerical artifacts. In fact, it is surprising that so many segments have reasonable actions as chapter 4 states that trapped orbits are exclusively governed by resonance channels.

Another remarkable feature of the actions of the horseshoe in Fig. A.10(b) is that at some point also the action  $I_1$  gets zero and even negative. This is despite the regular tori of the horseshoe being extended objects in the phase space. The explanation is that in higher-dimensional phase spaces the action equation Eq. (2.4), or see above, essentially integrates over projections to the individual degree of freedoms. In these projections regular tori can for instance appear as figure eights, encircling two separate areas with opposite sense of rotation. Such scenarios are not possible in 2D maps and can result in both zero and negative action. This situation may not be confused with fold and cusp singularities in the frequency space [76, 187], e.g., the bending of the horseshoe away from the family  $\mathcal{M}_1^{\text{fp}}$  due to the resonance  $3 : 1 : 1$ , see Sec. 3.4 and Figs. 3.1 and 3.2. Such singularities of the frequency map induce a change of the torsion  $\delta\nu/\delta I$  [12, 15].

In Fig. A.10(c) the actions for the regular tori of the coupled twist maps  $F_{\text{Twist}}$  shown in Fig. 3.6(c). In contrast to Figs. A.10(a) and A.10(b), regular tori on resonance lines are sorted out beforehand to avoid artifacts. The relevant resonant lines are obtained from the results presented in Fig. A.8. The action space strongly resembles the frequency space as expected from the construction of the map. The resemblance of the action spaces of Figs. A.10(a) and A.10(c) with the edges and the surface towards the chaotic sea again nicely illustrate how the coupled twist maps  $F_{\text{Twist}}$  displays features of a generic map. Note how the folds in the frequency space of Fig. 3.6(c) are no longer present in the action space Fig. A.10(c) as they are due to the frequency map.

## A.6 Action from fixed points in higher dimensions

At any fixed point of a symplectic map of arbitrary dimension, the linearized dynamics is a combination of elliptic (2D), hyperbolic (2D), and complex unstable (4D) degrees of freedom. Any elliptic degree of freedom can be approximated in first order by an harmonic oscillator. This produces linear approximations for the actions  $I$  of the Lyapunov family belonging to the degree of freedom. In this section, expressions for this action with respect to different parameters of the family are derived. A comparison with numerical results is presented in Sec. 3.2.1.

Consider a harmonic oscillator described by the Hamiltonian [1]

$$H = G\frac{p^2}{2} + F\frac{q^2}{2} = 2\pi I\nu = I\sqrt{GF}$$

with position–momentum coordinates  $q, p$ , the action  $I$ , the frequency  $\nu \in [0, 1)$ , and coefficients  $G, F$ , and  $R = \sqrt{F/G}$ . The orbits of this system lie on ellipses

$$q = \sqrt{\frac{2I}{R}} \sin \Theta = a \sin \Theta \quad p = \sqrt{2IR} \cos \Theta = b \cos \Theta$$

with an angle coordinate  $\Theta$ , and the half-lengths  $a, b$  of the major and minor axes. Thus, the action on a ellipse can be expressed by its area

$$I = \frac{1}{2\pi} \oint p dq = \frac{\pi ab}{2\pi} = \frac{ab}{2}$$

where the integral describes the path around the ellipse  $\Theta \in [0, 2\pi)$ . The action can be expressed in terms of the average squared radius  $\mathbb{E}[r^2]$  along an ellipse

$$\mathbb{E}[r^2] = \frac{1}{2\pi} \int_0^{2\pi} r^2 d\Theta \quad \underbrace{r^2 = p^2 + q^2}_{=} \quad \frac{a^2 + b^2}{2}$$

using  $R = b/a$

$$\boxed{I(\mathbb{E}[r^2]) = \frac{\mathbb{E}[r^2]}{R + \frac{1}{R}}} \quad (\text{A.51})$$

The action can also be expressed in terms of the circumference  $s$  of the ellipse

$$s = 4 \int_0^{\pi/2} \sqrt{a^2 \sin^2 \Theta + b^2 \cos^2 \Theta} d\Theta = 4a\sqrt{R} \underbrace{\int_0^{\pi/2} \sqrt{\frac{1}{R} \sin^2 \Theta + \cos^2 \Theta} d\Theta}_{s_0(R)}$$

that is

$$\boxed{I(s) = \frac{s^2}{32s_0(R)}} \quad (\text{A.52})$$

In order to obtain the coefficient  $R$ , consider the fixed point being at the origin  $\mathbf{0}$  with the Jacobi-Matrix  $M(\mathbf{0})$  and the two normalized eigenvectors  $\mathbf{v}_{\pm\nu}$ ,  $\|\mathbf{v}_{\pm\nu}\| = 1$  belonging to an elliptic degree of freedom with corresponding eigenvalues  $\lambda_{\pm\nu} = \exp(\pm 2\pi i\nu)$ . Since the eigenvectors are complex conjugated to each other  $\mathbf{v}_\nu = \bar{\mathbf{v}}_{-\nu}$ , real vectors  $\mathbf{v}_\nu^{\text{Re}}, \mathbf{v}_\nu^{\text{Im}}$  can be defined

$$\boxed{\mathbf{v}_\nu^{\text{Re}} = \text{Re } \mathbf{v}_\nu} \quad \boxed{\mathbf{v}_\nu^{\text{Im}} = \text{Im } \mathbf{v}_\nu} \quad (\text{A.53})$$

for which the eigenvalue equations transform to

$$\begin{aligned} M(\mathbf{0})^t \mathbf{v}_\nu^{\text{Re}} &= \cos(2\pi\nu t) \mathbf{v}_\nu^{\text{Re}} - \sin(2\pi\nu t) \mathbf{v}_\nu^{\text{Im}} \\ M(\mathbf{0})^t \mathbf{v}_\nu^{\text{Im}} &= \sin(2\pi\nu t) \mathbf{v}_\nu^{\text{Re}} + \cos(2\pi\nu t) \mathbf{v}_\nu^{\text{Im}} \end{aligned}$$

with an arbitrary  $t \in \mathbb{N}$ . Since the frequency  $\nu$  is irrational, any angle  $\Theta = 2\pi\nu t$  is realized for some iteration  $t$  and thus any point on the ellipse is reached by the orbit  $\mathbf{x}(t) = M(\mathbf{0})^t \mathbf{v}_\nu^{\text{Re}}$ . The angles  $\Theta_{a,b}$  at which the orbit is on the major or minor axis of the ellipse are the extremal points of the norm squared  $f(\Theta) = \|M(\mathbf{0})^t \mathbf{v}_\nu^{\text{Re}}\|^2$

$$\begin{aligned} f(\Theta) &= \cos^2 \Theta \|\mathbf{v}_\nu^{\text{Re}}\|^2 + \sin^2 \Theta \|\mathbf{v}_\nu^{\text{Im}}\|^2 - 2 \cos \Theta \sin \Theta (\mathbf{v}_\nu^{\text{Re}} \cdot \mathbf{v}_\nu^{\text{Im}}) \\ \frac{df(\Theta_{a,b})}{d\Theta} &= 0 \end{aligned}$$

that is

$$\boxed{\Theta_a = \frac{1}{2} \arctan \left( \frac{2(\mathbf{v}_\nu^{\text{Re}} \cdot \mathbf{v}_\nu^{\text{Im}})}{\|\mathbf{v}_\nu^{\text{Re}}\|^2 - \|\mathbf{v}_\nu^{\text{Im}}\|^2} \right)} \quad \boxed{\Theta_b = \Theta_a \pm \frac{\pi}{2}} \quad (\text{A.54})$$

from which the half-widths  $a$  and  $b$  follow

$$\boxed{a, b = \|\cos(\Theta_{a,b})\mathbf{v}_\nu^{\text{Re}} - \sin(\Theta_{a,b})\mathbf{v}_\nu^{\text{Im}}\|} \quad (\text{A.55})$$

from which  $R = b/a$  follows. Note that the notation of  $a$  and  $b$  is arbitrary and nothing is implied about which is bigger. There are some special solutions for Eq. (A.54): If the vectors are perpendicular  $(\mathbf{v}_\nu^{\text{Re}} \cdot \mathbf{v}_\nu^{\text{Im}}) = 0$ , then  $R = \|\mathbf{v}_\nu^{\text{Re}}\|/\|\mathbf{v}_\nu^{\text{Im}}\|$ . If the norms of the vectors are equal  $\|\mathbf{v}_\nu^{\text{Re}}\|^2 - \|\mathbf{v}_\nu^{\text{Im}}\|^2 = 0$ , then  $\Theta_{a,b} \in \{\pi/4, 3\pi/4, \dots\}$ . If the vectors are both perpendicular and of equal norm, then the ellipse is a circle and  $R = 1$ .

## A.7 Sticky regions of 4D map $F_{SC}$

Chaotic orbits are trapped at the surface of regular regions as rehearsed in Sec. 2.6.3. In Sec. 4.1 the power-law trapping at individual regular regions of the map  $F_{SC}$  is evaluated by associating each trapped orbit to one of these regions. The regions are introduced in Sec. 2.6.1. In this section, the protocol for this procedure is listed.

For all trapped orbits  $\mathbf{x}_i(t)$  with recurrence times  $T_i > 10^4$  the two frequencies of the middle segment  $t \in [(T_i - \Delta t)/2, (T_i + \Delta t)/2]$  are computed for the projections onto the two degrees of freedom  $(z_1, z_2)$  and only the transformation i) is performed, as explained in Sec. 2.6.2, giving a set of frequency 4-tuples  $\Omega = \{(\nu_{i,1}, \nu_{i,2})\}_i$ ,  $\nu_{i,j} \in [0, 0.5)^2$ . These frequency tuples are attributed to the regular region closest to them in frequency space. Due to artifacts of the frequency analysis some frequencies lie in areas unrelated to any regular region. For each of these areas the according segments and orbits are inspected in phase space using 3D projections and compared to regular tori. By means of proximity and geometry the corresponding regular region is identified. This allows to assign problematic areas in frequency space to the proper regular region. From these examinations the following criteria are obtained, which are applied consecutively to the set  $\Omega$ , i.e.  $(\nu_1, \nu_2) \in \Omega$ :

for  $j = 1$  or  $j = 2$ :  $\nu_{j,2} < 1.215 \cdot \nu_{j,1} - 0.066$ ,  $\nu_{j,2} > 0.273$ ,  $0.289 < \nu_{j,1} < 0.2973 \Rightarrow$  horseshoe

for  $j = 1$  or  $j = 2$ :  $\nu_{j,2} < 0.297$ ,  $\nu_{j,2} > -0.338 \cdot \nu_{j,1} + 0.336$ ,  $0.121 < \nu_{j,1} < 0.144 \Rightarrow$  central island

for  $j = 2$ :  $\nu_{j,2} \leq 0.14$ ,  $\nu_{j,2} > -2.969 \cdot \nu_{j,1} + 0.997$ ,  $\nu_{j,2} = 0.121$ ,  $\nu_{j,2} < -3.02 \cdot \nu_{j,1} + 1.02$ ,  $|24\nu_{j,1} - 7| > 10^{-4} \Rightarrow$  central island

for  $j = 1$  or  $j = 2$ :  $0.108 < \nu_{j,2} < 0.121$ ,  $\nu_{j,2} > -2.969 \cdot \nu_{j,1} + 0.997$ ,  $\nu_{j,2} < -3.02 \cdot \nu_{j,1} + 1.02 \Rightarrow$  central island

for  $j = 1$  or  $j = 2$ :  $|\nu_{j,1} + 3\nu_{j,2}| < 3 \cdot 10^{-3}$ ,  $0.25 < \nu_{j,1} < 0.295 \Rightarrow$  region around the resonance  $-1 : 3 : 0$

for  $j = 1$  or  $j = 2$ :  $-\nu_{j,1} + 3\nu_{j,2} < -3 \cdot 10^{-3}$ ,  $\nu_{j,2} > 1.932 \cdot \nu_{j,1} - 0.485 \Rightarrow$  top tower

for  $j = 1$  or  $j = 2$ :  $0.28 < \nu_{j,2} < 0.295$ ,  $0.165 > \nu_{j,2} > 0.146 \Rightarrow$  outer ring

for  $j = 1$  or  $j = 2$ :  $|5\nu_{j,1} + 1\nu_{j,2} - 1| < 10^{-3}$ ,  $0.154 < \nu_{j,1} < 0.166 \Rightarrow$  outer ring

for  $j = 1$  or  $j = 2$ :  $|7\nu_{j,1} - 1| < 5 \cdot 10^{-3}$ ,  $(0.162 < \nu_{j,2} < 0.165)$  or  $(0.271 < \nu_{j,2} < 0.276) \Rightarrow$  period 7 islands

for  $j = 1$  or  $j = 2$ :  $|7\nu_{j,1} - 2| < 5 \cdot 10^{-3}$ ,  $(0.162 < \nu_{j,2} < 0.165)$  or  $(0.271 < \nu_{j,2} < 0.276) \Rightarrow$  period 7 islands

for  $j = 1$  or  $j = 2$ :  $5\nu_{j,1} + 5\nu_{j,1} - 2 < 0$ ,  $-\nu_{j,1} + 3\nu_{j,2} > 3 \cdot 10^{-3}$ ,  $0.285 < \nu_{j,2} < 0.295$ , and not assigned yet  $\Rightarrow$  inner end of the horseshoe

for  $j = 1$  or  $j = 2$ :  $\nu_{j,2} < -\nu_{j,1} \cdot 3.842 + 1.256$ ,  $5\nu_{j,1} + 5\nu_{j,1} - 2 > 0$ ,  $0.1 < \nu_{j,2} < 0.135$ , and not assigned yet  $\Rightarrow$  horseshoe

for  $j = 1$  or  $j = 2$ :  $|20\nu_{j,1} - 2\nu_{j,2} - 5| < 5 \cdot 10^{-3}$ ,  $0.26 < \nu_{j,2} < 0.27$ , and not assigned yet  $\Rightarrow$  top tower

for  $j = 1$ :  $0.28 < \nu_{j,2} < 0.295$ ,  $0.12 < \nu_{j,1} < 0.135$ , and not assigned yet  $\Rightarrow$  horseshoe



# List of Figures

2.1	Chaotic orbits trapped in hierarchy of 2D map $F_{2D}$ . . . . .	15
2.2	Comparison of 3D phase-space slice and frequency space of the 4D map $F_{SC}$ . . . . .	22
2.3	Statistics of Poincaré recurrences $P(T)$ for the map $F_{SC}$ . . . . .	26
2.4	Chaotic orbit trapped at the horseshoe in phase and frequency space . . . . .	27
3.1	Visualization of the families of elliptic 1D tori of the map $F_{SC}$ . . . . .	31
3.2	Actions $I_L$ of elliptic 1D tori of the families $\mathcal{M}_1^{fp}$ , $\mathcal{M}_2^{fp}$ . . . . .	35
3.3	Illustration of the break-up of resonant 2D tori . . . . .	37
3.4	Arrangement of EE, EH, and HH periodic orbits . . . . .	39
3.5	First level of the hierarchy with the three types $(\alpha 1)$ , $(\beta)$ , and $(\alpha 2)$ . . . . .	43
3.6	Frequencies of regular tori of the map $F_{Twist}$ for different couplings $\xi$ . . . . .	52
3.7	Trapped orbits of the map $F_{Twist}$ in frequency space . . . . .	54
3.9	Statistics of Poincaré recurrences $P(T)$ for the map $F_{Twist}$ . . . . .	57
4.1	Statistics $P(T)$ for the sticky regions of the map $F_{SC}$ . . . . .	61
4.2	Distribution of density $\rho$ and average escape time $\bar{T}$ in frequency space . . . . .	64
4.3	Distribution of eigenvalues $\sigma_{\leftrightarrow}^2$ , $\sigma_{\downarrow}^2$ of the covariance matrix in frequency space . . . . .	65
4.4	Distribution of $\rho$ , $\bar{T}$ , $\sigma_{\leftrightarrow}^2$ , $\sigma_{\downarrow}^2$ in frequency space for the map $F_{Twist}$ . . . . .	68
4.5	Trapped orbit of 2D map $F_{2D}$ in $\nu(t)$ -plot and phase space (class hierarchy) . . . . .	70
4.6	Trapped orbit of 2D map $F_{2D}$ in $\nu(t)$ -plot and phase space (level hierarchy) . . . . .	72
4.7	Trapped orbit of 2D map $F_{2D}$ in $\nu(t)$ -plot and phase space (frequent jumps) . . . . .	74
4.8	Trapped orbit of 4D map $F_{Twist}$ in $\nu_{1,2}(t)$ -plot and angle slices (region B) . . . . .	75
4.9	Trapped orbit of 4D map $F_{Twist}$ in $\tilde{\nu}_{1,2}(t)$ -plot and angle slices (region A) . . . . .	78
4.10	Trapped orbit of 4D map $F_{SC}$ in $\nu_{1,2}(t)$ -plot and $p_1$ slice (horseshoe) . . . . .	80
4.11	Comparison of the statistics $P(T)$ for 4D map $F_{Twist}$ and 3D map $F_{3D}$ . . . . .	82
4.12	Statistics of Poincaré recurrences $P(T)$ for particular actions $I_2$ of $F_{3D}$ . . . . .	83
4.13	Isolines of the average escape time $\bar{T}(\nu_1, \nu_2)$ for the maps $F_{SC}$ and $F_{Twist}$ . . . . .	84
4.14	Statistics of escape times $P(T)$ for individual resonances of the map $F_{SC}$ . . . . .	88
4.15	Statistics of escape times $P(T)$ for individual resonances of the map $F_{Twist}$ . . . . .	90
4.16	Statistics of escape times $P(T)$ for individual junctions of the map $F_{SC}$ . . . . .	92

---

4.17	Statistics of escape times $P(T)$ for individual junctions of the map $F_{\text{Twist}}$ . . .	94
4.18	Chaotic orbits within the channel $0 : 6 : 5$ of $F_{\text{Twist}}$ in 3D projections . . . . .	107
4.19	Stochastic layer of the channel $0 : 6 : 5$ of $F_{\text{Twist}}$ in 2D slices . . . . .	108
4.20	Volume $V(I_1^0)$ and $V'(I_1^0)/V(I_1^0)$ of the channel $0 : 6 : 5$ of $F_{\text{Twist}}$ . . . . .	111
A.1	Resonance channel $0 : 6 : 5$ of $F_{\text{Twist}}$ in 2D slices . . . . .	116
A.2	Resonance channel $0 : 6 : 5$ of the map $F_{\text{Twist}}$ in frequency space . . . . .	118
A.3	Transport along resonance channel $0 : 6 : 5$ with $I_1^0 = 0.52$ , $\Delta t = 1024$ . . . . .	120
A.4	Transport along resonance channel $0 : 6 : 5$ with $I_1^0 = 0.52$ , $\Delta t = 4096$ . . . . .	121
A.5	Transport along resonance channel $0 : 6 : 5$ with long pre-iteration . . . . .	124
A.7	Number $N(k)$ of unique resonances $k_1 : k_2 : k_3$ per order . . . . .	136
A.8	Fraction $A(k)$ of frequencies at resonances with width $2\epsilon_0$ . . . . .	141
A.9	Distribution $\rho(d)$ of frequencies over the distance $d$ to a resonance . . . . .	142
A.10	Action space for $F_{\text{SC}}$ , horseshoe, and $F_{\text{Twist}}$ . . . . .	154



# Bibliography

- [1] A. J. Lichtenberg and M. A. Leiberman: *Regular and Chaotic Dynamics*, (Springer–Verlag, New York), 2nd edn., (1992).
- [2] J. Laskar: *Large scale chaos and marginal stability in the solar system*, *Celest. Mech. Dyn. Astr.* **64** (1996), 115–162.
- [3] J. Laskar, M. Gastineau, J.-B. Delisle, A. Farrés, and A. Fienga: *Strong chaos induced by close encounters with Ceres and Vesta*, *Astron. & Astrophys.* **532** (2011), L4.
- [4] K. Kaneko and R. J. Bagley: *Arnold Diffusion, Ergodicity, and Intermittency in Coupled Standard Mapping*, *Phys. Lett. A* **110** (1985), 435–440.
- [5] S. Udry and D. Pfenniger: *Stochasticity in elliptical galaxies*, *Astron. & Astrophys.* **198** (1988), 135–149.
- [6] J. Laskar: *The chaotic motion of the solar system: A numerical estimate of the size of the chaotic zones*, *Icarus* **88** (1990), 266–291.
- [7] P. M. Cincotta: *Arnold diffusion: an overview through dynamical astronomy*, *New Astron. Rev.* **46** (2002), 13–39.
- [8] A. Malyshev and L. Chizhova: *Arnol'd diffusion in a system with 2.5 degrees of freedom: Classical and quantum mechanical approaches*, *J. Exp. Theor. Phys.* **110** (2010), 837–844.
- [9] L. Zachilas, M. Katsanikas, and P. A. Patsis: *The structure of phase space close to fixed points in a 4D symplectic map*, *Int. J. Bifurcat. Chaos* **23** (2013), 1330023.
- [10] R. I. Páez and C. Efthymiopoulos: *Modeling Trojan dynamics: diffusion mechanisms through resonances*, in: *Complex Planetary Systems*, vol. 9 of *Proceedings of the International Astronomical Union*, 96–97, (2014).
- [11] C. Jung and E. E. Zotos: *Order and chaos in a three dimensional galaxy model*, *Mechanics Research Communications* **69** (2015), 45–53.
- [12] H. S. Dumas and J. Laskar: *Global dynamics and long-time stability in Hamiltonian systems via numerical frequency analysis*, *Phys. Rev. Lett.* **70** (1993), 2975–2979.

- 
- [13] A. Bazzani, S. Siboni, and G. Turchetti: *Action diffusion for symplectic maps with a noisy linear frequency*, J. Phys. A **30** (1997), 27–36.
- [14] M. N. Vrahatis, H. Isliker, and T. C. Bountis: *Structure and Breakdown of Invariant Tori in a 4-D Mapping Model of Accelerator Dynamics*, Int. J. Bifurcat. Chaos **7** (1997), 2707–2722.
- [15] J. Laskar: *Frequency map analysis and particle accelerators*, in: *Proceedings of the 2003 Particle Accelerator Conference.*, vol. 1, 378–382, (2003).
- [16] Y. Papaphilippou: *Detecting chaos in particle accelerators through the frequency map analysis method*, Chaos **24** (2014), 024412.
- [17] P. Schlagheck and A. Buchleitner: *Stable classical configurations in strongly driven helium*, Physica D **131** (1999), 110–124.
- [18] S. Gekle, J. Main, T. Bartsch, and T. Uzer: *Extracting Multidimensional Phase Space Topology from Periodic Orbits*, Phys. Rev. Lett. **97** (2006), 104101.
- [19] S. Keshavamurthy: *Dynamical tunneling in molecules: quantum routes to energy flow*, Int. Rev. Phys. Chem. **26** (2007), 521–584.
- [20] R. Paškauskas, C. Chandre, and T. Uzer: *Dynamical Bottlenecks to Intramolecular Energy Flow*, Phys. Rev. Lett. **100** (2008), 083001.
- [21] H. Waalkens, R. Schubert, and S. Wiggins: *Wigner’s dynamical transition state theory in phase space: classical and quantum*, Nonlinearity **21** (2008), R1–R118.
- [22] I. I. Shevchenko: *Hamiltonian intermittency and Lévy flights in the three-body problem*, Phys. Rev. E **81** (2010), 066216.
- [23] L. P. Sanders, M. A. Lomholt, L. Lizana, K. Fogelmark, R. Metzler, and T. Ambjörnsson: *Severe slowing-down and universality of the dynamics in disordered interacting many-body systems: ageing and ultraslow diffusion*, New J. Phys. **16** (2014), 113050.
- [24] A. K. Mazur and D. Shepelyansky: *Algebraic Statistics of Poincaré Recurrences in a DNA Molecule*, Phys. Rev. Lett. **115** (2015), 188104.
- [25] S. Hallerberg and A. S. de Wijn: *Understanding and controlling regime switching in molecular diffusion*, Phys. Rev. E **90** (2014), 062901.
- [26] A. Buchleitner, D. Delande, J. Zakrzewski, R. N. Mantegna, M. Arndt, and H. Walther: *Multiple Time Scales in the Microwave Ionization of Rydberg Atoms*, Phys. Rev. Lett. **75** (1995), 3818–3821.
- [27] G. Benenti, G. Casati, G. Maspero, and D. L. Shepelyansky: *Quantum Poincaré Recurrences for a Hydrogen Atom in a Microwave Field*, Phys. Rev. Lett. **84** (2000), 4088–4091.

- [28] M. Michler, A. Bäcker, R. Ketzmerick, H.-J. Stöckmann, and S. Tomsovic: *Universal Quantum Localizing Transition of a Partial Barrier in a Chaotic Sea*, Phys. Rev. Lett. **109** (2012), 234101.
- [29] M. J. Körber, A. Bäcker, and R. Ketzmerick: *Localization of Chaotic Resonance States due to a Partial Transport Barrier*, Phys. Rev. Lett. **115** (2015), 254101.
- [30] A. Shojiguchi, C.-B. Li, T. Komatsuzaki, and M. Toda: *Fractional behavior in nonergodic reaction processes of isomerization*, Phys. Rev. E **75** (2007), 035204(R).
- [31] A. Shojiguchi, C.-B. Li, T. Komatsuzaki, and M. Toda: *Fractional behavior in multidimensional Hamiltonian systems describing reactions*, Phys. Rev. E **76** (2007), 056205, erratum ibid. **77**, 019902 (2008).
- [32] E. G. Altmann and H. Kantz: *Hypothesis of strong chaos and anomalous diffusion in coupled symplectic maps*, Europhys. Lett. **78** (2007), 10008.
- [33] C. Manchein, M. W. Beims, and J. M. Rost: *Characterizing the dynamics of higher dimensional nonintegrable conservative systems*, Chaos **22** (2012), 033137.
- [34] J. D. Meiss and E. Ott: *Markov-Tree Model of Intrinsic Transport in Hamiltonian Systems*, Phys. Rev. Lett. **55** (1985), 2741–2744.
- [35] B. V. Chirikov and D. L. Shepelyansky: *Statistics of Poincaré Recurrences and the Structure of the Stochastic Layer of a Nonlinear Resonance*, Tech. Rep. PPPL-TRANS-133, Princeton Univ., (1983).
- [36] M. Ding, T. Bountis, and E. Ott: *Algebraic escape in higher dimensional Hamiltonian systems*, Phys. Lett. A **151** (1990), 395–400.
- [37] D. L. Shepelyansky: *Poincaré recurrences in Hamiltonian systems with a few degrees of freedom*, Phys. Rev. E **82** (2010), 055202(R).
- [38] A. Bazzani, L. Bongini, and G. Turchetti: *Analysis of resonances in action space for symplectic maps*, Phys. Rev. E **57** (1998), 1178–1180.
- [39] C. Efthymiopoulos and M. Harsoula: *The speed of Arnold diffusion*, Physica D **251** (2013), 19–38.
- [40] M. Guzzo and E. Lega: *The numerical detection of the Arnold web and its use for long-term diffusion studies in conservative and weakly dissipative systems*, Chaos **23** (2013), 023124.
- [41] C. Martens, M. Davis, and G. Ezra: *Local frequency analysis of chaotic motion in multidimensional systems: energy transport and bottlenecks in planar OCS*, Chem. Phys. Lett. **142** (1987), 519–528.

- [42] J. Laskar: *Frequency analysis of a dynamical system*, *Celest. Mech. Dyn. Astr.* **56** (1993), 191–196.
- [43] J. Laskar: *Frequency analysis for multi-dimensional systems. Global dynamics and diffusion*, *Physica D* **67** (1993), 257–281.
- [44] C. Chandre, S. Wiggins, and T. Uzer: *Time-frequency analysis of chaotic systems*, *Physica D* **181** (2003), 171–196.
- [45] R. Paškauskas, C. Chandre, and T. Uzer: *Bottlenecks to vibrational energy flow in carbonyl sulfide: Structures and mechanisms*, *J. Chem. Phys.* **130** (2009), 164105.
- [46] A. Sethi and S. Keshavamurthy: *Driven coupled Morse oscillators: visualizing the phase space and characterizing the transport*, *Mol. Phys.* **110** (2012), 717–727.
- [47] S. Gekle, J. Main, T. Bartsch, and T. Uzer: *Hydrogen atom in crossed electric and magnetic fields: Phase space topology and torus quantization via periodic orbits*, *Phys. Rev. A* **75** (2007), 023406.
- [48] V. I. Arnol'd: *Instability of dynamical systems with several degrees of freedom*, *Sov. Math. Dokl.* **5** (1964), 581–585.
- [49] B. V. Chirikov: *A universal instability of many-dimensional oscillator systems*, *Phys. Rep.* **52** (1979), 263–379.
- [50] J. Tennyson: *Resonance transport in near-integrable systems with many degrees of freedom*, *Physica D* **5** (1982), 123–135.
- [51] M. A. Lieberman and J. L. Tennyson: *Chaotic Motion Along Resonance Layers in Near-Integrable Hamiltonian Systems with Three or More Degrees of Freedom*, in: *Long-time prediction in dynamics* (Eds. C. W. Horton Jr., L. E. Reichl and V. G. Szebehely), 179–211, (Wiley, New York), (1983).
- [52] B. V. Chirikov, M. A. Lieberman, D. L. Shepelyansky, and F. M. Vivaldi: *A theory of modulational diffusion*, *Physica D* **14** (1985), 289–304.
- [53] D. Treschev: *Arnold diffusion far from strong resonances in multidimensional a priori unstable Hamiltonian systems*, *Nonlinearity* **25** (2012), 2717–2757.
- [54] V. Kaloshin and K. Zhang: *Arnold diffusion for smooth convex systems of two and a half degrees of freedom*, *Nonlinearity* **28** (2015), 2699–2720.
- [55] L. Lerman and A. Markova: *On symplectic dynamics near a homoclinic orbit to 1-elliptic fixed point*, *Trans. Moscow Math. Soc.* **76** (2015), 271–299.
- [56] P. Lochack: *Arnold diffusion; A compendium of remarks and questions*, in: Simó [218], 168–183.
- [57] D. W. Oxtoby and S. A. Rice: *Nonlinear resonance and stochasticity in intramolecular energy exchange*, *J. Chem. Phys.* **65** (1976), 1676–1683.

- [58] F. Cachucho, P. Cincotta, and S. Ferraz-Mello: *Chirikov diffusion in the asteroidal three-body resonance (5, -2, -2)*, *Celest. Mech. Dyn. Astr.* **108** (2010), 35–58.
- [59] P. M. Cincotta, C. Efthymiopoulos, C. M. Giordano, and M. F. Mestre: *Chirikov and Nekhoroshev diffusion estimates: Bridging the two sides of the river*, *Physica D* **266** (2014), 49–64.
- [60] C. Martens, M. Davis, and G. Ezra: *Pathways for Energy Redistribution and Phase Space Bottlenecks in Many-Dimensional Systems*, unpublished, see [http://www.chem.cornell.edu/gse1/ocs\\_2.pdf](http://www.chem.cornell.edu/gse1/ocs_2.pdf).
- [61] V. Gelfreich, C. Simó, and A. Vieiro: *Dynamics of symplectic maps near a double resonance*, *Physica D* **243** (2013), 92–110.
- [62] B. P. Wood, A. J. Lichtenberg, and M. A. Lieberman: *Arnold diffusion in weakly coupled standard maps*, *Phys. Rev. A* **42** (1990), 5885–5893.
- [63] M. Guzzo, E. Lega, and C. Froeschlé: *First numerical evidence of global Arnold diffusion in quasi-integrable systems*, *Discrete Contin. Dyn. Sys. Ser. B* **5** (2005), 687–698.
- [64] S. Honjo and K. Kaneko: *Structure of Resonances and Transport in Multi-dimensional Hamiltonian Dynamical Systems*, in: *Geometric Structures of Phase Space in Multidimensional Chaos: Applications to Chemical Reaction Dynamics in Complex Systems* (Eds. M. Toda, T. Komatsuzaki, T. Konishi, R. S. Berry and S. A. Rice), vol. 130 of *Advances in Chemical Physics*, chap. 22, 437–463, (John Wiley & Sons, Inc., Hoboken, New Jersey), (2005).
- [65] K. Vadim and L. Mark: *Geometry of Arnold Diffusion*, *SIAM Review* **50** (2008), 702–720.
- [66] M. F. Mestre, A. Bazzani, P. M. Cincotta, and C. M. Giordano: *Stochastic approach to diffusion inside the chaotic layer of a resonance*, *Phys. Rev. E* **89** (2014), 012911.
- [67] S.-h. Kim and S. Ostlund: *Renormalization of Mappings of the Two-Torus*, *Phys. Rev. Lett.* **55** (1985), 1165–1168.
- [68] S. Wiggins: *On the geometry of transport in phase space I. Transport in  $k$ -degree-of-freedom Hamiltonian systems,  $2 \leq k < \infty$* , *Physica D* **44** (1990), 471–501.
- [69] R. S. MacKay and J. D. Meiss: *Cantori for symplectic maps near the anti-integrable limit*, *Nonlinearity* **5** (1992), 149–160.
- [70] J. D. Meiss: *Thirty years of turnstiles and transport*, *Chaos* **25** (2015), 097602.
- [71] A. Luque and J. Villanueva: *A KAM theorem without action-angle variables for elliptic lower dimensional tori*, *Nonlinearity* **24** (2011), 1033–1080.

- [72] S. Lange: *Trapping of chaotic orbits in 4D symplectic maps*, Diploma thesis, Technische Universität Dresden, Fachrichtung Physik, (2012).
- [73] M. Michler: *Neue Methoden zur Bestimmung der Verteilung Poincaré'scher Rückkehrzeiten*, Diplomarbeit, Technische Universität Dresden, Fachrichtung Physik, (2007).
- [74] E. Ott: *Chaos in Dynamical Systems*, (Cambridge University Press, Cambridge, United Kingdom), 2nd edn., (2002).
- [75] M. Born: *The Mechanics of the Atom*, (G. Bell & Sons, Ltd., London), (1927).
- [76] H. R. Dullin and J. D. Meiss: *Twist singularities for symplectic maps*, *Chaos* **13** (2003), 1–16.
- [77] L. Markus and K. R. Meyer: *Generic Hamiltonian Dynamical Systems are neither Integrable nor Ergodic*, no. 144 in Mem. Amer. Math. Soc., (American Mathematical Society, Providence, Rhode Island), (1974).
- [78] R. S. MacKay, J. D. Meiss, and I. C. Percival: *Stochasticity and Transport in Hamiltonian Systems*, *Phys. Rev. Lett.* **52** (1984), 697–700.
- [79] H. Kook and J. D. Meiss: *Periodic orbits for reversible, symplectic mappings*, *Physica D* **35** (1989), 65–86.
- [80] J. D. Meiss: *Symplectic maps, variational principles, and transport*, *Rev. Mod. Phys.* **64** (1992), 795–848.
- [81] G. Gómez, W. S. Koon, M. W. Lo, J. E. Marsden, J. Masdemont, and S. D. Ross: *Connecting orbits and invariant manifolds in the spatial restricted three-body problem*, *Nonlinearity* **17** (2004), 1571.
- [82] R. M. da Silva, M. W. Beims, and C. Manchein: *Recurrence-time statistics in non-Hamiltonian volume-preserving maps and flows*, *Phys. Rev. E* **92** (2015), 022921.
- [83] T. Kovács and Z. Regály: *Transient Chaos and Fractal Structures in Planetary Feeding Zones*, *The Astrophysical Journal Letters* **798** (2015), L9.
- [84] F. Schilder, H. M. Osinga, and W. Vogt: *Continuation of Quasi-periodic Invariant Tori*, *SIAM J. Appl. Dyn. Syst.* **4** (2005), 459–488.
- [85] F. Montoya, M. Rivera, J. Escalona, and P. Parmananda: *Construction of Arnold tongue structures for coupled periodic oscillators*, *Phys. Lett. A* **377** (2013), 3124–3127.
- [86] C. G. Antonopoulos, T. Bountis, and L. Drossos: *Coupled symplectic maps as models for subdiffusive processes in disordered Hamiltonian lattices*, *App. Numer. Math.* (None).

- 
- [87] C. Mulhern, D. Hennig, and A. D. Burbanks: *The coupled dynamics of two particles with different limit sets*, The European Physical Journal B **86** (2013), 1–6.
- [88] D. Hennig, C. Mulhern, and A. Burbanks: *From strong chaos via weak chaos to regular behaviour: Optimal interplay between chaos and order*, Physica D **253** (2013), 102–110.
- [89] R. M. Amro, B. Lindner, and A. B. Neiman: *Phase Diffusion in Unequally Noisy Coupled Oscillators*, Phys. Rev. Lett. **115** (2015), 034101.
- [90] Y. Li, N. Li, and B. Li: *Temperature dependence of thermal conductivities of coupled rotator lattice and the momentum diffusion in standard map*, The European Physical Journal B **88** (2015).
- [91] P. Gaspard and S. A. Rice: *Hamiltonian mapping models of molecular fragmentation*, J. Phys. Chem. **93** (1989), 6947–6957.
- [92] R. E. Gillilan and G. S. Ezra: *Transport and turnstiles in multidimensional Hamiltonian mappings for unimolecular fragmentation: Application to van der Waals predissociation*, J. Chem. Phys. **94** (1991), 2648–2668.
- [93] S. Keshavamurthy: *Scaling perspective on Intramolecular vibrational energy flow*, in: *Advances in Chemical Physics* (Eds. S. A. Rice and A. R. Dinner), 43–110, (John Wiley & Sons, Inc.), (2013).
- [94] L. Bunimovich: *Relative volume of Kolmogorov-Arnold-Moser tori and uniform distribution, stickiness and nonstickiness in Hamiltonian systems*, Nonlinearity **21** (2008), T13–T17.
- [95] M. Sevryuk: *KAM tori: persistence and smoothness*, Nonlinearity **21** (2008), T177–T185.
- [96] J. Guckenheimer, B. Krauskopf, H. M. Osinga, and B. Sandstede: *Invariant manifolds and global bifurcations*, Chaos **25** (2015), 097604.
- [97] H. Poincaré: *Sur le problème des trois corps et les équations de la dynamique*, Acta Math. **13** (1890).
- [98] V. I. Arnold and A. Avez: *Ergodic Problems of Classical Mechanics*, (Benjamin, NewYork), (1968).
- [99] I. P. Cornfeld, S. V. Fomin, and Ya. G. Sinai: *Ergodic Theory*, no. 245 in Grundlehren der Mathematischen Wissenschaften, (Springer Verlag, New York), (1982).
- [100] M. Weiss, L. Hufnagel, and R. Ketzmerick: *Can simple renormalization theories describe the trapping of chaotic trajectories in mixed systems?*, Phys. Rev. E **67** (2003), 046209.

- 
- [101] J. D. Meiss: *Average exit time for volume-preserving maps*, Chaos **7** (1997), 139–147.
- [102] B. V. Chirikov and D. L. Shepelyansky: *Asymptotic Statistics of Poincaré Recurrences in Hamiltonian Systems with Divided Phase Space*, Phys. Rev. Lett. **82** (1999), 528–531.
- [103] T. Geisel, A. Zacherl, and G. Radons: *Generic  $1/f$  noise in chaotic Hamiltonian dynamics*, Phys. Rev. Lett. **59** (1987), 2503–2506.
- [104] T. Geisel, A. Zacherl, and G. Radons: *Chaotic diffusion and  $1/f$ -noise of particles in two-dimensional solids*, Z. Phys. B **71** (1988), 117–127.
- [105] G. M. Zaslavsky, M. Edelman, and B. A. Niyazov: *Self-similarity, renormalization, and phase space nonuniformity of Hamiltonian chaotic dynamics*, Chaos **7** (1997), 159–181.
- [106] G. M. Zaslavsky and M. Edelman: *Hierarchical structures in the phase space and fractional kinetics: I. Classical systems*, Chaos **10** (2000), 135–146.
- [107] Y. I. Boev, T. E. Vadivasova, and V. S. Anishchenko: *Poincaré recurrence statistics as an indicator of chaos synchronization*, Chaos **24** (2014), 023110.
- [108] E. G. Altmann and A. Endler: *Noise-Enhanced Trapping in Chaotic Scattering*, Phys. Rev. Lett. **105** (2010), 244102.
- [109] T. S. Krüger, P. P. Galuzio, T. d. L. Prado, R. L. Viana, J. D. Szezech, and S. R. Lopes: *Mechanism for stickiness suppression during extreme events in Hamiltonian systems*, Phys. Rev. E **91** (2015), 062903.
- [110] B. V. Chirikov and D. L. Shepelyansky: *Correlation properties of dynamical chaos in Hamiltonian systems*, Physica D **13** (1984), 395–400.
- [111] J. D. Meiss and E. Ott: *Markov Tree Model of Transport in Area-Preserving Maps*, Physica D **20** (1986), 387–402.
- [112] B. V. Chirikov and D. L. Shepelyansky: *Chirikov and Shepelyansky Reply*, Phys. Rev. Lett. **89** (2002), 239402.
- [113] R. Artuso and C. Manchein: *Instability statistics and mixing rates*, Phys. Rev. E **80** (2009), 036210.
- [114] G. Cristadoro and R. Ketzmerick: *Universality of Algebraic Decays in Hamiltonian Systems*, Phys. Rev. Lett. **100** (2008), 184101.
- [115] R. Venegeroles: *Universality of Algebraic Laws in Hamiltonian Systems*, Phys. Rev. Lett. **102** (2009), 064101.
- [116] R. Ceder and O. Agam: *Fluctuations in the relaxation dynamics of mixed chaotic systems*, Phys. Rev. E **87** (2013), 012918.



- [117] E. G. Altmann, A. E. Motter, and H. Kantz: *Stickiness in Hamiltonian systems: From sharply divided to hierarchical phase space*, Phys. Rev. E **73** (2006), 026207.
- [118] E. G. Altmann: *Intermittent chaos in Hamiltonian Dynamical Systems*, Dissertation, Fachbereich Mathematik und Naturwissenschaften (Fachgruppe Physik), Bergische Universität Wuppertal, (2007).
- [119] J. D. da Fonseca, D. del Castillo-Negrete, and I. L. Caldas: *Area-preserving maps models of gyroaveraged  $E \times B$  chaotic transport*, Phys. Plasmas **21** (2014), 092310.
- [120] A. J. Dragt and J. M. Finn: *Lie series and invariant functions for analytic symplectic maps*, J. Math. Phys. **17** (1976), 2215–2227.
- [121] J.-M. Mao, I. I. Satija, and B. Hu: *Evidence for a new period-doubling sequence in four-dimensional symplectic maps*, Phys. Rev. A **32** (1985), 1927–1929.
- [122] C. Froeschle: *On the number of isolating integrals in systems with three degrees of freedom*, Astrophys. Space Sci. **14** (1971), 110–117.
- [123] G. Györgyi, F. H. Ling, and G. Schmidt: *Torus structure in higher-dimensional Hamiltonian systems*, Phys. Rev. A **40** (1989), 5311–5318.
- [124] B. P. Wood, A. J. Lichtenberg, and M. A. Lieberman: *Arnold and Arnold-like diffusion in many dimensions*, Physica D **71** (1994), 132–145.
- [125] S. Honjo and K. Kaneko: *Is Arnold diffusion relevant to global diffusion?*, in: *Over the resonance, 35th Symposium on Celestial Mechanics* (Eds. E. Kokubo, H. Arakida and T. Yamamoto), 367–376, Mitaka, Japan, (2003), National Astronomical Observatory.
- [126] E. Lega, M. Guzzo, and C. Froeschlé: *Detection of Arnold diffusion in Hamiltonian systems*, Physica D **182** (2003), 179–187.
- [127] A. Seibert, S. Denisov, A. V. Ponomarev, and P. Hänggi: *Mapping the Arnold web with a graphic processing unit*, Chaos **21** (2011), 043123.
- [128] S. M. Graff: *On the conservation of hyperbolic invariant tori for Hamiltonian systems*, J. Diff. Eqs. **15** (1974), 1–69.
- [129] E. Zehnder: *Generalized implicit function theorems with applications to some small divisor problems, II*, Comm. Pure Appl. Math. **29** (1976), 49–111.
- [130] L. H. Eliasson: *Perturbations of stable invariant tori for Hamiltonian systems*, Ann. Sc. Norm. Super. Pisa, Cl. Sci. **15** (1988), 115–147.
- [131] J. Pöschel: *On elliptic lower dimensional tori in Hamiltonian systems*, Math. Z. **202** (1989), 559–608.

- 
- [132] E. Todesco: *Analysis of resonant structures of four-dimensional symplectic mappings, using normal forms*, Phys. Rev. E **50** (1994), R4298–R4301.
- [133] À. Jorba and J. Villanueva: *On the Persistence of Lower Dimensional Invariant Tori under Quasi-Periodic Perturbations*, J. Nonlinear Sci. **7** (1997), 427–473.
- [134] À. Jorba and J. Villanueva: *On the normal behaviour of partially elliptic lower-dimensional tori of Hamiltonian systems*, Nonlinearity **10** (1997), 783–822.
- [135] M. Sevryuk and A. Lahiri: *Bifurcations of families of invariant curves in four-dimensional reversible mappings*, Phys. Lett. A **154** (1991), 104–110.
- [136] T. K. Roy and A. Lahiri: *Reversible Hopf bifurcation in four-dimensional maps*, Phys. Rev. A **44** (1991), 4937–4944.
- [137] A. Lahiri, A. Bhowal, and T. K. Roy: *Resonant collisions in four-dimensional reversible maps: A description of scenarios*, Physica D **112** (1998), 95–116.
- [138] S. Lange, M. Richter, F. Onken, A. Bäcker, and R. Ketzmerick: *Global structure of regular tori in a generic 4D symplectic map*, Chaos **24** (2014), 024409.
- [139] J. D. Meiss: *Class renormalization: Islands around islands*, Phys. Rev. A **34** (1986), 2375–2383.
- [140] O. Alus, S. Fishman, and J. D. Meiss: *Statistics of the island-around-island hierarchy in Hamiltonian phase space*, Phys. Rev. E **90** (2014), 062923.
- [141] A. M. Ozorio de Almeida: *Hamiltonian Systems: Chaos and Quantization*, (Cambridge University Press, Cambridge), (1988).
- [142] S.-i. Goto and K. Nozaki: *Dynamics near Resonance Junctions in Hamiltonian Systems*, Progress of Theoretical Physics **102** (1999), 937–946.
- [143] A. Kruscha, R. Ketzmerick, and H. Kantz: *Biased diffusion inside regular islands under random symplectic perturbations*, Phys. Rev. E **85** (2012), 066210.
- [144] O. Castejón and V. Kaloshin: *Random Iteration of Maps on a Cylinder and diffusive behavior*, arXiv:1501.03319 [math] (2015).
- [145] A. Delshams, M. Gidea, R. de la Llave, and T. M. Seara: *Geometric approaches to the problem of instability in Hamiltonian systems. An informal presentation*, in: *Hamiltonian Dynamical Systems and Applications* (Ed. W. Craig), NATO Science for Peace and Security Series, 285–336, (Springer Netherlands), (2008).
- [146] R. Bartolini, A. Bazzani, M. Giovannozzi, W. Scandale, and E. Todesco: *Tune evaluation in simulations and experiments*, Part. Accel. **52** (1996), 147–177.
- [147] G. Benettin, L. Galgani, A. Giorgilli, and J.-M. Strelcyn: *Lyapunov Characteristic Exponents for smooth dynamical systems and for Hamiltonian systems; A method for computing all of them. Part 1: Theory*, Meccanica **15** (1980), 9–20.

- [148] Ch. Skokos: *The Lyapunov Characteristic Exponents and Their Computation*, Lect. Notes Phys. **790** (2010), 63–135.
- [149] C. Froeschlé, E. Lega, and R. Gonczi: *Fast Lyapunov Indicators. Application to asteroidal motion*, Celest. Mech. Dyn. Astr. **67** (1997), 41–62.
- [150] C. Froeschlé, M. Guzzo, and E. Lega: *Graphical Evolution of the Arnold Web: From Order to Chaos*, Science **289** (2000), 2108–2110.
- [151] C. Froeschlé and E. Lega: *On the Structure of Symplectic Mappings. The Fast Lyapunov Indicator: a Very Sensitive Tool*, Celest. Mech. Dyn. Astr. **78** (2000), 167–195.
- [152] Ch. Skokos: *Alignment indices: a new, simple method for determining the ordered or chaotic nature of orbits*, J. Phys. A **34** (2001), 10029–10043.
- [153] N. P. Maffione, L. A. Darriba, P. M. Cincotta, and C. M. Giordano: *A comparison of different indicators of chaos based on the deviation vectors: application to symplectic mappings*, Celest. Mech. Dyn. Astr. **111** (2011), 285–307.
- [154] E. E. Zotos: *The Fast Norm Vector Indicator (FNVI) method: a new dynamical parameter for detecting order and chaos in Hamiltonian systems*, Nonlinear Dynamics **70** (2012), 951–978.
- [155] M. B. Sevryuk: *Invariant tori of intermediate dimensions in Hamiltonian systems*, Regul. Chaotic Dyn. **3(1)** (1998), 39–48.
- [156] À. Jorba and M. Ollé: *Invariant curves near Hamiltonian-Hopf bifurcations of four-dimensional symplectic maps*, Nonlinearity **17** (2004), 691–710.
- [157] À. Jorba and J. Villanueva: *The Fine Geometry of the Cantor Families of Invariant Tori in Hamiltonian Systems*, in: *European Congress of Mathematics* (Eds. C. Casacuberta, R. Miró-Roig, J. Verdera and S. Xambó-Descamps), vol. 202 of *Progress in Mathematics*, 557–564, (Birkhäuser Basel), (2001).
- [158] M. Gemmi and E. Todesco: *Stability and geometry of third-order resonances in four-dimensional symplectic mappings*, Celest. Mech. Dyn. Astr. **67** (1997), 181–204.
- [159] H. R. Dullin and J. D. Meiss: *Quadratic Volume-Preserving Maps: Invariant Circles and Bifurcations*, SIAM J. Appl. Dyn. Syst. **8** (2009), 76–128.
- [160] A. M. Fox and J. D. Meiss: *Greene’s residue criterion for the breakup of invariant tori of volume-preserving maps*, Physica D **243** (2013), 45–63.
- [161] H. Broer, H. Hanßmann, À. Jorba, J. Villanueva, and F. Wagener: *Normal-internal resonances in quasi-periodically forced oscillators: a conservative approach*, Nonlinearity **16** (2003), 1751–1791.

- 
- [162] J. Meiss: *The destruction of tori in volume-preserving maps*, Commun. Nonlinear Sci. Numer. Simulat. **17** (2012), 2108–2121.
- [163] À. Haro: *Center and center-(un)stable manifolds of elliptic-hyperbolic fixed points of 4D-symplectic maps. An example: The Froeschlé map*, in: Simó [218], 403–407.
- [164] À. Jorba: *A methodology for the numerical computation of normal forms, centre manifolds and first integrals of Hamiltonian systems*, Experimental Mathematics **8** (1999), 155–195.
- [165] M. Jolly and R. Rosa: *Computation of non-smooth local centre manifolds*, J. Num. Anal. **25** (2005), 698–725.
- [166] R. E. Gillilan and W. P. Reinhardt: *Barrier recrossing in surface diffusion: A phase-space perspective*, Chem. Phys. Lett. **156** (1989), 478 – 482.
- [167] R. E. Gillilan: *Invariant surfaces and phase space flux in three-dimensional surface diffusion*, J. Chem. Phys. **93** (1990), 5300–5314.
- [168] E. Lega, M. Guzzo, and C. Froeschlé: *Numerical studies of hyperbolic manifolds supporting diffusion in symplectic mappings*, Eur. Phys. J. Special Topics **186** (2010), 3–31.
- [169] E. G. Altmann, J. C. Leitão, and J. V. Lopes: *Effect of noise in open chaotic billiards*, Chaos **22** (2012), 026114.
- [170] R. M. da Silva, C. Manchein, M. W. Beims, and E. G. Altmann: *Characterizing weak chaos using time series of Lyapunov exponents*, Phys. Rev. E **91** (2015), 062907.
- [171] G. Contopoulos and M. Harsoula: *Stickiness effects in conservative systems*, Int. J. Bifurcat. Chaos **20** (2010), 2005–2043.
- [172] A. Morbidelli and A. Giorgilli: *Superexponential Stability of KAM Tori*, J. Stat. Phys. **78** (1995), 1607–1617.
- [173] C. Froeschlé: *Numerical Study of Dynamical Systems with Three Degrees of Freedom. I. Graphical Displays of Four-Dimensional Sections*, Astron. & Astrophys. **4** (1970), 115–128.
- [174] C. Froeschlé: *Numerical Study of a Four-Dimensional Mapping*, Astron. & Astrophys. **16** (1972), 172–189.
- [175] D. Pfenniger: *Numerical study of complex instability. I. Mappings*, Astron. & Astrophys. **150** (1985), 97–111.
- [176] Ch. Skokos, G. Contopoulos, and C. Polymilis: *Structures in the Phase Space of a Four Dimensional Symplectic Map*, Celest. Mech. Dyn. Astr. **65** (1997), 223–251.

- 
- [177] L. Martinet and P. Magnenat: *Invariant surfaces and orbital behaviour in dynamical systems with 3 degrees of freedom*, *Astron. & Astrophys.* **96** (1981), 68–77.
- [178] P. Magnenat: *Numerical study of periodic orbit properties in a dynamical system with three degrees of freedom*, *Celestial Mech.* **28** (1982), 319–343.
- [179] M. N. Vrahatis, T. C. Bountis, and M. Kollmann: *Periodic orbits and invariant surfaces of 4d nonlinear mappings*, *Int. J. Bifurcat. Chaos* **6** (1996), 1425–1437.
- [180] P. A. Patsis and L. Zachilas: *Using color and rotation for visualizing four-dimensional Poincaré cross-sections: With applications to the orbital behavior of a three-dimensional Hamiltonian system*, *Int. J. Bifurcat. Chaos* **4** (1994), 1399–1424.
- [181] M. Katsanikas and P. A. Patsis: *The Structure of Invariant Tori in a 3D Galactic Potential*, *Int. J. Bifurcat. Chaos* **21** (2011), 467–496.
- [182] M. Richter, S. Lange, A. Bäcker, and R. Ketzmerick: *Visualization and comparison of classical structures and quantum states of four-dimensional maps*, *Phys. Rev. E* **89** (2014), 022902.
- [183] M. Richter: *Classical and quantum investigations of four-dimensional maps with a mixed phase space*, Ph.D. thesis, Technische Universität Dresden, Fachrichtung Physik, (2012).
- [184] Y. P. Papaphilippou: *Application de la Méthode d’Analyse en Fréquence en Dynamique Galactique*, Ph.D. thesis, Université de Paris VII, (1997).
- [185] Y. P. Papaphilippou and J. Laskar: *Global dynamics of triaxial galactic models through frequency map analysis*, *Astron. & Astrophys.* **329** (1998), 451–481.
- [186] F. Onken, S. Lange, R. Ketzmerick, and A. Bäcker: *Bifurcations of families of 1D-tori in 4D symplectic maps*, *Chaos* **26** (2016), 063124.
- [187] H. R. Dullin, A. V. Ivanov, and J. D. Meiss: *Normal forms for 4D symplectic maps with twist singularities*, *Physica D* **215** (2006), 175–190.
- [188] À. Jorba: *Numerical computation of the normal behaviour of invariant curves of n-dimensional maps*, *Nonlinearity* **14** (2001), 943–976.
- [189] F. Onken: *Bifurcations of families of 1-tori in 4D symplectic maps*, Masterthesis, Technische Universität Dresden, Fachrichtung Physik, (2015).
- [190] K. Meyer, G. Hall, and D. Offin: *Introduction to Hamiltonian Dynamical Systems and the N-Body Problem*, (Springer-Verlag, New York), (2009).
- [191] M. Sevryuk: *On invariant tori of reversible systems in the neighbourhood of an equilibrium position*, *Russ. Math. Surv.* **42** (1987), 147–148.

- [192] M. Sevryuk: *Invariant  $m$ -dimensional tori of reversible systems with phase space of dimension greater than  $2m$* , J. Sov. Math. **51** (1990), 2374–2386.
- [193] E. Todesco: *Local analysis of formal stability and existence of fixed points in  $4d$  symplectic mappings*, Physica D **95** (1996), 1–12.
- [194] À. Jorba: *On practical stability regions for the motion of a small particle close to the equilateral points of the real Earth-Moon system*, in: *Proceedings of the III International Symposium HAMSYS-98. Geometrical Methods in Hamiltonian Systems and Celestial Mechanics. Patzcuaro (Mexico)*, 7–11, (2000).
- [195] E. Castellá and À. Jorba: *On the vertical families of two-dimensional tori near the triangular points of the Bicircular problem*, Celest. Mech. Dyn. Astr. **76** (2000), 35–54.
- [196] Y. Lan, C. Chandre, and P. Cvitanović: *Newton’s descent method for the determination of invariant tori*, Phys. Rev. E **74** (2006), 046206.
- [197] A. Haro and R. de la Llave: *A Parameterization Method for the Computation of Invariant Tori and Their Whiskers in Quasi-Periodic Maps: Explorations and Mechanisms for the Breakdown of Hyperbolicity*, SIAM J. Appl. Dyn. Syst. **6** (2007), 142–207.
- [198] G. Huguet, R. de la Llave, and Y. Sire: *Computation of whiskered invariant tori and their associated manifolds: New fast algorithms*, Discrete Contin. Dyn. Sys **32** (2012), 1309–1353.
- [199] F. Onken: *Selbstähnliche Strukturen im  $4D$ -Phasenraum der stark gekoppelten Standardabbildung*, Bachelor thesis, Technische Universität Dresden, Fachrichtung Physik, (2012).
- [200] K. M. Frahm and D. L. Shepelyansky: *Ulam method for the Chirikov standard map*, Eur. Phys. J. B **76** (2010), 57–68.
- [201] L. Sabbagh: *An inclination lemma for normally hyperbolic manifolds with an application to diffusion*, Ergodic Theory Dynam. Systems **35** (2015), 2269–2291.
- [202] D. F. Escande and F. Sattin: *When Can the Fokker-Planck Equation Describe Anomalous or Chaotic Transport?*, Phys. Rev. Lett. **99** (2007), 185005.
- [203] C. W. Gardiner: *Handbook of stochastic methods*, (Springer-Verlag, Berlin), (1990).
- [204] S. Redner: *A Guide To First-Passage Processes*, (Cambridge University Press, Cambridge), (2001).
- [205] E. G. Altmann: *Intermittent chaos in Hamiltonian dynamical systems*, Ph.D. thesis, Bergische Universität Wuppertal, (2007).

- 
- [206] J. Klafter and I. M. Sokolov: *First Steps in Random Walks: From Tools to Applications*, (OUP Oxford), (2011).
- [207] D. A. Darling and A. J. F. Siegert: *The First Passage Problem for a Continuous Markov Process*, Ann. Math. Statist. **24** (1953), 624–639.
- [208] N. G. V. Kampen: *Stochastic Processes in Physics and Chemistry*, (Elsevier), (2011).
- [209] A. E. Motter, A. P. S. de Moura, C. Grebogi, and H. Kantz: *Effective dynamics in Hamiltonian systems with mixed phase space*, Phys. Rev. E **71** (2005), 036215.
- [210] K. S. Fa and E. K. Lenzi: *Anomalous diffusion, solutions, and first passage time: Influence of diffusion coefficient*, Phys. Rev. E **71** (2005), 012101.
- [211] A. G. Cherstvy, A. V. Chechkin, and R. Metzler: *Anomalous diffusion and ergodicity breaking in heterogeneous diffusion processes*, New J. Phys. **15** (2013), 083039.
- [212] A. G. Cherstvy and R. Metzler: *Population splitting, trapping, and non-ergodicity in heterogeneous diffusion processes*, Phys. Chem. Chem. Phys. **15** (2013), 20220–20235.
- [213] G. Rangarajan and M. Ding: *First passage time distribution for anomalous diffusion*, Phys. Lett. A **273** (2000), 322–330.
- [214] G. Rangarajan and M. Ding: *Anomalous diffusion and the first passage time problem*, Phys. Rev. E **62** (2000), 120–133.
- [215] R. Metzler and J. Klafter: *Boundary value problems for fractional diffusion equations*, Physica A **278** (2000), 107–125.
- [216] V. Kaloshin, J. Zhang, and K. Zhang: *Normally Hyperbolic Invariant Laminations and diffusive behaviour for the generalized Arnold example away from resonances*, arXiv:1511.04835 [math] (2015).
- [217] R. J. Levit: *A Minimum Solution of a Diophantine Equation*, The American Mathematical Monthly **63** (1956), 646–651.
- [218] C. Simó (ed.): *Hamiltonian Systems with Three or More Degrees of Freedom*, vol. 533 of *NATO ASI Series: C - Mathematical and Physical Sciences*, (Kluwer Academic Publishers, Dordrecht), (1999).

## Acknowledgments

It is a pleasure to thank Prof. Dr. Roland Ketzmerick for this interesting research project, valuable discussions, and his continuous support.

I am truly indebted and thankful to my supervisor Prof. Dr. Arnd Bäcker and my colleague Franziska Onken for the stimulating cooperation especially regarding the organization of the regular tori.

I am particularly grateful to Srihari Keshavamurthy, Jacques Laskar, Rainer Klages, and James Meiss for extended and recurrent discussions which improved my comprehension of higher-dimensional phase spaces and frequency analysis. I further had the privilege to consult Holger Kantz, Henk Broer, Christos Efthymolopoulos, Holger Dullin, David Zwicker, Eduardo Altman, Kathrin Padberg-Gehle, Matthias Wagner, Haris Skokos, and Matthaios Katsanikas.

I thank Martin Körber, Clemens Löbner, and Martin Richter for consistently helpful discussions and comments during several stages of this work.

I am grateful to Martin Körber, Franziska Onken, Veronika Bierbaum, Felix Fritsch, Alexander Schnell, Konstantin Clauss, Martin Richter, and Christian Förster for proof-reading parts of this thesis.

Furthermore, I thank all members of the computational physics group and the secretary Gundula Schädlich for the pleasant work atmosphere.

Especially I would like to thank my parents for their support during the past years.

I owe sincere gratefulness to my girlfriend Dr. Veronika Bierbaum for her empathy in stressful moments and her versed support and counsel in both science and the rest of life.



## **Versicherung**

Hiermit versichere ich, dass ich die vorliegende Arbeit ohne unzulässige Hilfe Dritter und ohne Benutzung anderer als der angegebenen Hilfsmittel angefertigt habe; die aus fremden Quellen direkt oder indirekt übernommenen Gedanken sind als solche kenntlich gemacht. Die Arbeit wurde bisher weder im Inland noch im Ausland in gleicher oder ähnlicher Form einer anderen Prüfungsbehörde vorgelegt.

Steffen Lange

Dresden, 26. Mai 2016